# Topology of ferroelectric polarization at the BaTiO3(001) surface from ab initio calculations and electron microscopy-spectroscopy

Jelle Dionot

UNIVERSITÉ PARIS-SUD

ÉCOLE DOCTORALE 564 PHYSIQUE EN ÎLE-DE-FRANCE

SPECIALTY: PHYSICS

DOCTORAL DISSERTATION

Presented by

**JELLE DIONOT**

# Topology of ferroelectric polarization at the $BaTiO_3(001)$ surface from ab initio calculations and electron microscopy and spectroscopy

Service de Physique de l'État Condensé (SPEC), CEA–CNRS UMR 3680

| | |
|---|---|
| **Director :** | Dr. Grégory Geneste |
| **Co-director :** | Dr. Nicholas Barrett |

**Committee members:**

| | |
|---|---|
| Referees: | Dr. Jorge Íñiguez |
| | Pr. Igor Kornev |
| Examiners: | Pr. Patrick Soukiassian |
| | Dr. Tevfik Onur Menteş |

UNIVERSITÉ PARIS-SUD

ÉCOLE DOCTORALE 564 PHYSIQUE EN ÎLE-DE-FRANCE

DISCIPLINE : PHYSIQUE

THÈSE DE DOCTORAT

Présentée par

JELLE DIONOT

# Topologie de la polarisation ferroélectrique à la surface (001) de $BaTiO_3$ par calculs ab initio et microscopie-spectroscopie d'électrons

Service de Physique de l'État Condensé (SPEC), CEA–CNRS UMR 3680

**Directeur de thèse :** Dr. Grégory Geneste

**Co-directeur de thèse :** Dr. Nicholas Barrett

**Composition du jury :**

Rapporteurs : Dr. Jorge Íñiguez

Pr. Igor Kornev

Examinateurs : Pr. Patrick Soukiassian

Dr. Tevfik Onur Menteş

# Abstract

We have investigated the properties of in-plane and out-of-plane polarization at the (001) surface of the ferroelectric $BaTiO_3$, from first-principles calculations and electron microscopy and spectroscopy. Screening of the depolarizing effects is efficiently performed by domain ordering. The effects of surface termination, in-plane strain, system size (slab thickness and domain periodicity) and surface stoichiometry (with oxygen vacancies) have been studied from ab initio calculations based on density functional theory under the local density approximation. The influence of surface oxygen vacancies on the polarization at the (001) surface of $BaTiO_3$ single crystals have been studied from low-energy and photoemission electron microscopy (LEEM and PEEM). The results provide an experimental support to the results obtained from the simulations.

Nous avons étudié les propriétés de surfaces ferroélectriques de $BaTiO_3$(001) polarisées dans le plan et hors-plan, à partir de calculs ab initio et de microscopie et spectroscopie d'électrons. L'écrantage des champs dépolarisants est assuré par la mise en ordre en domaines. L'effet de la terminaison de surface, de la contrainte dans le plan, de la taille du système (épaisseur de la couche de matière et périodicité des domaines) ainsi que de la stœchiométrie en oxygène ont été étudiés par des calculs ab initio basés sur la théorie de la fonctionnelle de la densité, dans l'approximation de la densité locale. L'influence des lacunes d'oxygène sur la polarisation à la surface (001) de monocristaux de $BaTiO_3$ a été étudiée par microscopie d'électrons lents (LEEM) et photoémis (PEEM). Les résultats ainsi obtenus apportent un soutien expérimental aux simulations numériques.

# Acknowledgements

Je remercie tout d'abord mon co-directeur et encadrant de thèse, Nick Barrett, qui m'a confié ce travail doctoral, pour tout l'enseignement que j'ai reçu dans un environnement scientifique et technique très privilégié. Je remercie très chaleureusement mon directeur de thèse, Grégory Geneste, qui a encadré la partie portant sur les calculs numériques avec une confiance et un optimisme sans égal. Un grand merci pour tout l'enseignement enthousiasmant qu'il m'a procuré.

J'adresse mes sincères remerciements à François Daviaud, chef du Service de l'État Condensé du CEA-Saclay, ainsi que Myriam Pannetier-Lecoeur, responsable des thèses au sein du service, pour tout leur engagement professionnel et leur bienveillance. Je remercie également Gilles Montambaux, Directeur de l'École Doctorale Physique en Ile-de-France, pour son suivi et son écoute.

Je remercie les membres du jury pour leur évaluation ainsi que les remarques et questions qui ont permis d'apporter davantage d'éclaircissements et précisions aux résultats présentés dans ce manuscrit. Je remercie les rapporteurs Igor Kornev et Jorge Íñiguez, ainsi que les examinateurs Onur Menteş et Patrick Soukiassian, président du jury, pour tous les échanges stimulants dont ils m'ont fait l'honneur ainsi que leur accueil chaleureux lors de la soutenance.

Au sein de mon groupe, je remercie Claire Mathieu pour tout son soutien et sa disponibilité, tout au long de mon passage, du stage de Master, furtivement le jour, jusqu'aux ultimes corrections du manuscrit, tardivement la nuit, et même dans les moments les plus difficiles. Je remercie vivement Jocelyne Leroy, Bruno Delomez et Christophe Lubin pour leur soutien technique et moral, année après année.

À travers les deux services que j'ai connus au sein de l'IRAMIS du CEA-Saclay, je remercie chaleureusement Serge Palacin, alors chef du SPSCI, ainsi que Luc Barbier, alors son adjoint au SPCSI puis responsable des thèses à l'IRAMIS, ainsi que Catherine Julien et Christine Prigian, pour tout leur engagement et disponibilité depuis le tout début de mon passage. Je remercie très vivement Dominique Martinotti pour m'avoir initié au LEEM et avoir été présent de longues heures à mes côtés aux commandes de cette engin qui n'avait plus de secret pour lui. Je remercie également Frédéric

Merlet qui m'a aidé à de nombreuses reprises à me sortir de situations techniques délicates, notamment auprès du LEEM. Je remercie enfin Ludovic Douillard, pour les multiples discussions éclairées sur la microscopie d'électrons, Cindy Rountree, pour m'avoir initié à l'AFM-PFM, Ludovic Tortech, pour toute sa geekerie souvent spectaculaire, ainsi que Sylvain Latil, Bruno Lectard, Yannick Dappe, Cyrille Barreteau, Daniel Bonamy, Fabien Silly, Sylvain Foucquard, Hélène Magnan, Antoine Barbier, Laurent Pham-Van, pour tous les échanges scientifiques ou non et toujours agréables au quotidien.

Au-delà des grilles du CEA-Saclay, je tiens à remercier les membres du LPMS de l'Université de Cergy-Pontoise, dont Karol Hricovini, Christine Richter et Olivier Heckmann. Je remercie également les membres de l'Unité Mixte de Physique CNRS/Thalès, dont Stéphane Fusil, Manuel Bibès et Vincent Garcia. Je remercie aussi chaleureusement les membres du laboratoire SPMS de l'École Centrale de Paris, dont Brahim Dkhil et Ingrid Canero Infante. Je remercie Vitaliy Feyer pour son extrême gentillesse et son accueil toujours positif au synchrotron Elettra, à Trieste en Italie.

Une thèse n'existerait pas s'il n'y avait pas de thésards. J'ai eu la chance de croiser le chemin de nombreuses et belles personnes tout au long de mon passage. Je remercie d'abord Maxime Rioult, qui m'a toujours épaulé, avec une constante amitié, gaieté et indispensable gaillardise. Je te remercie pour les discussions très variées que nous avons eues, tu as été un exemple pour moi. Merci à Sara Gonzalez, pour sa présence et sa gentillesse. Je te souhaite le meilleur pour la suite. Merci à Guillaume Nataf, d'avoir toujours été là, même à quelques heures de route, pour toute sa présence et son amitié. Sois heureux ! Merci également à Julien Rault, pour m'avoir mis sur les rails et encouragé jusqu'au bout. Je remercie également mon collègue de galère Ruidy Némausat, pour toute son amitié et les traits d'esprit qu'il a toujours su inspirer. Je te souhaite d'atteindre tout ce que tu vises ! Je remercie également tous les doctorants, stagiaires et amis que j'ai eu tant de chance de rencontrer durant ce travail, Jiale Wang, Daniel Gottlob, Xihui Liang, Vincent Barth, Qirong Zhu, Quentin Arnoux, Thomas Aghavnian, Tiphaine Bourgeteau, Romain Brisse, Patrick Hsia, Claire Soum, Jérémy Hieulle, David Peyrot, Laurent Nicolaï, Lisa Levasseur, Charles Paillard, Héloise Tissot, Marina Barlet, Dongzhe Li, Cédric Zobrist, Vincent Martinez, Jelena Orlovic, Camille Blouzon, Alexandra Senegas, Carole Jégou, Daniel Sando, David Le Bourdais, Romain Faye, Alexander Van Der Torren, Marten Patt. J'adresse enfin mes plus vifs remerciements à Jérôme Polesel pour son soutien, les discussions très enthousiasmantes et enrichissantes, et pour son choix de stagiaires.

Cette thèse a pu voir le jour grâce au support inconditionnel de ma famille et de mes amis. J'adresse mes premières pensées et remerciements à mes parents. Vous

m'avez appris à ne pas baisser les bras, à être curieux et à vouloir aller au bout des choses (parfois trop…) ; c'est grâce à vous que j'ai pu mener à terme ce travail, pour toutes les valeurs que vous m'avez enseignées. Je remercie mes frères et ma sœur, pour leur soutien dans les moments décisifs. Merci à mes très chers amis étudiants de longue date ; merci à mes très chers amis du LRS de l'UPMC qui m'ont tant épaulé ; merci aux Parisiens ZinzinS et celles et ceux en devenir, qui m'ont toujours soutenu et encouragé.

Enfin, je remercie très amoureusement Noémie qui m'a tant soutenu, aidé et encouragé mais aussi supporté ! Tu as ouvert et orné un pan entier de ma vie, et ta présence si bénéfique durant ce travail unique m'a été d'un secours et d'une valeur infinis.

# Contents

# Chapter I.

# Introduction

Ferroelectricity is defined by the presence of a spontaneous polarization that can be reversed by the application of an external electric field. At least two polarization states are therefore available as a measurable and tunable physical quantity, opening the way of an extremely wide variety of use and applications. Often associated with a very high dielectric permittivity, ferroelectric materials are piezoelectric and pyroelectric. The resulting properties have long made them of primary use in the development of sensors and transducers, and in the electronics industry with the mass production of multi-layer ceramic capacitors. Technological applications in the semiconductors industry have recently ensued, with the production of ferroelectric random access memory. Moreover, emerging computation technologies in the field of neuromorphic engineering, benefitting from recently evidenced memristive behavior of ferroelectric tunnel junctions, are under development.

The advent of nanosciences have sealed the need for further understanding of the fundamental properties of ferroelectric materials at low scale, in order to envision novel applications especially in the field of information technology. Namely, the dominant contribution of bound charges at polarization discontinuities supposes that the stability of ferroelectric systems strongly depends on their geometry and size, as derived by Kittel's law applied to ferroelectric thin films. Also, understanding the effect of lattice strain on the ferroelectric polarization is essential for instance in the development of multiferroic heterostructures, allowing to combine multiple ferroic orders together, even in association of semiconductors such as silicon.

The combined advent of nanoscale and surface science has settled the need for further understanding of the fundamental properties of ferroelectric materials. At the nanoscale, the fundamental properties stemming from the materials' surface, such as atomic relaxation phenomena, particular electronic structure and chemistry, become prominent. The combination of surface and ferroelectric properties in solids

therefore gives rise to a particular topology of the ferroelectric polarization. The study of the microscopic interactions embodied in the interplay between surface effects and ferroelectric polarization is therefore essential and can be performed by ab initio calculations; while the observation of the surface of ferroelectric materials under different external chemical or mechanical conditions can be made by combined electron microscopy and spectroscopy. These combined approaches are at the center of the present investigations of the topology of the ferroelectric polarization at the surface of the prototypical ferroelectric material, barium titanate.

# 1. Ferroelectricity

## 1.1. Definition and microscopic origin

A system is ferroelectric if on the one hand it displays a spontaneous electric polarization and on the other hand this polarization can be reversed under the application of an external electric field.

The spontaneous electric polarization is caused by atomic distortions from a centrosymmetric, and thus non polar, configuration. Typically, atoms carrying electric charges of opposite sign are displaced in opposite directions, inducing a dipolar moment. Ferroelectrics are therefore polar materials. They also exhibit pyroelectric and piezoelectric properties. In what follows, we describe phase transitions in ferroelectric systems with particular focus on microscopic aspects, before presenting the studied system which is the surface of $BaTiO_3$.

## 1.2. Phase transitions in ferroelectrics

In classical electrodynamics, the polarization can be defined as the average of local contributions (local dipole moments): it is thus a macroscopic quantity (note that the Modern Theory of Polarization [1, 2] gives a more complex picture of the polarization). It is non zero at low temperature because these local modes are correlated through dipole-dipole interactions, and are aligned in the same direction. At higher temperature, the average polarization becomes zero and the material becomes paraelectric. Thermal energy brings disorder to the local dipole moments and overcomes the stabilizing interactions between dipoles.

In their ferroelectric state, some materials (e.g. $BaTiO_3$ or $KNbO_3$) have different ferroelectric phases depending on temperature, each defined by the direction of its

spontaneous polarization. Such materials exhibit a series of transitions between crystalline structures characterized by the macroscopic polarization direction, defining different stable thermodynamic phases. The phase transition between the ferroelectric and paraelectric phases takes place at the Curie temperature $T_C$.

The ferroelectric-paraelectric phase transition can be described in an order-disorder or displacive view. In the *order-disorder* model, first proposed by Slater [3], permanent dipole moments exist in each unit cell at any temperature. These dipoles are correlated with each other in the ferroelectric phase and keep on average a given direction (that of the macroscopic polarization). In the paraelectric phase, however, they are disordered; each of them fluctuates in time, leading to zero macroscopic polarization. The hydrogen-bonded ferroelectric $KH_2PO_4$ is considered as the prototypical order-disorder type [4].

In the displacive model introduced by Cochran et al. [5], after the discovery of ferroelectricity in materials which do not exhibit hydrogen bonds, a specific transverse optic vibration mode, stable in the high temperature paraelectric phase, becomes unstable while approaching $T_C$. As the frequency of this mode becomes zero, polar off-center displacements take place, following the freezing of the soft mode, giving rise to the macroscopic polarization.

These models of phase transitions are two limits, and in reality ferroelectric materials show characters from the two descriptions. For perovskite ferroelectric materials, the displacive theory of Cochran et al. [5] has been first reconsidered and a pure order-disorder description (described hereafter) was proposed by Comès et al. [6,7]. Moreover, even in hydrogen-bonded ferroelectric materials, experimental evidence of the coexistence of order-disorder and displacive dynamics was measured by Nuclear Magnetic Resonance [8]. Conversely, in perovskite oxides which were long described within the displacive theory, many experimental and theoretical work have demonstrated the coexistence of characteristics from the two models [9–12]. Features of both models can be addressed to introduce the concept of ferroelectricity in barium titanate.

## 1.3. $BaTiO_3$

In this thesis, we focus on the particular case of the ferroelectric oxide of perovskite structure $BaTiO_3$. It is a ionocovalent crystal which undergoes a series of phase transitions with temperature [13]. $BaTiO_3$ is ferroelectric with a rhombohedral structure from 0 K to 183 K, orthorhombic from 183 K to 278 K, tetragonal from 278 K to 393 K and becomes paraelectric with a cubic structure above 393 K. The cubic and tetragonal

structures of $BaTiO_3$ are depicted in Figures 1.1a and 1.1b. The BaO and $TiO_2$ $(1 \times 1)$ surface terminations, that we study in this work, are represented in Figure 1.1c.

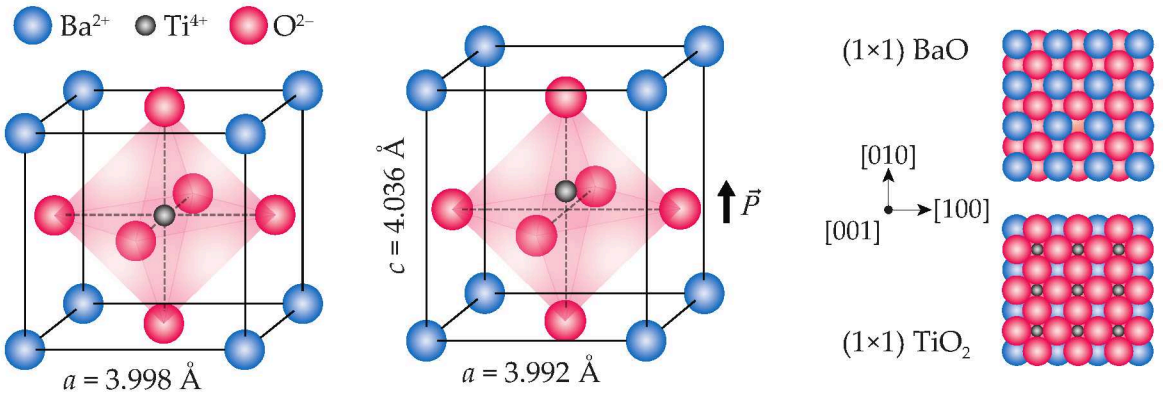


**(a)** cubic structure **(b)** tetragonal structure **(c)** surface terminations

**Figure 1.1.:** Schematic of the (a) cubic and (b) tetragonal unit cells of $BaTiO_3$ and (c) (001) surface terminations. The cubic structure is centrosymmetric while in the tetragonal structure the Ti and O atoms are relatively displaced inducing a permanent dipole moment.

In the paraelectric phase, the cubic unit cell lattice constant is $a = 3.996$ Å. The cubic structure can be described with barium at the corners, titanium at the center and oxygen in the middle of the faces. The O atoms form an octahedral cage around the central Ti. In the tetragonal phase, the unit cell elongates along the polar axis of lattice constant $c = 4.036$ Å while it shrinks along the perpendicular $a$ and $b$ axes down to $a = b = 3.992$ Å. The central Ti and the O atoms undergo a relative displacement along the polar axis, which makes the structure polar (i.e. non-centrosymmetric) and induces the dipole moment.

In the successive ferroelectric rhombohedral, orthorhombic and tetragonal phases, the macroscopic polarization is along <111>, <110> and <001>, respectively. The order-disorder model of the phase transition in $BaTiO_3$ was introduced by Comès et al. [6] with an eight-site model, based on diffuse X-ray scattering experiments. This model was further developed by Chaves et al. [14].

The eight-site model allows describing the sequence of phase transitions in $BaTiO_3$. The possible off-center displacements of the Ti ion are assumed along the <111> crystallographic directions (eight sites available), and such off-center position is energetically favorable. In the rhombohedral phase, all the Ti are trapped in *one* single site, the same for all the Ti of the crystal due to the dipole-dipole interactions. The polarization is thus along one of the <111> directions. As temperature increases, thermal energy makes neighboring sites available to the off-centered Ti. In the orthorombic phase, the Ti evolve in a subset of *two* neighboring sites (the same subset for all the Ti),

providing a polarization along one <110> direction. In the tetragonal phase, *four* sites are accessible. The local dipole moments are averaged over the accessible sites giving rise to polarization along the <001> axis. This situation is depicted in Figure 1.2

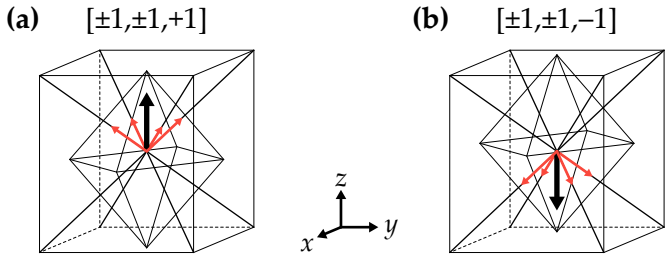


**Figure 1.2.:** Schematic of the eight-site model of the polarization in the case of a tetragonal structure. Four out of eight sites along the <111> directions are equally accessible for the Ti off-centered displacement, giving rise in average to the polarization pointing along (a) [001] and (b) $[00\bar{1}]$.

where the local dipole moment in each unit cell is oriented upwards (Fig. 1.2a) and downwards (Fig. 1.2b) in average over the four evenly accessible off-centered positions along <111>. In the paraelectric phase, the *eight* sites are all visited with the same probability, and the polarization is, on average, zero. This phase is disordered with average zero polarization in all unit cells, but correlations between neighboring unit cells can still be observed [15].

Recent X-ray absorption spectroscopy experiment performed by Ravel et al. [16] further confirmed the initial eight-site model from Comès et al. Moreover, numerical simulations based on effective Hamiltonians fitted from first-principles calculations [15, 17] also confirmed, to a certain extent, this 8-site model: for instance, in the paraelectric phase, the local modes exhibit maxima of probability along the <111> directions, but spend also much time between those sites, and the order-disorder picture is finally totally lost at a sufficiently high temperature.

In this thesis, we study the *surface* properties of ferroelectric $BaTiO_3$. General concepts of the physics of oxide surfaces [18, 19] and the particular case of ferroelectric oxide surface are thus addressed in the following.

# 2. Oxide surface physics

In this section, we describe phenomena specific to surfaces that will be encountered in this work: surface rumpling, surface stress, and electronic properties associated to the presence of the surface, as compared to the bulk.

## 2.1. Surface rumpling and relaxation

In crystalline bulk, the equilibrium positions of the atoms result from a balance between the forces generated by all the neighbors. At the surface, the atoms have a different environment: some neighbors are missing with respect to the bulk. Thus, the atoms relax to equilibrium positions different from the bulk ones. Given the translational symmetry parallel to the surface plane, the new equilibrium positions of the surface atoms involve displacements perpendicular to the surface (in this thesis we do not discuss the possibility of surface reconstruction or faceting). For ionic crystals and ionocovalent crystals such as $BaTiO_3$, the relative displacements of the cations with respect to the anions normal to the surface defines the rumpling. It usually consists of anions displaced outwards with respect to cations which are on the contrary displaced inwards. This was measured by low-energy electron diffraction (LEED) [20] and by reflection high-energy electron diffraction (RHEED) [21] on $SrTiO_3$, of similar perovskite structure as $BaTiO_3$. First-principles calculations [22–25] agree with the experimental observations on $SrTiO_3$ and show similar results for $BaTiO_3$ surfaces [26–28], and other perovskite structures [29]. The relative displacements induced by the rumpling corresponds to polar displacements which allows foreseeing a potential interplay between rumpling and ferroelectric polarization at the surface.

The average displacement (normal to the surface) of the atoms of a given plane defines the surface relaxation. The observed tendency is a reduction of interplanar spacing, at least between the surface layer and the first surface underlayer [18]. The farther from the surface atomic layer, the weaker this effect, as the properties tend to those of the bulk.

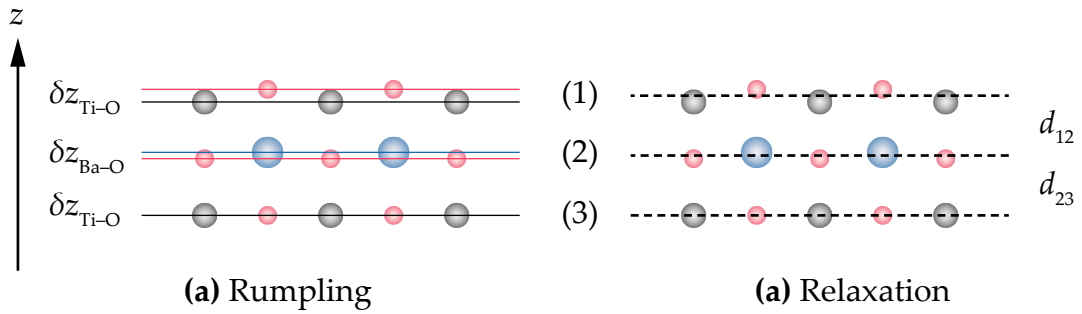


**Figure 1.3.:** Relative displacements between (a) the atoms within an atomic layer defining the rumpling and (b) the atomic layers defining the relaxation along the $z$ direction. $\delta z_{A-O}$ is the difference between the $z$ coordinate of ion A and oxygen (marked by the solid lines). $d_{ij}$ is the difference between the average $z$ coordinate of atomic layers $i$ and $j$ (marked by the dashed lines).

Figure 1.3 depicts the rumpling and relaxation between atoms and atomic layers along the vertical direction $z$. Oxygen atoms (red) are relatively displaced outwards

with respect to Ti atoms (gray), such that $\delta z_{\mathrm{Ti-O}} = z_{\mathrm{Ti}} - z_{\mathrm{O}} < 0$ defines a negative rumpling at the surface. The interplanar spacing $d_{12}$ is often smaller than $d_{23}$ as a result of surface relaxation.

## 2.2. Surface stress

Contrary to the surface rumpling and relaxation mentioned above, atomic relaxation parallel to the surface is not permitted because the surface atoms are pinned by the underlying bulk atoms. The tendency of the interatomic bond length to shorten at the surface results in an extra stress tensor, called the surface stress [30]. This surface stress is often tensile [31].

An elastic energy is associated to the surface stress. The minimization of this energy can be achieved by different mechanisms, leading to the surface stress relief. For instance, first-principles calculations predict surface reconstruction for aluminum [32], silicon [33] and perovskite surfaces [34], adsorption of polar molecules at the surface of metallic species [35] and of $TiO_2$ [36], as possible surface stress relief mechanisms [37, 38].

At the nanoscale, the surface effects influence the in-plane equilibrium lattice constant. The lower coordination numbers with respect to the bulk, which usually tend to shorten bond lengths, may result in a reduction of the equilibrium lattice constant of the system. For example, $BaTiO_3$ nanowires show compressive strain which can suppress axial ferroelectricity due to a large contraction of the unit cell [39]. Also, different surface terminations (for example AO or $BO_2$ in the case of a perovskite $ABO_3$ oxide) can be associated to different elastic energy and surface stress, translating into different stress relief mechanisms.

## 2.3. Surface electronic structure of charge transfer insulating oxides

In a charge transfer insulating oxide such as $BaTiO_3$, electron transfer from the metal to oxygen creates a microscopic electrostatic potential in the crystal. On the anionic sites (oxygen atoms), the electrostatic potential is positive as it arises from the surrounding cations. This stabilizes the electronic states formed by linear combinations of O $2p$ orbitals, which form the valence band. Conversely, on the cationic sites, the potential is negative as it arises from the surrounding anions. In turn, the electronic states formed by linear combinations of orbitals of the metal, are destabilized. They form the conduction band. This results in the opening of a band gap, and the insulating character of the oxide. The bandgap is thus mainly controlled by the difference of electrostatic

potential between anionic and cationic sites. In $BaTiO_3$, the first conduction band states mainly consist of $3d$ orbitals of titanium. It is empty as the Ti cations are fully oxidized in a formal $Ti^{4+}$ state ($4s^0\ 3d^0$).

The case of the charge transfer insulator $BaTiO_3$ can be opposed to other titanates such as $GdTiO_3$, $LaTiO_3$ or $YTiO_3$ [40], that have Ti metal in the formal $Ti^{3+}$ state. For these three transition metal oxides, the $3d^1$ electron is highly localized. It forms a narrow occupied band separated from the conduction band due to electron correlation effects (Mott insulators) [41].

At the surface of charge transfer insulating oxides, the change in covalency and coordination numbers lowers the difference of microscopic potential, also called the Madelung potential, between anions and cations, responsible for the separation of the valence and conduction bands [42]. Consequently, some electronic states from the valence band raise in the gap whereas the energy of some metallic states from the conduction band is lowered from the bottom of the conduction band. Therefore, the band gap is reduced, although not closed. These states which are affected by the lowering of the Madelung potential are referred to as surface states [18, 19], and are spatially localized at the surface. They have been investigated on $BaTiO_3$ surfaces by Cai et al. [43] from first-principles calculations. The difference in electron occupancy between the surface and bulk of $SrTiO_3$ has been studied from photoemission spectroscopy by Vanacore et al. [44], who demonstrated that bulk and surface exhibit behavior associated to charge-transfer and Mott insulators, respectively.

# 3. Ferroelectric surfaces

## 3.1. Depolarizing field

In a finite system, ferroelectricity is more complex than in an hypothetical infinite bulk system where the ferroelectric polarization is uniform. Due to the presence of boundaries and discontinuities, the polarization is usually not uniform. It can thus be described by a polarization field $\vec{P}(\vec{r})$. Both magnitude and direction of the local dipoles are altered by the presence of boundaries and the polarization field gives rise to polarization with different directions or polarization patterns. For instance, complex polarization patterns (such as vortices) have been predicted and described in $BaTiO_3$ nanoparticles from first-principles based effective Hamiltonian approach [45] and phase field modeling [46], observed and controlled in nanowires [47] and thin films [48, 49]. From classical electrodynamics, it is know that non uniform polarization

fields $\vec{P}(\vec{r})$ may be associated with a distribution of polarization charge density (bound charges), defined as:

$$\rho_b = -\vec{\nabla} \cdot \vec{P}(\vec{r}) \tag{I.1}$$

The electrostatic and elastic energy minimization of the system gives rise to the formation of the polarization patterns inside the material. The electrostatic energy is associated to the macroscopic electric field generated by $\rho_b$, called the depolarizing field $\vec{E}_{\text{dep}}$. In particular, the abrupt changes in the polarization, and polarization discontinuities induce bound charges. This is the case at a surface when $\vec{P}$ is perpendicular to the surface.

To address the causes and effects of the depolarizing field, we take the particular case of a slab, which is a slice of matter surrounded by vacuum, with uniform polarization perpendicular to both top and bottom surfaces. At the system boundaries, owing to the polarization field discontinuity, a surface charge density appears $\sigma = \vec{P} \cdot \vec{n}$ (where $\vec{n}$ is a unitary vector normal to the surface pointing outwards) and generates in the slab a depolarizing field $\vec{E}_{\text{dep}} = -\frac{1}{\epsilon_0} \vec{P}$ (where $\epsilon_0$ is the dielectric permittivity of vacuum, in SI units). $\vec{E}_{\text{dep}}$ opposes the polarization and tends to cancel the atomic polar displacements, thus destabilizing and even suppressing the ferroelectricity. The depolarizing field is a crucial notion to understand the polarization distribution in finite ferroelectric systems.

In order for the ferroelectric polarization to maintain in a finite system, in particular in configurations where the polarization is perpendicular to the surface, the depolarizing field must be screened, i.e. compensated by an opposite macroscopic electric field.

## 3.2. Screening of the depolarizing field

In real systems where polarization perpendicular to the surface is observed, $\vec{E}_{\text{dep}}$ is indeed screened by another macroscopic electric field, that has various possible origins, depending on the charge carriers that compensate the polarization charge density. The compensation of the polarization bound charge suppresses the depolarizing field, thus stabilizing the ferroelectric distortions.

**Extrinsinc screening:**

First, the charge carriers can have an external origin. Metallic electrodes grown on the ferroelectric surface in short-circuit conditions can provide charge carriers to screen the polarization charge density. At the metal-ferroelectric interface, a region of space charge is created in the metal which generates a macroscopic electric field across the ferroelectric, that screens the depolarizing field. This screening mechanism is complex and depends on the metal-ferroelectric interface which is characterized by a finite screening length, interface chemistry and strain. The ferroelectricity in a $BaTiO_3$ ultrathin film in short-circuit between two metallic $SrRuO_3$ electrodes has been addressed by Junquera and Ghosez [50], from first-principles calculations. Stable polarization perpendicular to the interface could be maintained owing to the electrode-induced charge compensation. The stability and magnitude of the polarization was enhanced with increasing film thickness; however, a critical film thickness of 6 unit cells ($\approx 26$ Å) below which ferroelectricity could not be maintained has been reported [50] and attributed to the residual depolarizing field (since $E_{\text{dep}} \propto 1/d$ with $d$ the distance between the electrodes), and to the finite screening length of the electrode.

Another ab initio study of the stabilization of the polarization normal to the surface in $PbTiO_3$ ultrathin films between platinum or $SrRuO_3$ electrodes [51] has demonstrated the existence of ferroelectricity below 10 Å. These results showed that the critical thickness predicted in $BaTiO_3$ could depend on the nature of the metallic electrode, which plays a predominant role in the stabilization of the polarization of the film. Furthermore, Stengel et al. [52] demonstrated an overall enhancement of ferroelectricity in $BaTiO_3$ and $PbTiO_3$ ultrathin films sandwiched between Pt electrodes, from first-principles calculations. They further investigated the metal-oxide interface at the microscopic level by accounting for electronic and ionic relaxations at the interface, showing that the only free charges brought by the electrodes do not suffice to fully compensate the polarization bound charge near the interface. The importance of ionic relaxations which provide an additional stabilization of the ferroelectricity with respect to the free carriers brought by the electrode, was reported also from first principles by Gerra et al. [53] on the study of $SrRuO_3/BaTiO_3$ interfaces. Pure surface effects have been opposed to depolarizing effects in the investigations on the origin of a critical thickness, combined with the effect of epitaxial strain [54, 55].

Another mechanism at the origin of the disappearance of ferroelectricity in ultrathin films resides in the leakage current, which can be due to defects and impurities increasing the conductivity [56], and to a band lineup owing to a deformation of the Schottky barrier height at the metal-oxide interface [25, 57]. A systematic study on the nature of the metallic electrodes and their effect on the ferroelectricity of $PbTiO_3$ has been recently realized [58], showing that simple metallic electrodes (such as Pt) confer larger polarization and overall ferroelectric stability than oxide electrodes.

However, experimental comparisons of $SrRuO_3$ and $IrO_3$ [59] and $SrRuO_3$ and Pt [60] electrodes on (Ba,Sr)$TiO_3$ reported that oxide electrodes give substantially higher screening performance.

In the case of a free surface, i.e. without electrodes, screening can be ensured by the adsorption of molecules providing surface charge compensation. Major work has been performed by Kalinin et al. using local-probe microscopy techniques such as scanning surface potential microscopy (SSPM) and piezo-response force microscopy (PFM) to map the potential at ferroelectric surfaces. Evidence of complete screening of the bound charges from adsorbates, although not excluding intrinsic screening by free carriers (see next section) was reported [61]. Specifically for out-of-plane polarized surfaces [62], study of the stability of the ferroelectric polarization at temperature around the ferroelectric-paraelectric transition showed that polar adsorbates contribute to stabilize out-of-plane polarization [63]. Scanning local probe techniques are well suited to study the potential modulations at ferroelectric surfaces arising from the polarization charge density. They demonstrated by tip-surface interactions studies [64, 65] that the presence of surface adsorbates can change these interactions. For instance, adsorbed water molecules between the surface and the tip act as screening charges and modulate the polarization switching performed with the conductive tip [66]. Stabilization from adsorbates of uniform polarization perpendicular [67] and parallel [68] to the surface were also predicted from first-principles calculations. Experimental evidence of adsorbate layers screening the polarization charge density, hence reducing the internal electric field in $BaTiO_3$ ultrathin films, was given by a combination of PFM and X-ray photoemission spectroscopy [69]. A thermodynamic theory of ionic surface charge compensation provided by the environment (partial pressure above the surface) has been developed [70]. It was experimentally confirmed by grazing angle X-ray scattering measurements at the surface of $PbTiO_3$ under controlled oxygen partial pressure, showing stabilization [67] and even switching [71, 72] of the ferroelectric polarization.

These results show the crucial role of polar adsorbates at ferroelectric surfaces. Great care must be taken when investigating the surface potential generated by polarization charge density since highly reactive molecules present in air or uncontrolled atmosphere can modulate and even invert the observed surface potential. Adsorption of polar molecules on ferroelectric surfaces raises the issue of the reactivity of the ferroelectric surfaces, which is important in the field of surface catalysis [73].

**Intrinsic screening:**

We call intrinsic screening the charge compensation arising from defects and impurities. Vacancies or dopants change the stoichiometry and can lead to excess charge

carriers that are available to screen the polarization bound charge. Among all the defects and impurities studied in oxides [74–78] and their effect on ferroelectricity [79–81], we focus in this thesis on the effect of oxygen vacancies.

Neutral oxygen vacancies act as donor defect [82–84] such that the excess electrons and the vacancy site can induce electronic and ionic charge available to compensate the polarization bound charge [85]. Direct change of oxygen vacancy concentration can stabilize out-of-plane, inwards pointing polarization as experimentally showed and supported by first-principles calculations by Mi et al. [86] in reduced $BaTiO_3$, and by Wang et al. [71] in $PbTiO_3$. Stabilization of non uniform polarization in domains, as developed in the next paragraph, has been observed and attributed to pinning defects by Yang et al. [87]. He and Vanderbilt [88] demonstrated from first-principles calculations that defects such as oxygen vacancies can stabilize non uniform polarization distribution in $PbTiO_3$ owing to a lower formation energy at regions of polarization discontinuities (domain walls). Similarly, space charge compensation induced by excess charge carriers created by vacancies, at polarization discontinuities has been demonstrated by Eliseev et al. [89] and by Zuo et al. [90] from numerical calculations based on the Landau-Ginzburg-Devonshire theory.

The exact mechanism behind polarization bound charge screening due to vacancies is not yet completely elucidated. However, vacancies and impurities have been observed to induce conductivity without loosing ferroelectricity: Seidel et al. [91] reported, from PFM and conductive Atomic Force Microscopy (c-AFM) measurements, conductivity at domain walls in La-doped $BiFeO_3$ which could be enhanced with increasing oxygen vacancy concentration. Enhancement of electron transport properties in ferroelectric La-doped $BaTiO_3$ has been reported by Gilbert et al. [92]. In Ca-doped $BiFeO_3$, in which the Ca cations act as acceptors for the excess electrons generated by oxygen vacancies, combined ionic and electronic conduction showed modulation of the ferroelectric state as a function of doping ratio. The nature and properties of vacancies (oxygen or cations) and the interplay with the ferroelectric distortions in $PbTiO_3$ were investigated by Shimada et al. [81] from first-principles calculations.

Since ferroelectric displacements are stabilized by long range Coulomb (dipole-dipole) interactions, the presence of free charge carriers (electrons or holes) in ferroelectric materials are expected to destabilize ferroelectricity. Nevertheless, coexistence of ferroelectric distortions and conductivity has been predicted [85] and measured [93] as a function of free charge carriers released by oxygen vacancies. A critical doping level is however reported [93]. Above a certain oxygen vacancy concentration, or equivalently $n$ doping level, a metal-insulator transition is observed, incompatible with a stable ferroelectric state. Our group reported experimental evidences of

ferroelectric-paraelectric transition induced by doping from oxygen vacancies [94]. In this thesis, we further investigate the influence of oxygen vacancies on the stability of the ferroelectric state, and on the insulating-metallic character of $BaTiO_3$, from first-principles and experimental investigations.

**Domain ordering:**

Another screening mechanism found in ferroelectric materials is the domain ordering. Domains are regions of the material where the ferroelectric polarization is uniform. The boundaries between such regions are called domain walls. Polarization forms such patterns in order to reduce the total electrostatic and elastic energy. Figure 1.4 shows an idealized representation of domain ordering in a tetragonal $BaTiO_3$ slab. Polarization (black arrows) exhibit discontinuities which induce polarization bound charges ("+" and "−" symbols). The macroscopic electric field (red curved and straight arrows) created by each domain of uniform polarization (back arrows) allows screening of the depolarizing field (red straight arrows) in the neighboring domains. Domain ordering at the surface of $BaTiO_3$ have been reported soon after its discovery from polarized light microscopy [95–97]. More recently, a theoretical formulation of the domain ordering resulting from depolarizing effects in thin films has been made by Speck et al. [98].

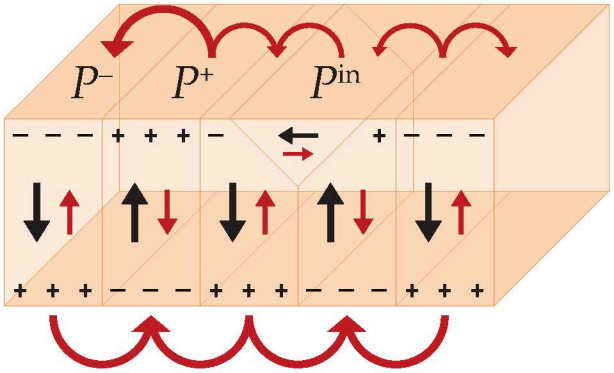


**Figure 1.4.:** Schematic of the idealized ferroelectric domain ordering in tetragonal $BaTiO_3$. Surface polarization gives rise to surface charge density which is depicted by the plus and minus symbols. Polarization and depolarizing fields are drawn with black and red arrows.

Neighboring domains which display polarization (black arrows) oriented in opposite directions are separated by 180° domain walls whereas neighboring domains which show polarization oriented perpendicularly are separated by 90° domain walls. According to the projection of the polarization at the surface, we label $P^+$ and $P^-$ the surface region of out-of-plane polarized domains pointing outwards and inwards, respectively. The surface of domain whose polarization is parallel to the surface, or in-plane, are referred to as $P^{in}$. The overall domain ordering allows minimization of

the electrostatic (and elastic) energy. In this picture, the macroscopic electric fields generated by neighboring 180° separated domains, and the overall reduction of polarization charge due to the rotation of the polarization forming closure domains at the surface tend to minimize the energy of the system.

In ultrathin films, due to the strong depolarizing field, domains often order in thin stripes. Alternating out-of-plane polarized domains are separated by 180° domain walls. Such configuration has been observed in $PbZr_{1-x}Ti_xO_3$ by transmission electron microscopy (TEM) [99] and in $PbTiO_3$ by X-ray diffraction analyses [100]. Observation of rotating polarization forming closure domains have been recently reported [49] using TEM. When ordered in stripes, the relation between the thin film (or slab) thickness $L$ and domain width $l$ is normally driven by Kittel's law [101], which states that $L \propto l^2$. This law was initially derived for ferromagnetic domains and has been extended to ferroelectrics by Mitsui and Furuichi [97]. This relashionship can be qualitatively understood by considering the basic contributions to the energy of a ferroelectric in terms of short/long-range interactions and longitudinal/lateral correlations [15]. Extending the domain width $l$ adds destabilizing (lateral) electrostatic contributions. Thus maintaining the ferroelectric state requires elongating the domain in the direction of the polarization (increase $L$), adding stabilizing (longitudinal) electrostatic contributions. When the system size is reduced to the nanoscale, stabilizing a realistic ferroelectric state at very small slab thickness $L$ becomes difficult because of the increasing impact of the surfaces. Accounting for the domain width, a better description of the scaling law between domain period and system thickness has been obtained by Scott [102], and experimentally evidenced by Streiffer [103] and Schilling et al. [104].

Domain formation in the presence of uncompensated depolarizing field has been addressed by Kornev et al. [105] from first-principles based Monte Carlo simulations, considering polarization parallel or perpendicular to the surface of (Pb,Zr)$TiO_3$ under tensile or compressive strain. They demonstrated that polarization parallel to the surface was more favorable in the presence of residual depolarizing field, at the expense of polarization perpendicular to the surface, in stress free systems. In addition, the strong interplay between in-plane strain and polarization was investigated, showing that in-plane and out-of-plane polarization could be maintained with tensile and compressive strain, respectively. In the latter case, polarization rotation arising from the uncompensated bound charge was evidenced.

Following the first-principles calculations of Junquera and Ghosez [50] which demonstrated the efficient screening of the depolarizing fields in $BaTiO_3$ by $SrRuO_3$ electrodes, Aguado-Puente and Junquera [106] added domain formation to complete the screening by the free charges. They simulated domains of opposite polarization

perpendicular to the ferroelectric-electrode interface and demonstrated that ferroelectricity could exist lower than the predicted critical thickness associated with the uniform polarization [50], giving insight into the capacity of domain formation to screen the depolarizing field in thin films.

First-principles simulation of ferroelectric surfaces without screening mechanism of external (electrode, adsorbates) or internal (defects, impurities) origin, using domain formation as the screening mechanism has been proposed by Shimada et al. [107] on $PbTiO_3$. Stabilization of polarization perpendicular to the surface was demonstrated, with evidence of closure domains at the surface. Previous first-principles studies of ferroelectric systems with polarization perpendicular to the surface had been proposed, on the one hand by Cohen [108–110] and Fechner et al. [111] and on the other hand by Meyer and Vanderbilt [112]. For the former, the ferroelectric distortions were frozen in the bulk part, while for the latter, an external electric field that exactly matches the depolarizing field was applied to the slab. These two methods are detailed and discussed further, while the method proposed by Shimada et al. [107] is applied and extended in $BaTiO_3$ slabs in the present work.

# 4. Outline

The present thesis is dedicated to the study of polarization topology at the surface of $BaTiO_3$, using experimental and numerical tools.

Chapter II describes the first-principles calculations and the methodology adopted to study the ferroelectric surface with polarization oriented in-plane or out-of-plane. The key issue of simulating polarization perpendicular to the surface (without using electrodes or external electric field to screen the depolarizing fields) from Density Functional Theory (DFT) is addressed. A description of the parameters such as surface termination, in-plane strain, slab thickness and domain periodicity is developed.

The results are presented in two chapters.
In Chapter III, the first-principles results obtained on perfect $BaTiO_3$(001) slabs are presented. The influence of the surface termination is investigated with the study of the relative stability of the ferroelectric phases with respect to the bulk as a function of compressive and tensile in-plane strain. Out-of-plane polarization is simulated in a compressive strain regime and the influence of the surface in terms of termination and slab thickness is studied. Computation of the local polarization per unit cell allows visualizing polarization pattern. Surface atomic relaxation and rumpling and their relation with polarization are addressed. Finally, the electronic structure of

the ferroelectric slabs are described with the study of the total and atom-projected density of states, where a strong influence of the surface termination is observed. The insulating character of all the simulated perfect slabs is demonstrated.

In the same chapter, we further investigate the case of out-of-plane polarization with the introduction of surface oxygen vacancies in the case of highly strained, $TiO_2$ terminated slabs. Atomic displacements resulting from the defect and their influence on the local polarization are investigated. The role of oxygen vacancies on the electronic structure of out-of-plane polarized systems is elucidated with the observation of metallic states in the conduction band.

In Chapter IV, experimental studies on $BaTiO_3$(001) single crystals performed by full-field electron microscopy and spectroscopy are exposed. An introduction to the employed techniques is given. Moderate conductivity in single crystals is achieved by vacuum annealing which introduces oxygen vacancies, allowing the use of Low-Energy Electron Microscopy (LEEM) and Photoemission Electron Microscopy (PEEM) to study structural, chemical and electronic properties of the surface as a function of ferroelectric polarization. The obtained results are put into perspective with the case of the ferroelectric systems incorporating oxygen vacancies simulated by first-principles, in terms of surface polarization, electronic structure and role of the oxygen vacancy as a screening mechanism at the surface.

In Chapter V, the results are discussed and set in the context of the current understanding in the simulation of ferroelectric systems. The issue of depolarizing field screening, surface effects from termination to slab thickness as well as surface relaxation and stress, and the influence of oxygen vacancies in the electronic structure are addressed.

# Chapter II.

# First-principles density functional method

## 1. The quantum many-body problem

### 1.1. The Schrödinger equation

The non-relativistic, time-dependent Schrödinger equation of a system of $N$ electrons and $M$ ionic nuclei writes:

$$i\hbar\frac{\partial\Psi(\{\vec{x}_i\},\{\vec{R}_I)\}}{\partial t} = \hat{H}\Psi(\{\vec{x}_i\},\{\vec{R}_I\}) \tag{II.1}$$

The wave function $\Psi$ accounts for the $N$ electrons and $M$ ionic nuclei characterized respectively by the set of coordinates $\{\vec{x}_i\}$ and $\{\vec{R}_I\}$. The coordinates of electron $i$ comprise the space coordinates $\vec{r}_i$ and spin degrees of freedom $\sigma_i$. Assuming spin degeneracy, one writes $\vec{x}_i = \vec{r}_i$. For such a system of interacting electrons and nuclei, the Hamiltonian $\hat{H}$ decomposes as:

$$\hat{H} = \hat{T}_{\mathrm{e}} + \hat{T}_{\mathrm{ion}} + \hat{V}_{\mathrm{e-e}} + \hat{V}_{\mathrm{e-ion}} + \hat{V}_{\mathrm{ion-ion}} \tag{II.2}$$

The kinetic energy is that of a particle of mass $m$ ($m_{\mathrm{e}}$ and $m_{\mathrm{ion}}$ for electrons and nuclei, respectively). The potential energy is written according to Coulomb's law. The

operators in the Hamiltonian therefore write:

$$\hat{T}_{\mathrm{e}} = -\frac{\hbar^2}{2m_{\mathrm{e}}} \sum_{i=1}^{N} \nabla_i^2 \quad \text{the kinetic energy of electrons,} \tag{II.3}$$

$$\hat{T}_{\mathrm{ion}} = -\frac{\hbar^2}{2m_{\mathrm{ion}}} \sum_{I=1}^{M} \nabla_I^2 \quad \text{the kinetic energy of nuclei,} \tag{II.4}$$

$$\hat{V}_{\mathrm{e-e}} = \frac{1}{8\pi\epsilon_0} \sum_{i\neq j}^{N} \frac{e^2}{|\vec{r}_i - \vec{r}_j|} \quad \text{the interaction energy between electrons,} \tag{II.5}$$

$$\hat{V}_{\mathrm{e-ion}} = \frac{1}{4\pi\epsilon_0} \sum_{i=1}^{N} \sum_{I=1}^{M} \frac{-eZ_I}{|\vec{r}_i - \vec{R}_I|} \quad \text{the interaction energy between electrons and nuclei,} \tag{II.6}$$

$$\hat{V}_{\mathrm{ion-ion}} = \frac{1}{8\pi\epsilon_0} \sum_{I\neq J}^{M} \frac{Z_I Z_J e^2}{|\vec{R}_I - \vec{R}_J|} \quad \text{the interaction energy between the nuclei.} \tag{II.7}$$

The resolution of the Schrödinger equation stated in equation II.1 is a quantum many-body problem as the Hamiltonian written in equation II.2 accounts for interacting electrons and nuclei. The wave function $\Psi(\{\vec{x}_i\}, \{\vec{R}_I\})$ is a function of $3N + 3M$ spatial coordinates of electrons and nuclei. It is possible to define an energy functional as:

$$E[\Psi] = \langle \hat{H} \rangle = \frac{\langle \Psi | \hat{H} | \Psi \rangle}{\langle \Psi | \Psi \rangle} = \frac{\int \Psi^\star \, \hat{H} \, \Psi \, \mathrm{d}\vec{r} \, \mathrm{d}\vec{R}}{\int \Psi^\star \, \Psi \, \mathrm{d}\vec{r} \, \mathrm{d}\vec{R}} \tag{II.8}$$

The ground state energy $E_0$ is obtained by minimizing this functional with respect to the many-body wave function: $E_0 = \min_{\Psi}(E[\Psi])$.

The problem of minimizing the energy functional is equivalent to diagonalizing the Hamiltonian operator, $\hat{H}$, stated in the following eigenstate equation (and retaining the lowest eigenvalue), provided proper normalization conditions:

$$\hat{H} \, |\Psi\rangle = E \, |\Psi\rangle \tag{II.9}$$

where $\hat{H}$ is the Hamiltonian operator to be diagonalized in order to find the eigenvalues $E$ and the eigenvectors $|\Psi\rangle$, respectively the energy and wave function of the stationary states.

The above calculations, as expressed in equation II.8, require integration of the wave function over all spatial coordinates of all particles which is analytically impractical. Solely the two-particles problem can be solved analytically in some cases. Moreover, given the number of particles, any numerical resolution of such problem is impossible, provided that the current computing performance is of the order of $10^{15} - 10^{18}$ operations per second, the brute-force resolution would take geological

times. For example, the Schrödinger equation on a $10 \times 10 \times 10$ grid for each spatial coordinate represents $10^{3N}$ independent variables. In the case of a system containing 10 particles, and accounting for the spin ($2^N$ times more variables), the evaluation of the ground state would require almost $10^{30}$ operations, which would be performed at most within 15 000 years. A set of approximations is therefore needed to solve numerically the quantum many-body problem.

## 1.2. Born-Oppenheimer approximation

The first accepted approximation consists in decoupling the electrons and the nuclei degrees of freedom. In 1927, Max Born and Robert Oppenheimer stated that the degrees of freedom of the electrons can be separated from that of the atomic nuclei, the latter being *clamped* due to their larger masses. Within this assumption, the wave function $\Psi^{\text{el}}_{\{\vec{R}_I\}}(\{\vec{r}_i\})$ accounts for the spatial coordinates of the nuclei as parameters instead of variables. In other words, for a given atomic nuclei configuration, the wave function solely depends on the electrons coordinates.

Under such conditions, equation II.1 and II.2 become purely electronic, as the kinetic energy of the nuclei vanishes $\hat{T}_{\text{ion}} = 0$, and the Coulomb potential from the nuclei is formulated as a fixed "external" potential affecting the electrons $\hat{V}^{\text{ext}}_{\{\vec{R}_I\}}(\{\vec{r}_i\}) = \hat{V}_{\text{e-ion}} + \hat{V}_{\text{ion-ion}}$, where $\hat{V}_{\text{ion-ion}}$ is a scalar constant. The electronic time-independent Schödinger equation to be solved writes:

$$\hat{H}^{\text{el}}_{\vec{R}_I} = -\frac{\hbar^2}{2m_{\text{e}}}\sum_{i=1}^{N}\nabla_i^2 + \frac{1}{8\pi\epsilon_0}\sum_{i\neq j}^{N}\frac{e^2}{|\vec{r}_i - \vec{r}_j|} + \hat{V}^{\text{ext}}_{\{\vec{R}_I\}}(\{\vec{r}_i\}) \tag{II.10a}$$

$$(\hat{T}_{\text{e}} + \hat{V}_{\text{e-e}} + \hat{V}_{\text{ext}})\,\Psi^{\text{el}}_{\{\vec{R}_I\}}(\{\vec{r}_i\}) = E^{\text{el}}\,\Psi^{\text{el}}_{\{\vec{R}_I\}}(\{\vec{r}_i\}) \tag{II.10b}$$

Given the formulation of the many-electron Hamiltonian, the calculation complexity lies in the electron-electron interaction term $\hat{V}_{\text{e-e}}$. The model provided by the Hartree approximation and later within the Hartree-Fock method permits to perform electron structure calculations under some approximations, determining the wave function and the energy of the many-electron system. In the Hartree-Fock case, it is based on a Slater determinant definition of the many-electron wave function. The corresponding many-electron system is then minimized and a set of $N$ coupled single-electron equations is derived: the Hartree-Fock equations. The Hartree-Fock theory reduces the many-electron problem into a set of single-particle equations, numerically solvable, but neglects electronic correlations. The Hartree-Fock method was rarely used until

the advent of fast computers in the 1950's. This theory was more accurate than its predecessor (Hartree approximation) thanks to the formulation of the many-electron wave function as a Slater determinant. Such formulation allowed accounting for the *exchange* energy term, which arises from the Pauli exclusion principle affecting the electrons of same spin. However, the Hartree-Fock method lacks accounting for the electronic correlations arising from interactions of electrons. With a view to accounting for the correlations, so-called post-Hartree-Fock methods, such as for example the Configuration Interaction [113, 114] and Coupled Cluster [115, 116] methods were developed and are nowadays used in scientific electron structure calculations packages. These methods are however limited to small systems.

# 2. Density Functional Theory

## 2.1. Hohenberg and Kohn theorems

The first Hohenberg-Kohn theorem [117] states that the external potential $\hat{V}^{\text{ext}}_{\{\vec{R}_I\}}(\{\vec{r}_i\})$ affecting the $N$ interacting electrons is *uniquely* determined as a functional of the ground state electron density $n_0(\vec{r})$, up to an additive constant. In other words, two different Hamiltonians of non-degenerate ground states cannot have the same ground state electron density. Therefore, the knowledge of the ground state electron density allows the formulation of the external potential. In turn, the Hamiltonian can be derived and the system characterized. However, the Hamiltonian is still that of the many-electron Schrödinger equation, which is unsolvable as is.

As a consequence to the first Hohenberg-Kohn theorem, the ground state energy can be expressed as a functional of the ground state electron density: $E[n(\vec{r})]$. A universal functional $F_{\text{HK}}(n(\vec{r}))$ can then be defined according to:

$$F_{\text{HK}}(n(\vec{r})) = E[n(\vec{r})] - \int \mathrm{d}^3 r\, \hat{V}_{\text{ext}}(\vec{r})\, n(\vec{r}) \tag{II.11}$$

The second theorem [117] is a consequence of the variational principle [118]: it states that the energy and ground state density can be obtained by minimizing (with respect to $n(\vec{r})$) the functional $E_{\hat{V}}[n(\vec{r})] = F_{\text{HK}}[n(\vec{r})] + \int \mathrm{d}^3 r\, \hat{V}(\vec{r})\, n(\vec{r}))$, in a fixed external potential $\hat{V}$.

Considering the $N$-electron ground state wave function $\Psi_0$, the ground state electron density $n_0$, the universal functional $F_{\text{HK}}$ and the Hohenberg-Kohn energy func-

tional $E_{\hat{V}}$ are defined as:

$$n_0(\vec{r}) = \langle \Psi_0 | \sum_{i=1}^{N} \delta(\vec{r} - \vec{r}_i) | \Psi_0 \rangle \tag{II.12}$$

$$F_{\mathrm{HK}}[n_0(\vec{r})] = \langle \Psi_0 | \hat{T}_{\mathrm{e}} + \hat{V}_{\mathrm{e-e}} | \Psi_0 \rangle \tag{II.13}$$

$$E_{\hat{V}}[n_0(\vec{r})] = \int \mathrm{d}^3 r \, \hat{V}_{\mathrm{ext}}(\vec{r}) \, n_0(\vec{r}) + F_{\mathrm{HK}}[n_0(\vec{r})] \tag{II.14}$$

Where the condition of conservation of number of electrons holds as:

$$\int n_0(\vec{r}) \, \mathrm{d}^3 r = N \tag{II.15}$$

The Hohenberg-Kohn theorems ascertain that the Hamiltonian of a system of $N$ interacting electrons in an external potential can be derived from the ground state density, and that the ground state energy can be found by minimizing the energy functional $E_{\hat{V}}[n]$, instead of determining the many-electron wave function from the electronic Schrödinger equation. However, they do not provide an explicit formulation of $E_{\hat{V}}[n]$.

## 2.2. The Kohn and Sham equations

In 1965, Kohn and Sham proposed a new formulation of the many-electron Schrödinger equation in terms of one-electron equations within the maturing framework of the density functional theory [119]. Given the unique correspondence between the ground state electron density and the Hamiltonian of $N$ interacting electrons in an external potential as stated by the second Hohenberg-Kohn theorem, Kohn and Sham introduced the idea of a fictitious system of $N$ non-interacting electrons with the same electron density as that of the actual system of $N$ interacting electrons. If such fictitious system exists, then the external potential affecting the non-interacting electrons should compensate for the absence of electron-electron interactions and therefore can be viewed as an effective potential for the non-interacting electrons, and is also called "Kohn-Sham" potential. This effective potential is denoted as $\hat{V}_s(\vec{r})$ in the following, where $s$ stands for single electron. In this system, the electrons are independent, therefore the kinetic energy functional is that of non-interacting single electrons $T_{\mathrm{s}}[n]$. The energy functional of this system would read:

$$E_{\mathrm{KS}}[n] = T_{\mathrm{s}}[n] + \int \mathrm{d}^3 r \, \hat{V}_{\mathrm{s}}(\vec{r}) \, n(\vec{r}) \tag{II.16}$$

From equation II.13 and II.14, the energy functional can be written in terms of the non-interacting electron system and terms of the real system, by setting $F_{\mathrm{HK}}[n] = T_{\mathrm{s}}[n] + E_{\mathrm{H}}[n] + E_{\mathrm{xc}}[n]$, as follows:

$$E_{\mathrm{KS}}[n] = T_{\mathrm{s}}[n] + \int \mathrm{d}^3 r\, \hat{V}_{\mathrm{ext}}(\vec{r})\, n(\vec{r}) + E_{\mathrm{H}}[n] + E_{\mathrm{xc}}[n] \tag{II.17}$$

Where $E_{\mathrm{H}}[n]$ is the Hartree energy functional which by definition accounts for the electron-electron interactions of the system (calculated as in classical electrodynamics for a continuous distribution of charges) and finally $E_{\mathrm{xc}}[n]$ defined as the *exchange-correlation* functional. $E_{\mathrm{xc}}[n]$ contains all the quantum effects not included in $T_{\mathrm{s}}[n]$ and $E_{\mathrm{H}}[n]$.

The exchange-correlation functional should account for (i) the correction of kinetic energy between the system of non-interacting electrons and that of interacting electrons, (ii) the correction of the self-interaction term present in the Hartree energy, (iii) the exchange term describing the repulsion effects between electrons of same spin, as accounted for in the Hartree-Fock theory and (iv) the correlation effects.

The electron density $n(\vec{r})$ minimizes the energy functional of both the fictitious and the real systems, expressed in equations II.16 and II.17, respectively. The expression of the effective potential affecting the system of non-interacting electrons can be subsequently derived:

$$\hat{V}_{\mathrm{s}}(\vec{r}) = \hat{V}_{\mathrm{ext}}(\vec{r}) + \frac{e^2}{4\,\pi\,\epsilon_0} \int \mathrm{d}^3 r' \frac{n(\vec{r}\,')}{|\vec{r} - \vec{r}\,'|} + \hat{V}_{\mathrm{xc}}(\vec{r}; [n]) \tag{II.18}$$

The ground state electron density can be defined by the one-electron wave functions $\psi_i$ (the Kohn-Sham wave functions), multiplied by the occupation factor $f_i$. The fictitious system of $N$ non-interacting electrons in the potential $\hat{V}_{\mathrm{s}}(\vec{r})$ can therefore be described by a set of $N$ one-electron Schrödinger equations based on the Kohn-Sham wave functions (assuming spin degeneracy):

$$n(\vec{r}) = \sum_{i=1}^{N} f_i |\psi_i(\vec{r})|^2 \tag{II.19}$$

$$\left[ -\frac{\hbar^2\,\nabla^2}{2\,m_{\mathrm{e}}} + \hat{V}_{\mathrm{ext}}(\vec{r}) + \frac{e^2}{4\,\pi\,\epsilon_0} \int \mathrm{d}^3 r' \frac{n(\vec{r}\,')}{|\vec{r} - \vec{r}\,'|} + \hat{V}_{\mathrm{xc}}(\vec{r}; [n]) \right] \psi_i(\vec{r}) = \epsilon_i \psi_i(\vec{r}) \tag{II.20}$$

The set of equations II.20 are the Kohn-Sham equations. The Hartree potential $\frac{e^2}{4\pi\epsilon_0} \int \mathrm{d}^3 r' \frac{n(\vec{r}\,')}{|\vec{r} - \vec{r}\,'|}$ as well as the exchange-correlation term both depend on the elec-

tron density $n(\vec{r})$. However, the latter depends on the orbitals $\psi_i$ which depend on the effective potential $V_s(\vec{r})$. Therefore the problem is expressed in terms of non linear, solvable one-electron Schrödinger equations. The practical implementation of the resolution of the Kohn-Sham equations is presented in section 3. Beforehand, a final word about the building blocks of density functional theory can be addressed with respect to the exchange-correlation energy functional.

## 2.3. Exchange-correlation: the Local Density Approximation

The exchange-correlation functional, included in the effective potential $V_s(\vec{r})$ (II.18) contains all the purely quantum effects, namely exchange and correlation, as well as a correction of the electron self-interaction. It can be written as the sum of exchange energy $E_x[n]$ and correlation energy $E_c[n]$. An exact expression of the exchange or correlation energy as a functional of the electron density is not known. A simpler model of interacting electrons can be considered, whence explicit expression of the exchange energy as a function of the density can be derived. In the case of the *homogeneous electron gas* (HEG), also known as *jellium*, the electron density is uniform over the volume $V$ of the system, such that $n(\vec{r}) = \bar{n} = N/V$. The kinetic and Coulomb repulsion energy of the electrons ($\hat{T}_e$ and $\hat{V}_{e-e}$), the Coulomb interactions of the nuclei ($\hat{V}_{ion-ion}$) and the Coulomb interactions between electrons and nuclei ($\hat{V}_{e-ion}$) are considered. Based on the mean electron density $\bar{n}$, the exchange and correlation energy reads:

$$E_x^{HEG}(\bar{n}) = -\frac{3e^2}{4}\left(\frac{3}{\pi}\right)^{\frac{1}{3}} V\,\bar{n}^{\frac{4}{3}} = -C_x\,V\,\frac{N}{V}\,\bar{n}^{\frac{1}{3}} \tag{II.21}$$

$$E_c^{HEG}(\bar{n}) = -C_c\,V\,\frac{N}{V}\,e_c(\bar{n}) \tag{II.22}$$

Within the HEG model, compared to the exchange energy which is exact, the correlation energy can be obtained by Quantum Monte Carlo simulations [120] and extrapolated for the system of interest. The exchange and correlation energy is approximated by a sum of local contributions, as follows:

$$E_{xc}[n(\vec{r})] = \int \mathrm{d}^3r\, n(\vec{r})\, e_{xc}(n(\vec{r})) \tag{II.23}$$

Where $e_{xc}(n(\vec{r}))$ is the exchange-correlation energy per electron of a homogeneous electron gas of density $n(\vec{r})$. The formulation of the exchange-correlation functional in equation II.23 is that of the so called Local Density Approximation (LDA), which was introduced by Kohn and Sham as the first approximation of the exchange-correlation. LDA is routinely used and its drawbacks are well known and can be to a certain extent

circumvented. Indeed, the work presented in this thesis has been preformed under the LDA, with the use of Perdew-Wang 92 parametrization [121]. There exist various other approximations of the exchange-correlation such as the Generalized Gradient Approximation (GGA), which is supposed to be more accurate since the exchange-correlation energy is expressed as a function of the density and its gradients [122, 123]. However, the GGA provides poor results on tetragonal $BaTiO_3$, for instance due to a large $c/a$ overestimation [124–127]. This is why we use the LDA in the present work. In the following, practical implementations of the resolution of the Kohn-Sham equations are presented, namely with respect to the different approaches to develop the one-electron wave functions $\psi_i$, as well as within *pseudo-potentials*.

## 3. Practical implementations

Kohn-Sham equations are non linear and their resolution can be performed in an iterative process. In practice, a trial electron density $n^{(0)}(\vec{r})$ usually derived from trial orbitals $\psi_i^{(0)}$ allows to construct the effective one-electron Hamiltonian $\hat{H}^{(0)}$ explicitly formulated in equation II.20. The corresponding one-electron Schrödinger equation can be solved yielding a first iteration of Kohn-Sham orbitals $\psi_i^{(1)}$. In turn, according to equation II.19, the corresponding electron density $n^{(1)}(\vec{r})$ can be derived. From this iteration of the electron density, a new effective Kohn-Sham Hamiltonian $\hat{H}^{(1)}$ can be derived, and the cycle continues until a certain arbitrary convergence criterion is fullfilled: the *self-consistent cycle* has converged.

There are a variety of numerical implementations of the Kohn-Sham self-consistent density functional method within the different approximations of the exchange-correlation energy. Among them, two were used for this thesis, mainly ABINIT[1] [128] and in one case SIESTA[2] [129]. Both deal with periodic systems and thus, the Kohn-Sham wave functions take the form of Bloch functions. The main difference of these density functional theory frameworks lies in the expansion of the electron wave functions. In ABINIT, the periodic parts of the Kohn-Sham wave functions are expanded on a basis of plane waves. In SIESTA, they are expanded on a basis of numerical atomic orbitals. In the following, so called pseudo-potentials as used within ABINIT, and the development in plane waves, are briefly described.

[1] http://www.abinit.org/
[2] http://www.uam.es/siesta/

## 3.1. Pseudo-potentials and plane waves

### 3.1.1. Norm-conserving pseudo-potentials

In the previous formulation of the Kohn-Sham equations, the one-electron wave functions $\psi_i$ describe all the electrons of the system, regardless of their chemical and physical role in the system (i.e. either core or valence). The *frozen core approximation* [130] consists in ignoring the core electrons in the self-consistent resolution of the Kohn-Sham equations. For that, a kind of effective potential applied by the nuclei and their core electrons on the valence electrons is considered. Such an object is called a *pseudo-potential*. Briefly speaking, a norm-conserving pseudo-potential is built as follows. The all-electron problem is first solved for the isolated atom. Pseudo-valence wave functions are then constructed to satisfy the following rules. For each angular momentum,

1. Beyond a certain cut-off radius (that depends on the angular momentum), the pseudo valence wave function is equal to the all-electron wave function for the isolated atom.

2. Below this cut-off radius, the pseudo valence wave function is *smoothed*, in order to eliminate fluctuations and nodes and therefore make easier the plane wave treatment of the valence wave functions.

The pseudo wave functions are normalized exactly as the all-electron wave function, hence the name of "norm-conserving" pseudopotentials. In this thesis, norm-conserving Troullier-Martins pseudopotentials have been used [131].

### 3.1.2. Plane waves decomposition

In a crystal, the electron density and the effective potential keep the crystal periodicity. The direct and reciprocal lattices of the crystal are defined by their primitive lattice vectors $\vec{a}_i$ and $\vec{b}_i$ ($i = 1, 2, 3$ in three-dimension), as :

$$\vec{R} = \alpha_1 \vec{a}_1 + \alpha_2 \vec{a}_2 + \alpha_3 \vec{a}_3 \quad \text{with } (\alpha_1, \alpha_2, \alpha_3) \in \mathbb{Z}^3 \tag{II.24}$$

$$\vec{G} = \beta_1 \vec{b}_1 + \beta_2 \vec{b}_2 + \beta_3 \vec{b}_3 \quad \text{with } (\beta_1, \beta_2, \beta_3) \in \mathbb{Z}^3 \tag{II.25}$$

Where the primitive vectors verify the relation:

$$\vec{b}_i \cdot \vec{a}_j = 2\pi \, \delta_{ij} \quad \text{with} \quad \delta_{ij} = \begin{cases} 1 & \text{if } i = j \\ 0 & \text{if } i \neq j \end{cases} \tag{II.26}$$

The Bloch theorem [132] for such a periodic system states that the one-electron wave functions of the Kohn-Sham equations satisfies the property:

$$\psi_{n,\vec{k}}(\vec{r}+\vec{R}) = e^{i\vec{k}\cdot\vec{R}}\,\psi_{n,\vec{k}}(\vec{r}) \tag{II.27}$$

where $\vec{k}$ is a vector of the reciprocal space that can be chosen from the first Brillouin Zone (BZ). The first BZ is such that any vector $\vec{q}$ of the reciprocal space can be written as $\vec{q} = \vec{G} + \vec{k}$, with $\vec{k}$ belonging to the first BZ, and $\vec{G}$ being a vector of the reciprocal lattice. Consequently, the wave function can be decomposed as follows:

$$\psi_{n,\vec{k}}(\vec{r}) = \frac{1}{\sqrt{N\,\Omega_0}}\,e^{i\vec{k}\cdot\vec{r}}\,u_{n,\vec{k}}(\vec{r}) \quad \text{where} \quad u_{n,\vec{k}}(\vec{r}+\vec{R}) = u_{n,\vec{k}}(\vec{r}), \tag{II.28}$$

in which $n$ is the *band* index, describing the discrete energy levels of the possible Kohn-Sham eigenstates $\psi_{\vec{k}}$ (i.e. the discrete solutions of the Kohn-Sham equations obtained *for a specific* vector $\vec{k}$).

Equation II.28 defines the one-electron wave function as a *Bloch wave*. Function $u_{n,\vec{k}}(\vec{r})$ has the periodicity of the lattice modulated by the phase factor $e^{i\vec{k}\cdot\vec{r}}$.

The function $u_{n,\vec{k}}(\vec{r})$ can be expanded as a sum over the reciprocal lattice vectors $\vec{G}$ (equation II.25):

$$u_{n,\vec{k}}(\vec{r}) = \sum_{\vec{G}} e^{i\vec{G}\cdot\vec{r}}\,c_{n,\vec{k}}(\vec{G}) \tag{II.29}$$

where the $c_{n,\vec{k}}(\vec{G})$ are the Fourier coefficients of $u_{n,\vec{k}}(\vec{r})$.

Combining equations II.28 and II.29, the plane wave expansion of the Kohn-Sham wave function becomes:

$$\psi_{n,\vec{k}}(\vec{r}) = \frac{1}{\sqrt{N\Omega_0}} \sum_{\vec{G}} e^{i\,(\vec{k}+\vec{G})\cdot\vec{r}}\,c_{n,\vec{k}}(\vec{G}) \tag{II.30}$$

Such a representation of the wave function (into an infinite basis set of plane waves) is impractical for numerical treatment, which must use a discrete, but finite, expansion. However, the larger the plane wave basis with increasing norm of vectors $\vec{G}$, the more accurate is the representation of the wave function. As a consequence, the expansion is ordered by increasing $|\vec{G}|$ and then truncated to a finite number of reciprocal lattice vectors. The $\vec{G}$ retained satisfy, for a given $\vec{k}$:

$$\frac{\hbar^2|\vec{k}+\vec{G}|^2}{2m_e} \leq E_{\text{cut}} \tag{II.31}$$

where $E_{\text{cut}}$ is the plane-wave cut-off energy.

The number of bands to be calculated depends on the total number of electrons in the system. Assuming spin degeneracy, the number of occupied bands, $n_{\text{occ}}$, equals half the number of electrons in the system (since two electrons can populate the same band at most). However, this is a lower limit for the computation, and corresponds to the minimum necessary bands for the electrons to fulfill the principles of quantum mechanics. Therefore, even for insulators where the bands are filled with increasing energy towards the valence band maximum, the number of computed bands is usually set to a larger value than $n_{\text{occ}}$ in order to let empty states available above the valence band, and also to carry out density of states investigations with a clear interest in both occupied and unoccupied states.

### 3.1.3. Boundary conditions

The codes we use only deal with 3D periodic systems. Here we are interested in the simulation of surfaces, which are not 3D periodic objects. Thus we have to use a large supercell that constains the system of interest, which is itself periodically repeated in the three directions.

In Figure 2.1a, a schematic in two dimensions representation of the periodic boundary conditions is shown for an infinite bulk material. The bulk material is completely described by the atoms of one unit cell (delimited by the solid lines), displayed as filled circles. The atoms in the periodically repeated unit cells (delimited by the dashed lines) are represented as empty circles. For non-periodic systems, as most of the systems presented in section 5 which display a surface, the same boundary conditions apply. This is shown in Figure 2.1b: the whole non-periodic system is used as the unitary period and is repeated in space, with a slice of vacuum between regions separating the cause of non-periodicity, such as the surface. The non-periodic system is represented by a so called *slab* contained in the *supercell*. The slab is a set of atomic layers, infinitely repeated in the $(x, y)$ plane and finite along $z$ as delimited by surfaces. The vacuum slice separates the periodic images, ensuring the supercell to be genuinely free of electrostatic interactions, if large enough.

## 3.2. Numerical parameters and algorithms

Before presenting the detailed studied configurations and the output physical quantities of interest yielded by ABINIT, the general parameters and algorithms common to bulk and surface are presented.

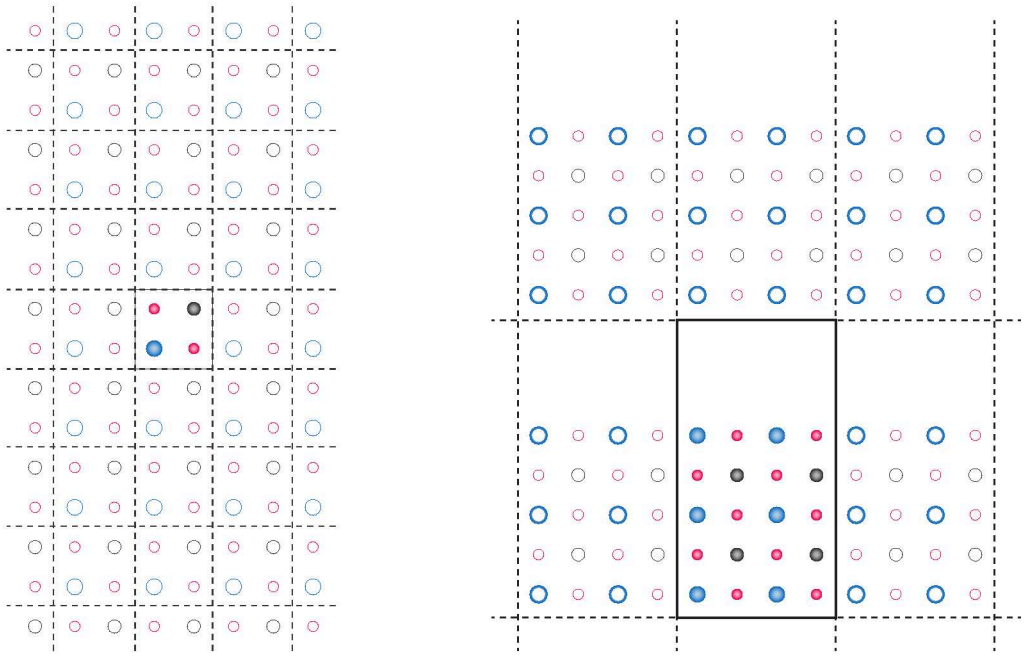

**(a)** Infinite bulk **(b)** Finite surface

**Figure 2.1.:** Schematic two-dimensional representation of the periodic boundary conditions for (a) infinite bulk and (b) finite supercell with surfaces. The atoms and image atoms are represented by filled and empty circles, respectively. The unit cell in (a) and supercell in (b) are detoured with the solid line. Blue, black and red (empty circles) circles depict barium, titanium and oxygen (images) atoms.

### 3.2.1. Numerical parameters

Beyond the theoretical approximations (local density approximation, frozen-core approximation and wave function pseudization with the Troullier-Martins pseudopotentials), our ab initio calculations require to fix correctly a set of numerical parameters, that ensure a numerical precision that should be smaller than the accuracy delibered by the theoretical approximations. There are three parameters that we need to fix:

1. the plane wave cut-off, that defines the extension of the plane wave basis set on which the periodic parts of the Kohn-Sham wave functions are expanded,
2. the sampling of the First Brillouin Zone,
3. the vaccuum thickness between the free-standing slabs of the supercell

The energy cut-off controls the size of the plane-wave basis set.

The $\vec{k}$ vectors indexing the Kohn-Sham wave functions are restricted to the first Brillouin Zone, which is sampled by a discrete $k$-point mesh. It corresponds to a finite number of points in the first Brillouin Zone, over which the computation of several

integrals is numerically performed (e.g. the electron density is written as an integral over the Brillouin Zone).

The role of the vacuum layer is to minimize the effect of possible spurious electric fields between the periodic images of the slab. The precision associated with its thickness must therefore be severely controlled.

The results have to be converged with each of these three parameters. The numerical precision associated with each of them is discussed in section 6.

### 3.2.2. Structural optimization

The self-consistent cycle solves the Kohn-Sham equations in order to compute the ground state properties of the system. Throughout successive iterations, the electron density and effective potential is refined further and further to reach the actual ground state properties, in particular the total energy and the forces on the atoms. It can therefore be used to perform so called *structural optimization*, which consists in finding the most stable spatial distribution of atoms in a system, in terms of interatomic distances and angles. The convergence criterion for such a procedure can be the atomic forces acting on the atoms, which are computed during each self-consistent cycle as the derivative of the energy with respect to atomic positions. Below a certain threshold on the maximal forces, one decides that the structure is optimized. We have used the Broyden-Fletcher-Goldfarb-Shanno minimization scheme of ABINIT (for SIESTA, this is a conjugate gradient algorithm). The full structural optimization is stopped when all the Cartesian components of the atomic forces are below $2.0 \times 10^{-4}$ atomic units, i.e. $\sim 0.01\,\mathrm{eV\,\AA^{-1}}$. The precision associated with this criterion is discussed further.

### 3.2.3. Valence electrons

Last point, as mentioned in section 3.1.1, the treatment of valence electrons is explicit whereas the core electrons are not included in the calculation. In order to reproduce correctly the ferroelectric distortion, the explicit treatment of so called *semi-core* electrons is mandatory. For Ti, wave functions of empty $3d$ states significantly overlap with the wave functions of the semi-core $3s$ and $3p$ states [133], owing to the particularly short bond length of Ti as shown in the case of transition metal clusters [134]. The explicitly treated valence and semicore electrons are presented in table 2.1, for each atomic species.

| chemical element | valence electrons | number of valence electrons |
|---|---|---|
| Ba | $5s^2\ 5p^6\ 6s^2$ | 10 |
| Ti | $3s^2\ 3p^6\ 4s^2\ 3d^2$ | 12 |
| O | $2s^2\ 2p^4$ | 6 |

**Table 2.1.:** Electrons treated as valence or semi-core for each element of barium titanate.

# 4. Outputs

We now describe the physical outputs that can be extracted from a first-principles calculation.

An initial slab of atoms respecting the desired symmetries is built. The detailed configurations that correspond to our modeled systems are described in section 5. All of these initial configurations are structurally optimized to obtain the corresponding ground state. The first output of interest is therefore the *relaxed positions* of the atoms, which is the set of $(x, y, z)$ positions of the atoms with interatomic distances and angles that correspond to the least total energy and zero atomic forces (within the optimization criterion).

Among ground state properties, the *total energy* is of primary importance. It allows to compare the relative stability of different structures at $T = 0$ K.

Another crucial result of density functional theory ground state calculations is the *electronic density of states*, i.e. the energy distribution of the one-electron Kohn-Sham eigenstates. By convention, in this work, in all the plotted densities of states, the zero of the energies is fixed at the Fermi energy, i.e. at the highest occupied eigenstate. We computed the total density of states with the ABINIT code. The partial density of states corresponds to the projection of the total density of states onto selected orbitals and/or selected atoms. It can be easily obtained with SIESTA, in which the Kohn-Sham wave functions are expanded on local functions (numerical atomic orbitals). Therefore, quantum states which can be localized on different regions of the system can be investigated, allowing to distinguish for example surface states from bulk states.

Finally, we studied the macroscopic total potential across the system, in order to detect depolarizing fields as well as spurious electric fields possibly introducing non-desirable interactions between the periodic images of the slab. These fields were computed using the MACROAVE utility [135, 136].

# 5. Methodology

## 5.1. Simulation of out-of-plane polarization

One of our objectives is to model the (001) surface of barium titanate with out-of-plane polarization. As described in section 3.1 of chapter I, polarization perpendicular to the surface plane induces nonzero surface density of charges $\sigma$, which in turn gives rise to a depolarizing field $\vec{E}_{\text{dep}}$. This field opposes to the macroscopic polarization $\vec{P}$, and if not compensated, destabilizes the ferroelectric state. Efficient screening of the depolarizing field is therefore necessary for such polarization to subsist. In the literature, three approaches have been proposed to overcome this difficulty, which are described and qualitatively compared below.

To compensate the external fields introduced by the surface polarization, an external electric field can be applied, that opposes the depolarizing field. In order to recover the periodicity of the corresponding electric potential, a discontinuity is introduced in the vacuum region. This approach has been used by Meyer and Vanderbilt [112]. While the atomic positions are free to relax, the value of the external field to apply has to be varied in order to study the ferroelectric properties of the system, since the exact value of this macroscopic field matching the depolarizing field is not known a priori.

Another approach consists in maintaining ferroelectric distortions inside the slab by fixing the atomic positions to the known ferroelectric bulk positions, leaving surface and near surface atomic layers free to relax. Such differential structural relaxation method, with a clear distinction of "bulk-like" layers with respect to those close to the surface, allows to maintain polarization. This method has been applied on ferroelectric perovskites by Cohen [108, 110] and Fechner et al. [111]. Its drawback is that the depolarizing field in the volume is not screened because the atomic positions in inner atomic layers are fixed.

The third method presented is the one adopted in this thesis. It is based on the approach proposed by Shimada et al. [107] who investigated the domain ordering in ferroelectric $PbTiO_3$, by direct simulation of alternating pattern of up and down out-of-plane polarization. The configuration of alternating domains indeed best mimics the real behavior and physical origin of polarization perpendicular to the surface. The screening mechanism inherent to the domain ordering permits the compensation of the depolarizing field while preserving ferroelectricity. The principle of formation of domains with polarization perpendicular to the surface allowed by the screening of the depolarizing field by neighboring domains is given in Figure 2.2. As in real materials, the surface charge density of each domain contributes to a macroscopic electric field $\vec{E}_0$

which opposes the depolarizing field of neighboring domains. Therefore, this method overcomes the main drawbacks of the two above described approaches, allowing namely to fully screen the depolarizing field while letting the atomic positions to fully relax. However, it also requires the use of much larger supercells than in the two previous methods.

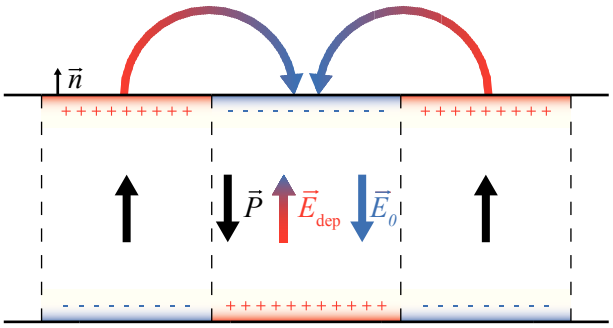


**Figure 2.2.:** Principle of formation of ferroelectric domains in a slab with polarization perpendicular to the surface. In the central domain, the depolarizing field $\vec{E}_{\mathrm{dep}}$ (red arrow) is created by the polarization charges accumulated at its surfaces, and mostly compensated by a field $\vec{E}_0$ (blue arrow) created by the polarization in the neighboring domains (or, equivalently, by the polarization charges accumulated at the surface of the neighboring domains).

## 5.2. Geometrical parameters and symmetry

The simulated slabs are defined by several geometrical parameters:

(i) the in-plane lattice constant $a$ which is used to adjust the in-plane strain applied on the system,

(ii) the slab thickness, expressed in terms of number $L$ of atomic layers, which is used to monitor the surface effects,

(iii) the slab width expressed in terms of number $N$ of unit cells along one of the in-plane directions, which is used to vary the domain width.

Periodic boundary conditions are applied. The direct space is described by a Cartesian coordinates system $(x_1, x_2, x_3) = (x, y, z)$ which coincides with pseudocubic directions $(a_1, a_2, a_3) = (a, b, c)$. $N_1$, $N_2$ and $N_3$ are the number of unit cells along $x$, $y$ and $z$.

A first example of modeled surface is represented in Figure 2.3, corresponding to the case $L = 5$ atomic layers, and $N_1 = 1$ unit cell along $x$ and $N_2 = 2$ unit cells along $y$. The atoms belonging to the slabs are depicted by filled spheres while periodic images are shown and drawn as empty circles. Solid lines delimit the supercell region in

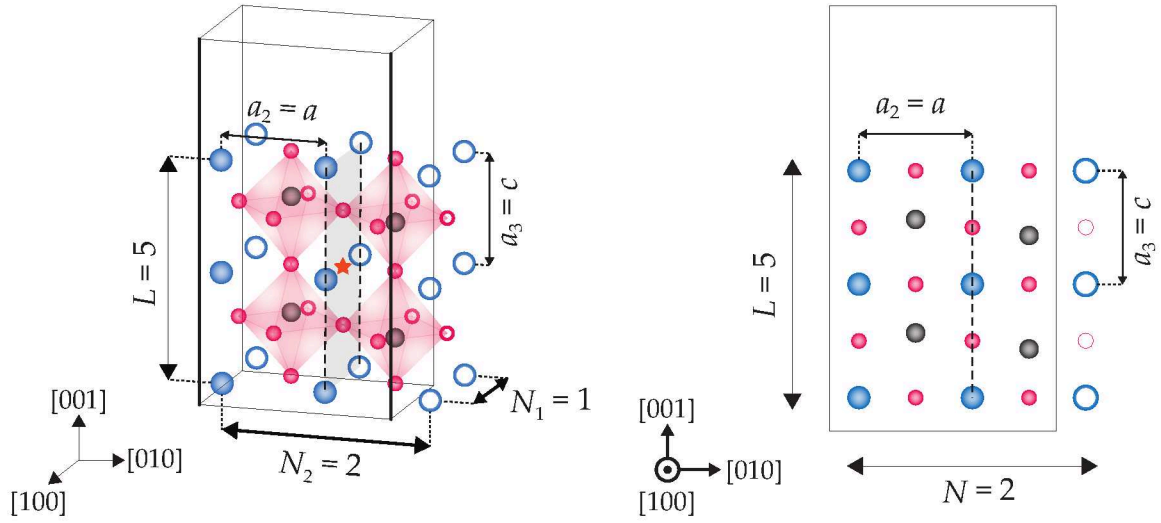


**(a)** 3D supercell **(b)** 2D projection

**Figure 2.3.:** Schematic view of a supercell (a) in the three dimensions and (b) as the projection on the $(y, z)$ plane. The lattice constants are $a_1 = a_2 = a$ and $a_3 = c$. The number of unit cells is $N_1 = 1$, $N_2 = 2$ and $N_3 = 2$ along $x$, $y$ and $z$ direction, respectively. The number of atomic layers along the vertical direction is $L = 5$.

which the atomic slab is topped by a vacuum layer. In Fig. 2.3a, the three dimensional representation of the supercell is given. In Fig. 2.3b, a two dimensional projection of the 3D supercell on the $(y, z)$ plane is shown. Since the slab contains only one unit cell along the [100] direction which is periodically repeated, the projection on the (100) plane simplifies the visualization of the simulated configuration without loss of information. We set $N = N_2$, the number of unit cells along [010]. The in-plane (i.e in the (001) plane) lattice constant is $a$ and the out-of-plane lattice constant along the polar axis is $c$.

In order to simulate alternating domains with out-of-plane polarization, the central Ti atoms are initially displaced along [001] for $y < N/2$ while they are displaced along $[00\bar{1}]$ for $y > N/2$. These displacements define two domains separated by a 180° domain wall (delimited by dashed lines). The domain wall is a BaO plane. Only the case of BaO domain walls have been considered in the present work.

At the center of the domain wall lies and inversion center for the slab (orange star). The presence of such an inversion center means that the *whole* supercell is not polar. The dipole moments of the two domains exactly compensate each other. In fact, the whole supercell carries a *quadrupole* and not a dipole. Moreover, the alternance of surface charges of the different domains contributes to create in the vacuum a short-range macroscopic field. It is crucial to verify that mutual interactions of the periodic images of the slabs are negligible. This last point is examined in section 6.

In this work, we have considered only the case of symmetric slabs, i.e. slabs which display the same top and bottom surface termination, either BaO or $TiO_2$. Symmetric slabs allows to avoid different chemical potentials at the two opposite surface layers in order to reduce the possible interactions between the periodic images [137, 138]. Moreover, symmetric slabs allows to preserve the inversion center in the center of the domain wall, in the case of the *c* phase, which is necessary for the supercell to be not polar as a whole.

The set of symmetry elements (space group) of the modeled configurations is fixed by the arrangement of the atoms in the initial, not yet relaxed, configuration. It is constrained throughout the structural optimization. In other words, the symmetry operations (e.g. mirror planes, inversion centers) are maintained during the relaxation and the resulting relaxed structure displays the same symmetries as the initial configurations.

The 2D projection of the supercell on the $(y, z)$ plane, as displayed in Fig. 2.3b, is the representation which will be used in the following to describe the results obtained on the relaxed ferroelectric slabs.

## 5.3. Structural relaxation of initial configurations

In all the structural relaxations, the in-plane lattice constant $a$ is fixed.

We simulated supercells (i) with polarization perpendicular to the surface, (ii) with polarization parallel to the surface and (iii) without polarization. Each type of supercell, depending on the polarization direction, can be assimilated to the particular *phases* that appear at high compressive and tensile strains on the isotherm $T = 0$ K of the temperature versus misfit strain phase diagrams of Pertsev et al. [139]. They are described hereafter.

### 5.3.1. *c* phase

This is the phase having its polarization perpendiculart to the surface. It is modeled by stripe domains infinitely long along $x$, periodic along $y$ and with polarization along $z$, alternating from a domain to another. In the initial configuration, titanium atoms are displaced off the center of the tetragonal cell, along $+z$ for the first half of the supercell along $y$, and along $-z$ for the second half. Therefore, two domains of opposite polarization are formed. This arrangement of atoms into *non-centrosymmetric*

*tetragonal* lattices defines the space group of the *c* phase as *P*4*mm* in each domain. The *c* phase configurations are depicted in Figure 2.4a. The values of the parameters which were used to simulate different configurations of *c* phase are presented aside in Table 2.4b. The range of in-plane *a* lattice constant corresponds to compressive strain (the LDA equilibrium lattice constant of bulk cubic $BaTiO_3$, i.e. 3.949 Å is taken as reference [140, 141]). The number of unit cells along the $y$ direction, $N$, defines the domain periodicity and width. For $N = 2$, domains of $N/2 = 1$ unit cell width are possible. For $N = 4$, domains of $N/2 = 2$ unit cells or $N/4 = 1$ unit cell width are possible, provided the inversion centers are preserved. For $N = 6$, domains of $N/2 = 3$ unit cells or $N/6 = 1$ unit cell width are possible. In this last case, domains of $N/3 = 2$ unit cells width are not permitted since it would require the disappearance of the inversion centers and the appearance of a mirror plane at the center of the central domain, resulting in a polar supercell. In other words, only an even number of domains are permitted in order to keep the whole supercell non polar.

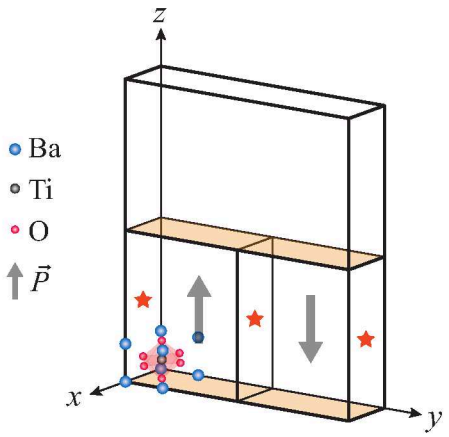


**(a)** *c* phase

| Parameters | Values |
|---|---|
| *a* (Å) | 3.800, 3.825, 3.850, 3.875†, 3.900† |
| *N* | 2, 4, 6 |
| *L* | 3, 5, 7, 9, 11, 13 |

†only for $L = 9$

**(b)** Parameter values

**Figure 2.4.:** (a) Three-dimensional schematic view of the modeled ferroelectric *c* phase supercells. The surfaces are highlighted in light orange and the inversion centers, positioned at the domain walls centers are represented with the orange star symbols. (b) Parameter values for in-plane lattice constant (*a* in Å), number of unit cells along $y$ ($N$) and number of atomic layers along $z$ ($L$) used for the simulation of the *c* phase.

### 5.3.2. *aa* phase

This is the phase with in-plane polarization. More precisely, the polarization is oriented along [110]. The corresponding configurations arise from initial displacements of the titanium along one <110> direction. The corresponding bulk *non-centrosymmetric orthorombic* structure has space group *Amm*2. The *aa* phase corresponds to the most stable phase with purely in-plane polarization [127] and is favored in a tensile in-plane

strain regime [142]. This is why we focus on the <110> direction to simulate slabs with purely in-plane polarization rather than the <100> direction which would result in a less stable phase of tetragonal symmetry. When the polarization lies along [110], no polarization charge density forms at the surface and therefore no depolarizing field has to be screened. Within periodic boundary conditions, slabs in the *aa* phase can be restricted to one unit cell in the $(x, y)$ plane. A schematic view of the supercell in the *aa* phase is presented in Figure 2.5a along with the values of the parameters which were used in the various simulations, in Table 2.5b.

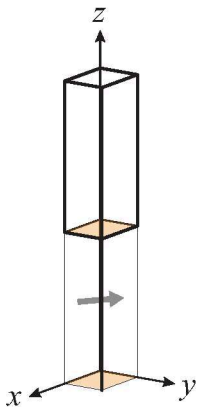


**(a)** *aa* phase

| Parameters | Values |
|---|---|
| $a$ (Å) | 3.850, 3.875, 3.900, 3.925, 3.950, 3.975, 4.000 |
| $L$ | 9 |

**(b)** Parameter values

**Figure 2.5.:** (a) Three-dimensional schematic view of the modeled ferroelectric *c* phase supercells. The surfaces are highlighted in light orange. (b) Parameter values for in-plane lattice constant ($a$ in Å), and number of atomic layers along $z$ ($L$) used for the simulation of the *aa* phase.

### 5.3.3. *p* phase

Both *c* and *aa* phases represent models of ferroelectric configurations with initial off center displacements. In order to compare the relative stability of these phases, a reference phase is needed. This reference is chosen as the centrosymmetric tetragonal structure (in bulk it would be of space group $P4/mmm$). In this configuration, called *p* phase (which stands for paraelectric), no off-center displacement is applied to the initial position of the atoms, therefore no polarization is enforced, and the non polar state is maintained in the ab initio calculations by symmetry constraints. The *p* phase configurations require only one unit cell in the $(x, y)$ plane, as does the *aa* phase, therefore $N \equiv 1$. As reference structures, the paraelectric configuration is modeled for every $a$ and $L$, as detailed in Table 2.2.

| Parameters | Values |
|---|---|
| $a$ (Å) | 3.800, 3.825, 3.850, 3.875, 3.900, |
| | 3.925, 3.950, 3.975, 4.000 |
| $L$ | 3, 5, 7, 9, 11, 13 |

**Table 2.2.:** Parameter values for in-plane lattice constant ($a$ in Å), and number of atomic layers along $z$ ($L$) used for the simulation of the $p$ phase.

## 5.4. Energy and local polarization

The relative stability of the $c$ and $aa$ phases with respect to the corresponding $p$ phase is obtained by the normalized energy difference:

$$\Delta E^c(a, N, L) = \frac{E^c_{\text{tot}}(a, N, L)/N - E^p_{\text{tot}}(a, L)}{L/2} \tag{II.32}$$

$$\Delta E^{aa}(a, L) = \frac{E^{aa}_{\text{tot}}(a, L) - E^p_{\text{tot}}(a, L)}{L/2}, \tag{II.33}$$

in which $E^c_{\text{tot}}(a, N, L)$ is the total energy of the $L$-layer 1×N slab in $c$ phase, $E^p_{\text{tot}}(a, L)$ that of the $L$-layer 1×1 slab in $p$ phase, and $E^{aa}_{\text{tot}}(a, L)$ that of the $L$-layer 1×1 slab in $aa$ phase.

Normalization with respect to layer thickness $L$, by $L/2$, is required to make the energies computed comparable. $\Delta E$ roughly corresponds to an energy difference per unit cell, because $L/2$ is supposed to be the number of unit cells in a $L$-layer 1×1 slab (it is non integer in all the cases considered here). However, this quantity converges to the bulk value when $L \to \infty$ and has a monotonic evolution with $L$, as will be shown hereafter.

### 5.4.1. Local polarization

The local polarization used in this thesis is defined as the polarization vector per unit cell. It is formally defined as [107]:

$$\vec{P}_i = \frac{e}{\Omega_i} \sum_{j \in i} w^i_j \, \overline{\overline{Z}}^*_j \, \delta\vec{u}_j \tag{II.34}$$

Where $e$ is the elementary charge, $\Omega_i$ is the volume of unit cell $i$, $w^i_j$, $\overline{\overline{Z}}^*_j$ and $\delta u_j$ are the weight, Born effective charge and displacement of atom $j$. These ingredients are described below.

The reference relaxed positions of the atoms in the *c* and *aa* phases are substracted to the relaxed positions of the atoms in the reference *p* phase in order to obtain the displacement $\delta u_j$ of atom $j$ arising from the ferroelectric distortions.

Associated to each atom, we use the Born effective charges computed with the present pseudopotentials for the optimized cubic phase of barium titanate (lattice constant 3.949 Å). The Born effective charge is a second-rank tensor. In the cubic phase, for Ba and Ti, it is a scalar tensor, due to the local cubic symmetry of the corresponding atomic sites. However, mainly for Ti, a large anomalous additional charge is observed compared to the nominal charge [54, 143, 144]. This is attributed to dynamical charge transfer involved in the Ti–O bond owing to the hybridization of occupied O 2*s* and O 2*p* orbitals with unoccupied Ti 3*d* orbitals associated with the ionic-covalent character of the bond [145, 146].

The Born effective charge tensors used for Ba and Ti are:

$$\overline{\overline{Z}}^*_{\mathrm{Ba}} = \begin{pmatrix} +2.76 & 0 & 0 \\ 0 & +2.76 & 0 \\ 0 & 0 & +2.76 \end{pmatrix} \quad \text{and} \quad \overline{\overline{Z}}^*_{\mathrm{Ti}} = \begin{pmatrix} +7.34 & 0 & 0 \\ 0 & +7.34 & 0 \\ 0 & 0 & +7.34 \end{pmatrix} \tag{II.35}$$

Compared to Ba and Ti, the Born effective charge of O atoms is anisotropic, and two components have to be distinguished, depending on the atom position with respect to the direction of the Ti–O bond it is involved in.

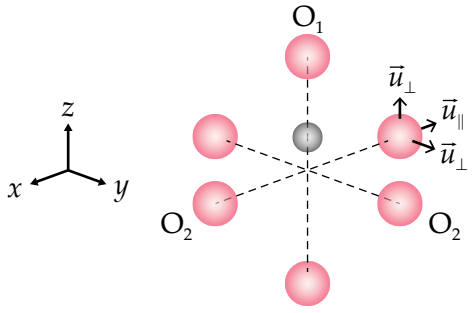


**Figure 2.6.:** Schematic of the Ti–O bonds in a $BaTiO_3$ unit cell. The Ti atom (dark grey) is relatively displaced along the [001] direction to illustrate the polarization axis. $O_1$ are oxygen atoms belonging to BaO layers. $O_2$ are oxygen atoms belonging to $TiO_2$ layers. Displacements of an oxygen atom are illustrated with $\vec{u}$ vectors. The displacements of a given O atom can be distinguished according to their direction with respect to the Ti–O bond direction.

In Figure 2.6, we have drawn the six oxygen surrounding a titanium ion in $BaTiO_3$. Ti is displaced vertically to illustrate polarization along the *z* axis. The Ti–O bonds are

depicted with the dashed lines. Depending on the bond direction, the displacements $\vec{u}$ of the O atoms are identified as $\perp$ or $||$ whether they are perpendicular or parallel to the Ti–O bond they are involved in. Following this nomenclature, two values of Born effective charge can be distinguished: $Z^*_{O_\perp}$ and $Z^*_{O_{||}}$. In turn, the Born effective charge for an O atom belonging to a Ti–O chain oriented along [001] ($O_1$) reads:

$$\overline{\overline{Z}}^*_{O_1} = \begin{pmatrix} Z^*_{O_\perp} & 0 & 0 \\ 0 & Z^*_{O_\perp} & 0 \\ 0 & 0 & Z^*_{O_{||}} \end{pmatrix} = \begin{pmatrix} -2.16 & 0 & 0 \\ 0 & -2.16 & 0 \\ 0 & 0 & -5.78 \end{pmatrix} \tag{II.36}$$

The components of the Born effective charge for the various atoms as accounted for in the computation of the local polarization vectors are given in Table 2.3.

| $j$ | Ba | Ti | $O_\perp$ | $O_{||}$ | Total |
|---|---|---|---|---|---|
| $Z^*_j$ | +2.76 | +7.34 | −2.16 | −5.78 | +0.00 |

**Table 2.3.:** Born effective charge components of the atoms calculated for the optimized cubic phase of barium titanate, in good agreement with previous reported calculated values by Ghosez et al. [144].

The volume $\Omega_i$ is computed for each unit cell $i$ using the formula of the volume of a hexahedron derived in Ref. [147].

Finally, each atom is shared by the adjacent unit cells such that only a fraction of it is accounted for in each unit cell. The weight of the atoms, depending on whether they belong to the volume or to the surface, for both surface terminations, are presented in Table 2.4.

## 6. Numerical precision

This section is dedicated to present the tests performed on the three parameters in order to determine the numerical precision of our ab initio calculations: the plane wave cut-off, the first Brillouin zone sampling and the vacuum thickness, as introduced in section 5.2.

| Termination | BaO | | $TiO_2$ | |
|---|---|---|---|---|
| $w_j$ | Volume | Surface | Volume | Surface |
| Ba | 1/8 | 1/4 | 1/2 | – |
| Ti | 1 | – | 1/4 | 1/2 |
| $O_1$ | 1/2 | 1 | 1/2 | – |
| $O_2$ | 1/2 | – | $4 \times 1/8$ and $1 \times 1/2$ | $4 \times 1/4$ and $1 \times 1$ |
| $n_{\text{atom}}$ | $N\left(2\frac{L+1}{2}+3\frac{L-1}{2}\right)$ | | $N\left(2\frac{L-1}{2}+3\frac{L+1}{2}\right)$ | |

**Table 2.4.:** Atomic weigths $w$ used for the calculation of the local polarization, depending on whether the atoms belong to the volume or the surface, in the case of the supercells with surface termination BaO or $TiO_2$. $n_{\text{atom}}$ is the number of atoms in the supercell.

## 6.1. Plane wave cut-off

We have fixed this parameter to $E_{\text{cut}} = 40$ Ha. This value provides a convergence of the energy difference between the bulk $Pm\bar{3}m$ and $P4mm$ phases of $\sim 1$ meV/u.c.

However, in the following chapter, we will have to compare the stability of different phases with very close energies, namely different domain structures ($N = 2, 4, 6$) of a given free-standing slab. Since these total energies are compared to each other in similar conditions (same supercell, i.e. same lateral lattice constant and vacuum thickness with same Brillouin zone sampling, or supercells of commensurate dimensions with equivalent $k$-point samplings), we find that the precision using the 40 Ha cut-off is in fact much better. To test this, we have taken the $L = 9$ free-standing slab, with an in-plane lattice constant $a = 3.80$ Å, a vacuum thickness of ∼24 Å (the total supercell dimension along $z$ is 40 Å and the slab thickness is ∼16 Å), a Brillouin zone sampling of $12 \times 2 \times 2$ and optimized two domain structures, corresponding to $N = 2$ and $N = 6$ ($N = 2$ in the same supercell as $N = 6$). We have done this calculation for a cut-off energy of 40 Ha, 50 Ha and 80 Ha. The total energies, and their differences, are given in Table 2.5.

| $E_{\text{cut-off}}$ (Ha) | $E_{\text{tot}}(c)$ $N = 2$ (Ha) | $E_{\text{tot}}(c)$ $N = 6$ (Ha) | Difference (meV/u.c.) |
|---|---|---|---|
| 40 | −3701.2886331993 | −3701.2873850783 | −1.25789 |
| 50 | −3701.5092001775 | −3701.5078858002 | −1.32466 |
| 80 | −3701.5760588258 | −3701.5747475840 | −1.32151 |

**Table 2.5.:** Total energy of the $c$ phase for $L = 9$ atomic layers and $N = 2$ and $N = 6$ unit cells width, for a set of energy cut-off values (direct output of the ABINIT code) given in meV/u.c. The number of unit cells is $6 \times \frac{9}{2} = 27$ in both cases.

This test shows that the precision we have with respect to the plane wave cut-off is $\sim 0.1$ meV/u.c., as far as the comparison between domain structures with same slab thickness, equivalent $k$-point sample, same vacuum layer and same in-plane lattice constant is concerned.

## 6.2. First Brillouin zone sampling

We have performed our structural optimizations by using a very fine $k$-point mesh. Initially, the $L = 9$ atomic layers slab was optimized using a $k$-point meshes of $6 \times 3 \times 1$ ($N = 2$), $6 \times 2 \times 1$ ($N = 4$) and $6 \times 1 \times 1$ ($N = 6$). After structural optimization, the calculation was refined using a denser mesh, namely $12 \times 6 \times 1$ ($N = 2$), $12 \times 3 \times 1$ ($N = 4$) and $12 \times 2 \times 1$ ($N = 6$), which exactly correspond to the same $k$-point density in the first Brillouin zone. For the other values of $L$, we directly optimized the system using this lateral density of $k$-points, which would correspond to 12 $k$-points in any direction of the first Brillouin zone of the bulk. Along $z$, one $k$-point was taken, which is largely sufficient owing to the very large size of the supercells along this direction (30 Å for $L = 5, 7, 9$ and 40 Å for $L = 9, 11, 13$).

In order to know precisely the precision associated to this sampling, we performed a test on the slab in $c$ phase with $L = 9$ atomic layers, and $N = 6$ unit cell width, in-plane lattice constant $a = 3.80$ Å, a plane wave cut-off of 50 Ha and a large vacuum thickness provided by a supercell size along $z$ of 40 Å, which we optimized using a $12 \times 2 \times 2$ and a $24 \times 4 \times 2$ mesh. The total energies and their difference are given in Table 2.6.

| $k$-point mesh | $E_{\text{tot}}(c)$ $N = 6$ (Ha) | Difference (meV/u.c.) |
|---|---|---|
| $12 \times 2 \times 2$ | $-3701.5078858002$ | $7.5 \times 10^{-4}$ |
| $24 \times 4 \times 2$ | $-3701.5078850512$ | |

**Table 2.6.:** Total energy of the $c$ phase for $L = 9$ atomic layers and $N = 6$ unit cells width (for a specific set of convergence parameters described in the text), with different $k$-point meshes.

The precision associated to the first Brillouin zone sampling we use is therefore excellent, much better than the one associated with the plane wave cut-off.

## 6.3. Vacuum thickness

The next parameter we have to test is the vacuum thickness. It is absolutely crucial, because we will simulate surfaces with out-of-plane polarization. We might think that such systems generate long-range electric field in the vacuum, and therefore we would have to use very large vacuum thicknesses to get converged results and periodic images without interaction. However, as described in section 5.3 about the $c$ phase, all the systems with out-of-plane polarization that we study consist of alternating up and down polarization patterns, so that all the supercells we construct are always non polar, because they contain two domains with opposite polarization that exactly compensate each other. The supercell contains therefore an electrostatic quadrupole. The electric field generated by a quadrupole in the vacuum decays more rapidly than the one generated by a dipole, but this is still a long-range field. In fact, the situation is much more favorable: thanks to the lateral periodic boundary conditions, the alternating up/down dipoles lattice generates a short-range field in the vaccuum. All the fields created by the dipoles of the domains, although long-ranged, compensate each other to create a short-range field in the direction perpendicular to the surface. This fact was already pointed out by Shimada et al. [107] in their study of free-standing out-of-plane polarized $PbTiO_3$ slabs. We have numerically tested this crucial point, in the case of $L = 9$ atomic layers and $N = 6$ unit cell wide free-standing slab in the $c$ phase with in-plane lattice constant $a = 3.80\,\text{Å}$, i.e. one of the systems we have obtained with the largest out-of-plane polarization magnitude in the domains. We have thus performed structural optimizations of this system by varying the vacuum thickness and maintaining all the other numerical parameters unchanged. The calculation has been performed with ABINIT and with SIESTA. The obtained results are summarized in Table 2.7.

| Code | Vacuum thickness (Å) | $E_{\text{tot}}(c)$ | Difference (meV/u.c.) |
|---|---|---|---|
| ABINIT | $\sim 14$ | $-3701.5092055777$ Ha | 0.0054 |
| | $\sim 24$ | $-3701.5092001775$ Ha | |
| SIESTA | $\sim 14$ | $-101100.5653$ eV | 0.174 |
| | $\sim 29$ | $-101100.5606$ eV | |

**Table 2.7.:** Total energy of the free standing slab in the $c$ phase for different vacuum thickness (see text for the list of parameters). Note that the structural optimization with SIESTA was performed using a $6 \times 1 \times 1$ $k$-point mesh and a criterion on the forces of $0.02\,\text{eV Å}^{-1}$. Then the energy was refined using $12 \times 2 \times 1$ mesh (but the structure not reoptimized). However the maximal force was still low $< 0.03\,\text{eV Å}^{-1}$.

We see that the precision associated with this method is excellent. The difference between ABINIT and SIESTA on this last point probably comes from the better control of the precision that we have with plane waves than with numerical atomic orbitals. However, since all our calculations (except when mentioned) are performed with ABINIT, we can say that the precision associated to the numerical scheme we use to compare total energies of different domain structures in the same conditions (same supercell and $k$-point sampling or commensurate supercells with equivalent $k$-point samplings) is $\sim 0.1$ meV/u.c. We will see in the following chapter that it is in general sufficient to discriminate between the slabs of $N = 2$, $N = 4$ and $N = 6$ unit cells width for a given thickness $L$.

## 6.4. Structural optimization

The last numerical parameter is the tolerance on the maximal forces in the structural optimizations. It is fixed here to $2\times10^{-4}$ Ha/bohr, i.e. $\sim 0.01$ eV/Å. The precision on the total energies associated with this parameter is more difficult to estimate. For instance, one can compare the total energies of the same system optimized starting from different initial configurations, or examine the total energies of the last steps in the structural optimizations. Typically, we have a precision of a few $10^{-4}$ Ha for the biggest slabs, and below $10^{-4}$ Ha for the smallest ones. Divided by the number of unit cells, the precision is a few 0.1 meV/u.c.

In conclusion, our numerical scheme allows comparison of the total energies of different domain configurations with a precision of a few 0.1 meV/u.c.

## 6.5. Test of the pseudopotentials and numerical scheme on bulk $BaTiO_3$

The present numerical scheme has been first tested on bulk $BaTiO_3$. Cubic $Pm\bar{3}m$ $BaTiO_3$ is found to have an equilibrium lattice constant of 3.949 Å.

If we fix the lattice constants at the experimental values of the tetragonal phase ($a = b = 3.994$ Å and $c = 4.036$ Å in the $P4mm$ space group), the structural optimization leads to atomic positions corresponding to the following ferroelectric displacements (assuming $\delta z_{\mathrm{Ba}} = 0$): $\delta z_{\mathrm{Ti}} = 0.055$ Å, $\delta z_{\mathrm{O}_1} = -0.118$ Å and $\delta z_{\mathrm{O}_2} = -0.075$ Å ($O_1$ and $O_2$ correspond to oxygen atoms belonging to the Ti–O chain parallel and perpendicular to the polarization, respectively).

The fully relaxed ferroelectric tetragonal structure has lattice constants $a = b = 3.943\,\text{Å}$ and $c = 3.980\,\text{Å}$ with a spontaneous polarization of $24\,\mu\text{C}\,\text{cm}^{-2}$ and ferroelectric displacements $\delta z_{\text{Ti}} = 0.043\,\text{Å}$, $\delta z_{\text{O1}} = -0.073\,\text{Å}$ and $\delta z_{\text{O2}} = -0.051\,\text{Å}$. These preliminary results are in very good agreement with previous LDA calculations [26, 111, 140].

**Stability of the bulk phases:**

We now optimize the $P4/mmm$, $Amm2$ and $P4mm$ (bulk phases) under fixed in-plane lattice constant. The total energy of the paraelectric ($P4/mmm$), ferroelectric polarized along [110] ($Amm2$) and ferroelectric polarized along [001] ($P4mm$) are plotted as a function of in-plane strain in Figure 3.1.

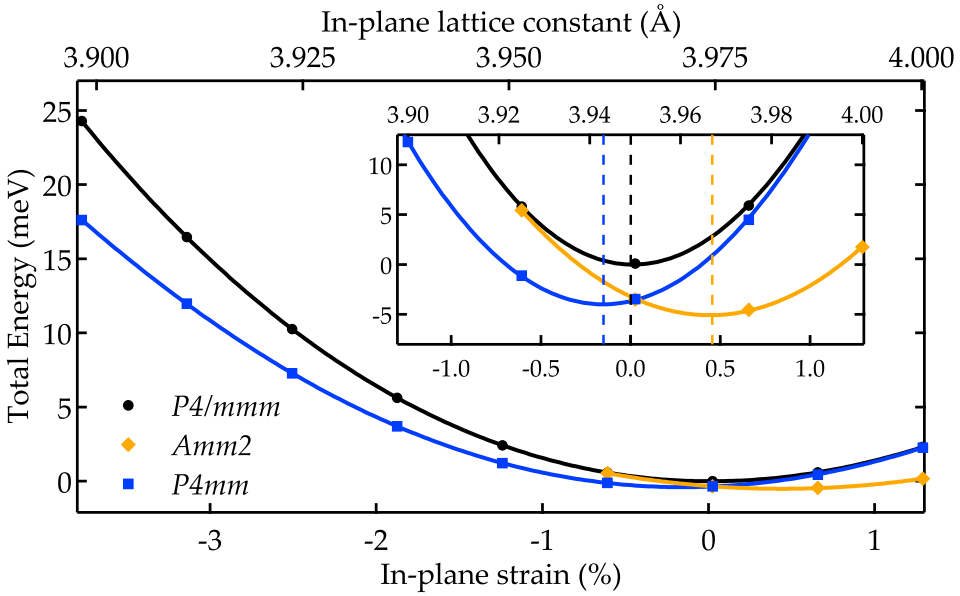


**Figure 2.7.:** Total energy (meV/u.c.) of bulk $BaTiO_3$ in the paraelectric $P4/mmm$ and ferroelectric $Amm2$ and $P4mm$ (polarization along [110] and [001], respectively) as a function of in-plane lattice constant $a$. The $P4/mmm$ structure uses as energy reference. The calculated data are in excellent agreement with Ref. [142]. The solid lines are guides for the eyes.

The calculated LDA equilibrium lattice constant for the bulk $P4/mmm$, $Amm2$ and $P4mm$ are 3.949 Å (i.e. 0 % strain), 3.966 Å (i.e. 0.44 % strain) and 3.943 Å (i.e. −0.16 % strain), respectively. Note that our simulation methodology (the paraelectric and ferroelectric structure are imposed by symmetry) does not allow to simulate the intermediate monoclinic structures (space group $Cm$) reported by Diéguez et al. [142] and Pertsev et al. [139]. Nevertheless, the results, further described in the following chapter, are in very good agreement with the work of Diéguez et al. [142].

**Density of states:**

The electronic density of states (DOS) has been computed for bulk $Pm\bar{3}m$ structure and is displayed in Figure 2.8.

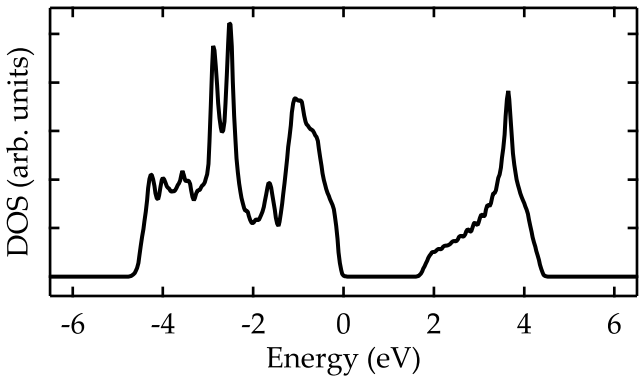


**Figure 2.8.:** Electronic density of states of bulk $Pm\bar{3}m$ structure for $a = 3.95$ Å. The Fermi energy $E_F$ is at 0 eV.

The Kohn-Sham band gap for bulk $BaTiO_3$ is $\sim 1.8$ eV, and the overall DOS shows good agreement with previous DFT calculations based on LDA [43,148,149], GGA [150] and LDA+U [151].

# Chapter III.

# First-principles results on $BaTiO_3$(001) slabs

In this chapter, in-plane and out-of-plane polarized $BaTiO_3$(001) surfaces are studied by density-functional calculations. The surface and associated atomic distortions influence the necessary balance between the long and short-range forces that maintain ferroelectricity. Both surface terminations (BaO and $TiO_2$) are investigated as a function of in-plane strain $a$, slab thickness $L$ and domain width $N$. In order to address the effects of the surface on the ferroelectric stability (relative total energies of $c$, $aa$ and $p$ phases) and polarization amplitude, it is first necessary to investigate the corresponding properties in the bulk.

Moreover, atomic surface distortions and electronic structure have to be also studied in the non polar $p$ phase as a function of in-plane strain and surface terminations to address the effect of the ferroelectricity and polarization direction.

The bulk and $p$ phase are thus first studied as reference systems.

## 1. Reference systems: bulk and $p$ phase

### 1.1. Bulk results

First, we present the stability and polarization amplitude of ferroelectric $BaTiO_3$ bulk phases as a function of in-plane strain. We study bulk phases of $BaTiO_3$ similar to the $c$, $aa$ and $p$ phases of $BaTiO_3$(001) surfaces, namely tetragonal $P4mm$ (polarization along [001]), orthorhombic $Amm2$ (polarization along [110]) and tetragonal $P4/mmm$ (zero polarization). These preliminary bulk calculations, performed on a 5-atom unit cell, follow the method employed for instance by Dieguez et. al [142]: the

lattice constants are fixed in-plane ($a = b$) and maintained orthogonal while the third lattice vector $c$ is relaxed until the $zz$ stress tensor components vanish (the $zx$ and $zy$ components are zero by symmetry in these three phases). Note that the reference non polar phase is tetragonal centrosymmetric as a result of the in-plane (along $xy$) lattice constants constrain as opposed to the out-of-plane (along $z$) lattice constant which is not constrained ($a = b$ fixed while relaxation is along $c$). The equilibrium LDA lattice constant of bulk cubic $BaTiO_3$ (3.949 Å) is taken as reference for the calculation of the strain.

### 1.1.1. Stability

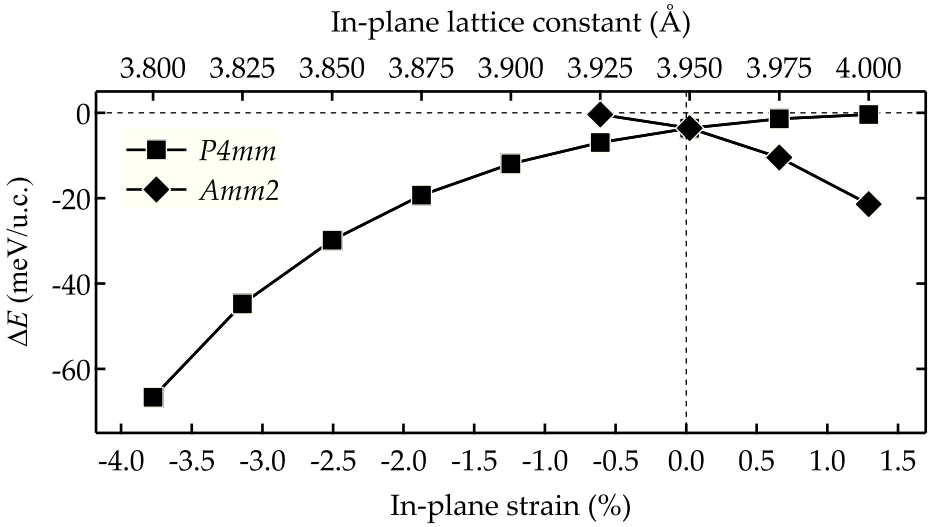


**Figure 3.1.:** Energy (meV/u.c.) of the $P4mm$ (polarization along [001]) and $Amm2$ (polarization along [110]) bulk phases relative to the $P4/mmm$ paraelectric bulk phase, as a function of in-plane strain. The transition between $P4mm$ and $Amm2$ occurs at 0 % strain, which corresponds to the lattice constant $a = 3.949$ Å.

The stability of the ferroelectric bulk phases as a function of in-plane strain $a$ is studied by comparing the total energy of the $P4mm$ and $Amm2$ phases ($E_{\text{tot}}^{P4mm}$ and $E_{\text{tot}}^{Amm2}$) with that of the $P4/mmm$ phase ($E_{\text{tot}}^{P4/mmm}$). The total energies $E_{\text{tot}}$ are expressed in meV per formula unit. The total energy differences, $\Delta E$, between the ferroelectric and paraelectric phases as a function of the in-plane lattice constant $a$ or equivalently the in-plane lattice strain $\eta$ are plotted in Figure 3.1.

The $P4mm$ phase (polarization along [001]) is stabilized under compressive strain ($\eta < 0$ %) whereas the $Amm2$ phase (polarization along [110]) is stabilized under tensile strain ($\eta > 0$ %). The crossover between the two phases occurs at $\eta = 0$ %, i.e. at an in-plane lattice constant $a = 3.949$ Å, which corresponds to the LDA lattice constant of perfect cubic $BaTiO_3$.

### 1.1.2. Polarization amplitude

| | $P4mm$ | | | | | $Amm2$ | | | |
|---|---|---|---|---|---|---|---|---|---|
| $a$ (Å) | 3.800 | 3.825 | 3.850 | 3.875 | 3.900 | 3.925 | 3.950 | 3.975 | 4.000 |
| $\eta$ (%) | −3.8 | −3.1 | −2.5 | −1.9 | −1.2 | −0.6 | 0.0 | 0.7 | 1.3 |
| $\lvert\vec{P}\rvert$ (µC cm$^{-2}$) | 57.1 | 48.6 | 41.3 | 35.3 | 29.9 | 10.4 | 19.7 | 26.6 | 32.5 |

**Table 3.1.:** Polarization amplitude of bulk $P4mm$ and $Amm2$ phases as a function of in-plane lattice constant $a$.

The spontaneous polarization amplitude of the modeled ferroelectric bulk phases can be calculated using expression II.34 (see section 5.4 on page 37). The values of the amplitude of the polarization $|\vec{P}|$ calculated from the ferroelectric $P4mm$ and $Amm2$ bulk phases as a function of in-plane strain are given in Table 3.1. For $P4mm$, the amplitude of the polarization is enhanced in the compressive strain regime. Conversely, for $Amm2$, it is enhanced in the tensile strain regime. In other words, compressive strain increases atomic displacements perpendicular to the strain axis, therefore enhancing polarization for the $P4mm$ phase, whereas tensile strain increases atomic displacements parallel to the strain axis, therefore leading to a polarization enhancement for the $Amm2$ phase. In what follows, these values will be used as reference for the polarization amplitude calculated for the $BaTiO_3$(001) slabs with in-plane polarization (section 2) and with out-of-plane polarization (section 3).

## 1.2. Non-polar $p$ phase

For the simulated slabs, the $p$ phase is the non ferroelectric reference used to compare the relative stability of the ferroelectric $aa$ and $c$ phases. The atomic displacements between the $p$ phase and the $c$ and $aa$ phases are used to compute the local polarization in the ferroelectric slabs. In this section, we present two aspects of the fully relaxed $p$ phases: the surface rumpling and electronic density of states.

### 1.2.1. Surface atomic displacements and rumpling

We focus on the atomic displacements along the [001] direction, that is normal to the surface. For each atomic layer, we define the *rumpling* as the following:

$$r = \frac{\langle z_{\text{cat}} \rangle - \langle z_{\text{O}} \rangle}{a} \tag{III.1}$$

Where $\langle z_{cat} \rangle$ and $\langle z_O \rangle$ are the average of the $z$ coordinates of the cations (Ba or Ti) and oxygen atoms, respectively, in the considered BaO or $TiO_2$ atomic layer. Hereafter, it is expressed in percentage of the in-plane lattice constant $a$.

Figure 3.2 presents the surface and subsurface unit cells of the BaO (Fig. 3.2a) and $TiO_2$ (Fig. 3.2c) terminations, in the case of the largest studied in-plane lattice constant $a = 4.000$ Å. The interatomic distances in the $(y,z)$ plane are indicated in Å. The values of the rumpling, as calculated from the fully relaxed slabs in the $p$ phase with $a$ from 3.800 Å to 4.000 Å are given aside.

The surface rumpling is always negative (i.e. oxygen atoms are displaced more outwards with respect to the cations). The rumpling in the subsurface atomic layer changes sign with respect to that in the surface atomic layer. In other words, BaO (respectively $TiO_2$) and $TiO_2$ (BaO) planes show negative and positive rumpling in BaO ($TiO_2$) terminated slabs. For the $TiO_2$ termination, the amplitude of the rumpling is larger than that in every atomic planes in the BaO-terminated slabs. With increasing tensile strain (i.e. increasing in-plane lattice constant $a$), the absolute value of the rumpling increases for every atomic planes in the BaO-terminated slabs whereas it alternatively decreases and increases in the case of the $TiO_2$-terminated slab, when starting from the surface plane.

Significant differences in out-of-plane atomic displacements are therefore observed between the two surface terminations. The values of $r$ for the $p$ phase will be used as reference for the study of the interplay between rumpling and ferroelectric distortions in the in-plane polarized $aa$ and out-of-plane polarized $c$ phases. For the $aa$ phase, we will compare the rumpling to that in the $p$ phase in the case of highest tensile strain ($a = 4.000$ Å), in section 2.4, for systems with ($L = 9$ atomic layers). For the $c$ phase, we will focus on the largest system ($L = 13$ atomic layers along $z$, $N = 6$ unit cells along $y$) in the highest compressive strain ($a = 3.800$ Å), in section 3.6, to compare the rumpling with that in the $p$ phase.

### 1.2.2. Density of states

The electronic density of states of the slabs in the $p$ phase has been calculated for all in-plane lattice constants ($a = 3.800$ Å to 4.000 Å) and slab thickness ($L = 3$ to 13 atomic layers). Figure 3.3 shows the electronic density of states for the BaO (Fig. 3.3a) and $TiO_2$ (Fig. 3.3b) terminations.

For the BaO termination, the Kohn-Sham band gap is $\sim 1.8$ eV and varies very little, within ca. 0.1 eV with varying in-plane strain ($a$) and slab thickness ($L$). It is comparable to the Kohn-Sham band gap of calculated for the bulk $Pm\bar{3}m$ structure (see

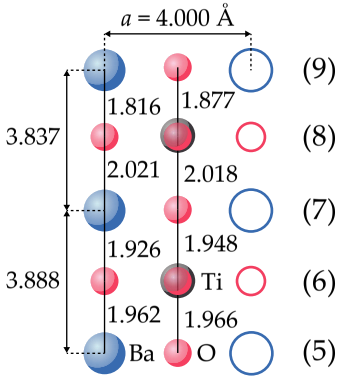


**(a)** Half slab

**BaO termination**

| $a$ (Å) | | 3.800 | 3.825 | 3.850 | 3.875 | 3.900 | 3.925 | 3.950 | 3.975 | 4.000 |
|---|---|---|---|---|---|---|---|---|---|---|
| $\eta$ (%) | | −3.8 | −3.1 | −2.5 | −1.9 | −1.2 | −0.6 | 0.0 | 0.7 | 1.3 |
| | (9) | −0.32 | −0.54 | −0.78 | −0.97 | −1.21 | −1.41 | −1.65 | −1.87 | −2.11 |
| | (8) | 0.40 | 0.42 | 0.44 | 0.45 | 0.48 | 0.51 | 0.52 | 0.54 | 0.57 |
| $r$ (%) | (7) | −0.24 | −0.29 | −0.32 | −0.36 | −0.41 | −0.46 | −0.52 | −0.58 | −0.66 |
| | (6) | 0.08 | 0.09 | 0.06 | 0.08 | 0.07 | 0.10 | 0.10 | 0.11 | 0.11 |
| | (5) | 0.00 | 0.00 | 0.00 | 0.00 | 0.00 | 0.00 | 0.00 | 0.00 | 0.00 |

**(b)** Rumpling

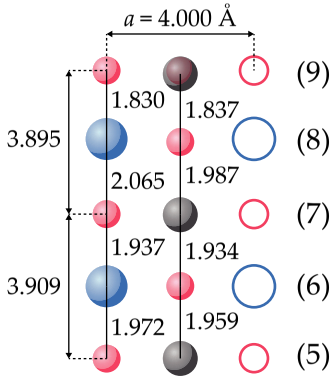


**(c)** Half slab

**$TiO_2$ termination**

| $a$ (Å) | | 3.800 | 3.825 | 3.850 | 3.875 | 3.900 | 3.925 | 3.950 | 3.975 | 4.000 |
|---|---|---|---|---|---|---|---|---|---|---|
| $\eta$ (%) | | −3.8 | −3.1 | −2.5 | −1.9 | −1.2 | −0.6 | 0.0 | 0.7 | 1.3 |
| | (9) | −3.31 | −3.10 | −2.93 | −2.79 | −2.63 | −2.50 | −2.36 | −2.27 | −2.16 |
| | (8) | 1.81 | 1.86 | 1.89 | 1.98 | 2.02 | 2.10 | 2.17 | 2.25 | 2.34 |
| $r$ (%) | (7) | −0.41 | −0.43 | −0.39 | −0.42 | −0.39 | −0.41 | −0.41 | −0.39 | −0.40 |
| | (6) | 0.19 | 0.22 | 0.21 | 0.24 | 0.25 | 0.27 | 0.28 | 0.32 | 0.34 |
| | (5) | 0.00 | 0.00 | 0.00 | 0.00 | 0.00 | 0.00 | 0.00 | 0.00 | 0.00 |

**(d)** Rumpling

**Figure 3.2.:** Surface and first subsurface unit cells of the slab in $p$ phase and rumpling values for the BaO (a, b) and $TiO_2$ (c, d) termination ($L = 9$ atomic layers, $a = 4.000$ Å). Full and empty circles depict supercell atoms and their periodic images. Interatomic distances along $z$ are indicated in Å. The rumpling $r$ is expressed in % of the in-plane lattice constant $a$.

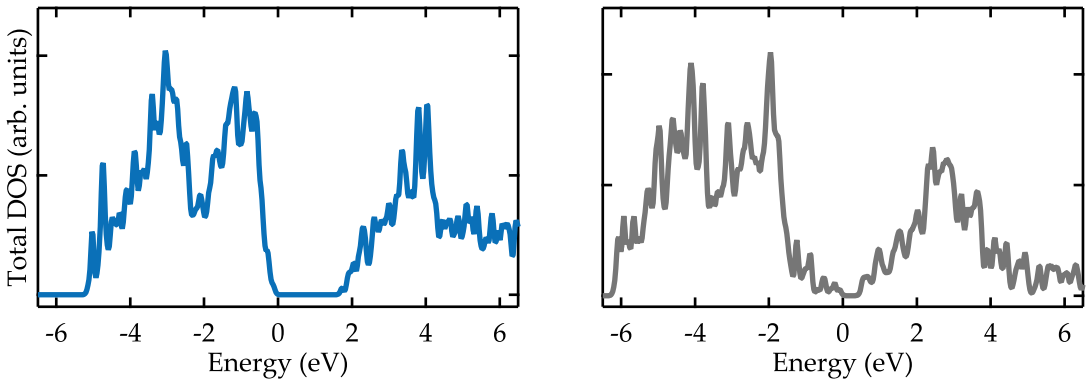


**(a)** BaO termination **(b)** $TiO_2$ termination

**Figure 3.3.:** Total electronic density of states of the $p$ phase for the (a) BaO and (b) $TiO_2$ termination, for $a = 3.800$ Å, $L = 11$ atomic layers. The Fermi energy $E_F$ is at 0 eV. The DOS shows no qualitative difference with varying $a$ and $L$.

Figure 2.8 on page 45). For the $TiO_2$ termination, however, the Kohn-Sham band gap is $\sim 0.5$ eV, therefore very much reduced with respect to the bulk. We will discuss this band gap reduction in terms of surface states when comparing the electronic density of states calculated for the ferroelectric *aa* (see section 2.5 on page 59) and *c* phases (see section 3.7.1 on page 82).

# 2. In-plane polarized *aa* phase

## 2.1. Configuration and parameters

We now focus on the case of in-plane polarized $BaTiO_3$(001) surfaces, with polarization along [110]. The modeled system is schematized in Figure 3.4 as a projection on the $(y, z)$ plane. With the applied periodic boundary conditions, the supercell is made of $1 \times 1$ unit cells stacked up along the vertical $z$ direction. Both BaO and $TiO_2$ surface terminations with $L = 9$ atomic layers (i.e. $\sim 16$ Å) are studied with a vacuum thickness of $\sim 14$ Å (supercell size $\sim 30$ Å along $z$).

The BaO-terminated slabs (Fig. 3.4a) contain 5 BaO and 4 $TiO_2$ atomic planes (= 22 atoms). The $TiO_2$-terminated slabs (Fig. 3.4b) contain 5 $TiO_2$ and 4 BaO atomic planes (= 23 atoms).
In both cases, there are 4 full unit cells along $z$. The medial atomic layer is a mirror plane such that only half of the atomic layer and unit cells are necessary to fully characterize the results obtained for supercells in the *aa* phase.

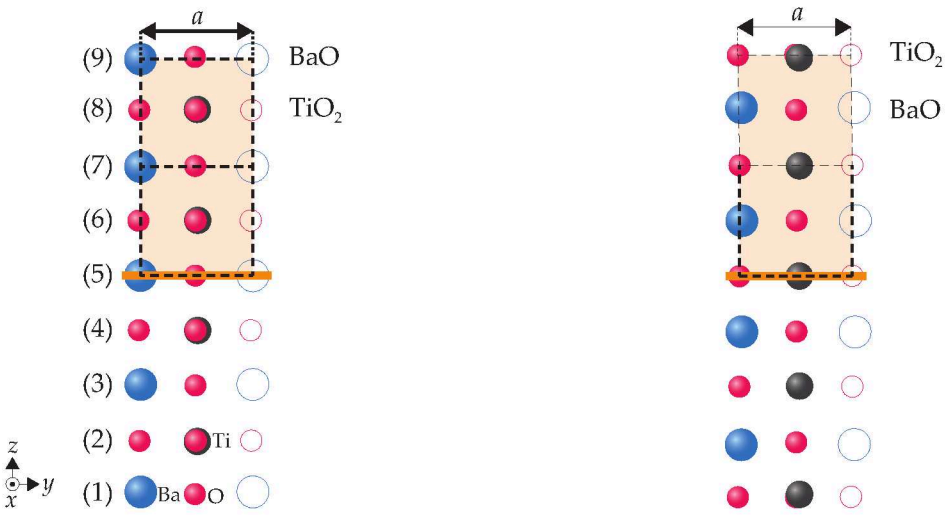


**(a)** BaO termination, *aa* phase **(b)** $TiO_2$ termination, *aa* phase

**Figure 3.4.:** (a) BaO and (b) $TiO_2$-terminated slabs in the *aa* phase projected on the $(y, z)$ plane. There are $L = 9$ atomic layers, resulting in 4 unit cells. The atomic layers are labeled from 1 to 9. The surface and first subsurface unit cells are colored and delimited by the dashed lines. The orange thick line in the fifth atomic layer indicates a mirror plane. Atoms from the supercell and their periodic images are drawn as full and empty circles, respectively.

The *aa* phase is obtained by imposing an initial displacement of the titanium ions along [110], the orthorhombic polar axis.
The in-plane strain is simulated by varying the in-plane lattice constant $a$ in both $x$ and $y$ directions from 3.850 to 4.000 Å (in steps of 0.025 Å). Therefore the *aa* phase is studied for strain ranging from $-2.5$ to $+1.3$ %.

We present the results on the stability, polarization, atomic displacements and density of states as a function of in-plane strain, for both BaO and $TiO_2$ terminations.

## 2.2. Stability of the *aa* phase

For both surface terminations the total energy difference between the slabs in the ferroelectric in-plane polarized *aa* phase and in the paraelectric $p$ phase ($\Delta E(aa) = (E_{\text{tot}}(aa) - E_{\text{tot}}(p))/\frac{L}{2}$) is plotted in Figure 3.5.

The energy difference between the ferroelectric and paraelectric configurations increases with increasing tensile strain. However, this stabilization is much more pronounced in the case of the $TiO_2$ termination, where the relative total energy at $+1.3$ % strain is approximately five times that of the BaO termination at the same strain. This result follows previous observations of a particularly strong enhancement of the

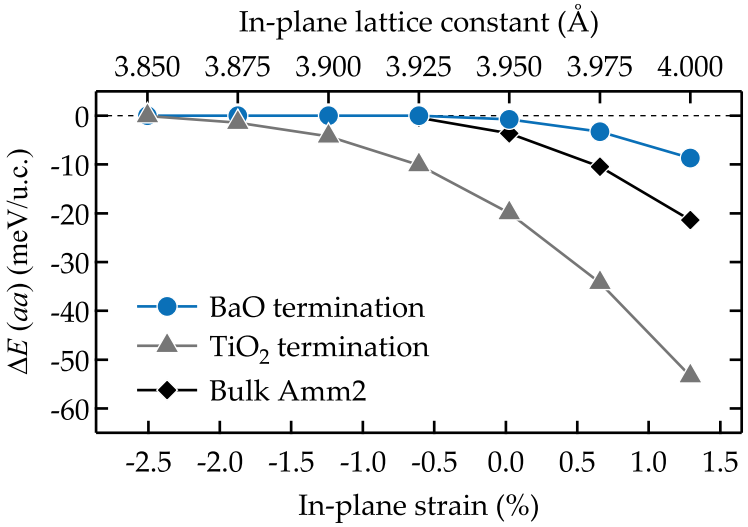


**Figure 3.5.:** Energy (meV/u.c.) of the in-plane polarized *aa* phase (polarization along [110]) relative to the paraelectric *p* phase (zero polarization), as a function of in-plane strain, for both BaO (blue circles) and $TiO_2$ (gray triangles) terminations. The energy of the bulk $Amm2$ phase relative to the bulk $P4/mmm$ phase (black diamond) shown in Fig. 3.1 is displayed for comparison.

stability of ferroelectric $TiO_2$ surfaces [26, 39, 127] polarized in-plane under tensile strain.

## 2.3. Polarization

Using the expression II.34, the polarization per unit cell is calculated for both BaO and $TiO_2$ terminations. As shown in Figure 3.4, the middle atomic layer is a mirror plane, allowing us to restrict to the surface and first subsurface unit cells for a complete description of the slabs.

The magnitude of the local polarization lying along [110] in the surface and subsurface unit cells is presented in Table 3.2.

For both surface terminations, the magnitude of the local polarization vector pointing along [110] increases with in-plane strain as for the bulk $Amm2$ structure.

In the case of the BaO termination, the surface local polarization is almost zero at $-0.6\,\%$ in-plane strain ($a = 3.925$ Å) and peaks at $26.6\,\mu C\,cm^{-2}$ at the highest studied in-plane tensile strain of $1.3\,\%$ ($a = 4.000$ Å). It ranges from 1.6 to $34.5\,\mu C\,cm^{-2}$ in the subsurface unit cell. The magnitude of the in-plane polarization is notably larger in the subsurface unit cell than in the surface unit cell. Therefore, at the vicinity of the BaO termination layer, the in-plane polarization is reduced.

| | $a$ (Å) | 3.925 | 3.950 | 3.975 | 4.000 |
|---|---|---|---|---|---|
| | $\eta$ (%) | −0.6 | 0.0 | 0.7 | 1.3 |
| BaO | surface u.c. | 0.3 | 4.0 | 12.8 | 26.6 |
| | subsurface u.c. | 1.6 | 17.9 | 27.0 | 34.5 |
| $TiO_2$ | surface u.c. | 42.8 | 51.8 | 59.9 | 67.3 |
| | subsurface u.c. | 19.4 | 27.1 | 33.7 | 39.8 |
| bulk *Amm*2 | | 10.4 | 19.7 | 26.6 | 32.5 |

**Table 3.2.:** Magnitude of the polarization ($\mu C\,cm^{-2}$) in the surface and first subsurface unit cells of the BaO and $TiO_2$-terminated slabs in in-plane polarized *aa* phase, as shown in Fig. 3.4.

For the $TiO_2$ termination, by contrast, the magnitude of the polarization is much larger than in the case of the BaO termination. Moreover, it is larger in the surface unit cell than in the first subsurface unit cell, which is the opposite as in the case of the BaO termination. In the surface unit cell, $|\vec{P}|$ ranges from 42.8 to 67.3 $\mu C\,cm^{-2}$ over the strain range −0.6 to 1.3 %. In the first subsurface unit cell, the magnitude of the polarization reaches 19.4 $\mu C\,cm^{-2}$ to 39.8 $\mu C\,cm^{-2}$ which corresponds to 45 % to 59 % that of the surface unit cell, over the considered strain range. Therefore, in the vicinity of the $TiO_2$ surface, the in-plane polarization is enhanced.

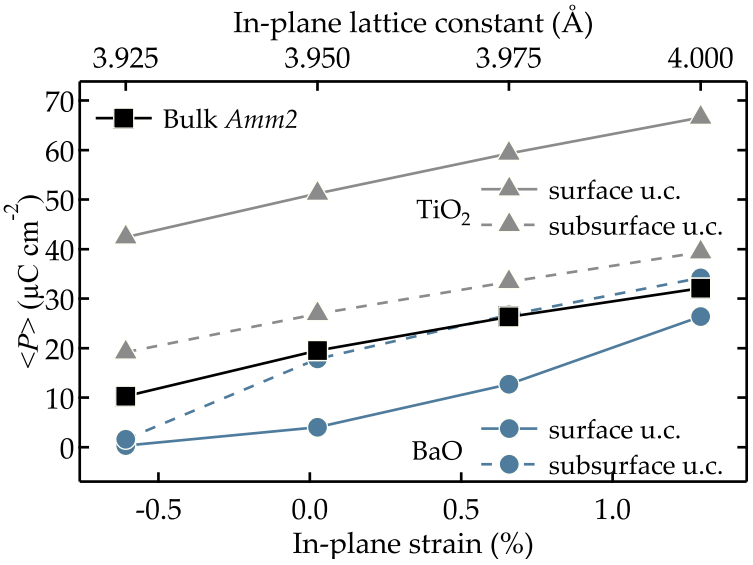


**Figure 3.6.:** Local polarization magnitude in surface and subsurface unit cells of the $L = 9$ atomic layers thick slab in *aa* phase in tensile strain regime, for both surface terminations. Bulk *Amm*2 polarization is also given.

In Figure 3.6, we compare the polarization amplitude in the surface (solid lines) and first subsurface (dashed lines) unit cell for the BaO (blue circles) and $TiO_2$ (gray triangles) terminated slabs with that of the bulk (black squares) over the considered

strain range. In the case of the $TiO_2$ termination, the polarization magnitude is always larger than in the bulk, especially in the surface unit cell, in the vicinity of the surface layer. In contrast, for increasing tensile strain the polarization magnitude in the surface unit cell of the BaO-terminated slab is always lower than in the bulk, whereas it tends to that of the bulk in the first subsurface unit cell. Therefore, the $TiO_2$ termination greatly enhances in-plane polarization with in-plane strain.

However, the surface effect on in-plane tensile strain is much more pronounced in the case of the BaO termination than for the $TiO_2$ termination. As shown in Figure 3.6, within $-0.6$ to 1.3 % in-plane strain, on average between the surface and subsurface unit cells, $|\vec{P}|$ is multiplied by a factor 31 for the former, and by 1.7 for the latter. As shown in the energy diagram in Figure 3.5, the $TiO_2$ termination stabilizes better the in-plane polarization compared to both BaO-terminated slabs in the *aa* phase and the bulk in-plane polarized *Amm*2 counterpart. This appears correlated to the strong polarization magnitude enhancement observed in the case of the $TiO_2$ termination compared to BaO termination, as well as the bulk in-plane polarization.

## 2.4. Surface atomic displacements and rumpling

Figure 3.7 shows the slab in the *aa* phase for the BaO and $TiO_2$ terminations, at $a = 4.000$ Å, along with the associated rumpling values (Fig. 3.7a, Tab. 3.7b and Fig. 3.7c, Tab. 3.7d, respectively), similarly to Figure 3.2 for the *p* phase.

**BaO termination:**

First, the surface rumpling is always negative, which corresponds to oxygen atoms moving outwards with respect to cations. This trend is common to most oxide surfaces, in particular perovskite surfaces [18,28,29]. For increasing in-plane strain, the rumpling in BaO and $TiO_2$ plane shows opposite behavior. In the surface BaO layer (9), the rumpling is enhanced as *a* is increased. This is more pronounced in the paraelectric *p* phase, with an increase of 0.70 % compared to 0.54 % in the *aa* phase, between $a = 3.925$ and 4.000 Å. This result suggests that the ferroelectric in-plane distortion in the *aa* phase decreases the surface rumpling at the BaO termination as observed in the paraelectric *p* phase. In other words, in the case of the BaO termination, the natural outward relative displacement of the topmost oxygen atoms with respect to the cations observed in the paraelectric phase is lowered in the presence of in-plane ferroelectric distortions.
With increasing in-plane strain, the absolute value of *r* increases. Therefore, as *a* increases, the difference $\langle z_{Ti}\rangle - \langle z_O\rangle$ becomes more negative owing to a farther outwards displacement of the oxygen atoms with increasing in-plane strain.

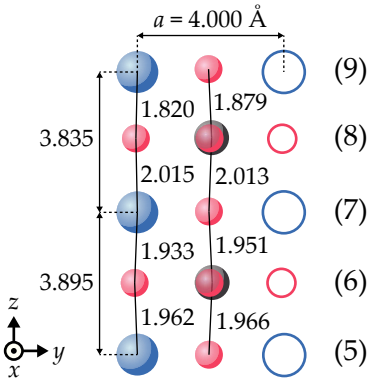


**(a)** Half slab

**BaO termination**

| $a$ (Å) | | 3.925 | 3.950 | 3.975 | 4.000 |
|---|---|---|---|---|---|
| $\eta$ (%) | | −0.6 | 0.0 | 0.7 | 1.3 |
| | (9) | −1.43 | −1.66 | −1.83 | −1.97 |
| | (8) | 0.49 | 0.50 | 0.51 | 0.52 |
| $r$ (%) | (7) | −0.47 | −0.48 | −0.52 | −0.55 |
| | (6) | 0.09 | 0.10 | 0.11 | 0.09 |
| | (5) | 0.00 | 0.00 | 0.00 | 0.00 |

**(b)** Rumpling

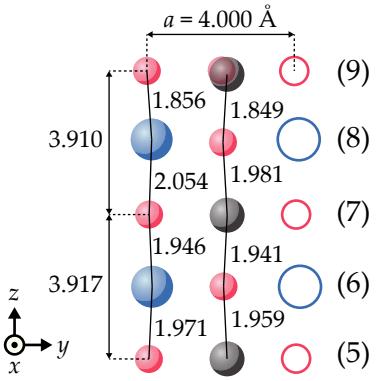


**(c)** Half slab

**$TiO_2$ termination**

| $a$ (Å) | | 3.925 | 3.950 | 3.975 | 4.000 |
|---|---|---|---|---|---|
| $\eta$ (%) | | −0.6 | 0.0 | 0.7 | 1.3 |
| | (9) | −2.62 | −2.52 | −2.43 | −2.39 |
| | (8) | 2.02 | 2.08 | 2.15 | 2.22 |
| $r$ (%) | (7) | −0.38 | −0.39 | −0.40 | −0.41 |
| | (6) | 0.25 | 0.27 | 0.28 | 0.29 |
| | (5) | 0.00 | 0.00 | 0.00 | 0.00 |

**(d)** Rumpling

**Figure 3.7.:** Surface and first subsurface unit cells of the slab in *aa* phase and rumpling values for the BaO (a, b) and $TiO_2$ (c, d) termination ($a = 4.000$ Å). Full and empty circles depict supercell atoms and their periodic images. Interatomic distances along $z$ are indicated in Å. The rumpling $r$ is expressed in % of the in-plane lattice constant $a$.

In the first $TiO_2$ subsurface layer (layer 8), the rumpling is found positive, meaning that the Ti are displaced towards the surface layer, compared to the oxygen atoms. Moreover, $r$ increases with $a$. Again, the relative change of vertical displacement between cations and oxygen atoms is slightly less pronounced in the *aa* phase than in the *p* phase. Even though the change of $r$ from $a = 3.925$ to 4.000 Å is tiny (of the order of 0.05 %), it is two times larger in the *p* phase (from 0.51 % to 0.57 %) compared to the *aa* phase (from 0.49 % to 0.52 %). The presence of ferroelectric distortions seems to relatively align the cations with the oxygen atoms, i.e. at same $z$ value, in the first subsurface layer.

The same observations and conclusions can be drawn for the remaining BaO and $TiO_2$ atomic layers (layers 7 and 6). The oxygen (layer 6, $r < 0$) and Ti (layer 7, $r > 0$) atoms are displaced towards the surface in the BaO and $TiO_2$ plane, respectively. The magnitude of these displacements is favored in the *p* phase.
In the medial BaO plane (layer 5), the rumpling is zero by symmetry.

Hence for the BaO termination in the *aa* phase, the rumpling follows the same trend as in the *p* phase but is slightly less pronounced (i.e. the cation/oxygen distances along $z$ decreases in each atomic layer) over the considered strain range.

**$TiO_2$ termination:**

First, the surface (layer 9) rumpling is negative as in the case of the BaO termination. However, the absolute value of $r$ decreases with increasing $a$, meaning that the difference $\langle z_{\mathrm{Ti}}\rangle - \langle z_{\mathrm{O}}\rangle$ changes very little with in-plane tensile strain (by less than 0.01 Å). Namely, at $a = 3.925$ Å ($-0.6$ % in-plane strain), the surface rumpling peaks at $-2.62$ %, representing an average vertical distance between O and Ti of $\sim 10.3$ pm. This distance is slightly reduced down to $\sim 9.6$ pm at $a = 4.000$ Å (1.3 % in-plane strain).

The situation is reversed in the first underlayer, matching that of the BaO termination, where the cations are displaced above the plane of oxygen atoms and with an increase of the distance with increasing strain. However, in the case of the $TiO_2$ termination, the rumpling is four times larger. In the first subsurface layer (layer 8), $r$ increases from 2.02 to 2.22 % within the considered in-plane strain range: $\langle z_{\mathrm{Ba}}\rangle - \langle z_{\mathrm{O}}\rangle$ increases from 7.9 to 8.9 pm.

From layer 7 and farther from the surface, the rumpling drops down and reaches zero (i.e. the bulk value for the $Amm2$ structure) in layer 5, by symmetry. For instance at $a = 3.925$ Å, from the surface (9) to the subsurface layer (8), the rumpling is opposite and reduced of about 23 %. From the subsurface layer (8) to layer 7, the rumpling is again opposite but reduced of about 81 %.

The same observations can be formulated in the case of the $TiO_2$-terminated slabs in the paraelectric *p* phase. The relative displacements of the cations with respect to the oxygen atoms along [001] follow the same trend as in the *aa* phase for the surface and subsurface layers. The surface rumpling is slightly more pronounced in the *aa* phase whereas in the first subsurface layer it is larger in the *p* phase. Hence the ferroelectric distortion in the *aa* phase, for the $TiO_2$ termination, opposes the natural rumpling as observed in the paraelectric *p* phase.

The $TiO_2$ termination has a strong influence on the amplitude of the vertical relative displacements of the cations and oxygen atoms in the surface and subsurface plane. Depending on $a$, this amplitude may be two to four times larger than in the case of the BaO termination. Moreover, a specificity is observed for the $TiO_2$ surface. With increasing tensile strain, negative rumpling is reduced in the surface layer of the $TiO_2$-terminated slab. Conversely, in the other atomic layers, positive or negative rumpling always increases with increasing tensile strain. This can be compared to the case of the

BaO-terminated slab, where the negative rumpling at the surface layer is increasing with tensile strain, as for the other atomic layers where positive or negative rumpling increases with increases strain.

The larger amplitude of the rumpling in the surface and subsurface atomic layers in the $TiO_2$ termination compared to the BaO termination is correlated with the larger amplitude of the local polarization in the surface and subsurface unit cells (Tab. 3.2). The $TiO_2$ termination has a stronger influence on the rumpling, polarization, as well as stability of the ferroelectric phase with polarization along [110].

## 2.5. Density of states

The total electronic density of states (DOS) of the BaO and $TiO_2$ terminated slabs are presented in Figure 3.8. The energy of the highest occupied state, the Fermi energy $E_F$, is used as the reference.

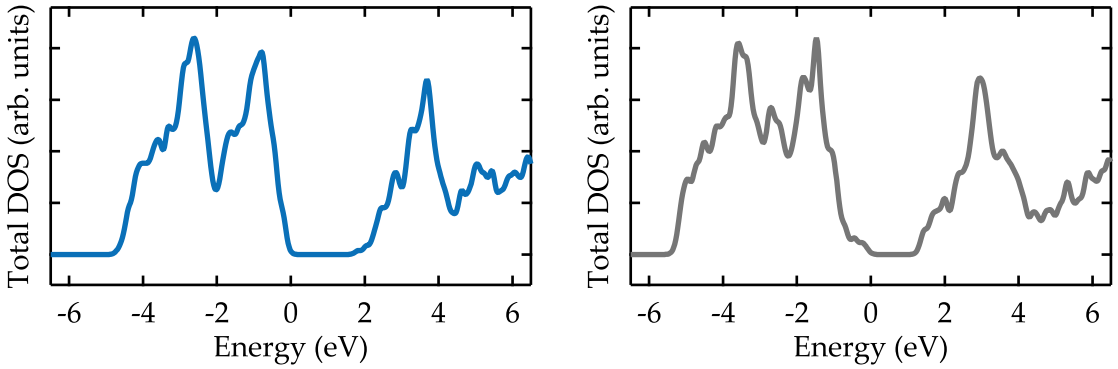


**(a)** BaO termination **(b)** $TiO_2$ termination

**Figure 3.8.:** Total electronic density of states of the *aa* phase for (a) BaO and (b) $TiO_2$ surface termination. The Fermi energy $E_F$ is at 0 eV. The lateral lattice constant corresponds to the highest tensile strain studied $a = 4.000$ Å ($\sim 1.3$ % strain).

For both terminations, the DOS exhibits a gap between valence and conduction bands. The Kohn-Sham band gap in the case of the BaO termination is $\sim$ 1.8 eV (Fig. 3.8a). It is reduced to $\sim$ 1.4 eV in the case of the $TiO_2$ termination (Fig. 3.8b). Therefore, both surface terminations in the *aa* phase show an insulating character. The main difference between the two terminations is the presence of surface states extending by $\sim$ 0.5 eV in the gap from the top of the (bulk) valence band, in the case of the $TiO_2$ termination. These states are responsible for the decrease of the Kohn-Sham band gap between the two terminations. Further investigations of these surface states are presented in the following, for the *c* phase. The in-plane strain has no notable influence on the Kohn-Sham band gap for the two terminations.

# 3. Out-of-plane polarized *c* phase

Under compressive in-plane strain, $BaTiO_3$(001) surfaces favor out-of-plane polarization, along [001]. We simulated the out-of-plane polarization within a large range of compressive strain (with varying fixed in-plane lattice constant $a$), for slabs of various thickness (expressed in number of atomic layers $L$, ranging from 3 to 13). The out-of-plane configuration of polarization is based on the use of alternating domains, as described in section 5.3 of chapter II (the depolarizing field is compensated by the field created by the neighboring domains). The width of the domains can be modulated by varying the slab width. Within the periodic boundary conditions, the domains have infinite length along $x$ and finite width along $y$. Therefore, the width of the domains depend on the size of the slab along $y$ which gives a higher limit for the up/down domain periodicity. The width of the slab is expressed in number of unit cells, labeled $N$, with $N = 2, 4$ or 6. The values of the considered parameters ($a$, $L$ and $N$) have been listed in Table 2.4b on page 35.

First, we present an overview of the stability and polarization amplitude as a function of slab thickness and width in the compressive strain regime $\eta = -2.5$ to $-3.8\,\%$ and a comparison for both BaO and $TiO_2$ terminations.
Then, we focus on the highest compressive strain ($\eta = -3.8\,\%$ for $a = 3.800$ Å), and study the most stable domain width as a function of slab thickness.
Finally, for $L = 9$ atomic layers, the total and atom-projected electronic structure, as a function of surface polarization and surface termination, are studied.

## 3.1. Stability

First we recall that our numerical scheme allows to compare the energies of the different domain configurations with a numerical precision of a few 0.1 meV/u.c.

We compare the stability of the out-of-plane polarized *c* phase with respect to the paraelectric *p* phase, for BaO and $TiO_2$ terminations. The total energy $E_{L,N}(c)$ of fully relaxed *c* phase slabs with different thickness $L$ and width $N$, is compared to that of the corresponding *p* phase, $E_L(p)$. $E_{L,N}(c)$ is normalized by $N$ in order to be comparable to $E_L(p)$, since for the *p* phase, $N = 1$. The energy difference is then normalized by $L/2$ to make comparable the energies computed for different thicknesses $L$, which roughly corresponds to an energy per unit cell.

Figures 3.9 and 3.10 present the energy difference of the *c* phase relative to the *p* phase as a function of in-plane lattice constant $a$, for the BaO and $TiO_2$ termination, respectively.

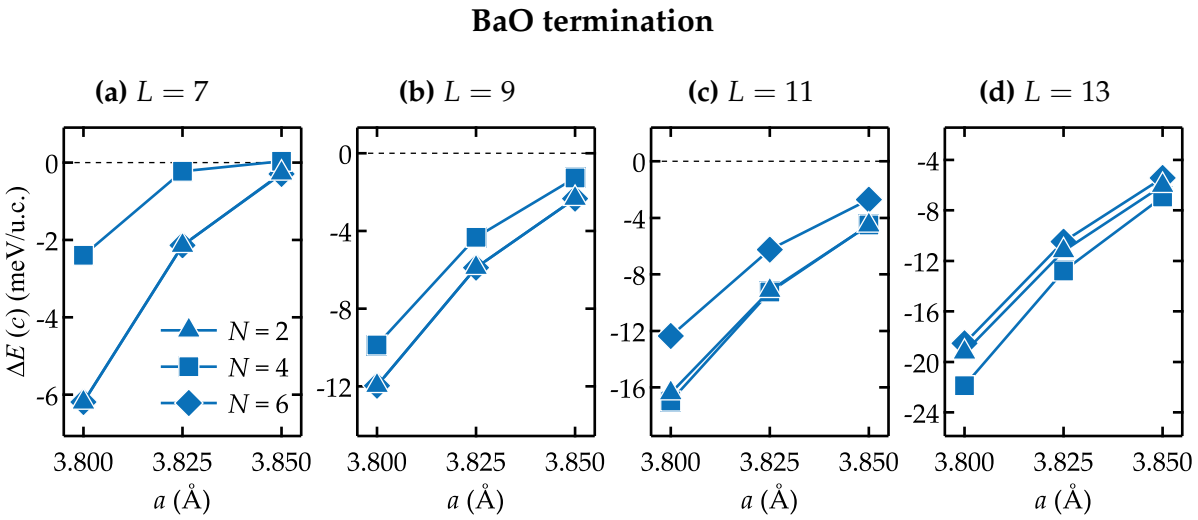


**Figure 3.9.:** Energy of the *c* phase relative to the *p* phase in the case of the BaO termination, calculated for $a = 3.800$, 3.825 and 3.850 Å. The thicknesses $L = 7$ to 13 atomic layers are compared from (a) to (d). For each $L$, the different widths $N = 2$, 4 and 6 unit cells are distinguished. For $L = 7$ and 9, $N = 2$ and 6 are identical because the two systems relax to the same configuration, with 1 unit cell wide domains ($N = 2$).

### 3.1.1. BaO termination

In the case of the BaO termination, at very small thickness $L = 3$ or 5 atomic layers, $\Delta E(c)$ is zero within the numerical precision. Therefore, below $L < 7$ atomic layers (that corresponds to 3 unit cells), we find that ferroelectricity cannot be stabilized perpendicular to the surface. However, for $L = 5$, $N = 2$, 6 and $a = 3.800$ Å (highest compressive strain), polar configurations have been found, with quite small polarization ($\sim 7\,\mu C\,cm^{-1}$). But since these configurations have the same energy as the non polar *p* phase ($-0.06$ eV/u.c.) within our numerical precision, we do not consider them as relevant ferroelectric phases.

For $L \geqslant 7$, ferroelectricity is observed as the *c* phase is found more stable than the *p* phase ($\Delta E < 0$ in the meV/u.c. range). This holds for all domain sizes (slab width $N = 2$, 4 and 6 unit cells). However, for each slab thickness $L$, specific energetic behaviors are revealed as a function of slab width $N$.

For $L = 7$ (Fig. 3.9a), the case $N = 4$ appears less favorable than the cases $N = 2$ and 6, which have the same energy. This is because $N = 6$ relaxes to the same configuration as $N = 2$. In this case, the two configurations are thus identical. Therefore, for $L = 7$, domain periodicity of 2 unit cells (obtained from $N = 2$ and 6) is more favorable than domain periodicity of 4 unit cells (obtained from $N = 4$). This corresponds to one unit cell wide domains.

As the slab thickness increases, the *c* phase becomes more stable. For $L = 9$ (3.9b), the energy difference with the *p* phase is twice as high as for $L = 7$, with $\Delta E(c) \approx -12\,\text{meV/u.c.}$ at the highest compressive strain. Therefore, the addition of only two atomic layers strongly stabilizes the ferroelectric phase. The same behavior as for $L = 7$ is observed as a function of $N$: configurations with $N = 2$ and 6 relax identically, and favor domain periodicity of 2 unit cells (i.e. one unit cell wide domains).

For $L = 11$ and 13 atomic layers (Figs. 3.9c and 3.9d), the energy of the *c* phase is increasingly lowered and the minimum is found for $N = 4$ in both cases. For the 6 unit cells thick $BaTiO_3$(001) slab ($L = 13$), the energy gain of the *c* phase over the *p* phases reaches 22 meV/u.c. at the highest considered compressive strain of $-3.8\,\%$ ($a = 3.80$ Å). Comparatively, at such compressive strain, the relative energy of bulk $P4mm$ (with respect to bulk $P4/mmm$) is $-66.7$ meV/u.c. which shows that even at $L = 13$ atomic layers, the surface influences strongly the relative stability of the system.

### 3.1.2. $TiO_2$ termination

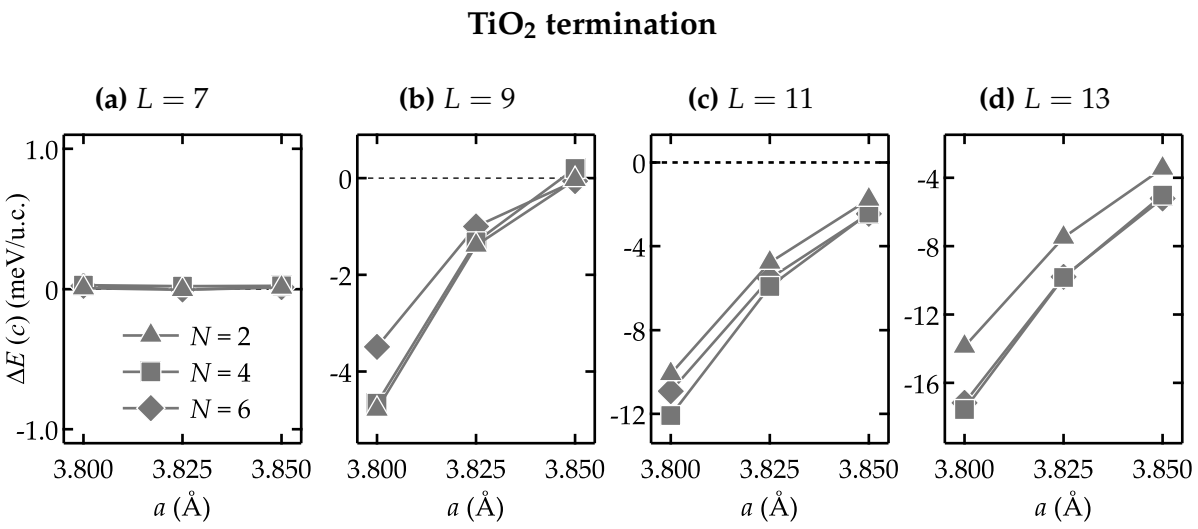


**Figure 3.10.:** Energy of the *c* phase relative to the *p* phase in the case of the $TiO_2$ termination, calculated for $a = 3.800$, 3.825 and 3.850 Å.

In the case of the $TiO_2$ termination, the onset of stable out-of-plane polarized $BaTiO_3$(001) starts with slab thickness of $L = 9$ atomic layers (Fig. 3.10b). For thinner slabs ($L = 7$ as shown in Fig. 3.10a), similar metastable polar configurations, as observed for the BaO termination at $L = 5$, have been found (for $N = 4$ and $a = 3.80$ Å and 3.825 Å) but their energy is equal to that of the *p* phase within the numerical precision. Thus we do not consider them as relevant ferroelectric phases. The onset of the *c* phase stabilization occurs therefore at a larger slab thickness for the $TiO_2$ termination than for the BaO termination. This first observation suggests that the $TiO_2$

surface termination effectively destabilizes the out-of-plane polarization more than the BaO termination does, and thus that screening of the depolarizing field is more difficult in the case of $TiO_2$ terminations.

For $L = 9$ (Fig. 3.10b), the configurations with domain periodicity of 2 unit cells (i.e. $N = 2$) and domain periodicity of 4 unit cells (i.e. $N = 4$) are more stable than those with domain periodicity of 6 unit cells (i.e. $N = 6$). At $-3.8\,\%$ strain and $L = 9$, the two most stable slabs (obtained for $N = 2$ and 4 within the numerical error) have relative energy $-4.5\,\mathrm{meV/u.c.}$, compared to $-3.5\,\mathrm{meV/u.c.}$ for the $N = 6$ case.

As the slab thickness increases, the *c* phase is more and more stabilized. For $L = 11$ (Fig. 3.10c) and $L = 13$ (Fig. 3.10d), the most stable configurations are those with $N = 4$ and $N = 4$ and 6, respectively. The stabilization is not as strong as in the case of the BaO termination, reaching $-15\,\mathrm{meV}$ for $L = 13$ atomic layers and $N = 4$ and 6 maximum domain period, in the most compressive case ($a = 3.80\,\text{Å}$). Therefore the same trend of *c* phase stabilization under compressive strain is observed with increasing slab thickness for the two surface terminations, but it is favored in the case of the BaO termination.

| $L$ | (term.) | 7 | 9 | 11 | 13 |
|---|---|---|---|---|---|
| $\Delta E(c)$ (meV/u.c.) | BaO | $-6$ | $-12$ | $-17$ | $-22$ |
| | $TiO_2$ | $\sim 0$ | $-5$ | $-12$ | $-17$ |
| $N$ | | 2 | 2 | 4 | 4 |

**Table 3.3.:** Energy of the BaO and $TiO_2$-terminated slabs in *c* phase relative to the *p* phase, with increasing thickness $L$, in the highest compressive strain ($-3.8\,\%$ i.e. $a = 3.800\,\text{Å}$). For each $L$, the value of the most stable $N$ is given.

Both BaO and $TiO_2$ surface terminations stabilize the out-of-plane polarized *c* phase with increasing compressive strain. The BaO termination favors more the out-of-plane polarization, since the onset of the *c* phase starts at $L = 7$, compared to 9 atomic layers for the $TiO_2$ termination. Furthermore, the energy is generally lower for the BaO termination, for all $L$ and all $N$. Therefore, in parallel to the strong stabilization of the *aa* phase in the case of the $TiO_2$ termination under tensile strain, the BaO termination stabilizes the out-of-plane polarization along [001] more than the $TiO_2$ termination does under compressive strain. This can be seen in Table 3.3 where the relative energy of the most stable configurations ($a = 3.80\,\text{Å}$, $L = 13$ atomic layers and the proper $N$) in *c* phase with respect to the *p* phase for both BaO and $TiO_2$ terminations is given and can be compared to that of bulk $P4mm$ (polarization along [001]) with respect to bulk $P4/mmm$ which is equal to $-67\,\mathrm{meV/u.c.}$ for $a = 3.800\,\text{Å}$.

## 3.2. Stability comparison between *c*, *aa* and bulk, in the case $L = 9$

In the case of $L = 9$ atomic layers, full relaxation of both *c* and *aa* phases from $a = 3.800$ Å to 4.000 Å with 0.025 Å step has been conducted, for both BaO and $TiO_2$ terminations. Within the corresponding range of compressive to tensile in-plane strain (from $-3.8$ to $+1.3$%), the relative stability of the *c* and *aa* phase can be compared. We chose *N* corresponding to the most stable slabs, as described in the previous section, and plot the energy of the *c* and *aa* phases relative to the *p* phase, for the two surface terminations. Figure 3.11 presents the energy of the *c* and *aa* phases as a function of strain for the BaO (Fig. 3.11a) and $TiO_2$ (Fig. 3.11b) terminations. In both cases, the energy of the ferroelectric bulk *P*4*mm* and *Amm*2 phases relative to that of the paraelectric bulk *P*4/*mmm* phase, presented in Fig. 3.1 (see section 1.1.1 on page 48), is recalled.

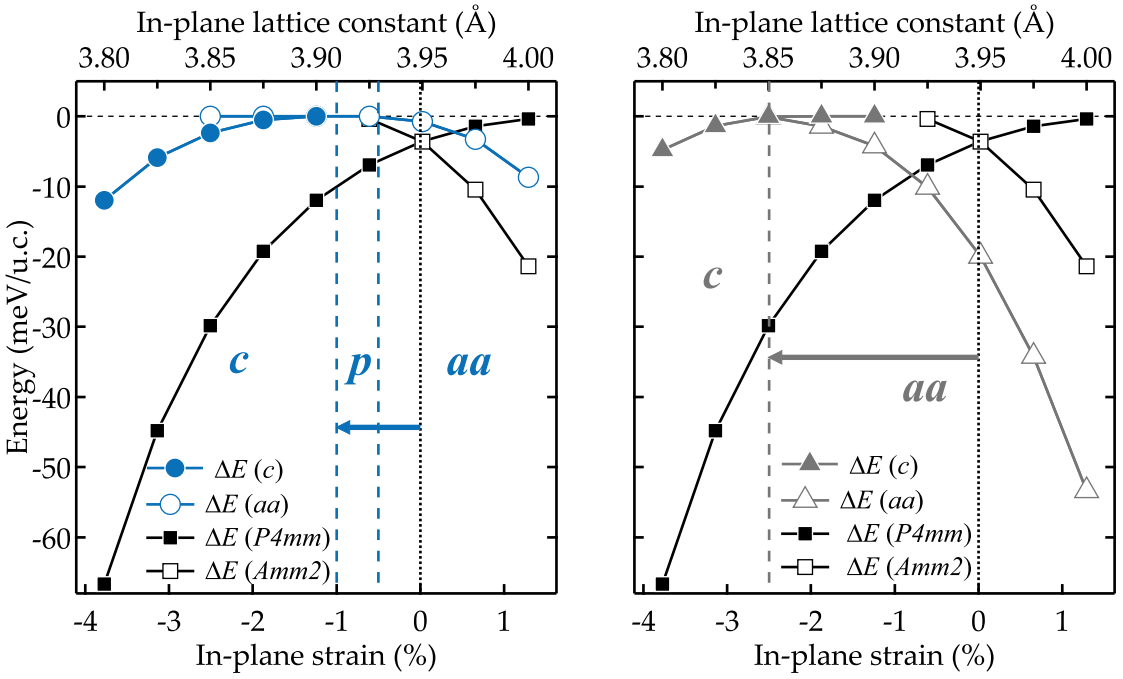


**(a)** BaO termination **(b)** $TiO_2$ termination

**Figure 3.11.:** Energy of the out-of-plane polarized *c* phase relative to the paraelectric *p* phase, as a function of in-plane strain, for (a) BaO and (b) $TiO_2$ terminations. The energy of the bulk *P*4*mm* and *Amm*2 phases (polarization along [001] and [110], respectively) relative to the bulk *P*4/*mmm* phase (zero polarization) shown in Fig. 3.1 are displayed for comparison. The dotted and dashed lines show the bulk and slab phase boundaries. The arrow depicts the shift between bulk and slabs of the transition from polarization along [110] (*Amm*2 and *aa* phase) to polarization along [001] (*P*4*mm* and *c* phase).

We have seen with Fig. 3.1 (in section 1.1.1) that the transition between bulk with polarization along [110] (*Amm*2) and polarization along [001] (*P*4*mm*) occurs

at 0 % strain and that the energy in the largest tensile and compressive strain is −21.4 meV/u.c. for *Amm*2 and −66.7 meV/u.c. for *P*4*mm*.

In the case of the $TiO_2$ termination, we saw in Fig. 3.5 that the *aa* phase is more stable than the bulk *Amm*2 phase, with an energy reaching −53 meV/u.c. at the highest tensile strain. In Fig. 3.11b, compared to the bulk *P*4*mm* phase, we see that the $TiO_2$ termination strongly destabilizes the polarization along [001]. The stability of the *aa* phase and the destabilizing influence of this surface on *c* phase translates into a shift of the transition $aa \rightarrow c$ which occurs at $\sim -2.5$ %, as depicted by the arrow. The stabilization of in-plane polarization at the $TiO_2$ surface with respect to bulk has already been reported by Padilla and Vanderbilt [26].

In the case of the BaO termination, we saw in the previous section that the *c* phase of the BaO appears relatively more stable than that of the $TiO_2$ termination, even though it is strongly destabilized with respect to the bulk *P*4*mm* structure (see Table 3.3 on page 63). Moreover, the *aa* phase is less stable than its bulk *Amm*2 counterpart and much less than in the case of the $TiO_2$ termination (see Fig. 3.1 on p. 48 and Fig. 3.5 on p. 54). Here in Figure 3.11a, the energy of the *c* ($L = 9$ and $N = 2$) and *aa* ($L = 9$) phases are presented. Since both *c* and *aa* ferroelectric phases are destabilized with respect to the bulk, there is no direct crossover from one to another, and the BaO-terminated slabs are no longer ferroelectric over a strain range from $\approx -1$ % to $-0.5$ %, lying in the *p* phase.

Note that the present methodology is not able to reproduce possible monoclinic phases (*r* phases) that are likely to appear as intermediate phases between *c* and *aa*, as it can be seen on the temperature-misfit phase diagrams of $BaTiO_3$ [139].

## 3.3. Domain width minimization of total energy at high compressive strain

The stability of the simulated out-of-plane polarization at the $BaTiO_3$(001) surface is ensured by applying high compressive in-plane strain. In this section, we fix the highest compressive strain and consider all the simulated *c* phase slabs, to investigate the out-of-plane domain pattern as a function of the slab thickness $L$ and width $N$.

At the highest compressive studied strain, for each slab thickness ($L$) corresponds a stable slab width ($N$) which translates into more or less favorable domain width. The corresponding polarization patterns are presented in the next section.

Figure 3.12 shows the relative energy (meV/u.c.) of the BaO-terminated *c* phase slabs at −3.8 % fixed in-plane strain ($a = 3.80$ Å) as a function of the slab width $N$,

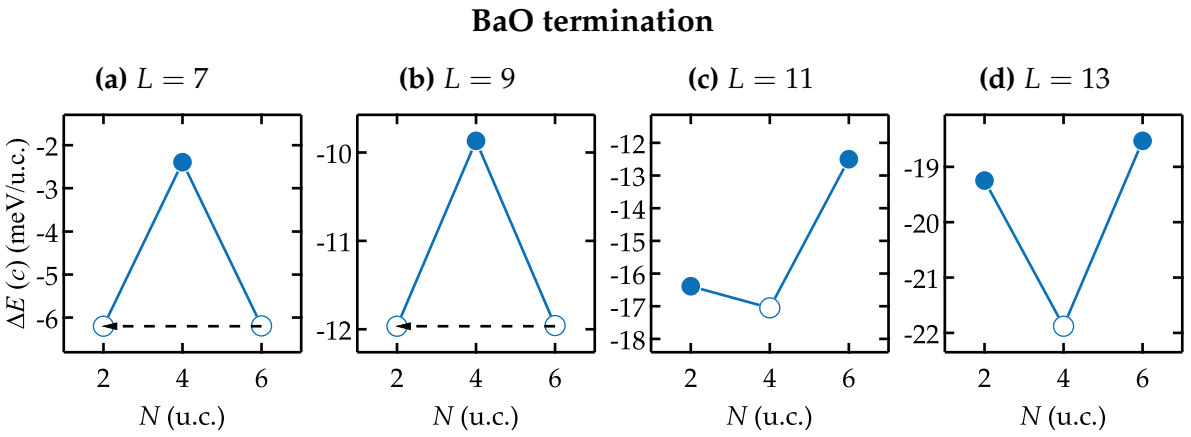


**Figure 3.12.:** Energy of the $c$ phase relative to the $p$ phase in the case of the BaO termination, calculated for $a = 3.800$ Å and $N = 2, 4$ and 6. Empty markers depict the most stable configurations. For $L = 7$ and 9, the black dashed arrow indicates that $N = 6$ relaxes to the same configuration as $N = 2$.

for slab 7 to 13 atomic layers thickness. For each slab thickness, the lowest energy is indicated by an empty circle.

For $L = 7$ and 9 atomic layers (Figs. 3.12a and 3.12b), the most stable BaO-terminated $c$ phase configurations correspond to $N = 2$ unit cells wide slabs. Note that the $N = 6$ u.c. wide slabs converge to the same stable configuration as the $N = 2$ u.c. wide slabs. By contrast, in the case of $N = 4$, the system relaxes towards a configuration with domains that are 2 u.c. wide. This structure corresponds to an local minimum of energy, reached at small thickness ($L < 11$) and corresponds to the absolute minimum of energy at larger thickness ($L \geq 11$).

For $L = 11$ and 13 (Figs. 3.12c and 3.12d), the BaO-terminated slab with $N = 4$ unit cells along [010] is the most stable. Again, the higher $L$, the lower the energy. Alternating out-of-plane domains 2 unit cells wide are the most stable for both slab thicknesses. The domain structure of these two $N = 4$ configurations is detailed in the next section.

The relative energy of $TiO_2$-terminated $c$ phase slabs as a function of slab width $N$ is shown for all slab thickness $L$ and $a = 3.80$ Å in Fig. 3.13.

As seen in Fig. 3.10a, we see in Fig. 3.13a that the 7 atomic layers thick $TiO_2$-terminated slab has the same energy as the corresponding $p$ phase within the numerical precision of $\sim 0.1$ meV/u.c.

At $L = 9$ atomic layers (Fig. 3.13b), the $c$ phase is stabilized for all studied $N$, mostly at $N = 2$, therefore providing a configuration with 1 unit cell wide domains. As $L$ increases, the larger (in $N$) $TiO_2$-terminated slabs are more and more stabilized. At

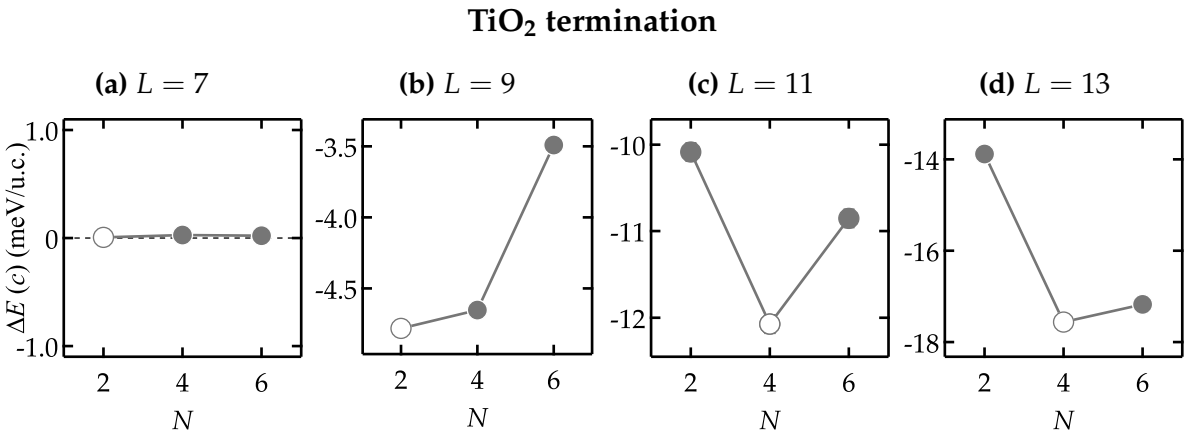


**Figure 3.13.:** Energy of the $c$ phase relative to the $p$ phase in the case of the $TiO_2$ termination, calculated for $a = 3.80$ Å and $N = 2, 4$ and 6. Empty markers depict the most stable configurations.

$L = 11$ and 13 atomic layers (Fig. 3.13c and 3.13d), the case $N = 4$ is the most stable. However, comparing the relative energies, we see that for $L = 11$, the configuration with $N = 4$ is 17 % more stable than the one with $N = 2$, and 10 % more favorable than that with $N = 6$ unit cells wide. This trend is more prominent with the largest studied slab. At $L = 13$, the $N = 4$ case is 39 % more stable than the $N = 2$ case, and solely 3 % more stabilized than the $N = 6$ case. In the next section, we show for $L = 13$, the stabilized domain structure for $N = 4$ consists in alternating 2 unit cells wide domains, while that of the almost as stable $N = 6$ cases presents alternating 3 unit cells wide domains.

Therefore, a clear tendency of enlargement of domain size is observed with increasing slab thickness, for both BaO and $TiO_2$ terminations of out-of-plane polarized strained $BaTiO_3$(001), in qualitative agreement with Kittel's law [101].

## 3.4. Polarization pattern

To illustrate the polarization pattern of the various simulated configurations of out-of-plane polarized $BaTiO_3$(001), we compute the polarization in each unit cell for the highest compressive strain of $-3.8$ %, which corresponds to the in-plane lattice constant $a = 3.800$ Å. For each value of $L$, the $c$ phase configuration corresponding to the most stable width $N$ is presented. The atoms in their fully relaxed position in the $p$ phase are drawn in the $(y, z)$ plane, with their individual displacements in the $c$ phase and the resulting local polarization vectors marked as arrows.

***L* = 7 atomic layers (∼ 1.2 nm):**

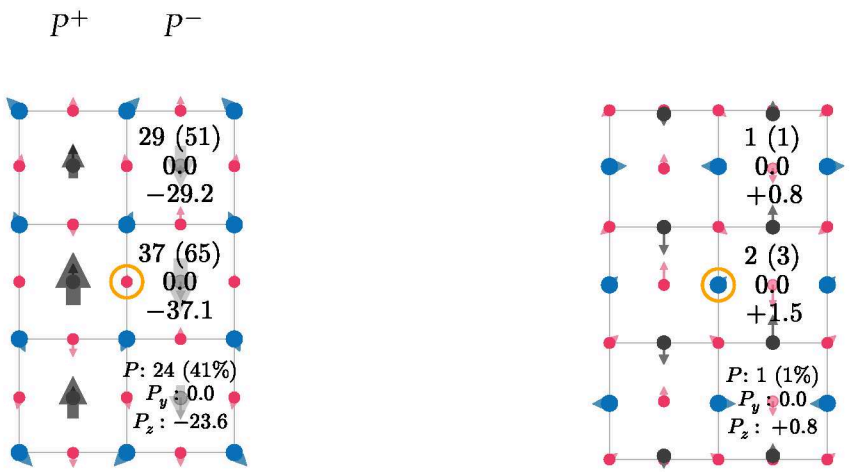


**(a)** BaO termination
$L = 7, N = 2$

**(b)** $TiO_2$ termination
$L = 7, N = 2$

**Figure 3.14.:** Most stable polarization pattern of the (a) BaO and (b) $TiO_2$-terminated slabs in $c$ phase for $L = 7$, $N = 2$ and $\eta = -3.8\,\%$ in-plane strain ($a = 3.80\,\text{Å}$). The atomic positions (colored full circles) are those of the relaxed $p$ phase. The atomic centered colored arrows show the direction and $3\times$ in (a) and $150\times$ in (b) the amplitude of the atomic displacements in the $c$ phase. The cell-centered dark arrows depict the local polarization vectors. The values of $P$ (and its percentage with respect to the bulk), $P_y$ and $P_z$ per unit cell are also reported in $\mu C\,cm^{-2}$. The atom circled in orange at the domain wall center is an inversion center.

Figure 3.14 shows a planar projection of the polarization pattern for the two surface terminations of the $L = 7$ atomic layers thick and $N = 2$ unit cells wide slabs.

At the surface of the BaO-terminated slab shown in Fig. 3.14a, the polarization magnitude is larger in inward polarized surface unit cells, with $P = 29\,\mu C\,cm^{-2}$ (51 % of the bulk $P4mm$ at $-3.8\,\%$ strain). It is larger in the inner unit cell and lower in the upward polarized surface unit cell. The average domain polarization (averaged over the unit cells) is $\langle P \rangle = 30.0\,\mu C\,cm^{-2}$. We recall that surface regions outward and inward polarized are denoted $P^+$ and $P^-$, respectively, the sign being referenced to the positively ascending vertical $z$ axis.

In the $TiO_2$-terminated slab, the atomic displacements between the fully relaxed $p$ and $c$ phases are extremely small ($< 0.01\,\text{pm}$ along $y$ and $< 0.1\,\text{pm}$ along $z$). The amplitude of the displacement vectors (atom centered arrows length) have been multiplied by 150 in this latter case for the actual displacements to be visible on the schematic. The resulting local polarization is $\approx 1\,\mu C\,cm^{-2}$.

Since the polarization is along the out-of-plane [001] direction, the ferroelectric induced atomic displacements are mostly oriented along that polar direction, as shown by the resulting local polarization vector which has vanishing $P_y$ components.

However, nonzero in-plane component of the atomic displacements along the [010] axis can be observed, as shown with the atom-centered arrows, especially in the surface layer and first underlayer, for both terminations. Nonzero $P_y$ components at the surface could result in the formation of *closure domains* due to the rotation of the local polarization towards the domain wall near the surface. This has been observed at the surface of $PbTiO_3$ [107] by Shimada et al., using the same methodology as in the present work, and in $BaTiO_3$ films in short circuit between metallic electrodes [106]. Such rotation of the surface polarization allows for the system to reduce the surface density of charge ($\sigma = \vec{P} \cdot \vec{n}$), by reducing the $P_z$ in favor of the $P_y$ component of the polarization. In the present case, the $N = 2$ unit cells wide slabs can not exhibit nonzero $P_y$, because the corresponding periodicity is equal to the lattice constant (nonzero $y$ contributions vanish in the calculation of the local polarization).

However, for increasing slab width and domain periodicity, clear closure domains configuration of polarization are observed. This will be shown in the following.

The mean polarization, obtained as an average of the local polarization over one domain (from the bottom $P^-$ to the top $P^+$ surface), is $29.9\,\mu C\,cm^{-2}$ for the BaO termination and $1.05\,\mu C\,cm^{-2}$ for the $TiO_2$ termination. This shows that the BaO termination allows ferroelectricity for $L = 7$ whereas the $TiO_2$ termination prevents it at this thickness. This confirms that for $L = 7$, the $TiO_2$-terminated slab in the *c* phase relaxes towards the paraelectric *p* phase as shown in the energy diagram of Fig. 3.13a. The numerical precision on the atomic positions in our structural relaxation calculations is a few $\sim$0.001 Å. For $L = 7$, the relative displacements of the atoms between the relaxed *c* phase and *p* phase used in the calculation of the local polarization are below 0.001 Å, below the numerical precision on the atomic positions. Therefore, the polarization in the $TiO_2$-terminated slab with $L = 7$ can be considered as zero.

**$L = 9$ atomic layers ($\sim 1.6$ nm):**

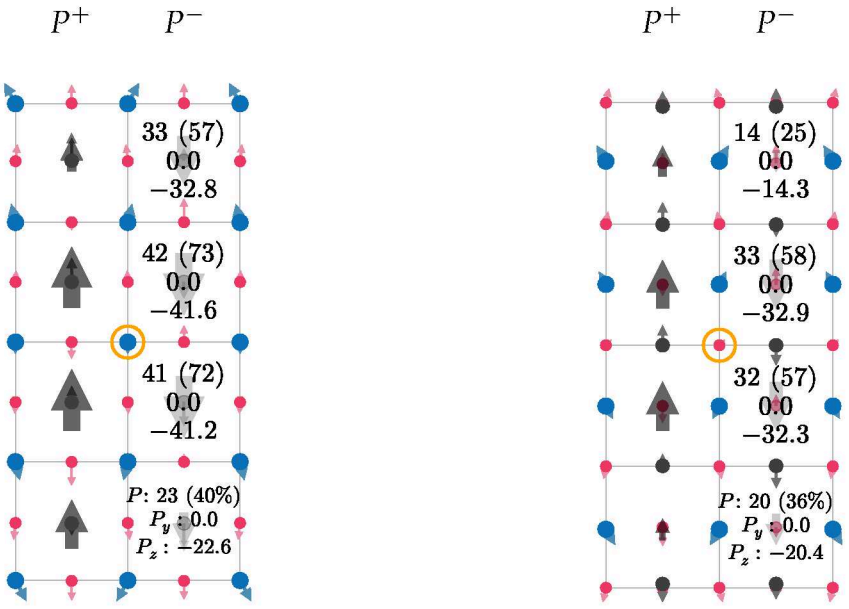


**(a)** BaO termination
$L = 9, N = 2$

**(b)** $TiO_2$ termination
$L = 9, N = 2$

**Figure 3.15.:** Most stable polarization pattern of the (a) BaO and (b) $TiO_2$-terminated slabs in $c$ phase for $L = 9$, $N = 2$ and $\eta = -3.8\,\%$ in-plane strain ($a = 3.800$ Å). The atomic positions (colored full circles) are those of the relaxed $p$ phase. The atomic centered colored arrows show the direction and $3\times$ the amplitude of the atomic displacements in the $c$ phase. The cell-centered dark arrows depict the local polarization vectors. The values of $P$ (and its percentage with respect to the bulk), $P_y$ and $P_z$ per unit cell are also reported. The atom circled in orange at the domain wall center is an inversion center.

In Figure 3.15, the $(y, z)$-projected BaO and $TiO_2$-terminated slabs with $N = 2$ unit cells along $y$ and $\frac{L-1}{2} = 4$ unit cells along $z$ are represented, again in the case of the highest studied compressive strain of $-3.8\,\%$ ($a = 3.80$ Å).

In the case of the BaO termination (Fig. 3.15a), the $N = 2$ configuration corresponds to the most stable configuration at $L = 9$, as shown by the energy diagram of Fig 3.12b[1] in which we see that the $N = 2$ and 6 converge to the same energy, with domains 1 unit cell wide, similarly to the case $L = 7$ and $N = 2$ of Fig. 3.14a. In the surface unit cells, the magnitude of the local polarization depends notably on the polarization direction, whether $\vec{P}$ is pointing outward or inward. Positive surface polarization ($P^+$) gives rise to a magnitude of 22.6 µC cm$^{-2}$. Oppositely, negative surface polarization ($P^-$) has a larger magnitude of 32.8 µC cm$^{-2}$. In the surface and first subsurface unit cells, the $P^+$ outward polarization is stabilized by larger cation displacements outwards the surface compared to the oxygen displacements inwards. Conversely, the $P^-$ polarization is

[1] See section 3.3 on page 66.

stabilized by larger oxygen displacements outwards the surface compared to the cation displacements inwards. In other words, the direction of the out-of-plane polarization at the surface, i.e. the sign of $\vec{P} \cdot \vec{n}$ seems dictated by the sign of the ions which exhibit the largest displacements.

The magnitude of the polarization in the surface unit cell is lower than that in the first subsurface unit cell. It is $\sim 41\,\mu C\,cm^{-2}$ in the subsurface unit cells. Hence this 4 unit cells thick system gives a first insight into the tendency of inner unit cells to behave as bulk unit cells, reaching 73 % of the bulk polarization under the same compressive strain.

In the case of the $TiO_2$ termination, the polarization pattern of Fig. 3.15b is also that of the $N = 2$ configuration, which corresponds to the most stable $TiO_2$-terminated slab at $L = 9$ and $-3.8$ % in-plane strain ($a = 3.80$ Å), as seen on Fig. 3.13b[2]. Compared to the case $L = 7$ where the polarization was zero within the numerical precision, here the local polarization has reached values comparable to those of the BaO-terminated slab. Outward polarized unit cells displays hence a polarization magnitude of $20.4\,\mu C\,cm^{-2}$, similar to the analogous BaO-terminated outward polarized surface unit cells. However, the inward polarized $TiO_2$ terminated unit cells show a drop of polarization magnitude of 56 % compared to their BaO-terminated counterparts, down to $14.3\,\mu C\,cm^{-2}$. Therefore, the BaO surface favors larger magnitude for $P^-$ than for $P^+$. Conversely, the $TiO_2$ surface favors larger magnitude for $P^+$ than for $P^-$.

The polarization magnitude is larger in every unit cells for the BaO termination compared to the $TiO_2$ termination. Furthermore, the average domain polarization is $34.5\,\mu C\,cm^{-2}$ for the BaO termination and $25.0\,\mu C\,cm^{-2}$ for the $TiO_2$ termination. Compared to $L = 7$, the addition of one unit cell along [001] allows ferroelectric polarization in the $TiO_2$-terminated slab to develop even though it is small compared to the bulk polarization at the same compressive strain.

[2]See section 3.3 on page 67.

**$L = 11$ atomic layers ($\sim 2.0$ nm):**

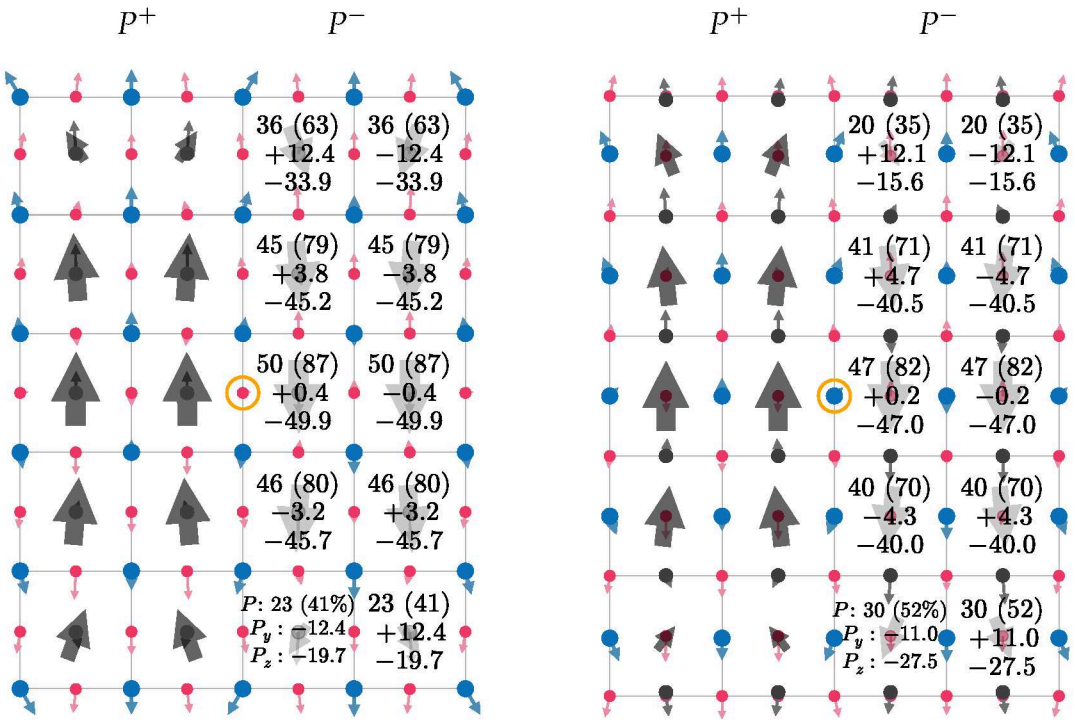


**(a)** BaO termination
$L = 11$, $N = 4$

**(b)** $TiO_2$ termination
$L = 11$, $N = 4$

**Figure 3.16.:** Most stable polarization pattern of the (a) BaO and (b) $TiO_2$-terminated slabs in $c$ phase for $L = 11$, $N = 4$ and $\eta = -3.8\,\%$ in-plane strain ($a = 3.800$ Å). The atomic positions (colored full circles) are those of the relaxed $p$ phase. The atomic centered colored arrows show the direction and $3\times$ the amplitude of the atomic displacements in the $c$ phase. The cell-centered dark arrows depict the local polarization vectors, resulting from the ferroelectric induced atomic displacements. The values of $P$, $P_y$ and $P_z$ per unit cell are also reported. The atom circled in orange at the domain wall center is an inversion center.

The most stable $c$ phase configurations with $L = 11$ atomic layers (i.e. 5 u.c. along $z$) and $a = 3.800$ Å are presented in Figure 3.16. For the two surface terminations, the domains are 2 u.c. wide ($N = 4$) and closure lines near the surface can be observed.

The rotation of the local polarization vector can be measured by the angle of $\vec{P}$ with respect to the surface normal $\vec{n}$, in the $(y, z)$ plane. In the case of the BaO surface, the polarization rotates by 32.2° for $P^+$ and 20.1° for $P^-$. Here, $P_y$ is constant and $P_z$ decreases at the $P^+$ surface. By contrast, in the case of the $TiO_2$ surface, $\vec{P}$ rotates by 21.8° for $P^+$ and 37.6° for $P^-$. Again, the in-plane component varies little at the surface compared to $P_z$.

The magnitude of the polarization is maximum in unit cells located in the middle of the slab, reaching 87 % (BaO termination) and 82 % ($TiO_2$ termination) of the $P4mm$ bulk value, and decreases towards the surface. It is generally larger in the case of the

BaO termination than for the $TiO_2$ termination, with an average domain polarization of 40.1 µC cm$^{-2}$ for the former and 35.5 µC cm$^{-2}$ for the latter.

Similarly to the previous case of $L = 9$ and $N = 2$, in the surface and subsurface unit cells, the magnitude of outward $P^+$ polarization is larger than the inward $P^-$ for the BaO surface while the opposite trend is observed for the $TiO_2$ surface.

**$L = 13$ atomic layers ($\sim 2.4$ nm) and $N = 4$ (most stable):**

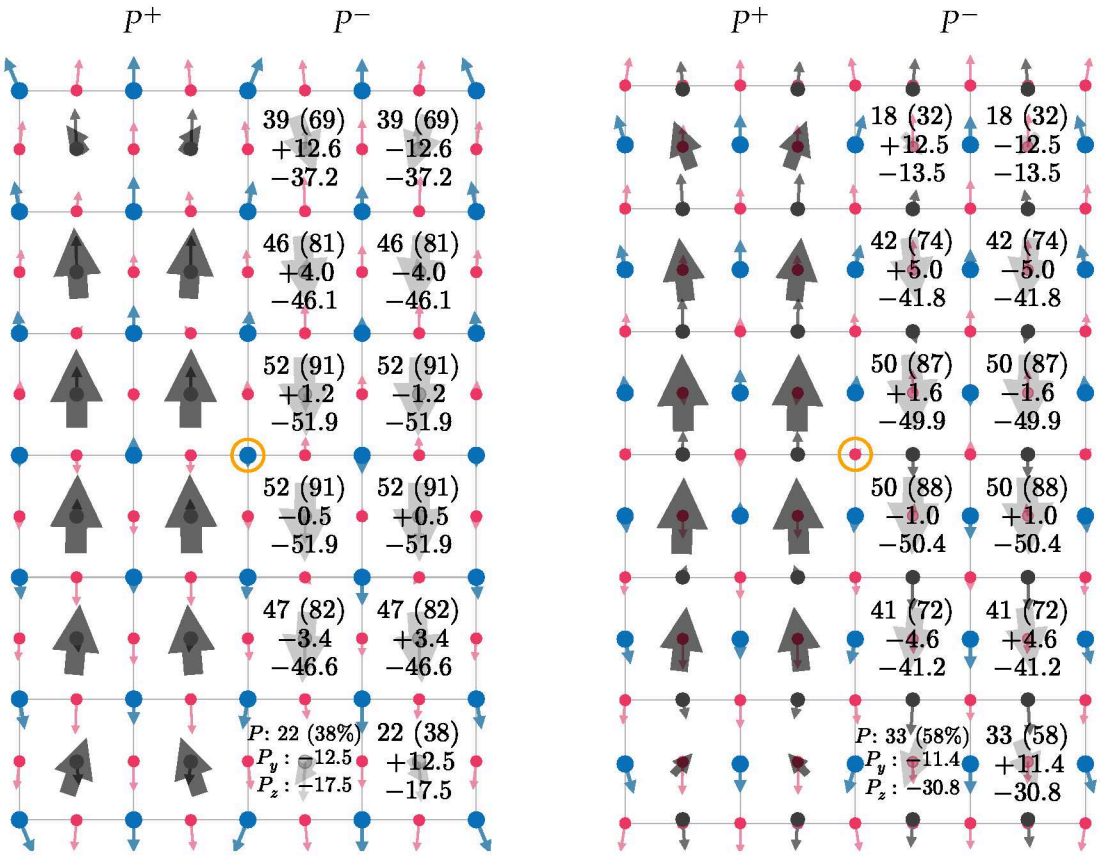


**(a)** BaO termination
$L = 13$, $N = 4$

**(b)** $TiO_2$ termination
$L = 13$, $N = 4$

**Figure 3.17.:** Most stable polarization pattern of the (a) BaO and (b) $TiO_2$-terminated slabs in $c$ phase for $L = 13$, $N = 4$ and $\eta = -3.8\,\%$ in-plane strain ($a = 3.800$ Å). The atomic positions (colored full circles) are those of the relaxed $p$ phase. The atomic centered colored arrows show the direction and $3\times$ the amplitude of the atomic displacements in the $c$ phase. The cell-centered dark arrows depict the local polarization vectors. The values of $P$ (and its percentage with respect to the bulk), $P_y$ and $P_z$ per unit cell are also reported. The atom circled in orange at the domain wall center is an inversion center.

Finally, the largest studied configurations contain $L = 13$ atomic layers, i.e. 6 unit cells along the polar axis [001]. In the energy diagrams of Figs. 3.12d and 3.13d, the $N = 4$ configurations are found the most favorable, with relative energy $\Delta E(c) = -21.9$ and $-17.6$ meV/u.c. for the BaO and $TiO_2$ termination, respectively, and are represented in Fig. 3.17. Similar observations as those for the case $L = 11$ can be made. The average polarization in the inner cells reaches $\sim 90\,\%$ that of the bulk for the two surfaces, illustrating the convergence towards bulk properties as $L$ increases.

As shown in the energy diagrams for the two surfaces, the configurations for $N = 6$ are found almost as stable, with energy very close to that of $N = 4$, respectively 16 %

and 3 % larger in meV/u.c. These configurations are represented in Figure 3.18 and described below.

**$L = 13$ atomic layers ($\sim 2.4$ nm) and $N = 6$:**

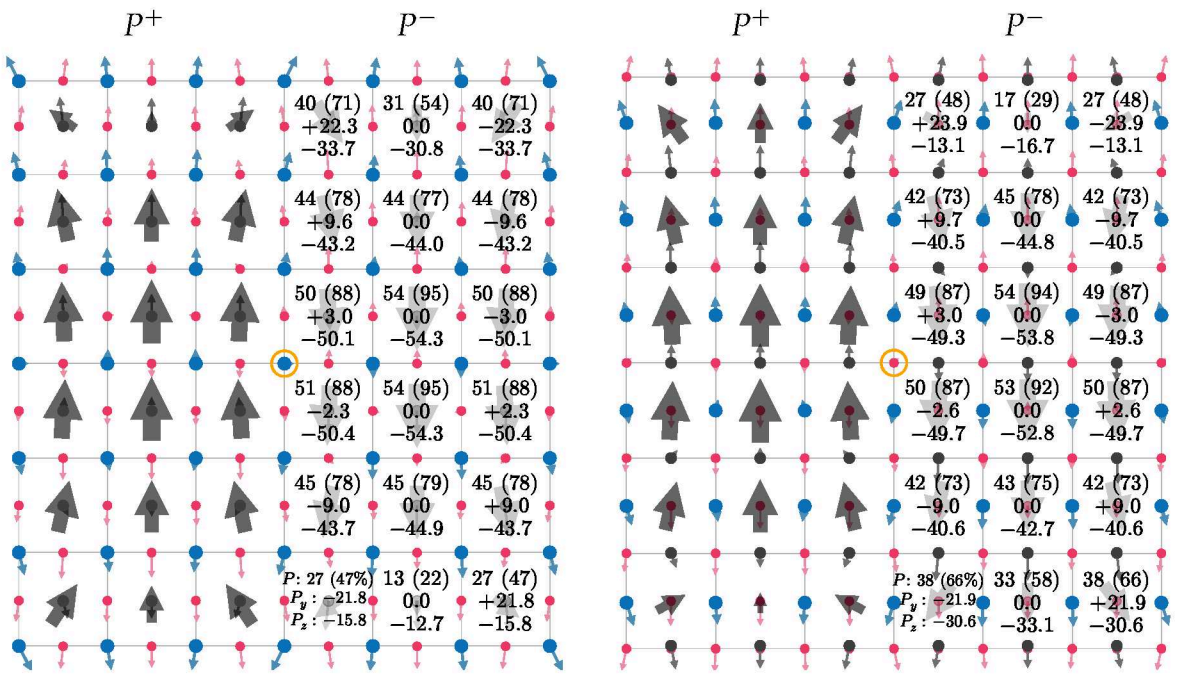


**(a)** BaO termination
$L = 13$, $N = 6$

**(b)** $TiO_2$ termination
$L = 13$, $N = 6$

**Figure 3.18.:** Polarization pattern of the (a) BaO and (b) $TiO_2$-terminated slabs in *c* phase for $L = 13$, $N = 6$ and $\eta = -3.8$ % in-plane strain ($a = 3.800$ Å). The atomic positions (colored full circles) are those of the relaxed *p* phase. The atomic centered colored arrows show the direction and 3× the amplitude of the atomic displacements in the *c* phase. The cell-centered dark arrows depict the local polarization vectors. The values of $P$ (and its percentage with respect to the bulk), $P_y$ and $P_z$ per unit cell are also reported. The atom circled in orange at the domain wall center is an inversion center.

For both terminations, the domains are 3 u.c. wide and clear formation of closure domains can be observed from the surface and subsurface unit cells that are close to the domain wall, with rotation of local polarization vectors and consequently relatively large $P_y$ components, comparable or even larger to the values of $P_z$. Inner slab unit cells close to the domain walls display almost vanishing $P_y$ component yet nonzero, while all unit cells in the middle of the domains have pure out-of-plane polarization.

**In the case of the BaO termination:** the minimum polarization magnitude is observed in outward polarized surface unit cells, reaching 13 to 27 $\mu C\,cm^{-2}$ depending on the distance from the domain walls. At the surface, in the middle of the domain (along $y$), the magnitude of the pure out-of-plane $P^+$ polarization resulting from the slightly larger off-center displacements of cations with respect to the oxygen atoms

(see the atom-centered arrows) corresponds to 22 % of the $P4mm$ bulk value. In the region of $P^+$ closure domains, the polarization amplitude doubles to reach 47 % of the bulk value. However, the major contribution to the polarization magnitude stems from the in-plane $P_y$ component, which is almost 30 % larger than the out-of-plane component $P_z$ near the domain wall, due to the rotation of the polarization by 54.1°. Conversely, in the surface unit cells of the inward polarized $P^-$ region, the polarization rotates by 33.5° with respect to the surface normal. Moreover, the magnitude of the local polarization in the $P^-$ region is larger than that of the $P^+$ region, ranging from 31 µC cm$^{-2}$ to 40 µC cm$^{-2}$ (i.e. 54 % to 71 % of the $P4mm$ bulk value), similarly to the smaller BaO-terminated slabs presented before.

In the middle part of the slab, in the center region of the domain, $\vec{P}$ lies along [001] and its amplitude peaks at 54 µC cm$^{-2}$, almost reaching that of the bulk (95 %). Therefore, bulk-like characteristics are observed in the most central region of the slab, with purely out-of-plane polarization of almost equal magnitude to that of the bulk $P4mm$ phase equally strained.

**In the case of the $TiO_2$ termination:** the surface polarization shows an opposite trend when compared to the BaO termination. Firstly, the polarization amplitude of the $P^+$ region is larger than that of the $P^-$ region, reaching 33.1 to 37.6 µC cm$^{-2}$ (58 to 66 % of bulk values) depending on the distance with respect to the domain wall. The minimum of $P$ is observed in the inward polarized $P^-$ surface unit cell. The closure domains exhibit larger in-plane components of the polarization, with the polarization rotated by 61.2° in the surface unit cells close to the domain walls. The values of $P_y$ and $P_z$ are comparable to that observed in the outward polarized surface $P^+$ region of the BaO-terminated slab. The analogous observations can be made between the $P^+$ $TiO_2$-terminated surface and the $P^-$ BaO-terminated surface. Therefore, in the surface unit cells, the opposite trend is followed by surface polarization magnitude and direction for the BaO and $TiO_2$ terminations.

Nevertheless a similar bulk-like behavior is observed in the middle of the slab, far from the surface. Pure out-of-plane polarization along [001] with magnitude culminating at $\approx$ 54 µC cm$^{-2}$ (94 % of the bulk value) is predicted. On either side of the most central unit cells, close to the domain walls, $P_y$ and $P_z$ are very close to the values observed for the BaO-terminated slab, with almost vanishing in-plane component, confirming the "bulk" character of the central region of the slabs, even close to the domain boundaries.

To sum it up, the domain size and local polarization magnitude of the out-of-plane polarized domains in strongly strained $BaTiO_3$ increase with the slab thickness $L$. Closure domains are formed at the boundary between alternating domains for

domain width 3 unit cells, with the rotation of the polarization vector in the surface and subsurface unit cells. Such relaxation of the polarization in the surface allows the system to reduce its electrostatic energy, by decreasing the discontinuity in $\vec{P}$ at the surface and hence the density of polarization surface charge $\sigma = \vec{P} \cdot \vec{n}$. The magnitude of the polarization in the surface unit cells strongly depends on the direction of $\vec{P}$ with respect to the surface normal $\vec{n}$ between the two terminations. In general, the inward polarized surface unit cells referred to as $P^-$ show larger (smaller) polarization magnitude for the BaO ($TiO_2$) termination than the outward polarized surface unit cells of the $P^+$ region.

## 3.5. Average polarization as a function of strain

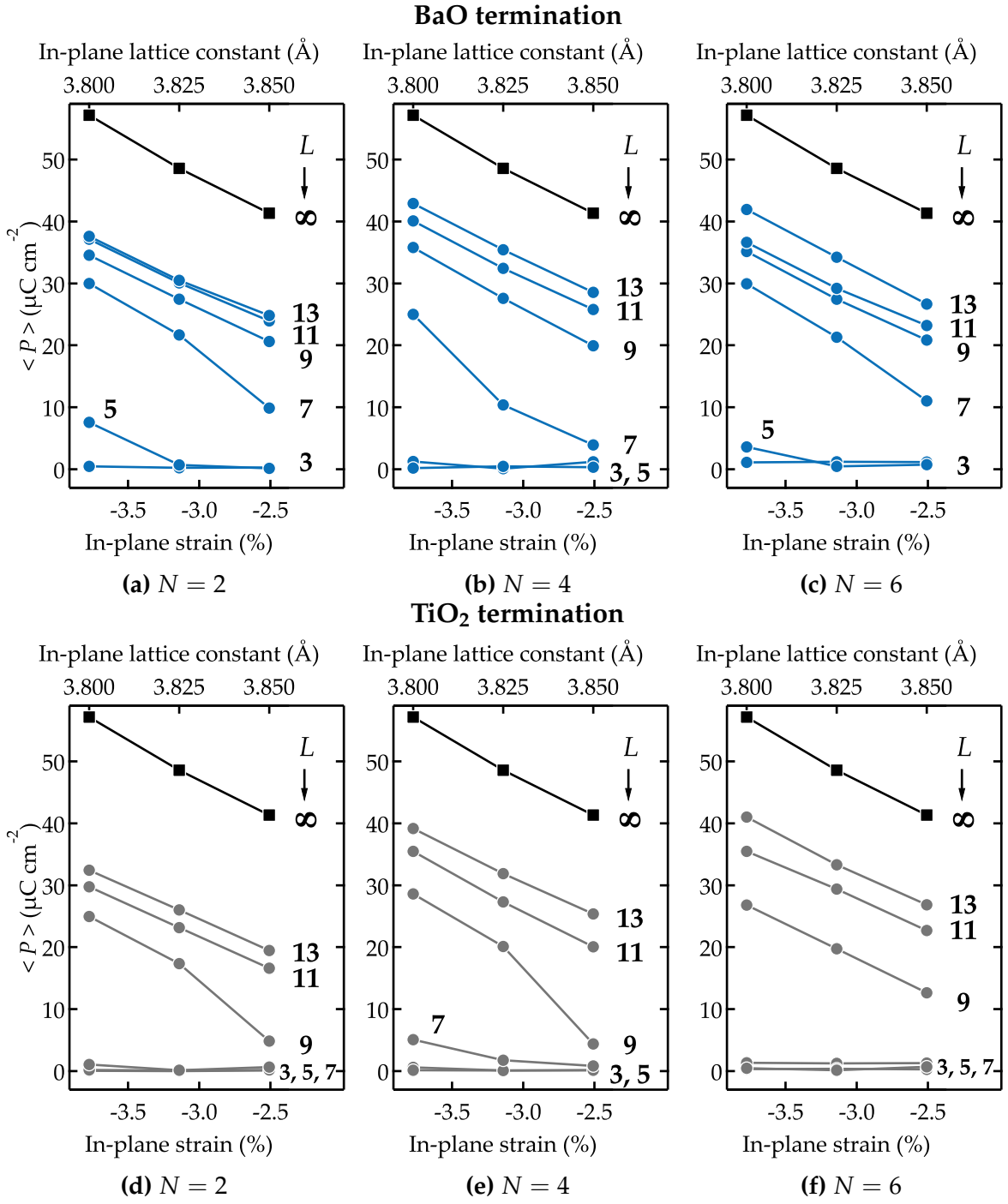


**Figure 3.19.:** Average polarization amplitude of the out-of-plane domains as a function of in-plane strain for the BaO and $TiO_2$-terminated slabs of varying thickness ($L$), for all slab width $N$. The polarization magnitude of the bulk $P4mm$ phase is also shown in each case.

The configurations presented in the previous section are those obtained for the highest compressive studied strain of $-3.8\,\%$ ($a = 3.80$ Å). To investigate the influence of strain on the polarization, we plot in Figure 3.19 the polarization magnitude $\langle P \rangle$

averaged over one whole domain as a function of the in-plane lattice constant $a$ for all slab thickness $L$ and width $N$. The polarization magnitude of the ferroelectric bulk $P4mm$ phase, as detailed in section 1.1.2 on page 49, is also reported in each case.

The present curves can be observed and commented in several ways:

1. at fixed strain, the average polarization tends slowly to its bulk value as $L$ increases. For instance, at $L = 13$ (2.4 nm thick slab), the polarization is only 2/3 (or below) of the corresponding bulk value for both terminations;

2. at fixed thickness $L$, the out-of-plane polarization increases upon compressive strain;

3. the minimum thickness necessary to have a given value of $|\vec{P}|$ decreases with compressive strain. For instance, a polarization of $\sim$30 µC cm$^{-2}$ is reached for $L = 13$ at $a = 3.85$ Å, and for $L = 7$ at $a = 3.800$ Å for the BaO termination (Fig. 3.19c).

4. the BaO termination always favors larger average polarization amplitude than the $TiO_2$ termination. Average polarization amplitudes reached for the BaO termination are reached at comparatively smaller slab thickness for the $TiO_2$ termination. For instance, in 2 u.c. wide domains (see Figs. 3.19b and 3.19e for large $L$), $P \approx 30$ µC cm$^{-2}$ to 35 µC cm$^{-2}$ for $L = 9$ for the BaO termination whereas these values are reached for $L = 11$ for the $TiO_2$ termination.

## 3.6. Surface and subsurface rumpling in *c* phase

The rumpling (see equation III.1 on page 49), is presented in Figure 3.20 for each (001) atomic layer, for both BaO (Fig. 3.20a) and $TiO_2$ (Fig. 3.20b) terminations. The configuration $L = 13$ and $N = 6$ have been chosen. Since these *c* phase configurations present an inversion center at the center of the domain walls, the surface can be described using solely half of the supercell. Therefore, we show the 6 atomic layers from the topmost surface one (layer 13) to the one in the center of the slab (layer 7). Hence, along [001] alternating BaO ($TiO_2$) and $TiO_2$ (BaO) planes are considered for the BaO ($TiO_2$) termination. For each atomic layer, we calculate the rumpling for every oxygen-cation sets which belong to a unit cell along the [010] direction. In other words, since the slab width is $N = 6$ unit cells along [010], six values of $r$ are obtained for each atomic layer.

For the two terminations, the value of the rumpling calculated in the *p* phase is shown, and repeated along $y$, by the small squares. For BaO and $TiO_2$ atomic layers,

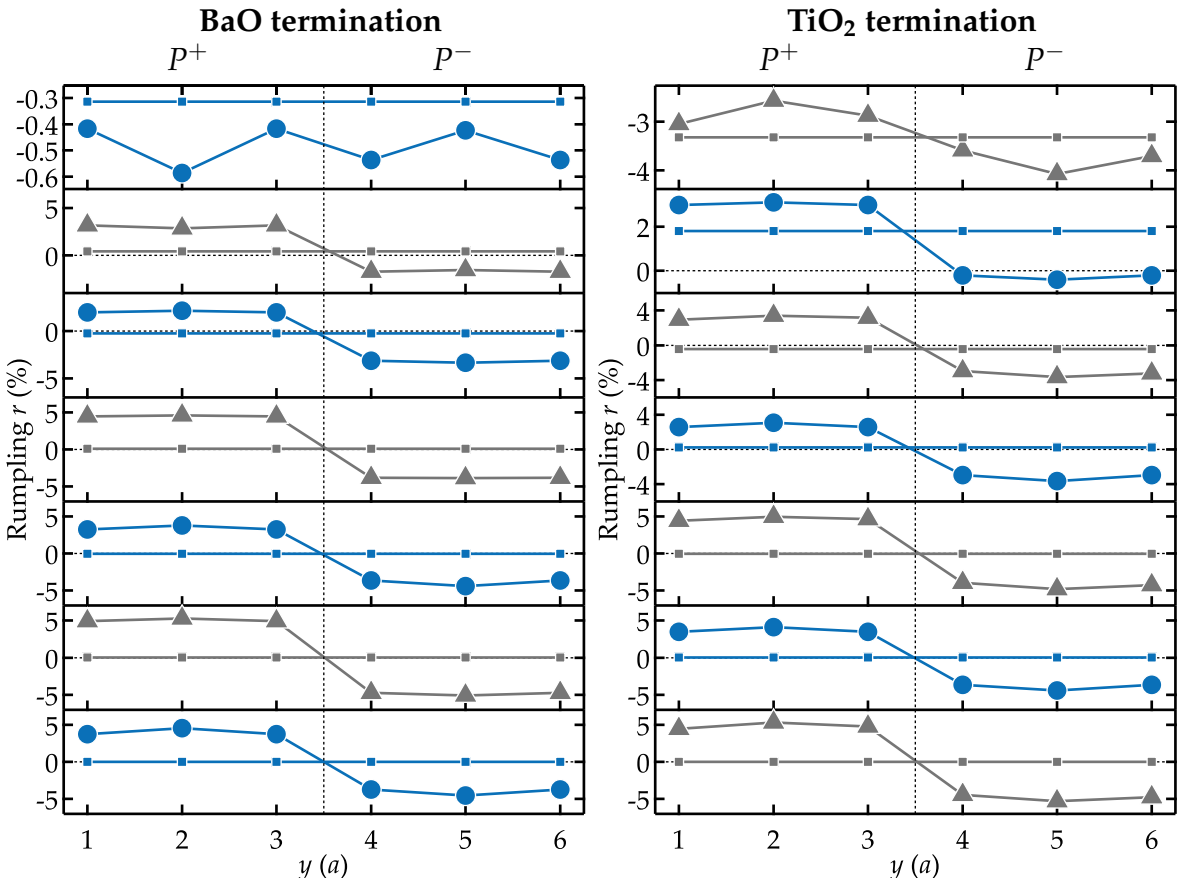


**(a)** $L = 13$, $N = 6$ **(b)** $L = 13$, $N = 6$

**Figure 3.20.:** Layer by layer rumpling of the $c$ and $p$ phase of the (a) BaO and (b) $TiO_2$-terminated slab with $L = 13$ and $N = 6$ shown in Fig. 3.18. From top to bottom, half of the slab, starting from the top surface (layer 13) down to the center (layer 7), is considered owing to the inversion center. Depending on the atomic layer, rumpling values between Ba (Ti) and O are marked with circles (triangles). For each atomic layer, the rumpling values from the $p$ phase are indicated with small squares.

the values of the rumpling along $y$ are shown by the blue circles and gray triangles, respectively.

The rumpling in the $p$ phase is equal to 0 from the center of the slab to the next five atomic layers towards the surface, and underlines the absence of polar distortion along [001] in this phase, as could be expected. However, in the first subsurface atomic layers, for the two terminations, $r$ increases: slightly for the BaO-terminated slab and strongly, up to 2 %, for the $TiO_2$-terminated slab. Finally, at the surface atomic layer, $r$ decreases and becomes negative, again with a larger amplitude in the case of the $TiO_2$ termination ($-0.3$ % for the BaO termination compared to $-3.2$ % for the $TiO_2$ one). Hence, polar distortions along the [001] are measured in the $p$ phase in the first subsurface and surface atomic layers, with a negative rumpling at the surface, for both terminations. This measured polar distortion is due to the presence of the surface, and

results in a configuration where the oxygen atoms are found upwards with respect to the cations, for both terminations.

For both terminations in the *c* phase, from the center of the slab to the first subsurface atomic layer, $r > 0$ for $y \leq 3$ and $r < 0$ for $y > 3$. This highlights the polar distortion induced by the ferroelectric $P^+$ and $P^-$ domain ordering. The amplitude of the rumpling is maximum in the center region of the slab, up to $\pm 5\,\%$ (depending on the polarization direction with respect to $z$) and decreases to $\pm 4\,\%$ in the second subsurface atomic layer.

For the BaO termination (Fig. 3.20a), in the first subsurface atomic layer, the amplitude of the rumpling decreases further, and the sign does not change, following the polar distortions induced by the domains. However, at the surface atomic layer, $r < 0$ for both domains, such that $r$ has changed sign for the $P^+$ domain. In other words, at the surface atomic layer, all O are displaced outwards with respect to Ba, following the surface rumpling observed in the *p* phase. The polar distortions induced by the surface, as observed for the *p* phase and resulting in a negative rumpling, overcome the ferroelectric induced distortions. Furthermore, at the center of $P^+$ and $P^-$ domains, i.e. for $y = 2$ and $y = 5$, the amplitude of $r$ is enhanced and reduced, respectively, which shows that the surface induced polar distortions even oppose the ferroelectric distortions.

For the $TiO_2$ termination (Fig. 3.20b), in the first subsurface atomic layer, $r \approx 3\,\%$ for $P^+$ and $\approx 0\,\%$ for $P^-$. In other words, the rumpling in the *c* phase follows the increase of $r$ observed for the *p* phase (from $0\,\%$ to $2\,\%$), showing the influence of the near surface on the polar distortions. This is confirmed at the surface atomic layer, where $r < 0$ for both domains, with the same amplitude distribution around the value of $r$ measured for the *p* phase. Hence, the same inversion of the relative position of oxygen with respect to the cations is observed for the $TiO_2$ termination, such that the surface rumpling overcomes the ferroelectric polar distortion at the surface atomic layer. However, contrary to the BaO termination, for $P^+$ and $P^-$, the (negative) amplitude of $r$ is reduced and enhanced, respectively, denoting the influence of the ferroelectric polar distortions over the negative rumpling imposed by the surface.

In conclusion, for both terminations in the *c* phase, there is an inversion of the dipole at the surface atomic layers with respect to the polar distortion induced by the ferroelectric ordering. The surface rumpling overcomes the ferroelectric distortions, and is always found negative, such that oxygen atoms are always displaced outwards with respect to the cations.

## 3.7. Electronic structure in *c* phase

In this section, we present the electronic density of states (DOS) calculations of the ferroelectric *c*, for the two surface terminations and the highest compressive strain ($a = 3.800$ Å). The total DOS of the slabs is compared for the different configurations, according to the thickness $L$ and width $N$ in section 3.7.1. Relationship between electronic structure and polarization pattern are investigated in section 3.7.2.

### 3.7.1. Density of states

For increasing domain width obtained by increasing $N$ and for the different slab thicknesses $L$, the total DOS are very similar for a given surface termination.

For the BaO termination, the total DOS obtained for the most favorable $N$ (i.e. $N$=2 for $L$=7,9 and $N$=4 for $L$=11,13, as shown in Fig. 3.12) are shown in Figure 3.21. For all slab thicknesses, the DOS shows a Kohn-Sham band gap slightly below 2 eV. The *c* phase is therefore insulating.

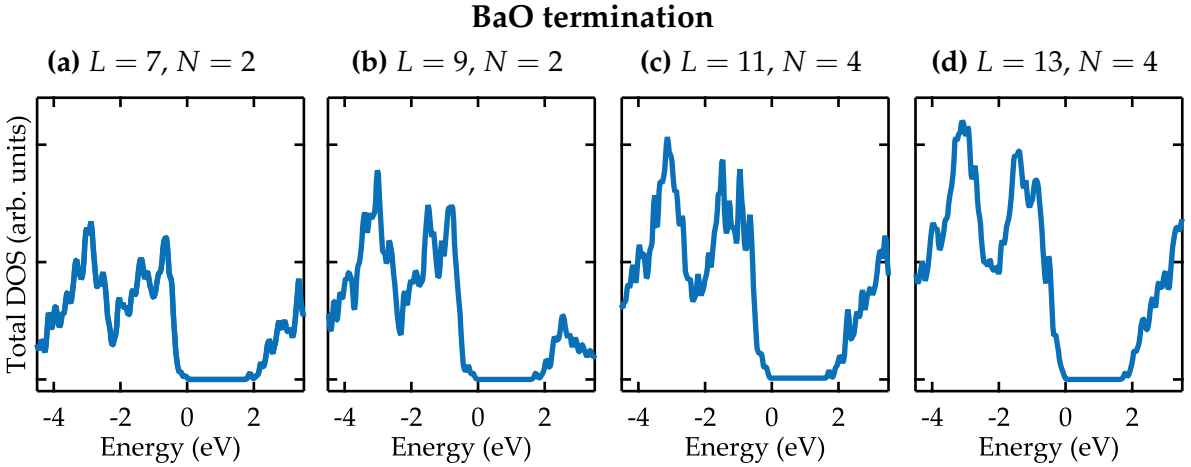


**Figure 3.21.:** Total electronic density of states of the *c* phase for the BaO termination, for $a = 3.80$ Å. The Fermi energy $E_F$ is at 0 eV. The most stable configurations as a function of $N$ (see Fig. 3.12) have been chosen for each $L$.

In Figure 3.22, we plot the total DOS obtained for the most favorable $TiO_2$-terminated slabs in *c* phase ($N$=2 for $L$=7,9 and $N$=4 for $L$=11,13, as shown in Fig. 3.13), for increasing slab thickness $L$. The resulting DOS shows a strong reduction of the Kohn-Sham band gap with respect to that of the BaO termination, dropping to $\approx 0.5$ eV. Nevertheless, even though it is reduced, the band gap is nonzero and the systems are found insulating.

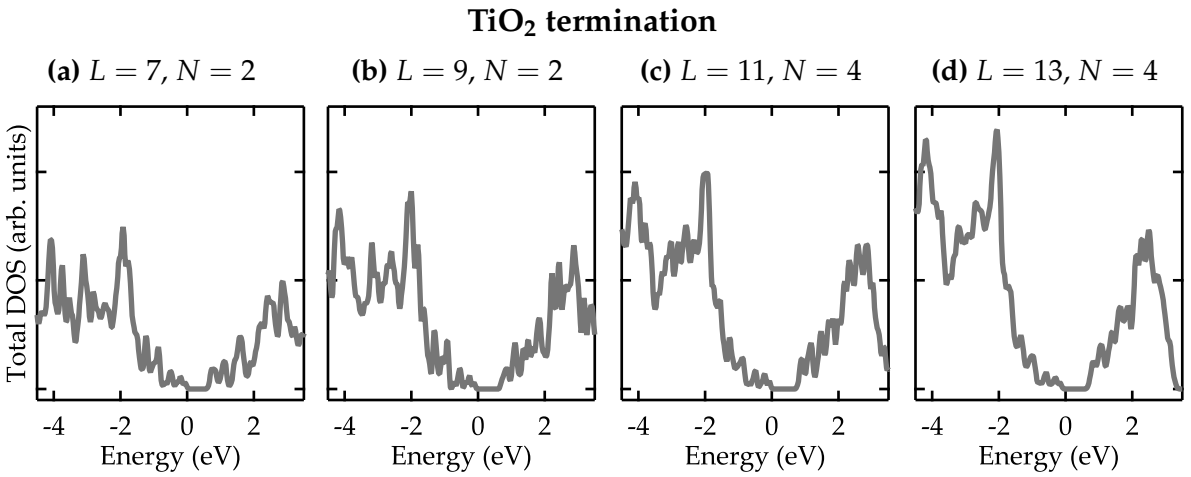


**Figure 3.22.:** Total electronic density of states of the *c* phases for the $TiO_2$ termination, for $a = 3.80$ Å. The Fermi energy $E_F$ is at 0 eV. The most stable configurations as a function of $N$ (see Fig. 3.13) have been chosen for each $L$.

### 3.7.2. Atom-projected Density of states

**Surface and bulk projections:**

In order to understand further the reduction of the band gap observed in the case of the $TiO_2$ termination, we investigate the contributions of specific regions of the slab to the electronic structure, by computing the atomic projection of the density of states. This calculation has been performed in one specific case ($L = 9$, $N = 6$, $a = 3.80$ Å, $TiO_2$ termination) with the SIESTA code (the configuration has been relaxed with this code before projecting the DOS).

In Figure 3.23a, the planar representation of the slab in question is shown. The local polarization vectors for each unit cell are indicated with the cell-centered large arrows. Two domains 3 unit cells wide opposes each other, as already described for instance for Fig. 3.18b on page 75. The topmost surface layer is divided into two highlighted regions, namely (i) $P^+$ (orange rectangle) and (ii) $P^-$ (green rectangle), labeling the outward and inward polarized regions. In the inner part of the slab, atoms corresponding to a (iii) "bulk" region of a domain are highlighted (gray square). Moreover, all the atoms belonging to (iv) a domain wall are also selected (pink rectangle) while atoms located in (v) the inner part of the domain wall are highlighted (blue rectangle). All these regions mark the atoms whose contributions to the DOS are studied.

Figure 3.23b displays the density of states projected onto the whole slab and projected onto the atoms of the above described (i-iii) regions. From top to bottom, the projected DOS for the total slab, $P^+$ surface, $P^-$ surface region and bulk regions are shown. The contributions of each element are distinguished. A distinction is made for

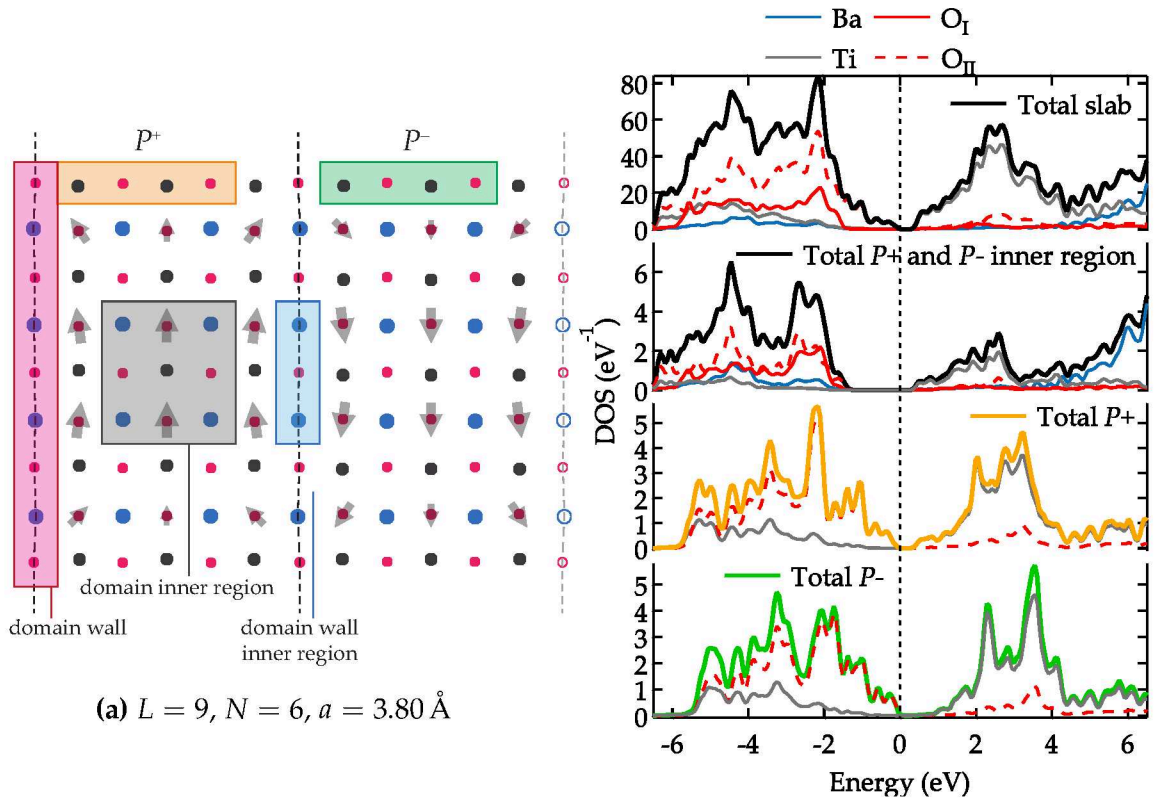


**(a)** $L = 9$, $N = 6$, $a = 3.80$ Å

**(b)** Atom-projected DOS

**Figure 3.23.:** (a) Polarization pattern of the highly strained $TiO_2$-terminated slab in $c$ phase with $N = 6$ and 4 unit cells along $y$ and $z$ directions, respectively. The atomic positions are those of the relaxed $c$ phase. The colored shapes highlight the atoms selected to study the projected density of states. (b) Atom-projected density of states on the total slab presented on the side (top), on the $P^+$ outward polarized surface layer (middle-top), the $P^-$ inward polarized surface layer (middle-bottom) and on a bulk region of the slab (bottom). For each regions, the DOS is projected on all the occupied orbitals of the atoms.

the oxygen atoms. We denote as $O_I$ and $O_{II}$ the oxygen atoms of the BaO and $TiO_2$ atomic planes, respectively.

The total DOS presented on the top part of Fig. 3.23b is similar to that shown in Fig. 3.22b (for which $N = 2$), with the above mentioned narrow Kohn-Sham band gap observed for the $TiO_2$ termination. The atomic contributions of the total DOS reveal that the top of the valence band, and namely the narrowing of the band gap stems mainly from $O_{II}$ atoms (red dashed line). The other major contribution of valence states is due to the oxygen atoms of the BaO planes (red solid line). Barium and titanium atoms contribute very little to the valence states (blue and gray solid lines). The latter, however forms almost the entire set of states in the conduction band above the gap. This is characteristic of a charge-transfer insulator (gap O $2p$ – Ti $3d$ states).

The DOS projected on the atoms of the innermost cells is presented in the second panel of Fig. 3.23b. The sum of the elemental contributions (thick solid line labeled total $P^+$ and $P^-$ inner region) shows a large Kohn-Sham band bap $\approx$ 2 eV wide. Note that the atom-projected DOS in this region is equivalent for both $P^+$ and $P^-$ domains because of the symmetry of the two domains. A strong stabilization of the states originating from $O_{II}$ atoms at the top of the valence band is observed, thus widening the band gap. This observation that the bulk region shows a wide band gap suggests that the narrowing of the band gap observed in the total DOS (the sum of the contributions of all the atoms of the slab) may originate from regions close to the surface. As recalled in the introduction chapter, in charge-transfer insulators, the gap is mainly controlled by the difference of electrostatic (microscopic) potential between anionic and cationic sites. At surfaces, this difference of potential is reduced due to missing neighbors [18]. Some states of the valence band top (mainly O 2*p* states), normally stabilized by the electrostatic potential of cations, are less stabilized and move up in the band gap. This is what we observe here.

This is well confirmed in the two lower panels of Fig. 3.23b. The $P^+$ and $P^-$ surface regions are probed and the resulting Kohn-Sham band gap is strongly reduced to the value observed for the total DOS $\approx$ 0.5 eV. The surface oxygen atoms ($O_{II}$) contribute mostly to the valence states and pushes the valence band maximum towards higher energy, whereas the surface titanium atoms contribute to the conduction states. The $O_{II}$ states are above the valence band maximum of the bulk region (without closing the gap), therefore responsible for the observed reduction of the Kohn-Sham band gap. The densities of state at the top of the valence band are very similar for $P^+$ and $P^-$. However, the $P^+$ and $P^-$ differ by their contribution to the bottom of the conduction band ($P^+$ has states $\sim$ 0.5 eV more stable than $P^-$). Given the nonzero Kohn-Sham band gap, our calculations do not show any evidence of a surface conductivity when the polarization is perpendicular to the surface as in the present case.

The DOS projected on the atoms which are located at the domain walls are shown in Figure 3.24.

We distinguish two DOS projections on the domain wall (regions (iv) and (v) described before). On the top graph, all atoms from the domain wall across the slab thickness are accounted. On the bottom graph, innermost atoms from the domain wall, excluding surface atoms are considered. In the latter case, the Kohn-Sham band gap is $\sim$ 2 eV. Including the surface atoms, the Kohn-Sham band gap reduces to 0.5 eV. This further demonstrates that the Kohn-Sham band gap reduction observed for the $TiO_2$ termination originates from surface states. Moreover, no Kohn-Sham band gap reduction can be observed at the domain wall, sufficiently far from the surface.

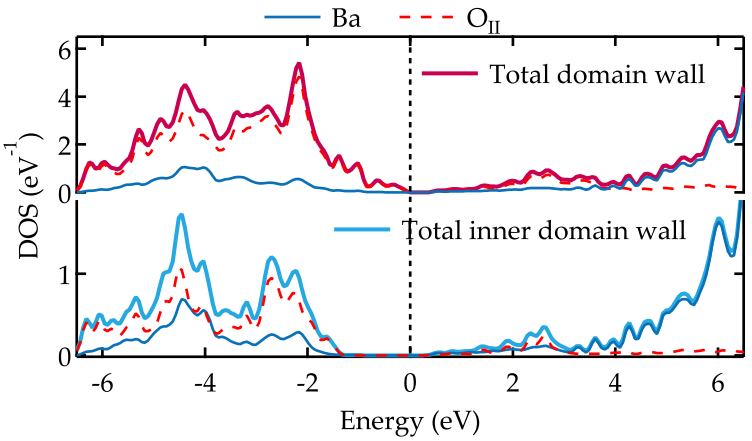


**Figure 3.24.:** Atom-projected density of states on (top) the total height of a domain wall and (bottom) the inner part of a domain wall.

Therefore for $BaTiO_3$, with stable out-of-plane polarization and 180° domain walls, no evidence of band gap reduction can be seen at the domain wall, contrary to what has been reported in the case of 180° domain walls in $BiFeO_3$ by Siedel et al. [152].

**Atomic layers projection in one domain:**

For the $TiO_2$ termination, both $P^+$ and $P^-$ give rise to electronic surface states at the top of the valence band, located well above the bulk valence band maximum, as shown by Fig. 3.23b. The Kohn-Sham band gap is smaller in the *c* phase (0.5 eV) than in the *aa* phase (1.4 eV) at the highest compressive and tensile strain, respectively. In order to investigate further the origin of this difference of band gap, which depends on the polarization direction (whether out-of-plane or in-plane), we plot the atom-projected density of states on each atomic layer along the [001] direction for one domain. The bottom and top surface layers corresponds to $P^-$ and $P^+$ polarization, each layers are labeled from 1 to 9 with ascending $z$.

The surface states originating from the oxygen atoms of the $TiO_2$ surface planes are visible on the DOS of the surface layers. From the surfaces towards the inner atomic layers, a clear effect of band bending can be observed. We do not see any rigid shift of the states from $P^-$ to $P^+$, which would be caused by a significant macroscopic electric potential. Thus, this band bending is probably mainly produced by a difference in the microscopic (Madelung) potential between the oxygen sites at the surface and in the bulk [18, 137]. The atomic distortions induced by the ferroelectric polarization influence the Madelung microscopic potential. From the surface to the bulk, the difference in microscopic Madelung potential at the oxygen sites, $|\Delta V_{\text{micro}}|$, is thus higher in the *c* phase compared to the *aa* phase explaining the stronger Kohn-Sham band gap reduction of $\sim 1.4\,\text{eV}$ down to 0.5 eV in the *c* phase.

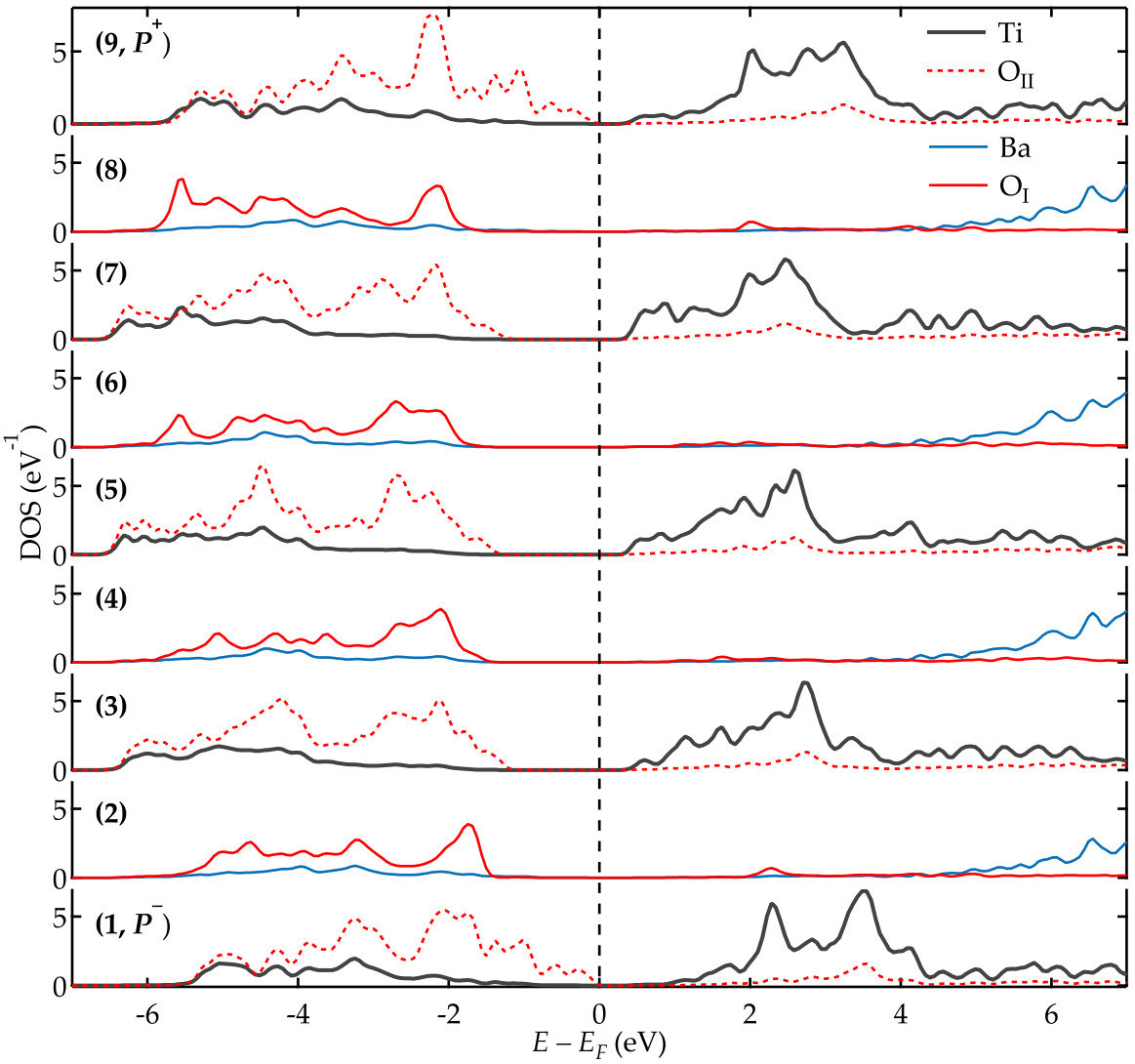


**Figure 3.25.:** Atom-projected density of states on each atomic layers of one full domain, from the bottom $P^-$ to the top $P^+$ surface. $TiO_2$ surface, $L = 9$, $N = 6$ and $a = 3.80$ Å.

A small difference of $\sim 0.2$ eV is observed between the valence band maximum at the $P^+$ and that at the $P^-$ surface (see $P^+$ and $P^-$ atom-projected DOS in Figs. 3.23b and 3.25). This potential difference which is added to the microscopic potential difference can be related to the presence of a macroscopic potential through the system, between the two oppositely polarized surfaces. Such $\Delta V_{\text{macro}}$ could be attributed to an imperfectly compensated depolarizing field originating from the different surface polarization charges. In order to determine whether this small difference is related or not to an imperfectly compensated depolarizing field, we plot in Figure 3.26 the electrostatic potential calculated as a double average over the atomic layers within each domain, first at fixed $z$ and then along $z$, using the MACROAVE program available in the ABINIT and SIESTA packages.

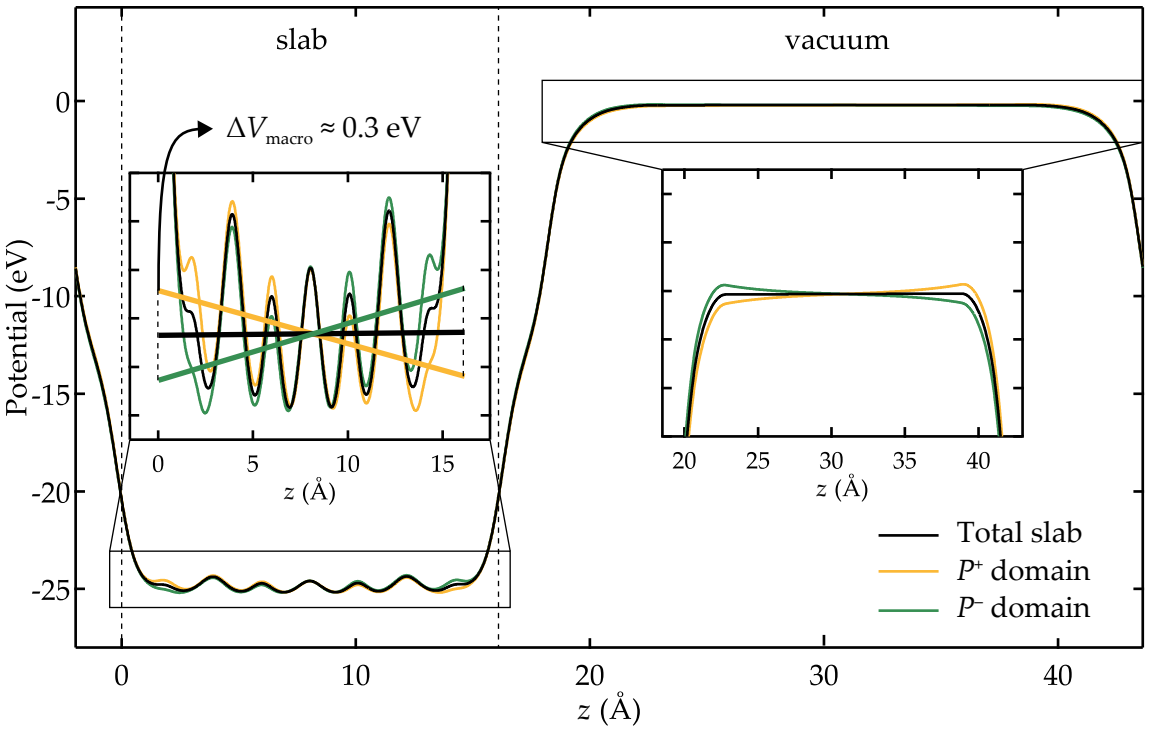


**Figure 3.26.:** Macroscopic average of the total potential in the slab and in the vacuum as a function of $z$ (Å), performed on the whole slab and on each domain. $L = 9$, $N = 6$, $a = 3.80$ Å, vacuum thickness $\approx 30$ Å. Left-hand-side inset: zoom on the slab and linear fit of the macroscopic potential. Right-hand-side inset: zoom on the vacuum macroscopic potential.

Within the slab, a small potential difference $\Delta V_{\text{macro}} \approx 0.3$ eV is present in one domain between the $P^+$ and $P^-$ surfaces, and is reversed in the other domain. This suggests the existence of a residual depolarizing field. The effect of this potential on the electronic surface states is nevertheless negligible with respect to that of the Madelung potential which is responsible to a much larger shift of the valence band maximum as described above. Fig. 3.26 also shows the rapidly decreasing potential from the slab to the vacuum layer, preventing spurious interactions between the periodic images of the slab. 3.3 DOS $p$ phase 3.8 DOS $aa$ phase 3.21 and 3.22 DOS $c$ phase The obtained results on the atom-projected density of states show that surface states shifts the valence band maximum at the $TiO_2$ surface in $c$ phase. Furthermore, the shift is not attributed to a residual depolarizing field which is found negligible and well compensated. This is consistent with the observed surface states at the valence band maximum that are related to a smaller Madelung potential at surface sites with respect to the bulk [18, 44]. The atomic distortions at the surface, induced by the ferroelectric polarization, contribute to the reduction of the microscopic potential at the surface and their effect is stronger in $c$ and $p$ phases. This is confirmed by the comparison of the density of states of the $c$ and $aa$ phases with respect to the $p$ phase. From the density of states computed for the reference paraelectric $p$ phase (see Fig. 3.3b), the Kohn-

Sham band gap is small and almost insensitive to the strain, with values from 0.4 eV to 0.7 eV for $a = 3.800$ Å to 4.000 Å. In the *c* phase, the ferroelectric displacements, superimposed to those of the natural rumpling which is present in the *p* phase, do not modify the Kohn-Sham band gap with respect to the *p* phase (see Fig. 3.22b). However, in the *aa* phase, the ferroelectric displacements are associated to the Kohn-Sham band gap of 1.4 eV (see Fig. 3.8b).

As a conclusion, the domain structure is efficient to provide screening of the depolarizing field in each of these small domains, since it allows ferroelectricity perpendicular to the surface to appear and the system to remain an insulator. A small, non significant residual depolarizing field is observed, that is responsible for a difference of potential of $\sim 0.3$ eV between both surfaces in the case of $N = 6$, $L = 9$ layers. The differences between the electronic structure of the *c* and the *aa* phase is thus mainly due to the microscopic Madelung potential at the surface.

# 4. Surface oxygen vacancy in *c* phase

## 4.1. System

Following the same methodology of alternating up and down domains, we have simulated a defective ferroelectric $BaTiO_3$(001) by adding an oxygen vacancy at the surface layers. We chose the $TiO_2$ termination with $L = 9$ atomic layers along [001] and $N = 6$ unit cell along [010], in the case of the highest compressive strain with the in-plane lattice constant $a = 3.800$ Å. The introduction of an oxygen vacancy is performed by removing an oxygen atom at the surface of the slab. Given the periodic boundary conditions, in order not to remove all oxygen from a surface O–Ti–O chain along [100] (by removing one oxygen atom in the supercell which contains only one unit cell along [100]), we have doubled the supercell along that direction. To preserve the free-standing slab symmetry between the two surfaces, the removal of a surface oxygen atom requires the removal of another oxygen atom from the opposite surface. Thus the whole system remains non polar and the short-range decay of the electric field in the vacuum should remain valid. This is schematized in Figure 3.27 which displays the modeled supercell, alongside with a detailed view of the slab surfaces comprising the oxygen vacancy in Figure 3.27b. The position of the oxygen vacancy is indicated by red and blue crosses. Finally the calculations have been performed here in a spin-polarized scheme, because the two electrons released by the neutral oxygen vacancy (which is a double donor) are expected to localize, and reduce the $Ti^{4+}$ in

$Ti^{3+}$, which are magnetic ions (in fact, such localization is not observed here, but this is probably due to the use of the LDA as the exchange-correlation functional).

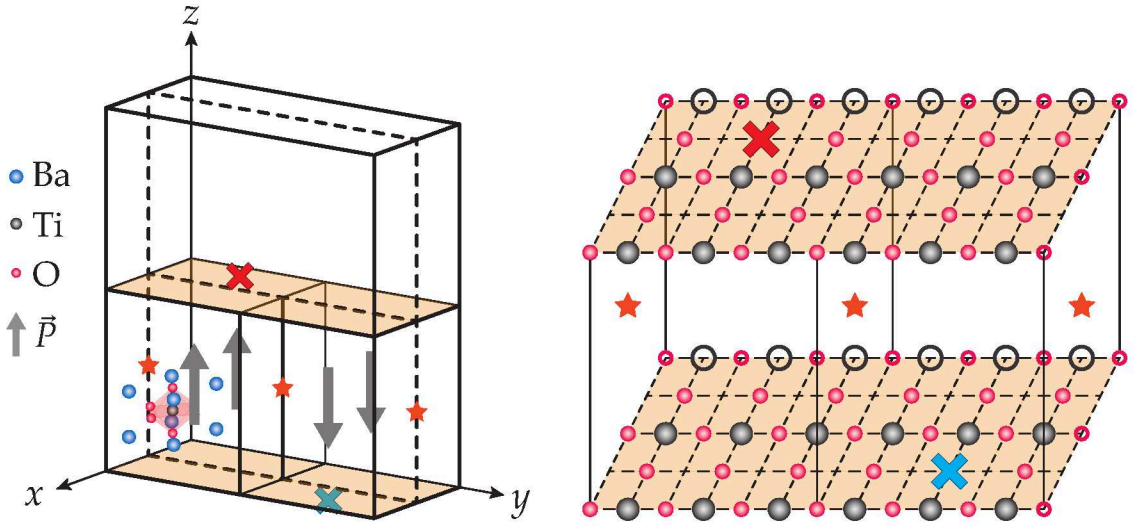


**(a)** Supercell **(b)** Slab surfaces

**Figure 3.27.:** (a) Schematic of the simulated $BaTiO_3$(001) supercell which includes an oxygen vacancy on both surfaces. The number of unit cells along $(x, y, z)$ is $(2, \frac{L}{2} = 4.5, N = 6)$. The position of the oxygen vacancy on the two equivalent surfaces is indicated by the red and blue crosses. (b) Detailed view of the slab surfaces with the oxygen vacancy on both surfaces. The empty circles depict periodic images of the atoms contained in the supercell. The orange stars marks inversion centers.

In this system, the total number of atoms is 274 ($n_{Ba} = 48$, $n_{Ti} = 60$ and $n_O = 166$). Since the two surfaces are equivalent, the system is not stoichiometric (whence $\frac{n_{Ba}}{4} = \frac{n_{Ti}}{5} = \frac{n_O}{4\cdot1+5\cdot2}$ owing to the 4 BaO and 5 $TiO_2$ atomic planes along the [010] direction). We calculate the concentration of oxygen vacancy to be $2/168 \approx 1.2\,\%$, where 168 is the number of oxygen atoms in the non-defective supercell.

The initial polarization configuration of the system comprises two alternating up and down domains, similar to the case of the $TiO_2$ terminated slab with $L = 9$ and $N = 6$, now with two unit cells along [100]. To investigate the stability of the polarization in the presence of a surface oxygen vacancy, two cases are distinguished, whether the oxygen vacancy is positioned at the $P^+$ or $P^-$ surface. The position of the oxygen vacancy is fixed at the center of either $P^+$ or $P^-$ as it is not allowed to diffuse. These two configurations are fully relaxed within the same structural optimization scheme used for the $c$ phase, when the Cartesian components of atomic forces are below 0.01 eV $Å^{-1}$. The $k$ point sampling is, however, more moderate with $3 \times 1 \times 1$ owing to the extremely demanding computation weight. It is however equivalent in the lateral directions to 6 $k$-points in the first Brillouin zone of the primitive cell,

a sampling sufficient to obtain correctly converged properties for the structure and energy.

In the following, we investigate the relative stability of these ferroelectric slabs incorporating oxygen vacancies. Local polarization vectors and the total electronic density of states are computed.

## 4.2. Stability and surface polarization

The fully relaxed slabs display two domains of opposite out-of-plane polarization, of dimensions 2 u.c., $N/2 = 3$ u.c. and $\frac{L-1}{2} = 4$ u.c. along $x$, $y$ and $z$, respectively. Despite the initial configuration difference where the oxygen vacancy is positioned at the outward polarized domain $P^+$ or at the inward polarized domain $P^-$, the two systems relax to the same ferroelectric structure which corresponds to the vacancy at a surface where the polarization is pointing inwards ($P^-$). The total energy difference between the two fully relaxed systems is $\sim 2 \times 10^{-3}$ meV/u.c., i.e. within the numerical error. In other words, the two systems are identical and we could not stabilize the oxygen vacancy at the surface of the $P^+$ domain. On the basis of these results, surface oxygen vacancies stabilize inward pointing polarization, $P^-$.

The polarization per unit cell was computed using the atomic displacements of the fully relaxed defective ferroelectric slab with respect to the perfect paraelectric slab (without vacancy). The contribution of the oxygen vacancy to the local polarization vector is set to zero.

In Figure 3.28, we plot the local polarization vectors and components. Contrary to the slabs in perfect *c* phase (without vacancy), here the slab has been doubled along the [100] direction and therefore the inversion centers are shifted 1 u.c. along [100], as the oxygen vacancies belong to different (100) planes, separated by 1 u.c. Therefore, in the chosen $(y, z)$ slice of the slab, the two halves of the slab along the [010] direction are not symmetry-equivalent. The symmetry-equivalent of each half along [010] is shifted 1 u.c. along [100] given the shift of the inversion centers. As a consequence, for completeness, the polarization vector and components are explicitly given for each unit cells in the $(y, z)$ plane projection of Fig. 3.28. The oxygen vacancy marked by the red cross is located in the first neighboring unit cell (in the [100] direction) away from the represented unit cells. The oxygen vacancy marked by the blue cross belongs to the same unit cell as the Ba and Ti atoms represented. Figure 3.29 shows planar views of the slab allowing to visualize the atomic displacements in all directions.

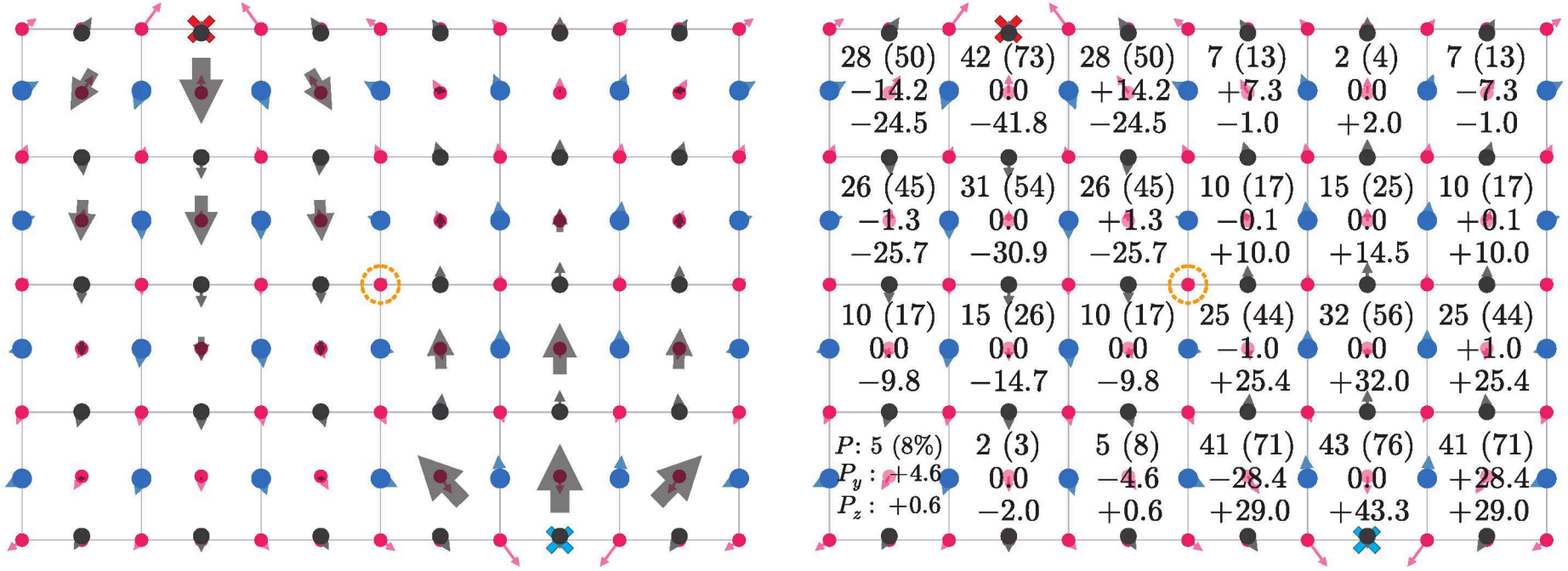


**(a)** Polarization vectors

**(b)** Polarization components

**Figure 3.28.:** Schematic $(y,z)$ projection of two atomic layers parallel to (010) and separated by $a/2$ of the fully relaxed ferroelectric $TiO_2$-terminated slab with an oxygen vacancy at the surface of $P^-$ domain, with the polarization (a) vectors and (b) components. $L = 9$, $N = 6$, $a = 3.800$ Å.

The atomic positions (colored circles) are those of the perfect $p$ phase system. The atomic displacements from these positions in the defective ferroelectric slab are marked with the atom-centered colored arrows. The oxygen vacancies are marked by red and blue arrows. The dashed orange circle indicates the position of the an inversion center. Note that the inversion center is located behind visible O atom in the foreground, i.e. 1 u.c. shifted in the [100] direction, similarly to the blue cross with respect to the red cross depicting the vacancies.

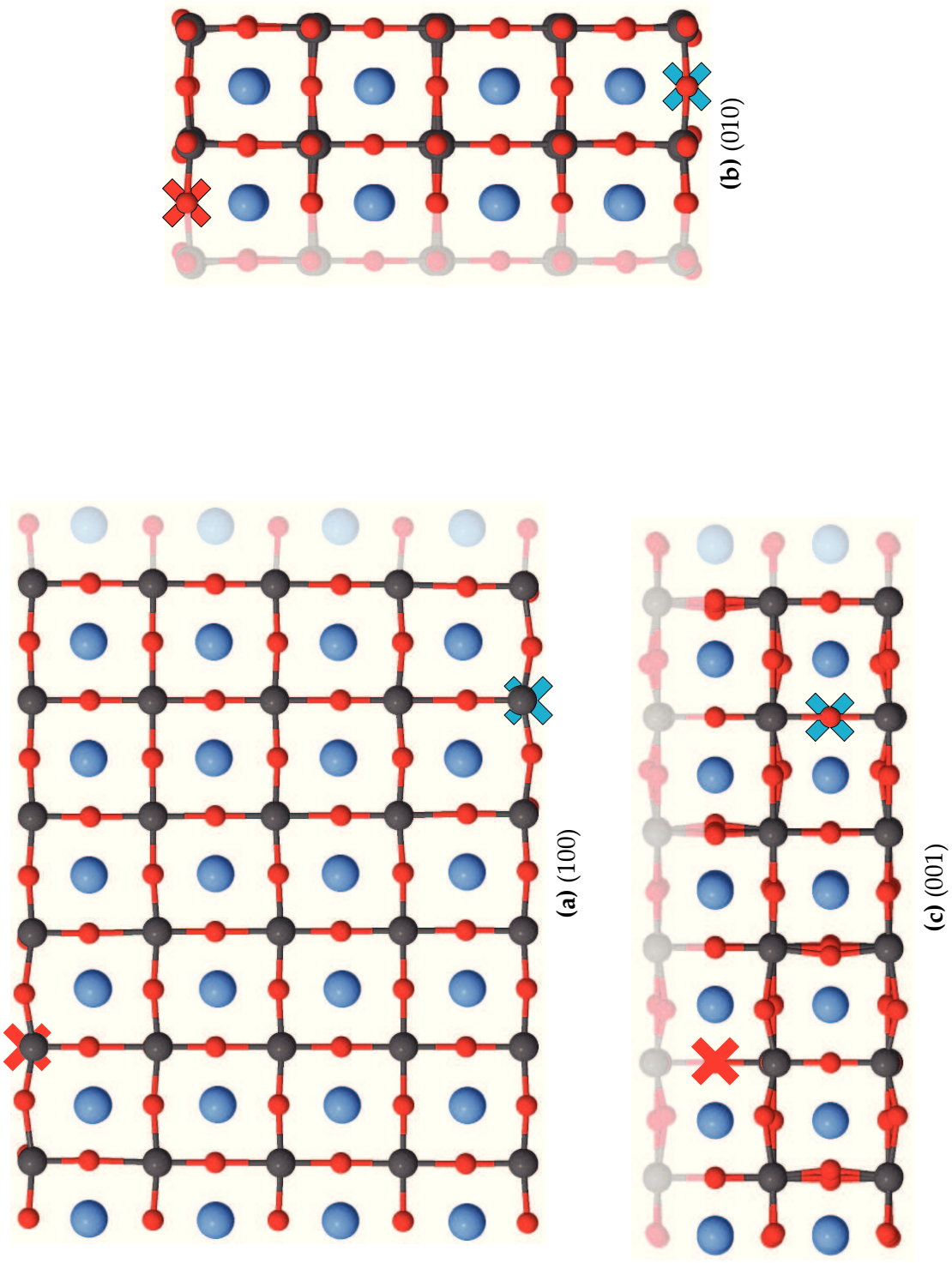


**Figure 3.29.:** Representation of the $TiO_2$-terminated slab with surface oxygen vacancies, shown for different planar views.

In Fig. 3.28a, the atomic displacements are maximum around the oxygen vacancy sites. The oxygen atoms surrounding the vacancy site show large displacements towards the vacuum and the vacancy site. The $(y,z)$ projection of the displacements does not allow to visualize displacements along $x$ (see Figs. 3.29b and 3.29c for such displacements). The oxygen atoms surrounding the vacancy site are displaced by $\approx 0.27$ Å, 0.15 Å and 0.20 Å along $x$, $y$ and $z$, towards the oxygen vacancy site. The surface Ti surrounding the vacancy site are displaced in the opposite directions, by $\approx 0.11$ Å and 0.02 Å along $x$ and $z$, away from the vacancy site. These opposite anionic and cationic displacements with respect to the oxygen vacancy strongly suggest that the vacancy site acts as a positive charge that polarizes to the surrounding matrix. From these atomic displacements, the computed polarization vectors show maximum magnitude in the unit cell comprising the oxygen vacancy and the first neighboring unit cells, owing to the particularly large outwards displacements of oxygen ions which enhance the negative charge at the surface. The local polarization magnitude decreases with increasing distance from the vacancy site.

In Fig. 3.28b, the polarization magnitudes ranges from 43 µC cm$^{-2}$ to 2 µC cm$^{-2}$ from the surface unit cell comprising the oxygen vacancy (marked by the blue cross) to the opposite surface unit cell. In the first neighboring surface unit cells in the [010] direction, the polarization rotates 45°. In the first subsurface unit cell, the polarization tilting almost vanishes. The rotation of the polarization (as well as its amplitude) is enhanced in the vicinity of the oxygen vacancy site. In the second neighboring surface unit cells, i.e. around the oxygen vacancy marked by the red cross, the polarization rotates 30°. Again, the rotation is observed only in the surface unit cells close to the domain walls, as in the subsurface unit cells $P_y \approx 0$ µC cm$^{-2}$.

These results show that the surface oxygen vacancy favors $P^-$ (even preventing stabilization of surface $P^+$ polarization), locally enhances the polarization amplitude and rotation close to the domain walls. The strong increase of the outwards (inwards) displacements of the oxygen (Ti) atoms towards (away from) the oxygen vacancy site appears for a large part responsible for the observed polarization properties. It should be noted that the local polarization far from the vacancy site is strongly reduced (down to 2 % that of the bulk at the same compressive strain), while it is enhanced at its vicinity. This suggests that the long-range stabilization of the polarization is perturbed in the presence of the vacancy, such that in the present case of the $TiO_2$-terminated slab with $L = 9$ atomic layers, it is possible that the main effect of the vacancy is to polarize the material by enhancing negative surface rumpling, favoring inwards polarization. However, such slab thickness is the lowest thickness at which the perfect (stoechiometric) $TiO_2$-terminated slab displays ferroelectricity, therefore even though the oxygen vacancy undoubtedly favors inwards polarization, it destabilizes the long-

range ferroelectric ordering as seen by the strong reduction of the local polarization. The effect of similar surface oxygen vacancy on the polarization of thicker $TiO_2$ or BaO-terminated slab could further address the overall effect of the oxygen vacancy on the stability of the ferroelectric ordering.

## 4.3. Electronic structure

The total density of states of the $TiO_2$-terminated ferroelectric slab comprising a surface oxygen vacancy is shown in Figure 3.30. The Fermi energy is found at the bottom of the conduction band, translating the presence of occupied conductive electronic states.

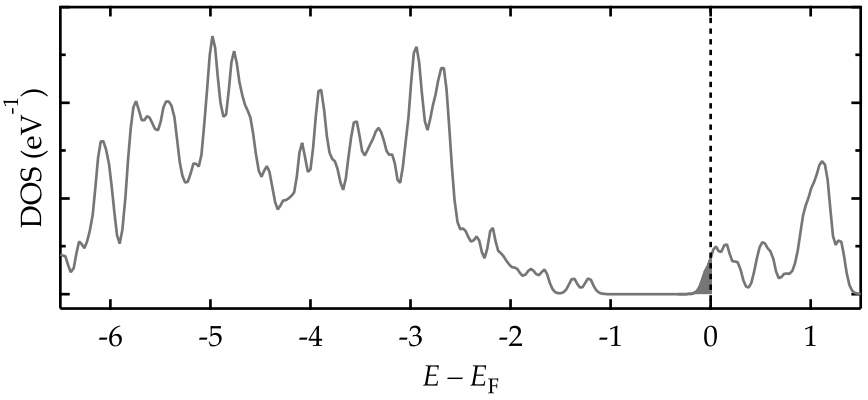


**Figure 3.30.:** Total electronic density of states of the $TiO_2$-terminated ferroelectric slab incorporating a surface oxygen vacancy. The energy scale is referenced to the Fermi energy which is located at the bottom of the conduction band. $L = 9$, $N = 6$, $a = 3.800$ Å.

This is expected since the neutral oxygen vacancy acts as a donor defect: as the neutral oxygen atom is removed, two electrons are released in the system that come to occupy states of the bottom of the conduction band. These states are mainly of Ti 3*d* nature (see Fig. 3.25). Previous calculations have shown that the bottom of the conduction band consists in Ti 3*d* states [85]. The question is whether the present calculation, that uses the local density approximation to DFT as the exchange-correlation functional, is able to correctly describe such states, as Ti 3*d* orbitals are considered usually as strongly correlated [40, 41]. In reality, the 3*d* states occupied by the released electrons could be stabilized by the electronic correlations and then slightly move inside the bandgap, rather than staying highly delocalized at the bottom of the conduction band. Experimental investigations on the influence of oxygen vacancy on the electronic structure rather suggest that the excess electrons occupy rather localized states in the gap, 1 eV below the bottom of the conduction band.

# 5. Summary of the results

(i) The properties (averaged polarization, energy) slowly converge to the bulk ones (at $L = 13$ atomic layers, the average polarization is only $\sim 2/3$ and below of the bulk value).

(ii) Out-of-plane and in-plane polarization, i.e. perpendicular and parallel to the surface, is stabilized under strong in-plane compressive and tensile strain (within the studied strain range $\sim -3.8\,\%$ to $1.3\,\%$). This behavior also depends on the surface terminations. The $TiO_2$ termination strongly favors in-plane polarization. Conversely, the BaO termination is more favorable than the $TiO_2$ termination with out-of-plane polarization under compressive strain.

(iii) Domain formation is efficient to screen the depolarizing field in the domains and stabilizes out-of-plane polarization, perpendicular to the surface, even for very small slab thickness. The surface termination modulates the critical thickness such that the onset of out-of-plane polarization for the BaO termination is at 7 atomic layers (i.e. 1.2 nm) and for the $TiO_2$ termination at 9 atomic layers (i.e. 1.6 nm). A very small residual macroscopic field is seen for $L = 9$ atomic layers, but the induced potential difference across the system (0.3 eV) is unable to metallize the system.

(iv) All the surfaces are found insulating, even though the Kohn-Sham band gap is significantly reduced in $c$ phase with $TiO_2$ termination.

(v) Surface rumpling is always negative, whatever the direction of $\vec{P}$, i.e. surface oxygen ions always point outwards with respect to the surface cations.

(vi) The polarization patterns for large domains periodicity ($N = 6$ unit cells) exhibit small closure domains at their surface, which is a way to minimize the depolarizing effects by lowering the electrostatic energy arising from polarization discontinuities.

(vii) We confirm the stabilization of oxygen vacancies at $P^-$ surfaces in $c$ phase. Oxygen vacancies provide free carriers which are simulated as delocalized states by the LDA.

# Chapter IV.

# Electron spectroscopy, microscopy and spectro-microscopy on $BaTiO_3$(001) surfaces

We have used Low-Energy Electron Microscopy (LEEM) [153, 154] and Photoemission Electron Microscopy (PEEM) [155] to investigate the (001) surface of $BaTiO_3$ single crystals. The two techniques are full-field electron microscopy, based on the use of an *immersion lens* and electron optics in ultrahigh vacuum. One contrast mechanism is common to both techniques: the local work function. It depends on surface charge density, doping, adsorbates. However, whereas the majority of the optics are identical, the probe is quite different. PEEM images photoelectrons generated by a photon source of specific energy which can be either UV lights, X-rays sources or synchrotron radiation. LEEM uses an electron gun as the source and is based on the reflection and scattering of incident electrons of tunable kinetic energy. A review of the past and prospective uses of these techniques can be found in Ref. [156].

The $BaTiO_3$ samples are single crystals manufactured by SurfaceNet GmbH[1] by top seeded solution growth. The samples are $(10 \times 10 \times 0.5)$ mm$^3$ with a polished, (001)-oriented, top surface. As received, the samples are stoichiometric, therefore insulating. As a consequence, incident electrons or photons can induce sample charging making imagery impossible. Furthermore, even slight surface charge strongly changes the surface potential which can cause electron optic caustics in the electron images. To circumvent this issue, the single crystals were annealed in ultrahigh vacuum prior to surface characterization and imaging. At the surface of $BaTiO_3$, controlled vacuum annealing can generate sufficient oxygen vacancies, which act as donor defects. These defects provide electron doping [43] and confer conductivity to the material, avoiding charging effects. Even if slightly conductive, ferroelectric properties can be maintained,

[1] http://www.surfacenet.de/

suitably for PEEM and LEEM investigations [94]. Recent results reported by our group on imaging ferroelectric materials with these techniques have been published [157].

The aim of this chapter is to present a selection of the results obtained with these microscopy techniques on $BaTiO_3$(001) that can shed some light on the calculations results described in section 4 of chapter III regarding surface oxygen vacancies. An introduction to the principles of the techniques, followed by results on the influence of oxygen vacancies as a screening mechanism are then presented using LEEM. Preferential surface polarization related to the surface oxygen vacancies concentration are addressed with PEEM.

# 1. Low-Energy and Photoemission electron microscopy

## 1.1. Immersion lens microscopy

The principle of immersion lens microscopy [156] resides in a voltage coupling between an objective lens and a sample, which allows fine tuning of the kinetic energy of the electrons collected to image the sample. It allows to image the surface, characterize the crystalline structure with diffraction or even map the surface band structure. In an immersion lens, the sample surface is part of the electron optics. LEEM and PEEM use electron optics (either magnetic or electrostatic lenses) in ultrahigh vacuum to collect and carry the electrons. However, the nature of the emitted electrons differs between both techniques because the initial excitation source is different. Therefore the interactions which lead to electron emission are different. LEEM is based on the reflection and elastic back-scattering of incident electrons whereas PEEM is based on the emission of photoelectrons. The setup instruments are described in the following.

## 1.2. Low energy electron microscopy

Figure 4.1 shows a photograph of the Elmitec III[2] LEEM microscope and a schematic of its components, which are described below.

In this LEEM [158], a thermoionic emitter, which consists in a lanthanum hexaboride ($LaB_6$) cyrstal, is at an accelerating voltage $U_0 = -20\,\mathrm{kV}$ (① in Fig. 4.1b). This cathode emits electrons inside the *illumination column* where they are focused in a collimated beam by a set of magnetic condenser lenses (② in Fig. 4.1b). A magnetic beam separator (③ in Fig. 4.1b) deviates the produced electrons towards the anode

[2] http://www.elmitec-gmbh.com/

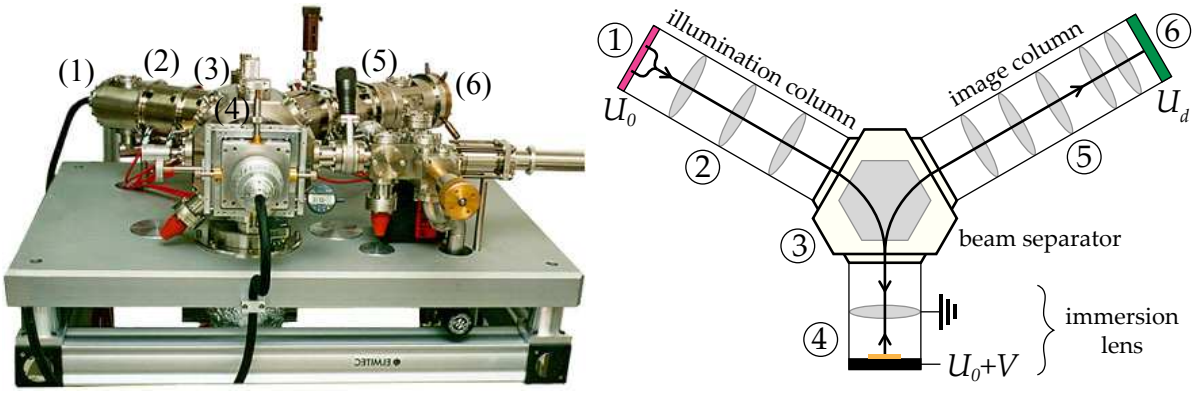


**(a)** Elmitec III **(b)** Optics schematic

**Figure 4.1.:** (a) Photograph of the Elmitec III LEEM. (b) Schematic of the electron optics composed of magnetic lenses. Description of the various parts labeled (1-6) is provided in the text.

part of the immersion lens, i.e. through the objective lens, and then towards the sample surface (④ in Fig. 4.1b). The anode of the immersion lens is grounded while the sample holder (hence the sample surface) is raised at $U_0 + V$ where $V$ is the *start voltage*, acting as the cathode part of the immersion lens. In such configuration, the incident electrons approaching the sample surface are decelerated down to the start voltage $V$, typically a few electronvolts, in order for low-energy electron interactions to take place. Reflected and backscattered electrons are then accelerated by the same potential back to the objective lens and then again properly deviated by the magnetic beam separator towards the *image column*, where a set of magnetic tetrode lenses (projective lenses) are dedicated to construct a magnified image out of collected electrons which have interacted with the sample (⑤ in Fig. 4.1b). In the back focal plane of the objective lens, a movable aperture can be positioned in order to cut out electrons emitted with high emission angles. This is the *contrast aperture* which is mainly used to enhance the diffraction contrast as well as the lateral resolution of the electron image. Finally, the electrons are projected onto multi-channel plates and a fluorescent screen which is recorded by a CCD camera (⑥ in Fig. 4.1b).

**Mirror Electron Microscopy:**

At very low kinetic energy ($V \rightarrow 0\,\mathrm{V}$), the incident electrons are reflected by the sample. The particular start voltage which marks the onset of total reflection is determined by the relative work function of the sample and the electron source. With constant electron source work function, modulations of the incident electrons reflection are therefore due to the surface potential $\phi(x, y)$. Such a configuration is referred to as *mirror electron microscopy* (MEM). At fixed start voltage in MEM regime, the data consist in a 2D image of the surface, with intensity $I(x, y)$. The origin of

the contrast is complex and accounts for surface potential as well as topographical modulations. In the case of a ferroelectric surface, the surface potential modulation can be mostly attributed to the surface charge density. However possible surface topography variations due for instance to domain twinning [159, 160] must also be accounted for.

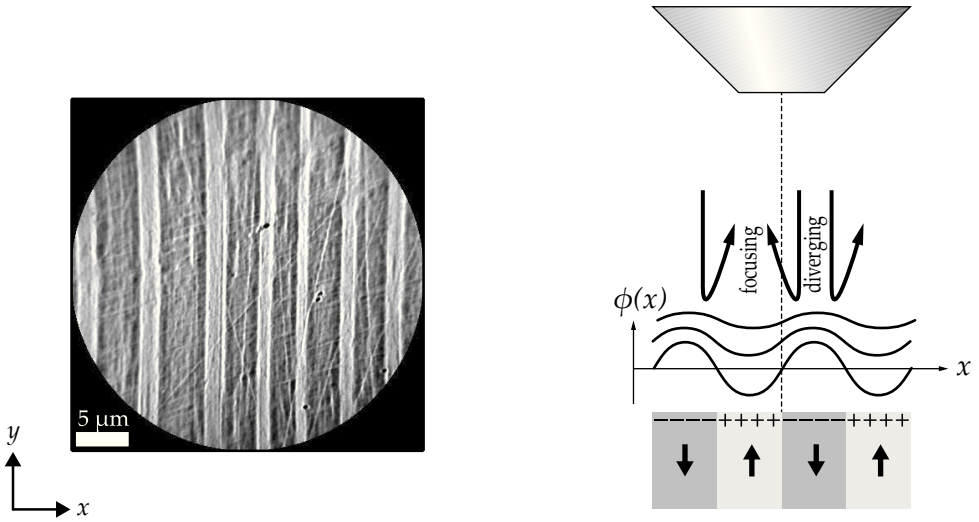


**(a)** MEM image **(b)** MEM schematic

**Figure 4.2.:** (a) Typical MEM image of $BaTiO_3$(001) acquired at start voltage $V = 1.45\,V$ and at room temperature. (b) Schematic of the immersion lens and the electron reflection modulation from the surface charge distribution. On the bottom, the sample contains alternating domains along $x$, with up/down polarization (straight arrows). The polarization charge density is depicted by the plus and minus sign. The oscillating lines schematizes the surface potential $\phi(x)$ arising from the charge distribution. The curved arrows depict electron paths. On top, the objective of the immersion lens is drawn.

A typical MEM image is presented in Figure 4.2a. In this image, alternating bright and dark stripes can be seen. These correspond to ferroelectric domains running along the $y$ direction with different out-of-plane polarization, leaving different polarization charge density at the surface. This surface charge density modulates the electrostatic potential above the surface, thus modulating the interaction of the incident reflected electrons [161–165]. This is schematized in Figure 4.2b, where an ideal periodic distribution of surface charge arising from out-of-plane polarized domains induces surface potential modulations. At fixed start voltage in MEM, the incident electrons interact with the surface potential such that positively charge regions act as focusing mirrors while negatively charge regions act as diverging mirrors for the incident electrons. This condition depends on the focal plan distance from the surface. Two focus conditions can be distinguished, both giving inverted contrast in MEM [166, 167]. The focus conditions used in this experiment are such that positively charged

domains regions appears brighter than neighboring negatively charge domains. The surface potential created by the surface charge decreases with increasing distance from the surface. Therefore, with lower kinetic energy, i.e. with a higher interaction distance from the surface, incident electrons interact with a weak potential, giving lower contrast. Slightly higher electron kinetic energy (a few 0.1 eV) allows stronger interactions with a better defined surface potential (as the interaction is closer to the surface where the potential is higher) and provide better contrast.

Furthermore, high and low intensity at the domain boundaries can be observed. The positively charged surface (outwards oriented out-of-plane polarization) are bordered with high intensity, whereas the negatively charged surface (inwards oriented out-of-plane polarization) are bordered with low intensity. This is attributed to the lateral deflection which occurs at the domain boundary owing to a lateral electric field generated by the different surface charge on the domains, as demonstrated by Nepijko et al., who studied a surface with non uniform potential distribution [166].

**Low-Energy Electron Microscopy:**

With increasing start voltage, the incident electrons penetrate the sample and interact with the lattice. At low kinetic energy ($V \sim 1\,\mathrm{V}$ to $10\,\mathrm{V}$), the dominant interaction is the elastic backscattering. Electrons interact with the first few layers from the surface and are back scattered without any energy transfer to the lattice. This regime is referred to as *low energy electron microscopy* (LEEM). At higher kinetic energy ($V \sim 10\,\mathrm{V}$ to $100\,\mathrm{V}$), the interaction is dominated more and more by inelastic backscattering processes. Nevertheless, elastic scattering cross-section is still high, and the diffracted electrons carry crystallographic information and can be used to produce diffraction pattern of the lattice in the vicinity of the surface, referred to as *low-energy electron diffraction* (LEED).

**MEM-LEEM transition:**

The electron current, collected to image the surface, and measured as a function of start voltage is often referred to as *reflectivity*. At the transition between MEM and LEEM regimes, a drop of reflectivity is observed while increasing $V$. The kinetic energy of the electrons becomes sufficiently high to overcome the surface potential and penetrate the surface. The MEM-LEEM transition can be therefore related to the *work function* of the sample and fitted with a complementary error function (erfc) [168]:

$$I(V) = I_0 + A \cdot \mathrm{erfc}\left(\frac{V - V_t}{\sqrt{2}\,\sigma}\right), \tag{IV.1}$$

where $I_0$, $A$ and $\sigma$ are the background intensity, the amplitude and width of the fitting function, respectively; the MEM-LEEM transition voltage is denoted $V_t$. This analytic expression essentially originates from the convolution of the electron gun output (Gaussian function) with the surface potential barrier overcome at the transition between reflection and elastic scattering (step function).

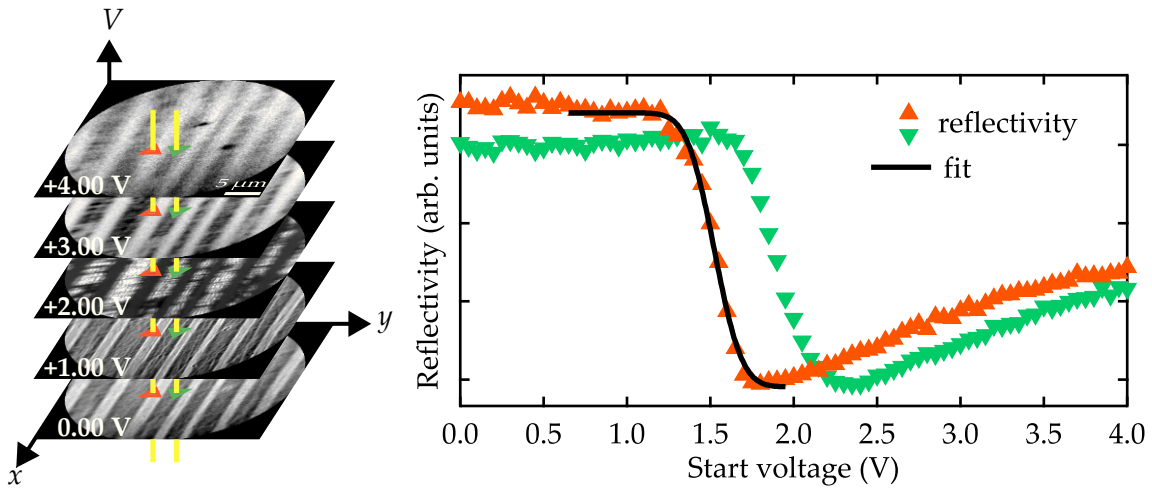


**(a)** 3D stack **(b)** Reflectivity curves

**Figure 4.3.:** (a) Images acquired as a function of $V$, showing contrast inversion through the MEM-LEEM transition as $V$ increases. (b) Reflectivity curves $I(V)$ extracted from the 3D data set from different domains.

By scanning the start voltage, the acquired data consist in 3D stack of images of the surface, with intensity $I(x, y, V)$. Each image has an intensity $I(x, y)$ at a specific start voltage $V$. Equivalently, each pixel column $(x, y)$ of the 3D stack corresponds to a reflectivity curve $I(V)$ which can be fitted to equation IV.1. A schematic representation of the 3D stack is shown in Figure 4.3a. Based on the previous description on the electron interaction as a function of start voltage, at $V = 0.00\,\mathrm{V}$ in MEM regime (bottom most image), the stripe domains are clearly visible. However the contrast is weak and the lateral resolution poor due the increase of spherical and chromatic aberrations at low start voltage [169]. With increasing $V$, the aberrations are reduced and the contrast enhanced, as seen on the image at 1.00 V. The start voltage at which the contrast is best enhanced uses to acquire MEM images such as that of Fig. 4.2a at $V = 1.45\,\mathrm{V}$. At $V = 2.00\,\mathrm{V}$, contrast inversion is observed due to different MEM-LEEM transition values between the two types of domains. Figure 4.3b shows the reflectivity curves from 0.00 V to 4.00 V extracted from a pixel on each domain, as illustrated by the vertical lines crossing the image stack in Fig. 4.3a. The MEM-LEEM transition is shifted due to different surface charge. The black solid line is the fit of the MEM-LEEM transition to equation IV.1.

An automated procedure which performs the fit from equation IV.1 for every pixels of the field of view allows extracting local MEM-LEEM transition values and therefore generate a map of the surface potential in the whole field of view.

## 1.3. Photoemission electron microscopy

In PEEM, the sample surface is illuminated by photons of specific energy to generate photoelectrons by photoelectric effect. Hence, contrary to LEEM, no illumination column is required since the excitation source are photons. Nevertheless, the objective of the immersion lens collects the photoelectrons towards an image column comparable to that in LEEM. In addition to the lateral origin of the collected electrons, the emission angle and energy of the photoelectrons are conserved through the electron optics allowing to unveil information on the surface chemical and electronic structures. This is made possible by the combination of an energy analyzer with the electron optics. The energy analyzer selects the kinetic energy of the photoelectrons, which is defined by the law of conservation of energy by:

$$E_K = h\nu - E_B - \Phi_S, \tag{IV.2}$$

where $E_K$ is the emitted electron kinetic energy, $h\nu$ is the incident photon energy, $E_B$ is the binding energy of the emitted electron in the material and $\Phi_S$ is the work function of the material.

With a photon source of chosen energy, the generated photocurrent contains photoelectrons with kinetic energy ranging from zero to $h\nu - \Phi_S$. By collecting all emitted electrons, a standard PEEM works as a low-pass filter, since all photoelectrons of kinetic energy limited by the photon source are collected. However, in order to access the binding energy of the initially bound electron, an energy analyzer is used, in the same way as in standard photoemission experiment [170], working as a band-pass filter.

**Instrument:**

A photograph and schematic of the PEEM used in this experiment is given in Figure 4.4. In Fig. 4.4b, photons of energy $h\nu$ impinge the sample (bottom left-hand corner), generating a photoelectron current depicted as the red line. The first part of the microscope is the PEEM column (①-④ in Fig. 4.4). It contains the immersion lens (① in Fig. 4.4) which is composed of the sample and the objective lens. The objective lens is at high voltage, in this experiment at 12 kV, while the sample is at a

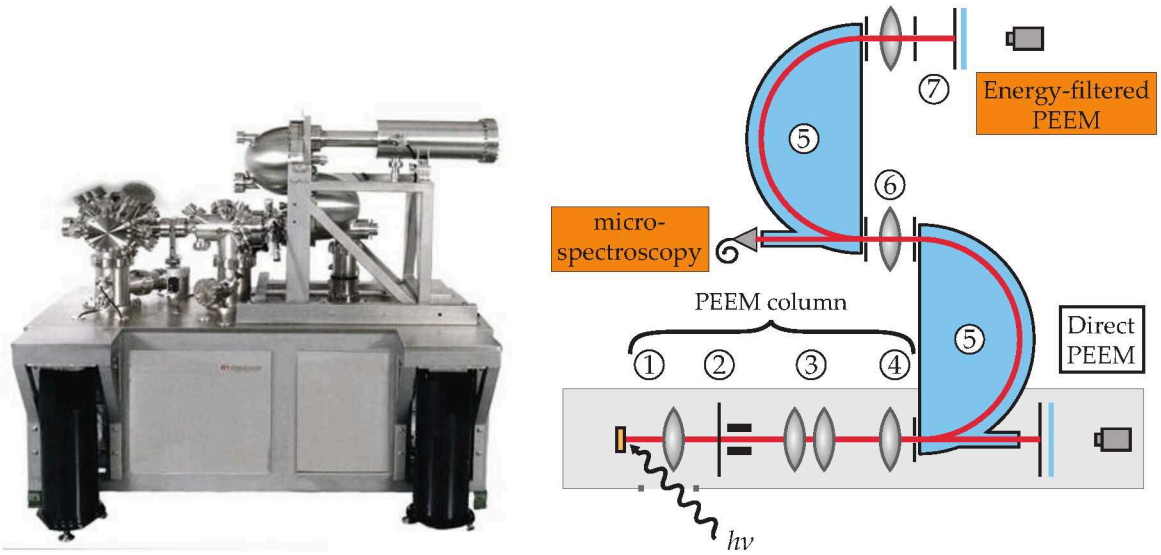


**(a)** NanoESCA PEEM **(b)** Instrument schematic

**Figure 4.4.:** (a) Photograph of the Scienta Omicron NanoESCA. (b) Schematic of the electron optics composed of electrostatic lenses in the PEEM column, with double hemispherical analyzers in series. See text for the description of the different parts.

tunable potential $V$ close to the ground. The resulting electric field $\vec{E}_{\text{ext}}$ generates a high extraction voltage (equivalent to $U_0$ in LEEM) which allows collecting electrons emitted with large angles. A contrast aperture can be positioned in the back focal plane of the objective (② in Fig. 4.4), to either collect or cut the electrons emitted with a large angle. Projective lenses (③ in Fig. 4.4) then carry the collected photoelectrons towards the entrance slit (④ in Fig. 4.4) of the imaging double energy analyzer (IDEA) (⑤ in Fig. 4.4). The band pass of the energy analyzer is set by the pass energy $E_P$ which is kept constant. Applying proper electron optics settings, electrons of chosen kinetic energy are slowed down at the entrance of the analyzer to a kinetic energy that matches $E_P$. Hence, chosen photoelectrons can travel through the analyzer, giving access to the binding energy of the initial photoelectrons, according to equation IV.2. Then, selected photoelectrons travel through the second analyzer which corrects the spherical aberrations generated by the first analyzer [171]. The two analyzers are linked by a transfer lens system (⑥ in Fig. 4.4). Finally, the selected photoelectrons reach an imaging unit (⑦ in Fig. 4.4) composed of multi-channel plates, a screen and a CCD camera. This corresponds to the energy-filtered PEEM imaging mode.

The collected and selected photoelectrons can be used to perform direct spectroscopy, by using a channeltron detector at the end of the first analyzer. In our instrument, such operating mode allows fast spectroscopic acquisition but limits the lateral resolution to the size of the iris which allows selecting a region of interest on the sample surface. Switching between energy-filtered imaging and direct spectroscopy modes allows choosing a region of interest by inserting a field aperture called iris

and perform local spectroscopy on a specific surface region ("micro-spectroscopy" in Fig 4.4). Therefore, photoemission spectra can be acquired over a particular ferroelectric domain for instance. A third mode consists in imaging all collected photoelectrons, in "direct PEEM", before the energy filter (not used in this work).

From this instrumental design, the remaining chromatic and spherical aberrations induced by the extractor field gives theoretical resolution limits in the 10 to 20 nm range [172]. In practice, the lateral resolution is governed by the aberrations of the immersion lens [173] and can be enhanced with the use of a contrast aperture in the back focal plane and smaller energy windows set by the energy filter. These enhancements come at the expense of the electron flux used to form the PEEM image. Comparatively, in LEEM the angular spread is lower for crystalline surfaces and therefore the lateral resolution is better, in the 1-10 nm range [169].

The PEEM experiment was conducted at the NanoESCA beamline[3] at the Elettra synchrotron facility in Trieste, Italy, with a NanoESCA microscope [174] (Scienta Omicron GmbH – Focus GmbH[4]).

### 1.3.1. Photoemission process

A full quantum mechanical description of the photoemission process in solids is formulated within the *one-step model*, as first derived by Mahan [175]. However, a prior semi-classical conception had been developed by Spicer and Berglund [176] known as the *three-step model*, which is described below.

**Excitation:**

First, an incident photon of sufficiently high energy can excite a bound electron inside the solid. The probability of the transition from an initial electron state to an excited state is proportional to the *photoionization cross-section*, which depends on the emitting element, energy level of the emitted electron, incident photon energy and polarization.

**Transport:**

Secondly, the excited electron can undergo scattering events with the atoms and other electrons of the solid. Four cases are distinguished depending on the amount and nature of the scattering events:

[3] https://www.elettra.trieste.it/it/lightsources/elettra/elettra-beamlines/nanoesca/nanoesca.html
[4] http://www.scientaomicron.com/

(i) There are no scattering events and the excited electron is emitted with maximum kinetic energy allowed by equation IV.2. Such electrons are referred to as *primary electrons*, and provide chemical (from core levels) and electronic structure (from the valence band) information.

(ii) Few scattering events can lead to kinetic energy loss, such as shake-up, shake-off and plasmon structrures which give insight into the electron density and atomic structure of the surrounding excited electrons.

(iii) Many inelastic scattering events lowers the excited electron kinetic energy. The electrons are still emitted but have lost electronic and chemical information. Such electrons are called secondary electrons, and can provide information regarding potential barriers that separate the solid from the vacuum or used as a measure for the photon-solid interaction strength.

(iv) Too many inelastic scattering events prevent the unbound electrons to escape from the solid. These electrons do not contribute to the photoemission signal.

The inelastic scattering therefore limits the depth from where electrons may be emitted. The inelastic mean free path (IMFP) defines the average distance that an electron with given kinetic energy travels between two successive inelastic collisions. This quantity depends on the element from which the electron is excited, and the electron kinetic energy. However, "universal curves" of IMFP as a function of electron kinetic energy have been reported. They provide approximations of the electron transport distance in the material, allowing to estimate the escape depth and surface sensitivity. An analytic formulation of the IMFP has been recently reported by Jablonski [177], namely on the basis of previous work with Powell [178–180]. However, the universality of this quantity has long been subject to debate [181]. In the present work, we consider that the surface sensitivity of our LEEM and PEEM measurements ranges from 1 nm to 10 nm.

A typical photoemission spectrum is given in Figure 4.5. The intensity of the collected photoelectrons is plotted as a function of kinetic energy. Based on equation IV.2, primary electrons give access to core levels and electronic structure in the valence band. At the photoemission threshold, the onset of secondary electrons gives access to the work function. In PEEM, the Fermi level of the sample and sample holder are aligned. The work function of the analyzer is accounted for such that the photoemission threshold is a direct measurement of the work function of the sample.

**Emission:**

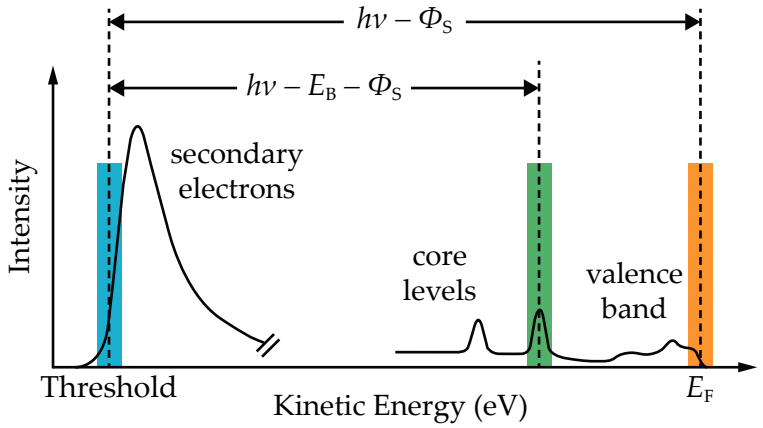


**Figure 4.5.:** Typical photoemission spectrum. The colored rectangles highlight the high intensity photoemission threshold corresponding to secondary electrons of low kinetic energy (blue), the core level region (green) and the valence band (orange). In PEEM, the kinetic energy is referred with respect to the Fermi level of the sample holder.

Primary electrons escape the sample with kinetic energy $E_K$ and wave vector $\vec{K}$ in vacuum. The emission geometry can be described in a spherical coordinates system, with the polar and azimuth emission angles $\theta$ and $\phi$ defined with respect the $z$ axis which coincides with the sample surface normal (the surface normal is also the axis of cylindrical symmetry of the immersion lens). The emission geometry is drawn in Figure 4.6a. The emission angle and energy are preserved and collected in the PEEM. Proper electron optics and energy analyzer configurations allow to image the sample surface either in real or in reciprocal space. In real space, the $(x, y)$ position of the emitted electrons from the surface is projected onto the image (lateral resolution) whereas in reciprocal space, the back focal plane of the objective lens is imaged giving direct access to the in-plane components of the wave vector $\vec{K}$ which carries the angular information $(\theta, \phi)$ of the emitted electrons (angular resolution). Real space (PEEM) and reciprocal space ($k$-PEEM) images of $BaTiO_3(001)$ are given in Figs. 4.6b and 4.6c.

Inside a crystalline material, given the periodicity of the lattice, the electron can be described by a Bloch wave of wave vector $\vec{k}$. Once the photoelectron has reached the vacuum, it can be considered as a free electron and therefore described by a plane wave of wave vector $\vec{K}$. From the emission angles $(\theta, \phi)$ of the electron, the magnitude

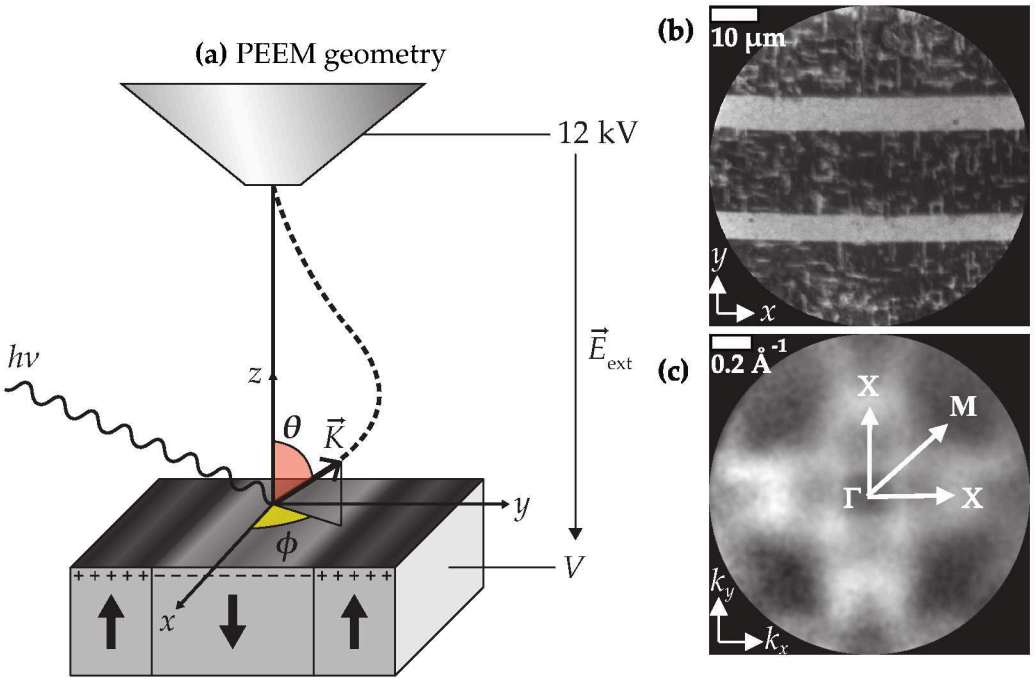


**Figure 4.6.:** (a) Geometry of the emission and collection of a photoelectron. The electron is emitted from the surface at position $(x, y)$ with energy $E_K$, wave vector $\vec{K}$ and emission angles $\theta$ and $\phi$ as depicted. A high extraction field is generated between the objective lens at high voltage and the sample at the potential $V$. (b) Real space image of $BaTiO_3$(001) acquired at the photoemission threshold ($E - E_F = 3.5\,eV$, $h\nu = 21.2\,eV$) (c) Reciprocal space ($k$-PEEM) image of the $BaTiO_3$(001) surface electron dispersion ($E - E_F = 8.7\,eV$, $h\nu = 50\,eV$).

and components of $\vec{K}$ in Fig. 4.6a are:

$$|\vec{K}| = \frac{1}{\hbar}\sqrt{2\,m_e\,E_K} \tag{IV.3}$$

$$K_x = |\vec{K}|\,\sin\theta\,\cos\phi \tag{IV.4}$$

$$K_y = |\vec{K}|\,\sin\theta\,\sin\phi \tag{IV.5}$$

$$K_z = |\vec{K}|\,\cos\theta \tag{IV.6}$$

Since the translational symmetry of the lattice is not perturbed by the surface [182], the in-plane component of the electron wave vector in the material $\vec{k}_{||}$ is conserved ($\vec{k}_{||} = \vec{k}_x + \vec{k}_y$). Therefore, from the law of conservation of momentum (with $\vec{K}_{||} = \vec{K}_x + \vec{K}_y$):

$$\vec{k}_{||} = \vec{K}_{||} = \frac{1}{\hbar}\sqrt{2\,m_e\,E_K}\cdot\sin\theta \tag{IV.7}$$

However, the perpendicular component $\vec{k}_\perp$ is not conserved ($\vec{k}_\perp = \vec{k}_z$) due to the discontinuity at the surface and the abrupt potential change along the $z$ axis. As the emitted electrons reach the PEEM column, they are accelerated to higher kinetic energy under the extraction voltage applied between the sample and the objective lens. At this stage, the perpendicular component $\vec{K}_z$ is therefore essentially determined by this potential (typically 12 kV with the NanoESCA microscope), independently from the emission energy and momentum at the surface.

With the NanoESCA PEEM, electron optics settings allows easy switching between the imaging (direct and reciprocal spaces) and spectroscopy modes. While imaging in direct space, the use of an iris allows selecting a region of interest from which the photoelectrons are collected. Hence, a specific region of the surface can be characterized by local core level spectroscopy (in direct spectroscopy) and band structure imaging (in reciprocal space imaging). These instrumental particularities differ from conventional Angular-Resolved Photoemission Spectroscopy (ARPES) [182] which brings spectroscopic information averaged over the beam size, without as easy control of the probed region.

To summarize, the conservation of the emitted electron energy, and momentum parallel to the surface associated with the energy and angular resolution of the PEEM setup allows to study the dispersion relation and hence the electronic band structure parallel to the surface. Depending on the electron kinetic energy, different spectroscopic information are accessible. At the onset of photoemission, or photoemission threshold, the sample work function can be measured. At higher kinetic energy, primary electrons are used to probe core levels and the valence band, giving access to the sample chemistry and electronic structure.

# 2. Surface polarization and chemistry

## 2.1. Annealing induced surface potential changes

We investigate the influence of vacuum annealing on the surface potential or work function of a $BaTiO_3$(001) single crystal with LEEM. The sample underwent repeated annealing cycles at 650 °C for 30 min at a base pressure of $\sim 1 \times 10^{-9}$ mbar in order to induce oxygen vacancies and allow domain reorganization. Between each annealing cycle, the surface potential is mapped by means of start voltage image series acquired at room temperature. Each vacuum annealing cycle is expected to increase the amount of oxygen vacancies at the sample surface. The vacuum conditions are constant throughout the whole experiment. However performing an annealing cycle

in situ requires to move the sample holder away from its imaging position in front of the objective lens. Therefore, the successive start voltage image series have not necessarily been acquired at exactly the same region. Nevertheless, we assume that the effects of vacuum annealing on the single crystal, i.e. the increase of oxygen vacancy concentration and the domain reorganization upon cooling across $T_C$, are homogeneous over the whole surface. In turn, for a given annealing cycle iteration, the potential at the surface of out-of-plane ($P^+$ or $P^-$) or in-plane polarized ($P^{in}$) domains, which depends on the polarization charge density, is considered equivalent whatever the region used for imaging.

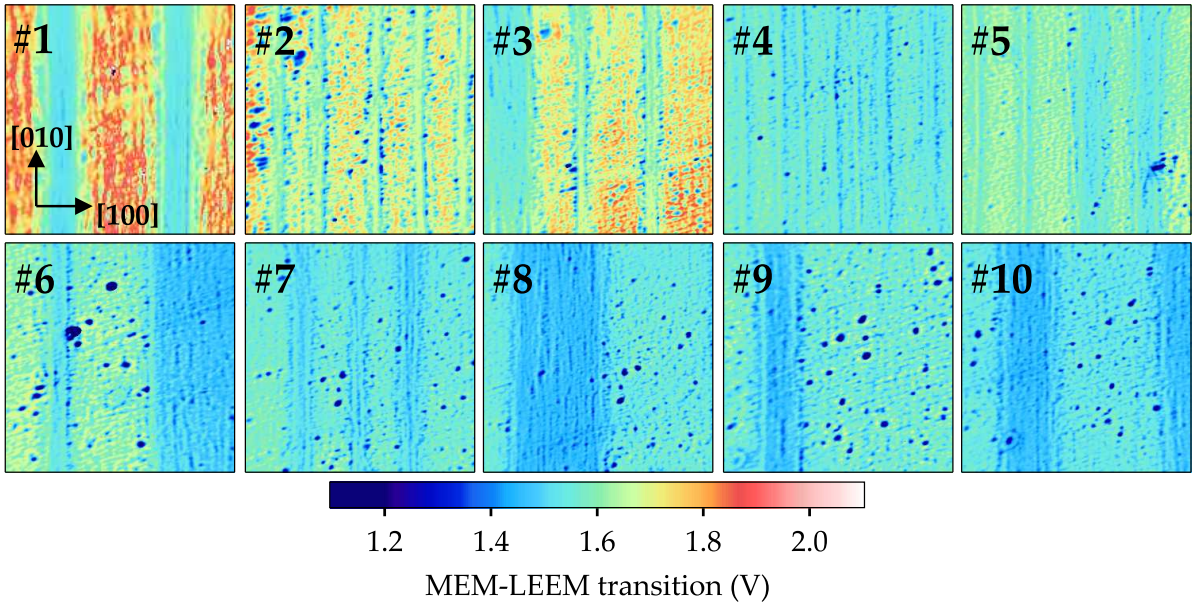


**Figure 4.7.:** $(20 \times 20)\,\mu m^2$ MEM-LEEM transition maps, each generated from a start voltage image series acquired after successive annealing cycles on a $BaTiO_3$(001) single crystal. The annealing cycle iteration is indicated for each map. The color scaling is the same for all images. The vertical stripes are ferroelectric domains.

Figure 4.7 presents the MEM-LEEM transition maps obtained after the 10 successive vacuum annealing cycles. The color scaling is the same for all images. The surface displays alternate stripe domains which can be seen in the maps as regions of different surface potential. After the first annealing cycle (#1), domains $\sim 5\,\mu m$ wide with macroscopic length along [010], display strong surface potential difference. Three values of the MEM-LEEM transition can be distinguished, corresponding to a maximum at $\sim 1.8\,V$, a minimum at $\sim 1.5\,eV$ an average intermediate value, gradually separated approximately by 150 meV. This means that three surface charge regions can be identified. At the MEM-LEEM transition, the electrons have enough kinetic energy to overcome the electrostatic potential barrier induced by the surface charge. Hence, the maximum value corresponds to the more negative surface charge whereas the minimum transition value corresponds to the more positive surface charge. The

intermediate value is attributed to neutral surface charge. As a consequence, considering the polarization bound charge at the surface, $P^-$, $P^+$ and $P^{in}$ are identified with the highest, lowest and intermediate MEM-LEEM transition values. We denote as $\phi^+$, $\phi^{in}$ and $\phi^-$ the surface potential at the $P^+$, $P^{in}$ and $P^-$ surface regions.

After annealing cycle #2, the MEM-LEEM transition map differs significantly from that obtained after the first cycle (#1). Firstly, the stripes are thinner, $\sim$2 µm wide, although evenly spaced. The annealing cycle requires heating well above the ferroelectric-paraelectric phase transition temperature $T_C$, which causes the domain ordering (i.e. surface charge and strain) to vanish. When cooling a new domain ordering is therefore possible.

Secondly, $\phi^+$, $\phi^{in}$ and $\phi^-$ have decreased and appear separated by $\sim$ 100 meV at most. The overall surface potential has therefore decreased, and the strongest decrease is observed for $\phi^-$. This behavior seems to be confirmed with further annealing as seen from the successive MEM-LEEM transition maps (from #3 to #10). The overall MEM-LEEM transition values decrease with successive annealing iterations, with the highest values decreasing the most. To quantitatively measure this behavior, histograms from the MEM-LEEM transition maps have been plotted.

In each histogram of Figure 4.8a, the three major components corresponding to $P^-$, $P^{in}$ and $P^+$ have been fitted by Gaussian functions with a constant full width at half maximum (FWHM). The strong contrast observed in map #1 (Fig. 4.7) translates into the broad distribution of three clearly separated peaks which is the signature of strong surface charge differences. After successive annealing cycles, the overall tendency of a decrease of the MEM-LEEM transition values can be seen as a shift of the histograms towards lower voltage values. The highest MEM-LEEM transition value ($\phi^-$, obtained from $P^-$ domains) is always shifted the most. In addition, the separation between the three components decreases with increasing number of annealing cycles. The tendency is therefore a decrease of the overall surface potential and the potential difference between the three surface domain types.

For each annealing cycle, the values of the three histogram components are plotted in Figure 4.8b (downwards triangles for $\phi^-$, squares for $\phi^{in}$ and upwards triangles for $\phi^+$). This representation allows to qualitatively follow the evolution of the charge at the surface of the three different ferroelectric domains as a function of vacuum annealing iterations. The positions of the different surface potential values are fitted with exponentially decaying functions. The results show that $\phi^-$ decays faster than both $\phi^{in}$ and $\phi^+$, suggesting a stronger influence of the annealing on the potential at the surface of $P^-$. It should be noted that $\phi^{in}$ decays also quite rapidly, although less than $\phi^-$, suggesting an intermediate influence of annealing cycles on the surface

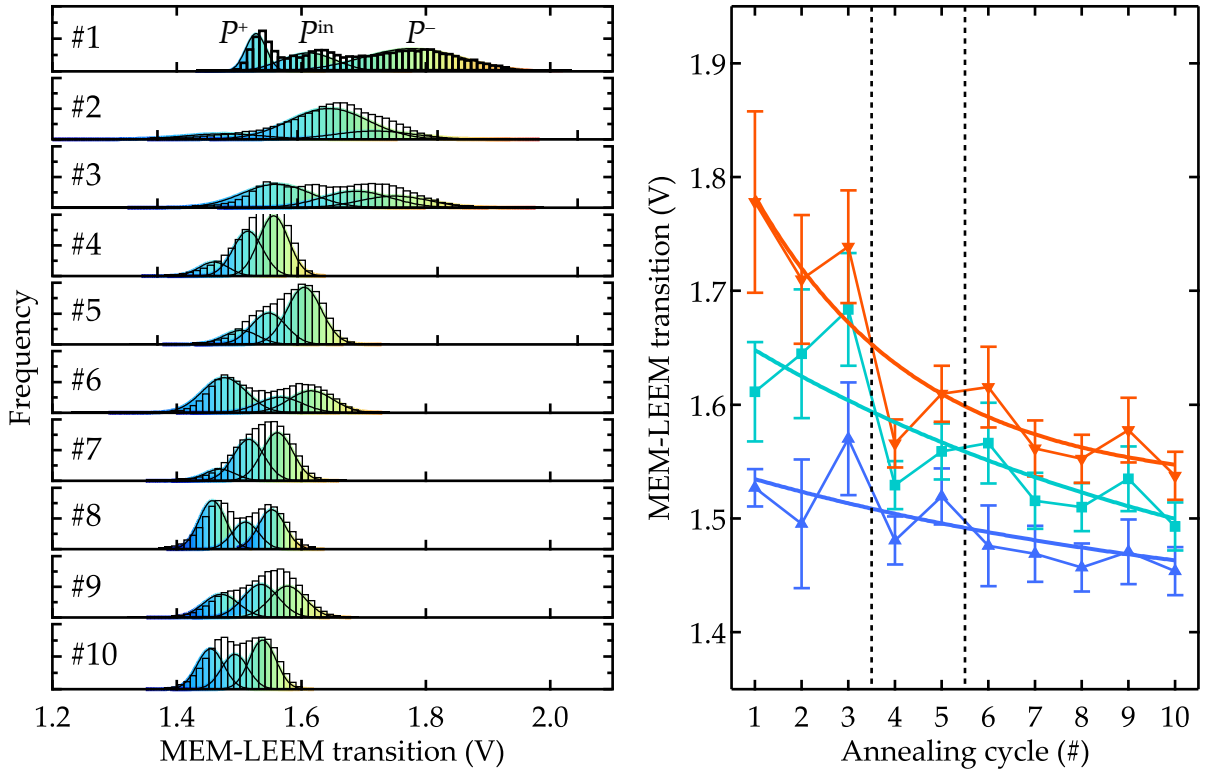


**(a)** MEM-LEEM transition histograms **(b)** MEM-LEEM transition values

**Figure 4.8.:** (a) Histograms of the MEM-LEEM transition values extracted from the MEM-LEEM transition maps shown in Fig. 4.7. Each histogram is fitted with three Gaussian peaks corresponding to $P^-$, $P^{in}$ and $P^+$ domains. (b) MEM-LEEM transition values, $\phi^-$, $\phi^{in}$ and $\phi^+$, for each ferroelectric domain, as a function of annealing cycle iterations.

potential of $P^{in}$. $\phi^+$ decays the least rapidly. The three surface potential values reach a plateau region after annealing cycle #7, with the following values $\phi^- = 1.58\,V$, $\phi^{in} = 1.52\,V$ and $\phi^+ = 1.46\,V$.

Assuming that the main result of ultrahigh vacuum annealing at 650 °C is the creation of oxygen vacancies, the results show a stronger influence of such defects on the surface potential of $P^-$ domain than on other domain types. The observations can be interpreted as a stabilization of $P^-$ surface polarization at regions with higher oxygen vacancy concentration. Since $P^-$ domains are negatively charged with strong inwards pointing dipoles (i.e. oxygen atoms displaced relatively more outwards than the neighboring cations), surface rumpling enhancement and polarization charge compensation in the vicinity of the vacancy sites could explain the observed results. With the increase of the oxygen vacancy concentration, upon cooling through the Curie temperature from the paraelectric phase, domains could order such that $P^-$ surface polarization is more stabilized, as manifested by an observed stronger surface potential change. However, this measurement does not allow to quantitatively verify

this interpretation, which suggests that the increase of oxygen vacancy concentration increases the amount of $P^-$ domains. This would require additional measurements, such as mapping the domain ordering on many different regions of the surface, after each annealing cycle, allowing to quantitatively measure the $P^-/P^+$ ratio as a function of oxygen vacancy concentration. Nevertheless, these experimental preliminary results echoes to some extent with the first-principles calculations presented in section 4 in chapter III which predict that oxygen vacancies are more stable in the $P^-$ region of the $BaTiO_3(001)$ surface, along with previous LEEM and DFT calculations [86].

## 2.2. Domain ordering from threshold photoemission

The sample was prepared by three cycles of Argon ion sputtering (at 500 eV for 10 minutes) and ultrahigh vacuum annealing at 650 °C for 30 minutes, followed by a vacuum annealing at 700 °C for 30 min, at a base pressure of $2 \times 10^{-8}$ mbar. The oxygen stoichiometry was altered by the ultrahigh vacuum annealing cycles. Therefore vacuum annealing with oxygen partial pressure $6 \times 10^{-6}$ mbar was then performed to partially recover the oxygen stoichiometry. Before and after the annealing under oxygen partial pressure, the surface displayed $(1 \times 1)$ ordering in low-energy electron diffraction [94], characteristic of a well ordered BaO terminated surface. Using PEEM, we have first characterized the domain ordering at the $BaTiO_3(001)$ surface, by means of threshold photoemission image series. Then, micro-spectroscopy has been performed on different ferroelectric domains, giving insight into the surface chemistry. Finally, we have investigated the polarization dependent surface band structure with linear dichroism using the *k*-PEEM imaging mode.

Figure 4.9a depicts the $BaTiO_3(001)$ surface imaged by PEEM at $E - E_F = 3.3$ eV, i.e. near the photoemission threshold, using a mercury discharge lamp ($h\nu = 4.9$ eV). Three levels of intensity can be distinguished. Regions $\sim 10$ µm wide with alternating bright and dark intensity along the [100] direction can be identified. We label $A$ and $B$ two of these regions (marked by dashed rectangles). Finer structures inside the regions can be observed, of typical size $\sim 500$ nm, displaying an intensity intermediate to that of the main $A$ and $B$ stripe domains. The fine zones of bright, intermediate and dark intensity are labeled 1, 2 and 3 and are present in the two main $A$ and $B$ regions in different proportions (marked by solid rectangles). The contrast observed at the photoemission threshold results from the different surface charge as a function of ferroelectric domain orientations.

We have acquired an image series from 2.5 eV to 5.0 eV, with 0.025 eV step. Similar to the LEEM experiment, the resulting image series consists in a 3D data set $I(x, y, E -$

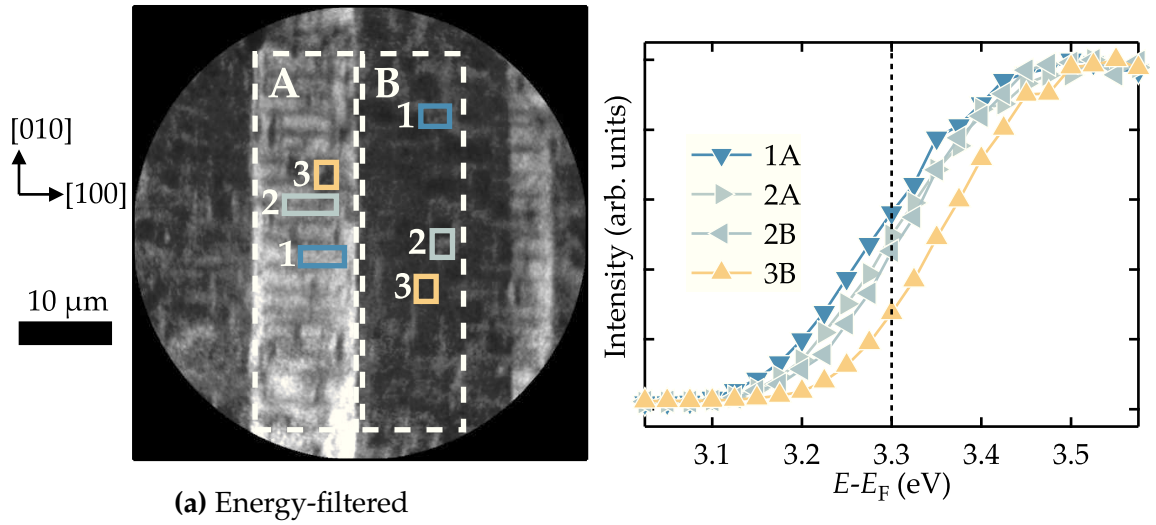


**(a)** Energy-filtered PEEM image

**(b)** Photoemission spectrum

**Figure 4.9.:** (a) Photoemission threshold image at $E - E_F = 3.3\,eV$ acquired with $h\nu = 4.9\,eV$ (Hg lamp). (b) Photoemission threshold spectra extracted from characteristics regions delimited by the colored rectangles drawn and labeled on left-hand side image. The dashed line corresponds to the energy at which the PEEM image was acquired.

$E_F$) which combines spatial and spectroscopic information. From this image series, we can extract, from a region of interest $(x, y)$, the intensity as a function of kinetic energy. Figure 4.9b shows the intensity $I(E - E_F)$ extracted from zones 1, 2 in region $A$ and zones 2, 3 in region $B$. Clear shifts of the photoemission threshold spectra illustrate changes in the local work function. The lowest kinetic energy arises from zone $1A$, as shown by the leftmost intensity curve (downward, blue triangles). The $1B$ spectrum (not shown) is almost identical to the $1A$. The photoelectron spectrum from zone 2 is also plotted, now for both regions $A$ and $B$. Both curves are superimposed, suggesting identical work function from regions $2A$ and $2B$. Region $3B$ corresponds to the surface areas with the highest threshold value (upward, orange triangles), corresponding to the highest local work function observed. The $3A$ photoemission spectrum (not shown) is identical to the $3B$.

Since the surface charge distribution modulates the work function, from the above different photoemission threshold values, ferroelectric domain can be identified. It has been shown that negative (positive) surface charge decreases (increases) the work function, shifting the photoemission threshold to lower (higher) values [183]. If the surface is neutral, the work function is intermediate. Therefore, zones 1, 2 and 3 can be attributed to ferroelectric domains $P^-$, $P^{in}$ and $P^+$, respectively.

By fitting the photoemission threshold spectra $I(E - E_F)$ for every pixel $(x, y)$ in the field of view using the error function, analogous to that used for the LEEM

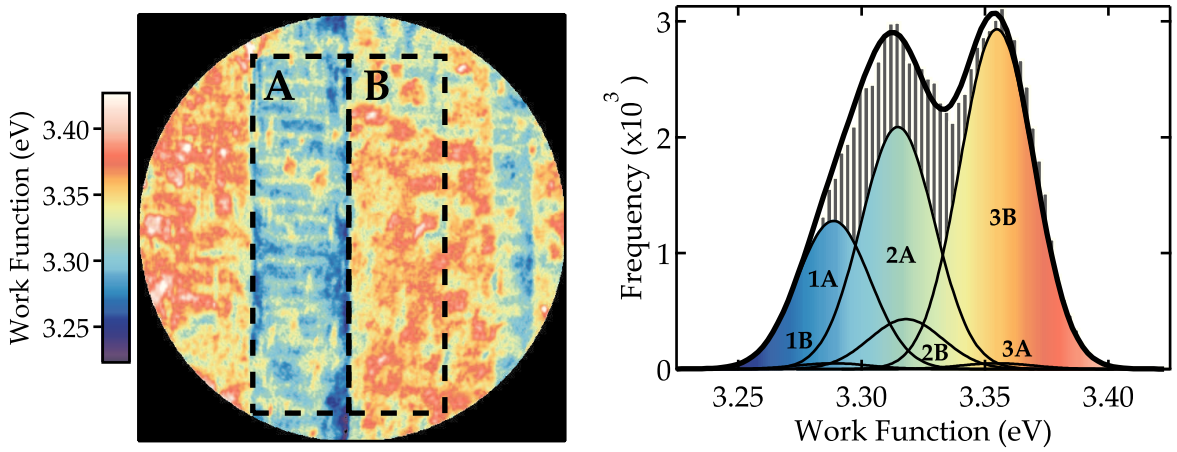


**(a)** Map **(b)** Histogram

**Figure 4.10.:** (a) Work function map of the $BaTiO_3$(001) surface generated from pixel by pixel fits of the threshold image series acquired with photon energy $h\nu = 4.9\,\text{eV}$ (Hg lamp). (b) Histogram of the work function values extracted from the dashed rectangular region displayed on the map, fitted with Gaussian functions with full width at half maximum 35 meV, giving a standard deviation of $\pm 15\,\text{meV}$.

experiment [183], a map of the local work function can be generated. Figure 4.10a shows such work function map. The fine structures (labeled 1, 2 and 3 in Fig. 4.9a) corresponding to $P^-$, $P^{\text{in}}$ and $P^+$, with different work function values are clearly visible within regions $A$ and $B$ (delimited by the dashed rectangles). Quantitative analyses can be performed by analyzing the work function distribution over the regions of interest $A$ and $B$. The histogram of the work function values extracted from the total delimited area is plotted in Figure 4.10b. The data are represented by the gray bars and fitted by Gaussian functions in order to measure the frequency distribution of the distinct work function values in each region.

In regions A and B, the presence of the three polarization directions and therefore three values of surface charge are confirmed. Region $A$ contains mainly $P^-$ ($1A$ peak at $3.290 \pm 0.015\,\text{eV}$) and $P^{\text{in}}$ ($2A$ peak at $3.320 \pm 0.015\,\text{eV}$) polarized domains. A very small contribution of $P^+$ ($3A$ peak at $3.360 \pm 0.015\,\text{eV}$) can be measured. Conversely, region $B$ is mainly composed of $P^+$ and $P^{\text{in}}$ domains, with a negligible proportion of $P^-$ domain.

The overall domain ordering consists of fine in-plane $P^{\text{in}}$ domains embedded in out-of-plane polarized domains. The $P^-$ rich domain (region $A$) contains a large proportion of in-plane substructures, relatively more than in the $P^+$ rich neighboring stripe domains (region $B$). The proportion of domain of opposite out-of-plane polarization inside both $P^-$ and $P^+$ is very small. The relative frequency of the three work function values attributed to the different surface domain polarization directions are given in table 4.1, in percentage for both regions $A$ and $B$.

| | work function | A | B |
|---|---|---|---|
| $P^-$ | $3.29 \pm 0.15$ eV | 96 | 4 |
| $P^{in}$ | $3.32 \pm 0.15$ eV | 83 | 17 |
| $P^+$ | $3.36 \pm 0.15$ eV | 2 | 98 |

**Table 4.1.:** Relative proportion of the different work function values for $P^-$, $P^{in}$ and $P^+$ surface domain polarization distributed in region $A$ and $B$, extracted from the histogram of Fig. 4.10b.

Micro-spectroscopy performed on these two domains brings further insight into the chemical and electronic structure differences of regions $A$ and $B$.

## 2.3. Polarization dependent chemistry

Figure 4.11 shows PEEM images with an iris (field aperture) positioned in the first image plane. In Fig. 4.11a, both $A$ and $B$ regions are visible. In Fig. 4.11a, the iris is almost fully closed to select photoelectrons only from one of the two domains (region $A$ or $B$ for instance). In the first case, the large illumination area of the Hg lamp allows to adjust the sample position in order to close the iris on a desired surface area. Once the sample position and iris size are adjusted, the synchrotron beam with photon of selected energy is directed onto the sample surface. The position of the micro-focused photon beam is adjusted to match the position of the iris on the desired surface region. The surface area delimited by the iris is $\sim (10 \times 10)$ µm$^2$ corresponding to the photon beam size on the NanoESCA beamline.

Figure 4.12 presents the core level spectra acquired from regions $A$ and $B$, with photon energy $h\nu = 650$ eV. Oxygen 1$s$, titanium 2$p_{3/2}$ and barium 4$d$ core levels were acquired in both regions $A$ and $B$. Hudson et al. [184] measured the corresponding bulk $BaTiO_3$ core level binding energies as 530.3 eV, 459.0 eV and 90.9 eV, respectively. The spectra were treated firstly with secondary electron background reduction using a Shirley procedure [185]. This procedure cancels the contributions of the secondary electrons which are larger in the vicinity of the probed core levels (at higher binding, or equivalently lower kinetic energy). The more electrons are excited by the photon (i.e. the photoemission process of a core level), the more electrons are likely to be scattered and form a secondary electron background. Voigt functions, which are convolution between Gaussian and Lorentzian functions were used to fit the photoemission peaks. The Lorentzian function accounts for the lifetime broadening of the probed electronic state, whereas the Gaussian function accounts for both vibrational phonon broadening and the finite instrumental energy resolution. The fitted components are represented by the solid gray shapes. The total fitted lines are represented with solid black lines.

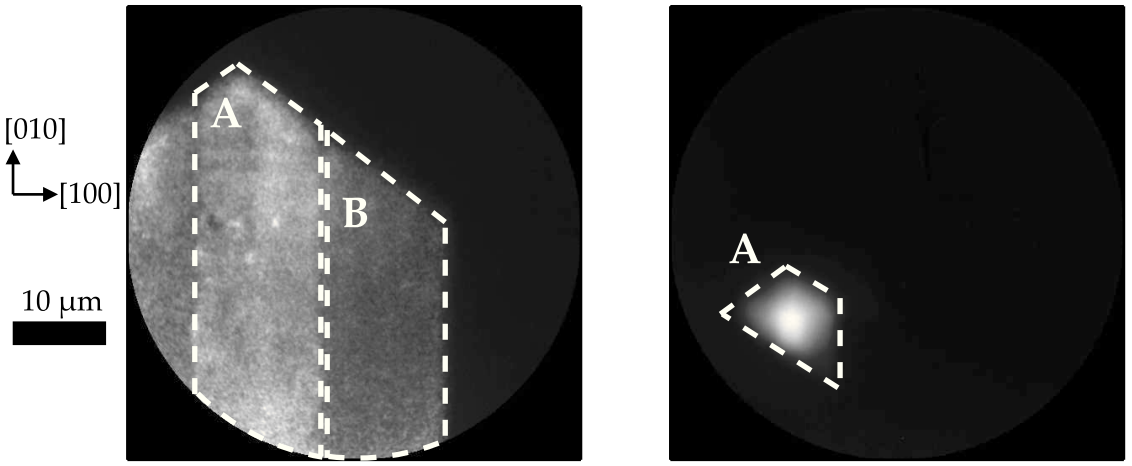


**(a)** Iris partly closed $h\nu = 4.9\,\text{eV}$

**(b)** Iris closed on region $A$ $h\nu = 650\,\text{eV}$

**Figure 4.11.:** PEEM images of (a) regions $A$ and $B$ partly covered by the iris halfway closed illuminated with Hg lamp and (b) region $A$ selected by the closed iris illuminated with the synchrotron beam of size comparable to that of the iris.

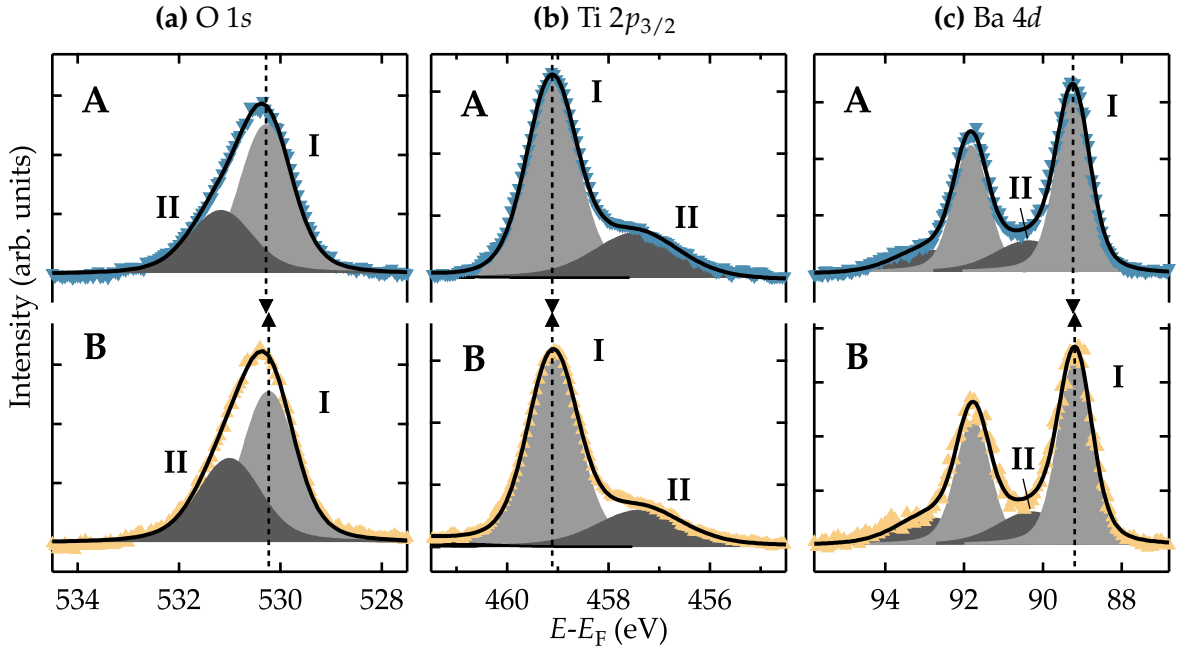


**Figure 4.12.:** Core levels microspectroscopy spectra acquired on regions A and B through an iris, of (a) oxygen 1$s$, (b) titanium $2p_{3/2}$ and (c) barium 4$d$. The photon energy is $h\nu = 650\,\text{eV}$.

The O 1$s$ and Ba 4$d$ from region $A$ are shifted 50 meV towards higher binding energy compared to those from region $B$. For Ti 2$p$, the shift is zero. Since the photoemission signal collected from regions $A$ and $B$ arises from both in-plane and out-of-plane polarized domains, the 50 meV shift could be attributed to the average of the thresh-

old differences. However, the energy resolution of the experiment which combines the resolution of the analyzer ($\delta_S \approx 200$ meV) and the bandwidth of the monochromatic photon source (BW $\approx 200$ meV), is estimated[5] at 280 meV. The observed core levels shifts cannot therefore be unambiguously related to the local differences in polarization.

For O 1*s* presented in Fig. 4.12a, two peaks can be identified. For region *A*, at low binding energy (LBE), the main peak labeled $O_I$ is found at $530.28 \pm 0.50$ eV. At high binding energy (HBE), the component $O_{II}$ is found at $531.15 \pm 0.60$ eV. $O_I$ is attributed to oxygen atoms coordinated in the perovskite structure [184,186]. $O_{II}$ can be assigned to oxygen atoms coordinated within hydroxyl or carbonate species such as $Ba(OH)_2$ or $BaCO_3$, as previously reported [186–188]. In a study of water adsorption performed on similar $BaTiO_3$ single crystals, Wang et al. [189] reported grazing angle photoemission analyses showing HBE components strongly enhanced compared to normal angle acquisition. Therefore the observed $O_{II}$ component can be attributed to oxygen atoms located closer to the surface, with different coordination numbers than in the bulk and subject to more residual water and carbonate contamination than in the bulk. The change of coordination numbers at the surface and the presence of residual adsorbates explain the energy shift which allows to distinguish photoemission arising from bulk or surface atoms. The relative intensity of component $O_{II}$ with respect to the total O 1*s* yield is 0.29 and 0.35 for *A* and *B* regions, respectively. Hence, in region *B*, a larger contribution of surface oxygen atoms is observed.

The Ti $2p_{3/2}$ core level spectrum is shown in Fig. 4.12b. Peak I is found at $459.1 \pm 0.5$ eV and shows a well defined shoulder, labeled II, at lower binding energy at $457.4 \pm 0.8$ eV. These two components separated by $\sim 1.7$ eV for both *A* and *B* regions are characteristic of distinct oxidation states of Ti cations in ionic perovskite $BaTiO_3$ [190]. In stoichiometric conditions within the tetragonal phase, Ti are 6-fold coordinated in an oxygen octahedron with a formal +4 oxidation state. Electron donor defects such as oxygen vacancies $V_O^{\bullet\bullet}$ can reduce the oxidation state of neighboring $Ti^{4+}$ atoms [84], according to equation $2\,Ti_{Ti}^{\times} + O_O^{\times} \rightarrow 2\,Ti_{Ti}' + V_O^{\bullet\bullet} + \frac{1}{2}\,O_2\,(g)$ (Kröger-Vink notation [191] is used[6]). $Ti^{3+}$ is less electronegative than $Ti^{4+}$, resulting in a core level shift towards lower binding energy. Estimation of the donated electron concentration,

[5] The energy resolution is given by $\Delta E = \sqrt{\delta_S^2 + BW^2}$.

[6] The lattice site, e.g. Ba, Ti, O or vacancy V is replaced by a point defect species indicated in index; the relative charge between the lattice site and the defect is indicated by $'$ or $\bullet$ for negative and positive formal charge, respectively

expressed in electron per unit cell ($e$/u.c.) can be calculated, as follows:

$$n = \frac{I(\mathrm{Ti}^{3+})}{I(\mathrm{Ti}^{4+}) + I(\mathrm{Ti}^{3+})},$$

where $I(\mathrm{Ti}^{3+})$ and $I(\mathrm{Ti}^{4+})$ are the intensity of the $\mathrm{Ti}^{3+}$ and $\mathrm{Ti}^{4+}$ peaks.

Assuming a simple charge-transfer of 2 electrons per oxygen vacancy to neighboring Ti ions [192], the number of oxygen vacancies is equal to $\frac{1}{2}$ the number of reduced $\mathrm{Ti}^{3+}$ ions. In stoichiometric $BaTiO_3$, the number of oxygen ions is equal to 3 times the total number of Ti ions. Therefore, in $BaTiO_{3(1-x)}$, the oxygen vacancy concentration $x$ can be estimated from the photoemission intensities as follows:

$$x = \frac{\frac{1}{2}[\mathrm{Ti}^{3+}]}{3\left([\mathrm{Ti}^{4+}] + [\mathrm{Ti}^{3+}]\right)} = \frac{n}{6}$$

The presence of oxygen vacancies in $BaTiO_3$ corresponds to an effective $n$-type doping [82, 83]. The electrons and more moderately holes (donated electrons and oxygen vacancies) confer thermally activated conductivity in $BaTiO_3$. Assuming an accuracy of 5 % in the photoemission intensity measurements $I(\mathrm{Ti}^{3+})$ and $I(\mathrm{Ti}^{4+})$, the electron doping concentration $n$ calculated from $A$ and $B$ micro-spectra is estimated[7] at $0.184 \pm 0.012$ e/u.c and $0.158 \pm 0.010$ e/u.c, respectively. From the micro-spectroscopy measurement, the oxygen vacancy concentration $x$ is estimated at $3.07 \pm 0.03$ % in region $A$ and $2.64 \pm 0.03$ % in region $B$. In other words, the oxygen vacancy concentration is estimated $14.01 \pm 0.06$ % higher in region $A$ than in region $B$. Note that a possible artifact could reside in the effect of the synchrotron beam on the surface which can change the oxygen vacancy concentration by heating, inducing oxygen desorption. To circumvent this issue, we have used the same acquisition times in both $A$ and $B$ regions, to prevent differential change of the oxygen vacancy concentration that could be induced by the beam. Therfeore, this result suggests stronger interaction between surface oxygen vacancies and $P^-$ surface polarization which is dominant in region $A$ and echoes back to the results obtained from LEEM and first-principles calculations.

## 2.4. Surface polarization and band structure

We have used photoemission linear dichroism to investigate further the ferroelectric state in regions $A$ and $B$. The combination of spectroscopic and angular resolution of the PEEM allows probing the electron dispersion relation $E_B(\vec{k}_{||})$, that is the surface

[7] The uncertainty on $n$ and $x$ write $\delta n = n\sqrt{\left(\frac{\delta I(\mathrm{Ti}^{3+})}{I(\mathrm{Ti}^{3+})}\right)^2 + \left(\frac{\sqrt{(\delta I(\mathrm{Ti}^{3+}))^2 + (\delta I(\mathrm{Ti}^{4+}))^2}}{I(\mathrm{Ti}^{3+}) + I(\mathrm{Ti}^{4+})}\right)^2}$ and $\delta x = x\,\frac{1}{6}\,\frac{\delta n}{n}$.

band structure. The field aperture is used to select a region of interest (e.g. region $A$ and $B$, distinctly).

With linear dichroism, both orbital and structural symmetry of the surface can be probed [193, 194]. We have used vertically (VP) and horizontally (HP) polarized light. The light polarization is defined with respect to the scattering plane which is the plane that contains the axis of the incident photons and the surface normal. In other words, VP corresponds to $p$ polarized light while HP corresponds to $s$ polarized light. The geometry of the experiment is given in Figure 4.13.

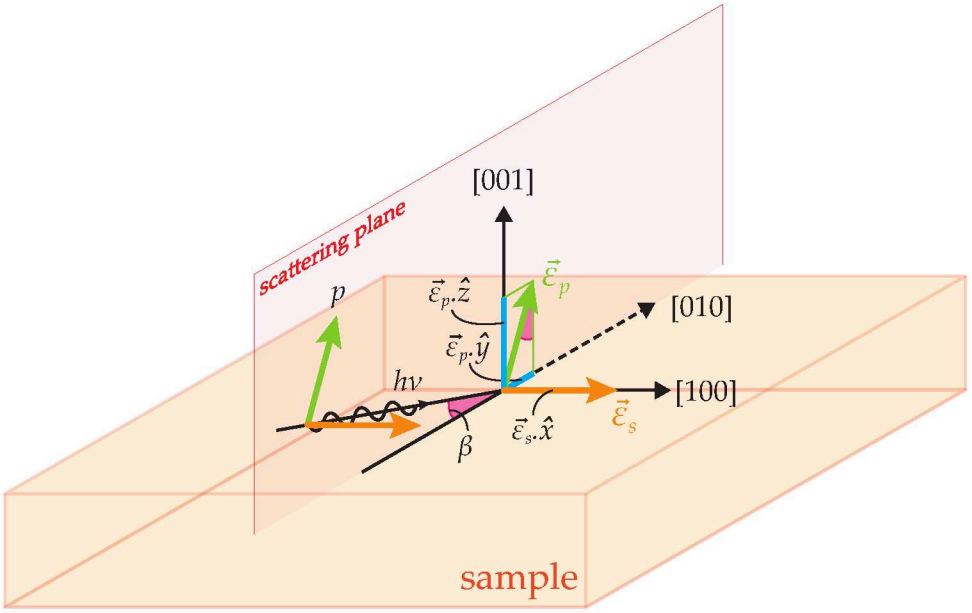


**Figure 4.13.:** Schematic of the incident light and polarization angle with respect to the crystallographic sample directions. The plane that contains the incident light axis and the surface normal is the scattering plane (red). $p$ and $s$ polarized light (i.e. parallel and perpendicular to the scattering plane) are described by vectors $\vec{\varepsilon}_p$ and $\vec{\varepsilon}_s$. $\vec{\varepsilon}_p$ has projections along $y$ and $z$ directions. $\vec{\varepsilon}_s$ is projected along $x$. Light angle of incidence is $\beta = 25°$ with respect to the surface normal.

Since the light is incident with an angle $\beta = 25°$ with respect to the surface plane, the projection of the VP polarization onto the sample is $\cos 25° = 0.91$ along the [001] direction and $\sin 25° = 0.18$ along [010]. Therefore, the projection of VP light along the [001] direction is 47 % larger than along [010]. HP light polarization is 100 % projected along the [100] axis.

**Electronic structure:**

We first investigate the integrated intensity $I(E - E_F) = \int\int I(k_x, k_y, E - E_F)\mathrm{d}k_x\mathrm{d}k_y$ from image series acquired at the valence band ($E - E_F$ from $-1$ eV to 10 eV with a 0.025 eV step). The data were acquired specifically on region $A$ and $B$, using the iris, and vertical light polarization, with a photon energy $h\nu = 50$ eV and vertical light

polarization. The resulting integrated intensity gives the valence band spectra of region $A$ and $B$.

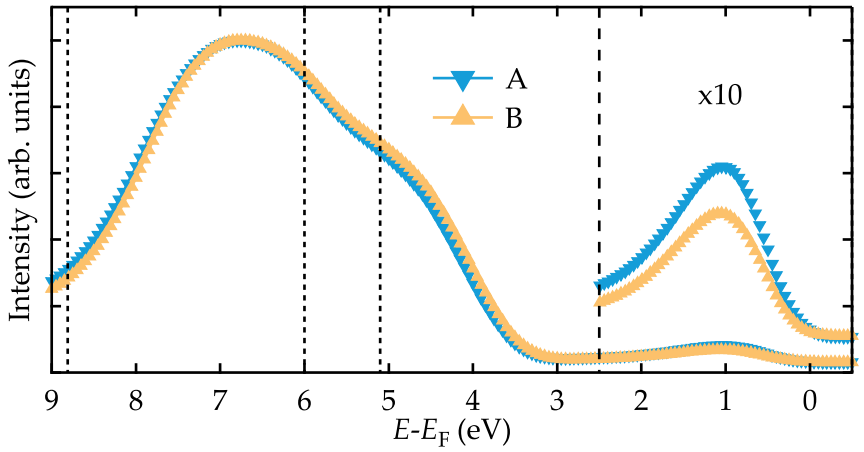


**Figure 4.14.:** Valence band from region A (blue, downward triangles) and B (orange, upward triangles), selected by an iris positioned in the first image plane. Gap states 1 eV below the Fermi level are magnified $\times 10$. The thin vertical dotted lines indicate the position of the constant energy cut shown in Fig. 4.15.

Figure 4.14 shows the valence band spectra for both $A$ and $B$ domains. The spectra have been normalized to the highest intensity reached at $E - E_F = 6.75\,\text{eV}$. In the inset from 2.5 eV to $E_F$, the intensity is magnified by a factor 10. A 50 meV energy shift can be seen between the two spectra, that of region $A$ being shifted towards higher binding energy. This follows threshold differences observed between $A$ and $B$ domains on Fig. 4.9b, also impacting core levels, except for Ti $2p_{3/2}$, in Fig. 4.12. Note that this energy shift is below the energy resolution of the experiment, estimated at 280 eV. The valence band maximum (VBM) obtained with the tangent at the valence band edge is, in average between regions $A$ and $B$, at $E - E_F = 3.45\,\text{eV}$. At $\sim 1\,\text{eV}$ below the Fermi level, a broad peak can be observed in both spectra. The electronic states in the gap correspond to the relatively localized electrons donated by the oxygen vacancies, reducing Ti atoms by filling Ti $3d$ orbitals. The observation of filled states in the gap close to the Fermi level confirms the $n$ type doping of the sample, induced by the oxygen vacancies. However, the carriers show a rather localized character.

The intensity of the gap states is $17.20 \pm 1.22\,\%$ higher for region $A$ compared to region $B$. In parallel to the Ti core levels micro-spectroscopy, the gap states confirm the higher concentration of oxygen vacancies in region $A$ ($P^-/P^{\text{in}}$) than in region $B$ ($P^{\text{in}}/P^+$).

Oxygen vacancies are therefore preferably found on $P^-$ polarized surface regions as shown by the higher in-gap electronic states signal arising from the excess electrons. The relative increase of oxygen vacancy in regions dominated by $P^-$ polarization

found from (i) Ti $2p$ core level micro-spectroscopy is $\sim 14\,\%$ and from (ii) the in-gap states, i.e. the states associated to the filling of Ti $3d$ states, is $\sim 17\,\%$. These results provide complementary evidence for polarization dependent chemistry stating that oxygen vacancies are preferentially found on surface with $P^-$ regions, as predicted by the first-principles calculations presented in section 4 of chapter III.

These results bring further evidence of an interplay between surface inwards polarization $P^-$ and oxygen vacancies, as obtained from LEEM and from first-principles calculations.

**Reciprocal space imaging: surface electron dispersion:**

Figure 4.15 shows the angular resolved images ($I(k_x, k_y, E - E_F)$) of valence electrons obtained with vertical and horizontal light polarization of energy $h\nu = 50\,\text{eV}$. As the $k$-PEEM images obtained for regions $A$ and $B$ show the same tendency, for both light polarization directions, we only present the results for region $A$. These $k$-PEEM images correspond to constant energy cuts of the valence band spectrum for region $A$, presented in Fig. 4.14.

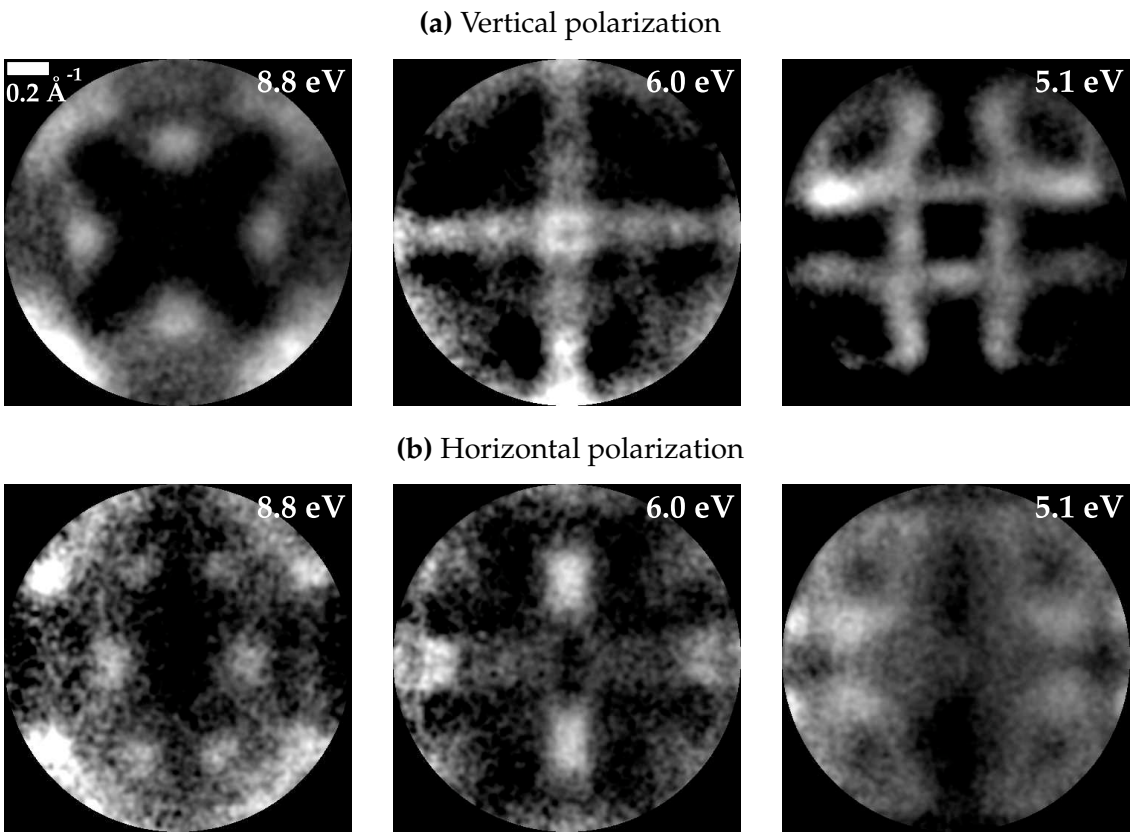


**Figure 4.15.:** Electron dispersion in the $(k_x, k_y)$ plane for different energies, as obtained from interactions with photons (a) vertically and (b) horizontally polarized with respect to the sample surface. The orientation of the images is the same as that in Fig. 4.6c.

For VP light (Fig. 4.15a), the surface dispersion in the $(k_x, k_y)$ plane shows four-fold symmetry ([100], [010], [110] and $[\bar{1}10]$ symmetry axes), whereas for HP light (Fig. 4.15b), two-fold symmetry is observed (from [100] and [010] axes).

The interaction of polarized light with the sample obeys rules of symmetry which depends on the structure of the material and geometry of the photoemission experiment [195]. The photoemission intensity is proportional to the square modulus of the dipole matrix element $|\langle\vec{K}|\hat{\varepsilon}\cdot\hat{k}|\vec{k}\rangle|^2$ (where $\hat{\varepsilon}$ and $\hat{k}$ are unitary vectors directed along the light polarization and the initial state wave vector inside the material, respectively). Since the symmetry of the real space lattice imposes the symmetry of the reciprocal space lattice, we can expect from $k$-resolved photoemission to give insights into the symmetry of the real space lattice [194]. Therefore, we would expect $p$-polarized light (VP, whose projection along [001] is 47 % larger than along [010]) to highlight lattice distortions mostly associated with off-center displacements along the [001] axis while $s$-polarized light (HP, 100 % parallel to [100]) should be sensitive to lattice distortions associated to off-center displacements along the [100] direction (i.e. perpendicular to the scattering plane) [196]. The four-fold symmetry observed using VP light confirms the presence of out-of-plane ferroelectric polarization, parallel to [001]. Using HP light, two-fold symmetry is consistent with the presence of in-plane ferroelectric polarization along the [100] directions.

In the case where the scattering plane is a mirror plane for the system, the dipole matrix element $|\langle\vec{K}|\hat{\varepsilon}\cdot\hat{k}|\vec{k}\rangle|^2$ translating the photon interaction with the bound initial electron must be even with respect to the scattering plane [170, 195], for the photoemission process to be allowed. In our experiment geometry, the scattering plane is a mirror plane for the $p$-polarized light vector, which has no component perpendicular to the scattering plane and is therefore even under reflection with respect to it. The initial state wave vector $\vec{k}$ must therefore also be even under reflection with respect to the scattering plane, for the overall dipole matrix element to be even. The symmetry of the lattice with polarization $P^+$, $P^-$ and $P^{\text{in}}$ with polarization along [010], which we denote as $P^{\text{in}}_{[010]}$, verifies this condition on $\vec{k}$.

Conversely, if a mirror plane is perpendicular to the scattering plane, as is the case for the lattice with ferroelectric polarization along [100] where $\vec{k}$ has odd symmetry with respect to the scattering plane, the photoemission process is allowed if and only if $\hat{\varepsilon}\cdot\hat{k}$ has also odd symmetry under reflection with respect to the scattering plane. This case is fulfilled for $s$-polarized light, which is even under reflection with the (100) plane that is a mirror plane for the electronic states in lattices polarized along [100], and odd with respect to the scattering plane. Hence, with HP light, the electronic states with odd symmetry with respect to the scattering plane can be probed, i.e. in

lattice with $P^{in}_{[100]}$ polarization (therefore $|\hat{\varepsilon}\cdot\hat{k}\,|\vec{k}\rangle$ has even symmetry with respect to the scattering plane).

The combinations of even/odd parity, denoted as "+" and "−" respectively, for the two incident light polarization directions and the ferroelectric polarization are given in Table 4.2.

| | $P^+$ | $P^-$ | $P^{in}_{[100]}$ | $P^{in}_{[010]}$ |
|---|---|---|---|---|
| $p$ (VP) | $+^{(*)}$ | $+^{(*)}$ | − | $+^{(**)}$ |
| $s$ (HP) | − | − | + | − |

$^{(*)}$ 72 % and $^{(**)}$ 28 % of the photoemission intensity

**Table 4.2.:** Parity of the dipole matrix element with respect to the scattering plane defining the allowed and forbidden photoemission processes in our photoemission geometry."+" and "−" denotes even and odd parity.

Based on these symmetry rules, the four-fold symmetry observed from the out-of-plane polarized domains arises from the fact that (100), (010), (110) and $(\bar{1}10)$ are mirror planes for $P^+$ and $P^-$ domains at the (001) surface. The two-fold symmetry observed using HP light, with light polarization along [100], is due to the fact that only (010) is a mirror plane for the domains polarized along [100].

The small projection of VP polarized light onto the [010] direction (28 % of the total VP polarization vector) should give rise to a component arising from in-plane polarized domains, giving two-fold symmetry dispersion in the band structure, which we do not observe. The larger (72 %) component of the light polarization vector parallel to [001], gives larger sensitivity to out-of-plane domains oriented along [001], which has four-fold symmetry around this axis. The subsequent four-fold symmetry dispersion apparently dominates the signal which arises from the fine neighboring in-plane polarized domains.

Using linear X-ray dichroism with real space PEEM on $PbZr_{0.2}Ti_{0.8}O_3$ with a similar experimental photoemission geometry, Polisetty et al. [197] showed that the photoemission intensity is proportional to $1-\cos^2(\theta_{FE})$, where $\theta_{FE}$ is the angle between the incident light polarization and the ferroelectric polarization inside the material. In such case, the photoemission intensity is maximum for $\theta_{FE} = 90°$ and minimum for $\theta_{FE} = 0°$. Comparatively, our results suggest that the photoemission intensity is proportional to $\cos^2(\theta_{FE})$, as demonstrated by the values of $\cos^2(\theta_{FE})$ given in Table 4.3.

| | $P^+$ | $P^-$ | $P^{in}_{[100]}$ | $P^{in}_{[010]}$ |
|---|---|---|---|---|
| $p$ (VP) | 0.81 | 0.81 | 0.00 | 0.19 |
| $s$ (HP) | 0.00 | 0.00 | 1.00 | 0.00 |

**Table 4.3.:** Values of $\cos^2(\theta_{FE})$, with $\theta_{FE}$ the angle between the incident light polarization and ferroelectric polarization vectors, which modulate the photoemission intensity due to linear dichroism.

With this experiment, we show that linear dichroism in photoemission associated with band structure imaging can give insight into the polarization ordering at the surface of a ferroelectric.

# 3. Summary of the results

(i) Annealing cycles in controlled atmosphere allows to moderately change the oxygen vacancy concentration and hence the conductivity induced by the released excess electrons, while keeping the sample ferroelectric. This allows LEEM and PEEM to be used to investigate the surface properties of $BaTiO_3$ single crystals.

(ii) Comparative surface potential analyses performed by LEEM studies through annealing cycles on the $BaTiO_3$(001) surface of a single crystal confirmed the strong interplay between oxygen vacancies and $P^-$ polarization.

(iii) Work function analyses allowing characterization of surface polarization, associated with local micro-spectroscopy measurements, performed by PEEM further confirmed these observations. The signature of increased excess electrons was measured in the increased concentration of $Ti^{3+}$ and in-gap states, at the surface of $P^-$ domains.

(iv) Photoemission linear dichroism was used to image the full surface electronic structure with $k$-PEEM. Surface polarization can be characterized by the band dispersion. Indeed, the domain polarization orientation can be determined by considering the dipole matrix elements involving the experimental geometry and the sample symmetries.

# Chapter V.

# Discussion

## 1. Domain ordering and screening of the depolarizing field

### 1.1. Efficiency of domain ordering as a screening mechanism

In this work, we have simulated polarization perpendicular to the $BaTiO_3$(001) surface by ordering the slab into domains with opposite polarization. As described in section 5.3.1 of chapter III, the system displays a ferroelectric instability in each domain, but is non polar as a whole. The supercell carries an electric quadrupole which results in a zero dipolar moment. Inside the slab, a very small residual difference of macroscopic potential ($\sim 0.3$ eV) has been found, attesting that the depolarizing field is negligible in the domains. At the surface, the periodic ordering of charge density results in an electric field with short-range decay in the vacuum (see section 3.7.2). The vacuum thickness has been varied to check that periodic images of the slab can be considered isolated (see section 6.3). Moreover, polarization field flux-closures (even closure domains) are predicted, participating to the overall reduction of the electrostatic energy. All these results highlight the efficiency of domain formation in the screening of the depolarizing field.

### 1.2. Slab termination dependent critical thickness

In the free-standing slabs we have studied, the domain formation is the only way the system has to screen the depolarizing field. In other words, there is neither external nor internal screening. However, at small thicknesses, this is not sufficient, and the price to pay to stabilize out-of-plane polarization in these ultrathin free-standing $BaTiO_3$(001) slabs is the application of large compressive in-plane strain. With in-plane compressive

strain as high as −3.8 %, polarization perpendicular to the surface could develop in BaO-terminated slabs as thin as $L = 7$ atomic layers (i.e. 1.2 nm) and from $L = 9$ atomic layers (i.e. 1.6 nm) in $TiO_2$-terminated slabs. These results suggest the presence of a critical thickness below which the polarization vanishes in free-standing slabs ordered in domains for a given in-plane strain. To further investigate this effect, we present in Figure 5.1 the average polarization magnitude $\langle P \rangle$ in one domain for all studied slab thicknesses ($L = 3$ to 13 atomic layers i.e. 0.4 nm to 2.5 nm) in the high compressive strain regime ($a = 3.800$ Å to 3.850 Å i.e. −3.8 % to −2.5 % strain), for the $TiO_2$ and BaO surface termination (see section 3.5 of chapter III).

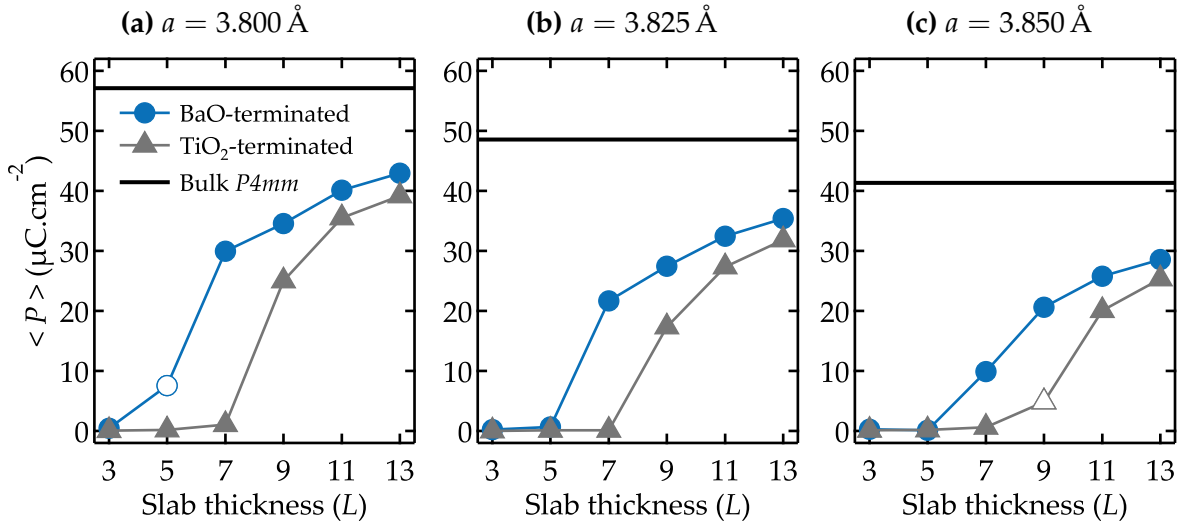


**Figure 5.1.:** Average domain polarization in $c$ phase as a function of slab thickness in the compressive strain regime, for the BaO (blue circles) and $TiO_2$ (gray triangles) terminations ($N = 2$ for $L = 3, 5, 7, 9$ and $N = 4$ for $L = 11, 13$). The $P4mm$ bulk polarization ($L \to \infty$) at the corresponding lattice constant is indicated as the solid black line. The empty markers ($L = 5$, BaO termination and $L = 9$, $TiO_2$ termination) indicate metastable $c$ phase configurations with nonzero polarization but with total energy equal to that of the $p$ phase within the numerical precision.

At the highest compressive strain (Fig. 5.1a, $a = 3.800$ Å i.e. −3.8 %) the onset of nonzero average polarization magnitude for the BaO and $TiO_2$-terminated slabs is $L = 7$ and $L = 9$ atomic layers with $\langle P \rangle = 30.0\,\mu C\,cm^{-2}$ and $25.0\,\mu C\,cm^{-2}$, respectively. With increasing slab thickness, $\langle P \rangle$ increases and tends to the bulk value calculated at the same compressive strain, $P = 57.1\,\mu C\,cm^{-2}$. The BaO-terminated slabs show larger average domain polarization magnitude compared to the $TiO_2$-terminated slabs, for all slab thicknesses. At the largest considered slab thickness ($L = 13$ atomic layers i.e. 2.5 nm), the polarization magnitude is $42.9\,\mu C\,cm^{-2}$ on average across the domain and peaks at $51.9\,\mu C\,cm^{-2}$ in the most inner unit cells of the slab. Comparatively, for the $TiO_2$-terminated slab, the average polarization is $39.2\,\mu C\,cm^{-2}$ in one domain and $P$ reaches $50.4\,\mu C\,cm^{-2}$ in the most inner unit cell.

With decreasing the in-plane compressive strain (Figs. 5.1b and 5.1c), the onset of nonzero polarization is shifted towards larger slab thickness for the $TiO_2$ termination, at $L = 11$ atomic layers for $a = 3.85$ Å (the case $L = 9$ at this in-plane strain is not considered since metastable) and the overall average polarization magnitude in one domain is lowered. However, the convergence towards the bulk polarization with increasing slab thickness is similar, and the BaO termination always shows higher average polarization amplitude than the $TiO_2$ one.

The in-plane compressive strain enhances the polarization magnitude in the thin slabs and can shift the apparent critical thickness, below which polarization vanishes, towards even lower values.

Critical thickness in ferroelectric slabs has been first reported by Junquera and Ghosez [50] for $BaTiO_3$ sandwiched between $SrRuO_3$ electrodes and estimated at 2.6 nm (6 unit cells). In their simulation, the free charges of the metallic electrodes provide screening of the depolarizing field. However, residual bound charges remained at the interface, generating a depolarizing field large enough to cancel the polarization at small thickness. Aguado-Puente and Junquera [106] showed that domain formation acts as a complementary screening mechanism to that provided by the $SrRuO_3$ electrodes: polarization perpendicular to the interface was maintained at lower thickness down to 1.8 nm and absence of macroscopic field inside the thin film was observed. This showed the efficiency of domain formation as a screening mechanism, allowing critical thickness to be reduced.

In lower dimension systems such as $BaTiO_3$ nanowires [39, 198], tensile strain applied along the polarization direction has been shown to enhance the polarization magnitude. These effects are comparable to the one we report here except that axial ferroelectricity in nanowires does not suffer from depolarizing effects, and shows in $BaTiO_3$(001) a strong interplay between elastic strain, nature of the surface termination and polarization.

Domain formation at the free surface is enough to provide sufficient screening of the depolarizing field and allows out-of-plane polarization to maintain, provided sufficient in-plane compressive strain is applied. However, a critical thickness below which polarization vanishes is observed and depends on the magnitude of the compressive in-plane strain and the surface termination. As long as sufficient screening of the depolarizing field is provided, strain as associated with lattice deformation acts as a driving force for ferroelectric polarization to develop and maintain.

## 2. Surface effects

At a free surface, chemical bonds are lacking and atomic coordination numbers decreased with respect to the underlying bulk. Our calculations have shown that the surface has strong impacts on the structure and on the ferroelectricity. These effects are reviewed and discussed hereafter.

### 2.1. Surface stress

The total energy of the slabs ($L = 9$ atomic layers, i.e. 1.6 nm) in the paraelectric $p$ and ferroelectric $c$ and $aa$ phases is plotted as a function of in-plane lattice constant in Figure 5.2 for both terminations. The energy minimum corresponds to the equilibrium in-plane lattice constant of the slab.

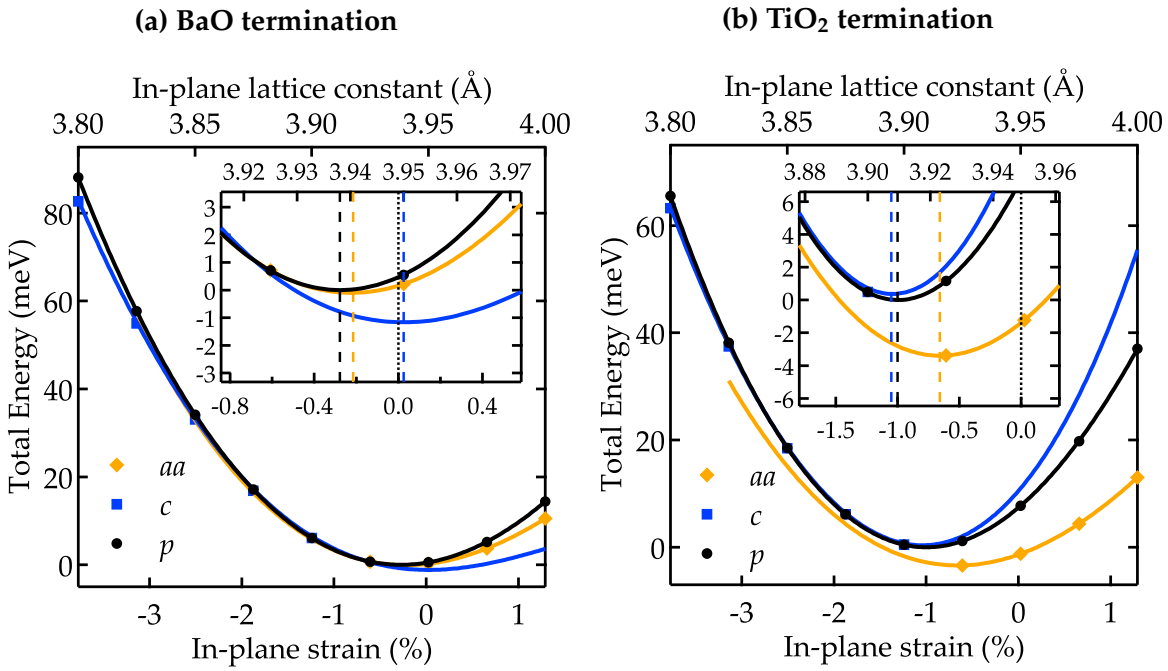


**Figure 5.2.:** Total energy (meV/u.c.) of the $p$, $c$ and $aa$ phases as a function of in-plane lattice constant $a$, for the (a) BaO and (b) $TiO_2$ terminations. The solid lines are guides for the eyes.

The zero of energy is positioned at the energy minimum of the $p$ phase. In each inset, the vertical black dotted line indicates the LDA equilibrium lattice constant of bulk cubic $BaTiO_3$. The vertical colored dashed lines indicate the energy minimum for each phase. In the case of the $TiO_2$ termination (Fig. 5.2b), the equilibrium lattice constant is shifted towards lower value ($\sim$ 3.91 Å for the $c$ and $p$ phases and $\sim$ 3.92 Å

for the *aa* phase). This is a direct consequence of the presence of the surface where interatomic bond lengths tend to shorten. The surface creates an extra stress tensor called surface stress which shifts the equilibrium lattice constant. Here, the shift is towards lower values, therefore the surface stress for the $TiO_2$ termination is tensile (at the bulk lattice constant), as the system is stabilized with in-plane compressive strain.

In contrast, for the BaO termination (Fig. 5.2a) the equilibrium lattice constant is $\sim 3.94$ Å for the *p* and *aa* phases, whereas the *c* phase is found unstressed at the bulk equilibrium lattice constant $a \approx 3.95$ Å.

Therefore the effect of surface stress appears significantly larger for the $TiO_2$ termination shifting the equilibrium in-plane lattice constant of the slabs by $\sim 0.04$ Å to 0.03 Å towards compressive strain, compared to almost zero shift for the BaO termination.

## 2.2. Surface termination and stability of ferroelectricity

The surface termination has an effect on the ferroelectric properties of the slabs in the *aa* and *c* phases. Here, we compare the results obtained for the ferroelectric systems (slabs in *aa* and *c* phase as well as bulk $Amm2$ and $P4mm$ structures), with respect to the paraelectric ones (slab in *p* phase as well as bulk $P4/mmm$ structure).

First, the ferroelectricity (in slabs, regardless of the termination, and in bulk) is enhanced by compressive strain if applied perpendicularly to the polarization direction (slab in *c* phase and bulk $P4mm$), and by tensile strain if applied parallel to the polarization direction (slab in *aa* phase and bulk $Amm2$) (see section 3.2 on page 64).

In the absence of the surface, i.e. for bulk systems, the transition between the ferroelectric $Amm2$ and $P4mm$ structures (as referenced to the paraelectric $P4/mmm$ structure) occurs at the LDA equilibrium lattice constant of bulk cubic $BaTiO_3$.

### 2.2.1. BaO termination

In the case of the BaO termination, the relative energy of the ferroelectric phases (*aa* and *c* phases with respect to *p* phase) is always found smaller (in absolute value) than the relative energy of ferroelectric bulk ($Amm2$ and $P4mm$ with respect to $P4/mmm$). Therefore, the presence of the BaO-terminated surface destabilizes ferroelectricity compared to bulk $BaTiO_3$ in all cases. Compressive strain is required for the different ferroelectric slabs to stabilize, since a transition $aa \rightarrow p$ is found at 0.5 % strain and $p \rightarrow c$ at $-1$ %. In other words, the BaO-terminated slabs are no longer found ferroelectric

from $-0.5\,\%$ to $-1\,\%$ compressive strain. Note, however that our simulations do not reproduce possible monoclinic *r* phases that could appear in this range of strain [139, 142].

### 2.2.2. $TiO_2$ termination

In the case of the $TiO_2$ termination, the *aa* phase is found more stable than bulk *Amm*2. The strong stabilization of polarization parallel to the $TiO_2$ surface has already been reported in $BaTiO_3$ surfaces [127] and nanowires [39, 198]. However, similarly to the BaO termination, polarization perpendicular to the surface in *c* phase is destabilized with respect to bulk *P*4*mm*. Therefore, the $TiO_2$ surface favors relatively much more in-plane polarization under tensile strain compared to out-of-plane polarization under compressive strain. Moreover, the *c* phase is further destabilized by the $TiO_2$ termination compared to the BaO termination.

For the BaO surface, the *c* phase under in-plane compressive strain is relatively more stable, displays larger polarization magnitude and lowers the critical thickness than for the $TiO_2$ surface, although both are less stable than bulk. Conversely, for the $TiO_2$ surface, the *aa* phase under in-plane tensile strain is much more stable and exhibits larger polarization than the BaO surface and than bulk. At the bulk lattice constant, the $TiO_2$ surface undergoes strong tensile surface stress compared to the BaO surface where it is very weak.

## 2.3. Surface electronic structure

The electronic structure of perfect $BaTiO_3$(001) surface shows significant differences according to the slab termination (BaO, $TiO_2$) and phase (*aa*, *c*, *p*), as developed in section 3.7 of chapter III. However, no significant difference has been observed as a function of slab thickness. Moreover, in a given simulated phase, the value of the in-plane strain change has no significant influence on the electronic structure. All simulated slabs except oxygen deficient ones are found insulating with a nonzero Kohn-Sham band gap. Below we discuss the case of $L = 9$ atomic layers thick slabs and distinguish the two terminations.

For the BaO termination, the Kohn-Sham band gap is slightly less than 2.0 eV for the *aa*, *c* and *p* phases, which is comparable to that in the bulk. It is however strongly reduced in the case of the $TiO_2$ termination: 1.4 eV for the *aa* phase and 0.5 eV for the *c* and *p* phases.

These results showing differences according to the surface termination gave insight into the presence of surface states. The projected density of states has shown the presence of electronic states at the $TiO_2$ surface layer which are not present in the bulk. At the $P^+$ and $P^-$ surface of the $TiO_2$-terminated slab in the *c* phase, the Kohn-Sham band gap reduction is due mostly to the raising of oxygen electronic states at the top of the valence band, and less significantly to the energy lowering of Ti states from the bottom of the conduction band. The coordination numbers reduction arising from the lack of neighbors at the surface induces changes of the microscopic potential felt by the surface anions and cations. Since $BaTiO_3$ is a charge transfer insulating oxide, the valence band arises from the stabilization of the oxygen filled states by the positive microscopic potential of the cations. At the surface, this microscopic potential is reduced and states raise in the gap from the top of the valence band. This phenomenon is observed at the $P^+$ and $P^-$ surface.

The $P^+$ and $P^-$ surface regions have opposite surface polarization and exhibit different surface rumpling (see section 3.6 of chapter IV). The interplay between the ferroelectric induced atomic distortions and the surface rumpling can play a role in the surface electronic structure difference seen for the oppositely polarized surface regions. A further insight into such interplay can be addressed by comparing the electronic structure of the *c* and *aa* phases. In the *aa* phase, the Kohn-Sham band gap is much less reduced compared to the *c* phase. The surface states at the top of the valence band do not extend as high in the gap in the *aa* phase compared to the *c* phase. For the $TiO_2$ termination, the rumpling is enhanced in the *c* phase and *p* phases and reduced in the *aa* phase. For the BaO termination, the contrary is observed. The way the surface accommodates the in-plane strain in the *aa* and *c* phases is therefore different, and this can play a role in the observed surface electronic structure differences.

## 3. Oxygen vacancies and conductivity

Pure $BaTiO_3$ is a charge transfer insulating oxide. Perfect surfaces, as simulated in the present work, are insulating whatever the surface termination or polarization direction. However, finite conductivity can be achieved by the introduction of defects such as neutral oxygen vacancies, which behave as electron donors. We have simulated the case of a $BaTiO_3$(001) surface with $TiO_2$ termination, polarization perpendicular to the surface permitted by domain formation and with a surface oxygen vacancy. From the experimental point of view, the free surface of $BaTiO_3$, which has been reduced by vacuum annealing, has been investigated by means of low-energy and photoemission electron microscopy techniques.

## 3.1. $P^-$ stabilized by oxygen vacancies

Our first-principles calculations suggest that the presence of a surface oxygen vacancy strongly stabilizes a $P^-$ surface polarization, i.e. polarization perpendicular to the surface, pointing towards the material. The electronic structure of the slab which incorporates the surface oxygen vacancy shows the presence of filled states at the bottom of the conduction band. Therefore the system is found metallic with the Fermi level inside the bottom of the conduction band.

Low-energy electron microscopy investigation of the $BaTiO_3$(001) surface of a single crystal has revealed that, with successive annealing in ultrahigh vacuum at 650 °C for 30 min, the surface charge associated to $P^-$ domains strongly decreases, whereas that associated to in-plane polarized and outwards polarized domains more moderately decreases. Assuming an increase of the oxygen vacancy concentration after each annealing cycle, this experiment suggests a strong interplay between oxygen vacancy and $P^-$ domains. Our group previously reported the stabilization of $P^-$ polarization induced by an increasing oxygen vacancy concentration, supported by first-principles calculations of out-of-plane polarized $BaTiO_3$ in an external electric field [86].

Photoemission electron microscopy study of the $BaTiO_3$(001) surface of similar reduced single crystals confirms these results. The micro-spectroscopy performed on domains of opposite surface polarization direction shows a quantitative difference in the reduced Ti signal, as well as in the in-gap electronic states observed 1 eV below the conduction band.

Our results strongly support the stabilizing interplay between surface oxygen vacancy and $P^-$ surface polarization.

## 3.2. Conductivity

As a corollary, we now discuss the origin of the observed conductivity in reduced $BaTiO_3$, in parallel with the metallic electronic structure predicted from first-principles when a surface oxygen vacancies is incorporated.

The neutral oxygen vacancy is a donor defect, as it results from the removal of atomic oxygen. Each oxygen vacancy releases two electrons in the system. These excess electrons are predicted from our DFT-LDA first-principles calculations to occupy metallic states at the bottom of the conduction band, and observed experimentally as reducing Ti ions and generating in-gap states $\sim 1$ eV below the conduction band. This

discrepancy is probably due to the poor description of the strongly correlated Ti 3*d* states by the Local Density Approximation.

The nature of the conductivity (and charge carriers) in reduced $BaTiO_3$ is still an open question. The presence of localized states within the bandgap, as experimentally observed, suggests that the Ti ions in the vicinity of the oxygen vacancy are reduced, forming an electronic polaron with the localized excess electron.

The model of small polaron to describe the localized excess electron populating Ti 3*d* states might be the one that best fits the picture. The excess electrons left by the oxygen vacancies reduce the Ti ions in the vicinity of the vacancy site. This induces lattice distortions associated to a local polarization field. Thermal activity induce motion of the lattice which can destroy the polarization field and lead to the mobility of the excess electron towards other Ti acceptor sites. From hybrid density functional calculations, Choi et al. [199] identified (i) the oxygen vacancy as a double shallow donor, at the origin of *n*-type conduction in $BaTiO_3$, and (ii) a metastable configuration of the lattice at the vicinity of the oxygen vacancy sites, associated with deep localized states in the band gap.

However, our DFT-LDA calculations can not reproduce this fact. Other exchange-correlation functionals (hybrid with exact exchange such as HSE06 [200]) should be more suitable to describe such localized electronic states as investigaed by Shimada et al. in $PbTiO_3$ [81].

Another interpretation for the nature of the charge carriers induced by the oxygen vacancies can be addressed. Both calculations and experiments show that the excess electron reduce Ti. The resulting $Ti^{3+}$ oxidation state can be observed by photoemission on the Ti 2p core level. Populating the Ti 3d states can stabilize the excess electrons and the associated correlation interactions can result in the formation of the relatively localized in-gap state, as the one observed 1 eV below the conduction band. This behavior is close to that of a Mott insulator [41], characteristic of other transition metal oxides such as $GdTiO_3$, $LaTiO_3$ and $YTiO_3$ [40], in which Ti are formally $Ti^{3+}$. However, the conductivity associated should not scale with temperature, similarly to heavily doped $BaTiO_3$ which displays a metallic character as compared to the lightly doped $BaTiO_3$ which is semiconducting.

# Conclusion

The main objective of this work was to bring further understanding in the surface properties of the ferroelectric $BaTiO_3$, with polarization oriented parallel or perpendicular to the surface. A microscopic study was performed by first-principles calculations based on the density functional theory under the local density approximation. Complementary experimental investigations brought further evidence to the results obtained from the simulations.

From first-principles calculations, we have shown that domain formation is efficient to screen the depolarizing fields and allow perpendicular polarization to develop at the $BaTiO_3$(001) surface, provided sufficient in-plane compressive strain is imposed. The stability of in-plane polarized and out-of-plane polarized slabs was investigated within a large in-plane strain range, for the both BaO and $TiO_2$ terminations.
Polarization along [001] under compressive strain was studied as a function of system thickness, from 0.4 nm to 2.4 nm, showing that the BaO termination (nonzero starting from 1.2 nm thick slab) stabilizes and enhances polarization, compared to the $TiO_2$ termination (nonzero starting from 1.6 nm thick slab). The slabs properties (polarization, energy) slowly converge to the bulk ones.
Conversely, in tensile in-plane strain, polarization along [110] is strongly stabilized by the $TiO_2$ termination, compared to the both BaO-terminated slabs and bulk.
All the surfaces are found insulating. Nevertheless, surfaces states have been observed to induce Kohn-Sham band gap changes. At the BaO surfaces, the electronic structure is almost insensitive to the ferroelectric distortions, with Kohn-Sham band gap very comparable to the bulk one. At the $TiO_2$ surfaces, in-plane polarization moderately reduces the Kohn-Sham band gap while out-of-plane polarization strongly reduces it (without closing it). The atomic distortions superimposed to the natural rumpling therefore influence the electronic structure by modifying the microscopic potentials at the surface. In-plane strain and system thicknesses do not appear to significantly influence the electronic structure. However, evidence of strong tensile surface stress was found at the $TiO_2$ surfaces, which shifts the equilibrium lattice constant of towards lower values (i.e. under $-0.5\,\%$ to $-1.0\,\%$ in-plane strain). This effect is very weak at

the BaO termination.

We have studied the influence of surface oxygen vacancies, a donor defect, on the polarization and electronic structure at $TiO_2$ surfaces. The ab initio calculations and experimental investigations brought compatible results. The oxygen vacancy stabilizes inwards pointing polarization. The electronic structure is predicted from the simulations to be metallic with occupied states at the bottom of the conduction band, composed of Ti 3*d* states. The micro-spectroscopy experiments showed that the excess electrons due to the oxygen vacancies are relatively localized on Ti sites, predominantly at the surface of inwards polarized domains.

# Bibliography


[1] R. D. King-Smith and David Vanderbilt. Theory of polarization of crystalline solids. *Physical Review B*, 47(3):1651–1654, 1993.

[2] R. Resta. Macroscopic polarization in crystalline dielectrics: the geometric phase approach. *Reviews of Modern Physics*, 66(3):899–915, 1994.

[3] J. C. Slater. Theory of the transition in KH2PO4. *The Journal of Chemical Physics*, 9(16):16, 1941.

[4] V. Hugo Schmidt. Review of order-disorder models for KDP-family crystals. *Ferroelectrics*, 72(1):157–173, 1987.

[5] W. Cochran. Crystal stability and the theory of ferroelectricity. *Physical Review Letters*, 3(9):412, 1959.

[6] R. Comes, M. Lambert, and A. Guinier. The chain structure of BaTiO3 and KNbO3. *Solid State Communications*, 6(10):715–719, 1968.

[7] R. Comès, M. Lambert, and A. Guinier. Désordre linéaire dans les cristaux (cas du silicium, du quartz, et des pérovskites ferroélectriques). *Acta Crystallographica*, A26(2):244–254, March 1970.

[8] N. Dalal, a. Klymachyov, and a. Bussmann-Holder. Coexistence of Order-Disorder and Displacive Features at the Phase Transitions in Hydrogen-Bonded Solids: Squaric Acid and its Analogs. *Physical Review Letters*, 81(26):5924–5927, December 1998.

[9] Edward Stern. Character of Order-Disorder and Displacive Components in Barium Titanate. *Physical Review Letters*, 93(3):037601, July 2004.

[10] Q. Zhang, T. Cagin, and A. Goddard. The ferroelectric and cubic phases in $BaTiO_3$ ferroelectrics are also antiferroelectric. *Proceedings of the National Academy of Sciences of the USA*, 13:14695–14700, 2006.

[11] a. Bussmann-Holder, H. Beige, and G. Völkel. Precursor effects, broken local symmetry, and coexistence of order-disorder and displacive dynamics in per-

ovskite ferroelectrics. *Physical Review B - Condensed Matter and Materials Physics*, 79(18):1–6, 2009.

[12] Hai-Yao Deng. On the terahertz dielectric response of cubic $BaTiO_3$: Coexistence of displacive and order-disorder dynamics. *EPL (Europhysics Letters)*, 100(2):27001, October 2012.

[13] G. H. Kwei, A. C. Lawson, S. J. L. Billinge, and S. W. Cheong. Structures of the ferroelectric phases of barium titanate. *Journal of Physical Chemistry*, 97(10):2368–2377, March 1993.

[14] A. Chaves, F. Barreto, R. Nogueira, and B. Zeks. Thermodynamics of an eight-site order-disorder model for ferroelectrics. *Physical Review B*, 13(1):207–212, January 1976.

[15] G. Geneste. Correlations and local order parameter in the paraelectric phase of barium titanate. *Journal of physics. Condensed matter : an Institute of Physics journal*, 23(12):125901, March 2011.

[16] B. Ravel, E. A. Stern, R. I. Vedrinskii, and V. Kraizman. Local structure and the phase transitions of BaTiO3. *Ferroelectrics*, 206:407–430, 1998.

[17] W. Zhong, D. Vanderbilt, and M. Rabe. First-principles theory of ferroelectric phase transitions for perovskites: The case of $BaTiO_3$. *Physical Review B*, 52(9):6301, 1995.

[18] Claudine Noguera. *Physics and Chemistry at Oxide Surfaces*. Cambridge University Press, Cambridge, 1996.

[19] J. Goniakowski, F. Finocchi, and C. Noguera. Polarity of oxide surfaces and nanostructures. *Reports on Progress in Physics*, 71(1):016501, January 2008.

[20] N. Bickel, G. Schmidt, K. Heinz, and K. Müller. Ferroelectric relaxation of the $SrTiO_3$(100) surface. *Physical Review Letters*, 62(17):2009–2011, 1989.

[21] T. Hikita, T. Hanada, M. Kudo, and M. Kawai. Structure and electronic state of the TiO2 and SrO terminated SrTiO3 (100) surfaces. *Surface Science*, 287/288:377, 1993.

[22] J Padilla and David Vanderbilt. Ab initio study of SrTiO surfaces. *Surface Science*, 418:64–70, 1998.

[23] E. Heifets, R. Eglitis, E. Kotomin, J. Maier, and G. Borstel. Ab initio modeling of surface structure for SrTiO3 perovskite crystals. *Physical Review B*, 64(23):1–5, 2001.

[24] E Heifets, Ri Eglitis, Ea Kotomin, J Maier, and G Borstel. First-principles calculations for SrTiO 3(100) surface structure. *Surface science*, 513:211–220, 2002.

[25] M. Mrovec, J.-M. Albina, B. Meyer, and C. Elsässer. Schottky barriers at transition-metal/SrTiO3(001) interfaces. *Physical Review B*, 79(24), 2009.

[26] J Padilla and David Vanderbilt. Ab initio study of $BaTiO_3$ surfaces. *Physical Review B*, 56(3):1625–1631, 1997.

[27] R.I. Eglitis, S. Piskunov, E. Heifets, E.a. Kotomin, and G. Borstel. Ab initio study of the SrTiO3, BaTiO3 and PbTiO3 (001) surfaces. *Ceramics International*, 30(7):1989–1992, 2004.

[28] R. Eglitis and David Vanderbilt. Ab initio calculations of $BaTiO_3$ and $PbTiO_3$ (001) and (011) surface structures. *Physical Review B*, 76(15):155439, October 2007.

[29] S. Piskunov, E.a. Kotomin, E. Heifets, J. Maier, R.I. Eglitis, and G. Borstel. Hybrid DFT calculations of the atomic and electronic structure for ABO3 perovskite (001) surfaces. *Surface Science*, 575(1-2):75–88, 2005.

[30] Pierre Müller, Andres Saùl, and Frédéric Leroy. Simple views on surface stress and surface energy concepts. *Advances in Natural Sciences: Nanoscience and Nanotechnology*, 5(1):013002, November 2013.

[31] Jelle Dionot, Grégory Geneste, Claire Mathieu, and Nick Barrett. Surface polarization, rumpling, and domain ordering of strained ultrathin $BaTiO_3$(001) films with in-plane and out-of-plane polarization. *Physical Review B*, 90(1):014107, July 2014.

[32] Richard J. Needs. Calculations of the surface stress tensor at aluminum (111) and (110) surfaces. *Physical Review Letters*, 58(1):53–56, 1987.

[33] David Vanderbilt. Absence of large compressive stress on Si(111). *Physical Review Letters*, 59(13):1456–1459, 1987.

[34] N Iles, F Finocchi, and K Driss Khodja. A systematic study of ideal and double layer reconstructions of ABO3(001) surfaces (A = Sr, Ba; B = Ti, Zr) from first principles. *Journal of physics. Condensed matter : an Institute of Physics journal*, 22(30):305001, 2010.

[35] M. J. Harrison, D. P. Woodruff, and J. Robinson. Density functional theory calculations of adsorption-induced surface stress changes. *Surface Science*, 602(1):226–234, 2008.

[36] Hideyuki Kamisaka and Koichi Yamashita. The surface stress of the (110)

and (100) surfaces of rutile and the effect of water adsorbents. *Surface Science*, 601(21):4824–4836, 2007.

[37] Harald Ibach. The role of surface stress in reconstruction, epitaxial growth and stabilization of mesoscopic structures. *Surface Science Reports*, 29(5-6):195–263, 1997.

[38] W Haiss. Surface stress of clean and adsorbate-covered solids. *Reports on Progress in Physics*, 64(5):591–648, 2001.

[39] G. Geneste, E. Bousquet, J. Junquera, and Ph. Ghosez. Finite-size effects in $BaTiO_3$ nanowires. *Applied Physics Letters*, 88(11):112906, 2006.

[40] Y. Okimoto, T. Katsufuji, Y. Okada, T. Arima, and Y. Tokura. Optical spectra in (La,Y)TiO3: Variation of Mott-Hubbard gap features with change of electron correlation and band filling. *Physical Review B*, 51(15):9581–9588, 1995.

[41] Antoine Georges, G Kotliar, Werner Krauth, and Mj Rozenberg. Dynamical mean-field theory of strongly correlated fermion systems and the limit of infinite dimensions. *Reviews of Modern Physics*, 68(1):13–125, 1996.

[42] J. Zaanen, G. a. Sawatzky, and J. W. Allen. Band gaps and electronic structure of transition-metal compounds. *Physical Review Letters*, 55(4):418–421, 1985.

[43] Meng-Qiu Cai, Yong-Jun Zhang, Zhen Yin, and Ming-Sheng Zhang. First-principles study of structural and electronic properties of $BaTiO_3$(001) oxygen-vacancy surfaces. *Physical Review B*, 72(7):075406, August 2005.

[44] G. M. Vanacore, L. F. Zagonel, and N. Barrett. Surface enhanced covalency and Madelung potentials in Nb doped SrTiO3 (100), (110) and (111) single crystals. *Surface Science*, 604(19-20):1674–1683, September 2010.

[45] Huaxiang Fu and L Bellaiche. Ferroelectricity in barium titanate quantum dots and wires. *Physical review letters*, 91(25):257601, 2003.

[46] L. Hong, a. K. Soh, S. Y. Liu, and L. Lu. Vortex structure transformation of BaTiO3 nanoparticles through the gradient function. *Journal of Applied Physics*, 106(2), 2009.

[47] a. Schilling, R. M. Bowman, G. Catalan, J. F. Scott, and J. M. Gregg. Morphological control of polar orientation in single-crystal ferroelectric nanowires. *Nano Letters*, 7(12):3787–3791, 2007.

[48] C H Ahn, K M Rabe, and J-M Triscone. Ferroelectricity at the nanoscale: local polarization in oxide thin films and heterostructures. *Science (New York, N.Y.)*,

303(5657):488–491, 2004.

[49] Y. L. Tang, Y. L. Zhu, X. L. Ma, A. Y. Borisevich, A. N. Morozovska, E. A. Eliseev, W. Y. Wang, Y. J. Wang, Y. B. Xu, Z. D. Zhang, and S. J. Pennycook. Observation of a periodic array of flux-closure quadrants in strained ferroelectric $PbTiO_3$ films. *Science*, 348(6234):547–551, 2015.

[50] Javier Junquera and Philippe Ghosez. Critical thickness for ferroelectricity in perovskite ultrathin films. *Letters to Nature*, 422(February):506–509, 2003.

[51] N. Sai, A. M. Kolpak, and A. M. Rappe. Ferroelectricity in ultrathin perovskite films. *Physical Review B*, 72(2):020101, July 2005.

[52] Massimiliano Stengel, David Vanderbilt, and Nicola a Spaldin. Enhancement of ferroelectricity at metal-oxide interfaces. *Nature materials*, 8(5):392–397, 2009.

[53] G. Gerra, a. K. Tagantsev, N. Setter, and K. Parlinski. Ionic polarizability of conductive metal oxides and critical thickness for ferroelectricity in BaTiO 3. *Physical Review Letters*, 96(10):1–4, 2006.

[54] W. Zhong, D. Vanderbilt, and K. M. Rabe. Phase Transitions in $BaTiO_3$ from First Principles. *Physical Review Letters*, 73(13):1861, 1994.

[55] a. G. Zembilgotov, N. a. Pertsev, H. Kohlstedt, and R. Waser. Ultrathin epitaxial ferroelectric films grown on compressive substrates: Competition between the surface and strain effects. *Journal of Applied Physics*, 91(3):2247–2254, 2002.

[56] R. Meyer, R. Liedtke, and R. Waser. Oxygen vacancy migration and time-dependent leakage current behavior of Ba0.3Sr0.7TiO3 thin films. *Applied Physics Letters*, 86(11):1–3, 2005.

[57] Massimiliano Stengel, Pablo Aguado-Puente, Nicola a. Spaldin, and Javier Junquera. Band alignment at metal/ferroelectric interfaces: Insights and artifacts from first principles. *Physical Review B*, 83(23):235112, June 2011.

[58] Q. Yang, J. X. Cao, Y. Ma, Y. C. Zhou, X. J. Lou, and J. Yang. Interface effect on the magnitude and stability of ferroelectric polarization in ultrathin PbTiO3 films from first-principles study. *Journal of Applied Physics*, 114(3):0–6, 2013.

[59] Cheol Seong Hwang. Thickness-dependent dielectric constants of (Ba,Sr)TiO 3 thin films with Pt or conducting oxide electrodes. *Journal of Applied Physics*, 92(1):432–437, 2002.

[60] N. A. Pertsev, R. Dittmann, R. Plonka, and R. Waser. Thickness dependence of intrinsic dielectric response and apparent interfacial capacitance in ferroelectric

thin films. *Journal of Applied Physics*, 101(7), 2007.

[61] Sergei Kalinin and Dawn Bonnell. Local potential and polarization screening on ferroelectric surfaces. *Physical Review B*, 63(12):125411, March 2001.

[62] Sergei V. Kalinin and Dawn a. Bonnell. Screening phenomena on oxide surfaces and its implications for local electrostatic and transport measurements. *Nano Letters*, 4(4):555–560, 2004.

[63] Sergei V Kalinin and Dawn a Bonnell. Effect of phase transition on the surface potential of the $BaTiO_3$(100) surface by variable temperature scanning surface potential microscopy. *Journal of Applied Physics*, 87(100):3950–3957, 2000.

[64] Yunseok Kim, Seungbum Hong, Seung Hyun Kim, and Kwangsoo No. Surface potential of ferroelectric domain investigated by kelvin force microscopy. *Journal of Electroceramics*, 17(2-4):185–188, 2006.

[65] Yunseok Kim, Jiyoon Kim, Simon Bühlmann, Seungbum Hong, Yong Kwan Kim, Seung Hyun Kim, and Kwangsoo No. Screen charge transfer by grounded tip on ferroelectric surfaces. *Physica Status Solidi - Rapid Research Letters*, 2(2):74–76, 2008.

[66] D. Dahan, M. Molotskii, G. Rosenman, and Y. Rosenwaks. Ferroelectric domain inversion: The role of humidity. *Applied Physics Letters*, 89(15):152902, 2006.

[67] D. Fong, A. Kolpak, J. Eastman, S. Streiffer, P. Fuoss, G. Stephenson, Carol Thompson, D. Kim, K. Choi, C. Eom, I. Grinberg, and A. Rappe. Stabilization of Monodomain Polarization in Ultrathin $PbTiO_3$ Films. *Physical Review Letters*, 96(12):127601, March 2006.

[68] Junsoo Shin, Von Braun Nascimento, Grégory Geneste, John Rundgren, E Ward Plummer, Brahim Dkhil, Sergei V Kalinin, and Arthur P Baddorf. Atomistic Screening Mechanism of Ferroelectric Surfaces : An In Situ Study of the Polar Phase in Ultrathin $BaTiO_3$ Films Exposed to $H_2O$. *Nano Letters*, 9(11):3720–3725, 2009.

[69] F. Peter, K. Szot, R. Waser, B. Reichenberg, S. Tiedke, and J. Szade. Piezoresponse in the light of surface adsorbates: Relevance of defined surface conditions for perovskite materials. *Applied Physics Letters*, 85(14):2896–2898, 2004.

[70] G. B. Stephenson and M. J. Highland. Equilibrium and stability of polarization in ultrathin ferroelectric films with ionic surface compensation. *Physical Review B*, 84(6):064107, August 2011.

[71] R. Wang, D. D. Fong, F. Jiang, M. J. Highland, P. H. Fuoss, C. Thompson, A. M.

Kolpak, J. A. Eastman, S. K. Streiffer, A. M. Rappe, and G. B. Stephenson. Reversible Chemical Switching of a Ferroelectric Film. *Physical Review Letters*, 102(4):047601, January 2009.

[72] M. J. Highland, T. T. Fister, D. D. Fong, P. H. Fuoss, C. Thompson, J. A. Eastman, S. K. Streiffer, and G. B. Stephenson. Equilibrium Polarization of Ultrathin $PbTiO_3$ with Surface Compensation Controlled by Oxygen Partial Pressure. *Physical Review Letters*, 107(18):187602, October 2011.

[73] K Garrity, A M Kolpak, S Ismail-Beigi, and E I Altman. Chemistry of ferroelectric surfaces. *Advanced materials*, 22(26-27):2969–73, July 2010.

[74] J. Nowotny and R. Mieczyslaw. Defect chemistry of $BaTiO_3$. *Solid State Ionics*, 49:135–154, 1991.

[75] S Kimura, J Yamauchi, M Tsukada, and S Watanabe. First-principles study on electronic structure of the (001) surface of SrTiO 3. *Physical Review B*, 51(16):49–54, 1995.

[76] K. Kowalski, M. Ijjaali, T. Bak, B. Dupre, J. Nowotny, M. Rekas, and C. C. Sorrell. Electrical properties of Nb-doped BaTiO3. *Journal of Physics and Chemistry of Solids*, 62(3):543–551, 2001.

[77] Finlay D. Morrison, Alison M. Coats, Derek C. Sinclair, and Anthony R. West. Charge compensation mechanisms in La-doped BaTiO3. *Journal of Electroceramics*, 6(3):219–232, 2001.

[78] Yoed Tsur and Clive a Randall. Point Defect Concentrations in Barium Titanate Revisited. *Journal of American Ceramic Society*, 84(9):2147–2149, 2001.

[79] P. V. Lambeck and G. H. Jonker. Ferroelectric domain stabilization in $BaTiO_3$ by bulk ordering of defects. *Ferroelectrics*, 22(February 2015):729–731, 1978.

[80] S. Piskunovs. *The electronic structure of perfect and defective perovskite crystals : Ab initio hybrid functional calculations*. PhD thesis, University of Osnabrück, 2003.

[81] Takahiro Shimada, Taku Ueda, Jie Wang, and Takayuki Kitamura. Hybrid Hartree-Fock density functional study of charged point defects in ferroelectric PbTiO3. *Physical Review B*, 87:1–12, 2013.

[82] C. N. Berglund and W. S. Baer. Electron transport in single-domain, ferroelectric barium titanate. *Physical Review*, 157(2):358–366, 1967.

[83] H. Ihrig and D. Hennings. Electrical transport properties of *n*-type $BaTiO_3$. *Physical Review B*, 17(12):4593, 1978.

[84] R. Scharfschwerdt, A. Mazur, O. F. Schirmer, H. Hesse, and S. Mendricks. Oxygen vacancies in $BaTiO_3$. *Physical Review B*, 54(21):15284–15290, December 1996.

[85] Yong Wang, Xiaohui Liu, J. D. Burton, Sitaram S. Jaswal, and Evgeny Y. Tsymbal. Ferroelectric Instability Under Screened Coulomb Interactions. *Physical Review Letters*, 109(24):247601, December 2012.

[86] Y. Mi, G. Geneste, J. Rault, C. Mathieu, A. Pancotti, and N. Barrett. Polarization dependent chemistry of ferroelectric $BaTiO_3$(001) domains. *Journal of physics: Condensed matter*, 24(27):275901, July 2012.

[87] T. Yang, Venkatraman Gopalan, P. Swart, and U. Mohideen. Direct Observation of Pinning and Bowing of a Single Ferroelectric Domain Wall. *Physical Review Letters*, 82(20):4106–4109, 1999.

[88] Lixin He and David Vanderbilt. First-principles study of oxygen-vacancy pinning of domain walls in $PbTiO_3$. *Physical Review B*, 68(13):134103, October 2003.

[89] E. a. Eliseev, a. N. Morozovska, G. S. Svechnikov, Venkatraman Gopalan, and V. Ya Shur. Static conductivity of charged domain walls in uniaxial ferroelectric semiconductors. *Physical Review B*, 83(23):1–8, 2011.

[90] Yinan Zuo, Yuri A Genenko, Andreas Klein, Peter Stein, and Baixiang Xu. Domain wall stability in ferroelectrics with space charges. *Journal of Applied Physics*, 115:084110, 2014.

[91] J. Seidel, P. Maksymovych, Y. Batra, A. Katan, S.-Y. Yang, Q. He, A. Baddorf, S. Kalinin, C.-H. Yang, J.-C. Yang, Y.-H. Chu, E. Salje, H. Wormeester, M. Salmeron, and R. Ramesh. Domain Wall Conductivity in La-Doped $BiFeO_3$. *Physical Review Letters*, 105(19):2010–2012, November 2010.

[92] S. R. Gilbert, L. a. Wills, B. W. Wessels, J. L. Schindler, J. a. Thomas, and C. R. Kannewurf. Electrical transport properties of epitaxial BaTiO3 thin films. *Journal of Applied Physics*, 80(2):969–977, 1996.

[93] T. Kolodiazhnyi. Insulator-metal transition and anomalous sign reversal of the dominant charge carriers in perovskite $BaTiO_{3-\delta}$. *Physical Review B*, 78(4):045107, July 2008.

[94] J E Rault, J Dionot, C Mathieu, V Feyer, C M Schneider, G Geneste, N Barrett, and Peter Gru. Polarization Sensitive Surface Band Structure of Doped $BaTiO_3$(001). *Physical Review Letters*, 111:127602, 2013.

[95] B. Matthias and A. von Hippel. Domain Structure and Dielectric Response of Barium Titanate Single Crystals. *Physical Review*, 73(11):1378, 1948.

[96] P. W. Forsbergh. Domain Structures and Phase Transitions in Barium Titanate. *Physical Review*, 76(8):1187–1201, October 1949.

[97] T. Mitsui and J. Furuichi. Domain Structure of Rochelle Salt and $KH_2PO_4$. *Physical Review*, 90(2):193, 1953.

[98] J. S. Speck, A. C. Daykin, A. Seifert, a. E. Romanov, and W. Pompe. Domain configurations due to multiple misfit relaxation mechanisms in epitaxial ferroelectric thin films. III. Interfacial defects and domain misorientations. *Journal of Applied Physics*, 78(3):1696–1706, 1995.

[99] S. K. Streiffer, C. B. Parker, a. E. Romanov, M. J. Lefevre, L. Zhao, J. S. Speck, W. Pompe, C. M. Foster, and G. R. Bai. Domain patterns in epitaxial rhombohedral ferroelectric films. I. Geometry and experiments. *Journal of Applied Physics*, 83(5):2742, 1998.

[100] R. Takahashi, Dahl, E. Eberg, J. K. Grepstad, and T. Tybell. Ferroelectric stripe domains in PbTiO3 thin films: Depolarization field and domain randomness. *Journal of Applied Physics*, 104(6), 2008.

[101] C. Kittel. Theory of the Structure of Ferromagnetic Domains in Films and Small Particles. *Physical Review*, 70:965, 1946.

[102] J F Scott. Nanoferroelectrics: statics and dynamics. *Journal of physics. Condensed matter : an Institute of Physics journal*, 18(17):R361–R386, 2006.

[103] S. Streiffer, J. Eastman, D. Fong, Carol Thompson, A. Munkholm, M. Ramana Murty, O. Auciello, G. Bai, and G. Stephenson. Observation of Nanoscale 180° Stripe Domains in Ferroelectric $PbTiO_3$ Thin Films. *Physical Review Letters*, 89(6):067601, July 2002.

[104] A. Schilling, T. Adams, R. Bowman, J. Gregg, G. Catalan, and J. Scott. Scaling of domain periodicity with thickness measured in $BaTiO_3$ single crystal lamellae and comparison with other ferroics. *Physical Review B*, 74(2):024115, July 2006.

[105] Igor Kornev, Huaxiang Fu, and L. Bellaiche. Ultrathin films of ferroelectric solid solutions under a residual depolarizing field. *Physical Review Letters*, 93(19):1–4, 2004.

[106] P. Aguado-Puente and J. Junquera. Ferromagneticlike Closure Domains in Ferroelectric Ultrathin Films: First-Principles Simulations. *Physical Review Letters*, 100(17):177601, April 2008.

[107] Takahiro Shimada, Shogo Tomoda, and Takayuki Kitamura. Ab initio study of ferroelectric closure domains in ultrathin $PbTiO_3$ films. *Physical Review B*,

81(14):144116, April 2010.

[108] Ronald E. Cohen. Surface Effects in Ferroelectrics: Periodic Slab Computations for $BaTiO_3$. page 19, September 1996.

[109] R. E. Cohen. Periodic slab LAPW computations for ferroelectric BaTiO3. *Journal of Physics and Chemistry of Solids*, 57(10):1393–1396, 1996.

[110] R. E. Cohen. Surface effects in ferroelectrics: Periodic slab computations for $BaTiO_3$. *Ferroelectrics*, 194(1):323–342, 1997.

[111] M. Fechner, S. Ostanin, and I. Mertig. Effect of the surface polarization in polar perovskites studied from first principles. *Physical Review B*, 77(9):094112, March 2008.

[112] B. Meyer and David Vanderbilt. Ab initio study of $BaTiO_3$ and $PbTiO_3$ surfaces in external electric fields. *Physical Review B*, 63(20):205426, May 2001.

[113] Martin Head-Gordon, Rudolph J. Rico, Timothy J. Lee, and Manabu Oumi. A Doubles Correction to Electronic Excited States from Configuration Interaction in the Space of Single Substitutions. *Chemical Physics Letters*, 219(March):21–29, 1994.

[114] C. D. Sherrill and H. F. Shaefer III. The Configuration Interaction Method: Advances in Highly Correlated Approaches. In *Advances in Quantum Chemistry 34*, pages 143–269. Academic Press, 1999.

[115] George D Purvis and Rodney J Bartlett. A full coupled-cluster singles and doubles model: The inclusion of disconnected triples. *The Journal of Chemical Physics*, 76(4):1910, 1982.

[116] Krishnan Raghavachari, Gary W. Trucks, John a. Pople, and Martin Head-Gordon. A fifth-order perturbation comparison of electron correlation theories. *Chemical Physics Letters*, 589(6):37–40, 2013.

[117] P. Hohenberg and W. Kohn. Inhomogeneous electron gas. *Physical Review B*, 136(3B):B864, 1964.

[118] D. J. Griffith. *Introduction to Quantum Mechanics*. Pearson Prentice Hall, 2nd editio edition, 2004.

[119] W. Kohn and L. J. Sham. Self-Consistent Equations Including Exchange and Correlation Effects. *Physical Review*, 140(4A):A1133, 1965.

[120] D. M. Ceperley and B. J. Alder. Ground state of the electron gas by a stochastic method. *Physical Review Letters*, 45(7):566–569, 1980.

[121] John P. Perdew and Yue Wang. Accurate and simple analytic representation of the electron-gas correlation energy. *Physical Review B*, 45(23):13244–13249, 1992.

[122] D.C. Langreth and J.P. Perdew. The gradient approximation to the exchange-correlation energy functional: A generalization that works. *Solid State Communications*, 31(8):567–571, 1979.

[123] Paul Ziesche, Stefan Kurth, and John P. Perdew. Density functionals from LDA to GGA. *Computational Materials Science*, 11(2):122–127, 1998.

[124] Zhigang Wu, R. E. Cohen, and D. J. Singh. Comparing the weighted density approximation with, the LDA and GGA for ground-state properties of ferroelectric perovskites. *Physical Review B - Condensed Matter and Materials Physics*, 70(10):1–7, 2004.

[125] S Piskunov, E Heifets, R.I Eglitis, and G Borstel. Bulk properties and electronic structure of $SrTiO_3$, $BaTiO_3$, $PbTiO_3$ perovskites: an ab initio HF/DFT study. *Computational Materials Science*, 29(2):165–178, February 2004.

[126] D. I. Bilc, R. Orlando, R. Shaltaf, G. M. Rignanese, Jorge Íñiguez, and Ph Ghosez. Hybrid exchange-correlation functional for accurate prediction of the electronic and structural properties of ferroelectric oxides. *Physical Review B - Condensed Matter and Materials Physics*, 77(16):1–13, 2008.

[127] Grégory Geneste and Brahim Dkhil. Adsorption and dissociation of $H_2O$ on in-plane-polarized $BaTiO_3$(001) surfaces and their relation to ferroelectricity. *Physical Review B*, 79(23):235420, June 2009.

[128] X. Gonze, J.-M. Beuken, R. Caracas, F. Detraux, M. Fuchs, G.-M. Rignanese, L. Sindic, M. Verstraete, G. Zerah, F. Jollet, M. Torrent, a. Roy, M. Mikami, Ph. Ghosez, J.-Y. Raty, and D.C. Allan. First-principles computation of material properties: the ABINIT software project. *Computational Materials Science*, 25(3):478–492, November 2002.

[129] M Soler, Emilio Artacho, Julian D Gale, Alberto Garc, Javier Junquera, Pablo Ordej, and S Daniel. The SIESTA method for ab initio order-*N* materials. *Journal of Physics: Condensed Matter*, 14:2745–2779, 2002.

[130] H. Hellmann. A New Approximation Method in the Problem of Many Electrons. *The Journal of Chemical Physics*, 3(1935):61, 1935.

[131] N. Troullier and J. L. Martins. Efficient pseudopotentials for plane-wave calculations. *Physical Review B*, 43(3):1993, 1991.

[132] Felix Bloch. Über die Quantenmechanik der Elektronen in Kristallgittern.

*Zeitschrift für Physik*, 52(7-8):555–600, 1929.

[133] Carlos Reis, J. Pacheco, and José Martins. First-principles norm-conserving pseudopotential with explicit incorporation of semicore states. *Physical Review B*, 68(15):1–6, 2003.

[134] Julio a Alonso. Electronic and atomic structure, and magnetism of transition-metal clusters. *Chemical Reviews*, 100:637–78, 2000.

[135] Alfonso Balderschi, Stefano Baroni, and Raffaele Resta. Band offsets in lattice-matched heterojunctions: A model and first-principles calculations for GaAs/AlAs. *Physical Review Letters*, 61(6):734–737, 1988.

[136] L. Colombo, R. Resta, and S. Baroni. Valence-band offsets at strained Si/Ge interfaces. *Physical Review B*, 44(11):5572–5579, 1991.

[137] Claudine Noguera. Polar oxide surfaces. *Journal of Physics: Condensed Matter*, 12(31):R367–R410, 2000.

[138] Philippe Ghosez and Javier Junquera. Chapter 134 : First-Principles Modeling of Ferroelectric Oxides Nanostructures. In *Handbook of Theoretical and Computational Nanotechnology*. 2006.

[139] N. A. Pertsev, A. G. Zembilgotov, and A. K. Tagantsev. Effect of Mechanical Boundary Conditions on Phase Diagrams of Epitaxial Ferroelectric Thin Films. *Physical Review Letters*, 80(9):1988–1991, March 1998.

[140] P. Ghosez. *First-principles study of the dielectric and dynamical properties of barium titanate*. PhD thesis, Université Catholique de Louvain, 1997.

[141] Javier Junquera, Magali Zimmer, Pablo Ordejón, and Philippe Ghosez. First-principles calculation of the band offset at $BaO/BaTiO_3$ and $SrO/SrTiO_3$ interfaces. *Physical Review B*, 67(15):155327, April 2003.

[142] O. Diéguez, S. Tinte, A. Antons, C. Bungaro, J. Neaton, K. Rabe, and D. Vanderbilt. Ab initio study of the phase diagram of epitaxial $BaTiO_3$. *Physical Review B*, 69(21):212101, June 2004.

[143] R. Resta, M. Posternak, and a. Baldereschi. Towards a quantum theory of polarization in ferroelectrics: The case of KNbO3. *Physical Review Letters*, 70(7):1010–1013, 1993.

[144] P. Ghosez, J.-P. Michenaud, and X. Gonze. Dynamical atomic charges: The case of $ABO_3$ compounds. *Physical Review B*, 58(10):6224, 1998.

[145] M. Posternak, R. Resta, and A. Baldereschi. Role of covalent bonding in the polar-

ization of perovskite oxides: The case of $KNbO_3$. *Physical Review B*, 50(12):8911–8914, 1994.

[146] P. Ghosez, X. Gonze, and J.-P. Michenaud. A microscopic study of barium titanate. *Ferroelectrics*, 164:113, 1995.

[147] J Grandy. Efficient computation of volume of hexahedra cells. Technical report, Lawrence Livermore National Lab., CA (United States), 1997.

[148] X.Y. Xue, C.L. Wang, and W.L. Zhong. The atomic and electronic structure of the TiO2- and BaO-terminated BaTiO3(001) surfaces in a paraelectric phase. *Surface Science*, 550(1-3):73–80, 2004.

[149] C. B. Samantaray, Hyunjun Sim, and Hyunsang Hwang. The electronic structures and optical properties of BaTiO3 and SrTiO3 using first-principles calculations. *Microelectronics Journal*, 36(8):725–728, 2005.

[150] H. Salehi, N. Shahtahmasebi, and S. M. Hosseini. Band structure of tetragonal BaTiO3. *European Physical Journal B*, 32:177–180, 2003.

[151] Paul Erhart, Andreas Klein, Daniel Å berg, and Babak Sadigh. Efficacy of the DFT + U formalism for modeling hole polarons in perovskite oxides. *Physical Review B - Condensed Matter and Materials Physics*, 90(3):1–8, 2014.

[152] J Seidel, L W Martin, Q He, Q Zhan, Y-H Chu, A Rother, M E Hawkridge, P Maksymovych, P Yu, M Gajek, N Balke, S V Kalinin, S Gemming, F Wang, G Catalan, J F Scott, N a Spaldin, J Orenstein, and R Ramesh. Conduction at domain walls in oxide multiferroics. *Nature materials*, 8(3):229–234, 2009.

[153] W. Telieps and E. Bauer. An analytical reflection and emission UHV surface electron microscope. *Ultramicroscopy*, 17:57–65, 1985.

[154] E. Bauer. Low energy electron microscopy. *Reports on Progress in Physics*, 57:895–938, 1994.

[155] B.P Tonner, D Dunham, T Droubay, and M Pauli. A photoemission microscope with a hemispherical capacitor energy filter. *Journal of Electron Spectroscopy and Related Phenomena*, 84(1-3):211–229, 1997.

[156] E. Bauer. Cathode lens electron microscopy: past and future. *Journal of physics: Condensed matter*, 21(31):314001, August 2009.

[157] N Barrett, J E Rault, J L Wang, C Mathieu, A Locatelli, and T O Mentes. Full field electron spectromicroscopy applied to ferroelectric materials. *Journal of Applied Physics*, 113:187217, 2013.

[158] L. H. Veneklasen. Design of a spectroscopic low-energy electron microscope. *Ultramicroscopy*, 36:76–90, 1991.

[159] G. Arlt. Twinning in ferroelectric and ferroelastic ceramics: stress relief. *Journal of Materials Science*, 25:2655–2666, 1990.

[160] Ekhard K H Salje and Jason C Lashley. Domain Boundary Engineering in Ferroic and Multiferroic Materials: A Simple Introduction. In Tomoyuki Kakeshita, Takashi Fukuda, Avadh Saxena, and Antoni Planes, editors, *Disorder and Strain-Induced Complexity in Functional Materials*, volume 148 of *Springer Series in Materials Science*. Springer Berlin Heidelberg, Berlin, Heidelberg, 2012.

[161] G. V. Spivak, E. Igras, I. A. Pryamkova, and I. S. Zheludev. Detection of the domain structure in barium titanate with an electron reflector. *Sovietic Physics Crystallography*, 4:115–117, 1959.

[162] K. Maffitt. Interpretation of Electron-Mirror Micrographs of Ferroelectric and Dielectric Surfaces. *Journal of Applied Physics*, 39:3878, 1968.

[163] S . A. Nepijko and N. N. Sedov. Aspects of Mirror Electron Microscopy. *Advances in Imaging and Electron Physics*, 102:273, 1997.

[164] S. Cherifi, R. Hertel, S. Fusil, H. Béa, K. Bouzehouane, J. Allibe, M. Bibes, and A. Barthélémy. Imaging ferroelectric domains in multiferroics using a low-energy electron microscope in the mirror operation mode. *Phys. Status Solidi RRL*, 4(1-2):22–24, February 2010.

[165] J. Rault, W. Ren, S. Prosandeev, S. Lisenkov, D. Sando, S. Fusil, M. Bibes, A. Barthélémy, L. Bellaiche, and N. Barrett. Thickness-Dependent Polarization of Strained $BiFeO_3$ Films with Constant Tetragonality. *Physical Review Letters*, 109(26):267601, December 2012.

[166] S. Nepijko, N. N. Sedov, and G. Schönhense. Peculiarities of imaging one- and two-dimensional structures using an electron microscope in the mirror operation mode. *Journal of microscopy*, 203:269–76, September 2001.

[167] A. B. Pang, A. Pavlovska, L. Däweritz, A. Locatelli, E. Bauer, and M. S. Altman. LEEM image phase contrast of MnAs stripes. *Ultramicroscopy*, 130:7–12, July 2013.

[168] J. W. Gadzuk and E. W. Plummer. Field emission energy distribution (FEED). *Reviews of Modern Physics*, 45(3):487–548, 1973.

[169] G. F. Rempfer and O. Hayes Griffith. Emission Microscopy and Related Techniques - Resolution in Photoelectron Microscopy, Low-Energy Electron-

Microscopy and Mirror Electron-Microscopy. *Ultramicroscopy*, 47:35–54, 1992.

[170] S. Hüfner. *Photoelectron Spectroscopy*. Springer Berlin Heidelberg, springer s edition, 1996.

[171] M Escher, N Weber, M Merkel, C Ziethen, P Bernhard, G Schönhense, S Schmidt, F Forster, F Reinert, B Krömker, and D Funnemann. Nanoelectron spectroscopy for chemical analysis: a novel energy filter for imaging x-ray photoemission spectroscopy. *Journal of Physics: Condensed Matter*, 17(16):S1329–S1338, 2005.

[172] R N Watts, S Liang, Z.H> Levine, T B Lucatorto, F Polack, and M R Scheinfein. A transmission X-ray microscope based on secondary electron imaging. *Rev. Sci. Instrum*, 93(1997):3464, 1997.

[173] G. F. Rempfer and O. H. Griffith. The resolution of photoelectron microscopes with UV, X-ray and synchrotron excitation sources. *Ultramicroscopy*, 27:273–300, 1989.

[174] M. Escher, N. Weber, M. Merkel, B. Krömker, D. Funnemann, S. Schmidt, F. Reinert, F. Forster, S. Hüfner, P. Bernhard, C. Ziethen, H. J. Elmers, and G. Schönhense. NanoESCA: imaging UPS and XPS with high energy resolution. *Journal of Electron Spectroscopy and Related Phenomena*, 144-147:1179–1182, 2005.

[175] G. D. Mahan. Theory of Photoemission in Simple Metals. *Physical Review B*, 2(11):4334, 1970.

[176] C. N. Berglund and W. E. Spicer. Photoemission Studies of Copper and Silver: Theory. *Physical Review*, 136:A1030, 1964.

[177] a Jablonski. Photoelectron transport in the surface region of solids: universal analytical formalism for quantitative applications of electron spectroscopies. *Journal of Physics D: Applied Physics*, 48(7):075301, 2015.

[178] A. Jablonski and C. J. Powell. Practical expressions for the mean escape depth, the information depth, and the effective attenuation length in Auger-electron spectroscopy and x-ray photoelectron spectroscopy. *Journal of Vacuum Science & Technology A: Vacuum, Surfaces, and Films*, 27(2):253, 2009.

[179] a. Jablonski and C. J. Powell. Improved analytical formulae for correcting elastic-scattering effects in X-ray photoelectron spectroscopy. *Surface Science*, 604(3-4):327–336, 2010.

[180] C. J. Powell and a. Jablonski. Progress in quantitative surface analysis by X-ray photoelectron spectroscopy: Current status and perspectives. *Journal of Electron Spectroscopy and Related Phenomena*, 178-179(C):331–346, 2010.

[181] C.J. Powell. The quest for universal curves to describe the surface sensitivity of electron spectroscopies. *Journal of Electron Spectroscopy and Related Phenomena*, 47:197–214, 1988.

[182] Andrea Damascelli. Probing the Electronic Structure of Complex Systems by ARPES. *Physica Scripta*, 2004:61, 2004.

[183] N. Barrett, J. Rault, I. Krug, B. Vilquin, G. Niu, B. Gautier, D. Albertini, P. Lecoeur, and O. Renault. Influence of the ferroelectric polarization on the electronic structure of $BaTiO_3$ thin films. *Surface And Interface Analysis*, 42(12-13):1690–1694, 2010.

[184] L. Hudson, R. L. Kurtz, and S. Robey. Photoelectron spectroscopic study of the valence and core-level electronic structure of $BaTiO_3$. *Physical Review B*, 47(3):1174, 1993.

[185] D. A. Shirley. High-resolution x-ray photoemission spectrum of the valence bands of gold. *Physical Review B*, 5(12):4709–4714, 1972.

[186] J. D. Baniecki, M. Ishii, T. Shioga, K. Kurihara, and S. Miyahara. Surface core-level shifts of strontium observed in photoemission of barium strontium titanate thin films. *Applied Physics Letters*, 89(2006):2004–2007, 2006.

[187] J Stoch and J Gablankowska-Kukucz. The effect of carbonate contaminations on the XPS O 1s band structure in metal oxides. *Surface and Interface Analysis*, 17(October 1990):165–167, 1991.

[188] Sanjiv Kumar, V. S. Raju, and T. R N Kutty. Investigations on the chemical states of sintered barium titanate by X-ray photoelectron spectroscopy. *Applied Surface Science*, 206:250–261, 2003.

[189] J. L. Wang, B. Vilquin, and N. Barrett. Screening of ferroelectric domains on $BaTiO_3$(001) surface by ultraviolet photo-induced charge and dissociative water adsorption. *Applied Physics Letters*, 101(9):092902, 2012.

[190] S. M. Mukhopadhyay and T. C. S Chen. Surface chemical states of barium titanate: Influence of sample processing. *Journal of Materials Research*, 10:1502, 1995.

[191] F. A. Kröger and H. J. Vink. Relations between the Concentrations of Imperfections in Crystalline Solids. *Solid State Physics*, 3:307–435, 1956.

[192] M. Müller, E. Soergel, and K. Buse. Light deflection from ferroelectric domain structures in congruent lithium tantalate crystals. *Applied Optics*, 43(34):6344–7, December 2004.

[193] Siham Ouardi, Gerhard H. Fecher, Xeniya Kozina, Gregory Stryganyuk, Benjamin Balke, Claudia Felser, Eiji Ikenaga, Takeharu Sugiyama, Naomi Kawamura, Motohiro Suzuki, and Keisuke Kobayashi. Symmetry of Valence States of Heusler Compounds Explored by Linear Dichroism in Hard-X-Ray Photoelectron Spectroscopy. *Physical Review Letters*, 107(3):036402, July 2011.

[194] N. A. Cherepkov and G. Schönhense. Linear Dichroism in Photoemission from Oriented Molecules. *Europhysics Letters*, 24(2):79–85, 1993.

[195] Andrea Damascelli. Angle-resolved photoemission studies of the cuprate superconductors. *Review of Modern Physics*, 75(April):473, 2003.

[196] E. Arenholz, G. van der Laan, A. Fraile-Rodríguez, P. Yu, Q. He, and R. Ramesh. Probing ferroelectricity in $PbZr_{0.2}Ti_{0.8}O_3$ with polarized soft x rays. *Physical Review B*, 82(14):140103, October 2010.

[197] S. Polisetty, J. Zhou, J. Karthik, A. R. Damodaran, D. Chen, and A. Scholl. X-ray linear dichroism dependence on ferroelectric polarization. *Journal of physics: Condensed matter*, 24:245902, 2012.

[198] G. Pilania, S. P. Alpay, and R. Ramprasad. Ab initio study of ferroelectricity in BaTiO3 nanowires. *Physical Review B*, 80(1):1–7, 2009.

[199] Minseok Choi, Fumiyasu Oba, and Isao Tanaka. Electronic and structural properties of the oxygen vacancy in $BaTiO_3$. *Applied Physics Letters*, 98(17):172901, 2011.

[200] Jochen Heyd, Gustavo E. Scuseria, and Matthias Ernzerhof. Hybrid functionals based on a screened Coulomb potential. *Journal of Chemical Physics*, 118(18):8207–8215, 2003.